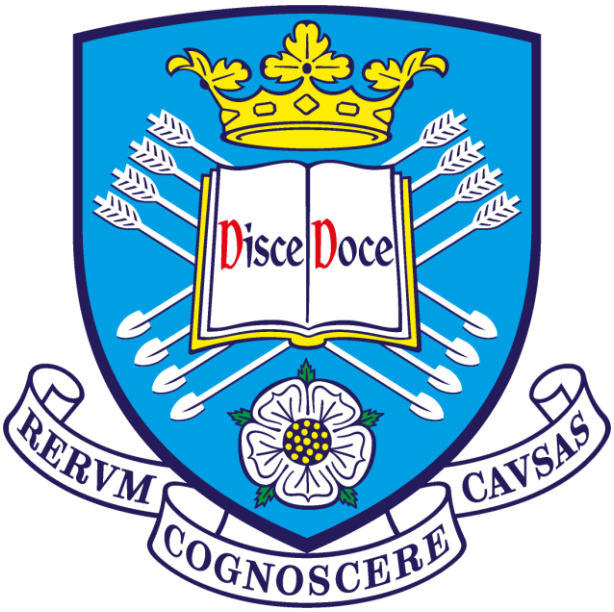

The University Of Sheffield

The calibration and measurement of spectrally resolved terrestrial solar irradiance using a low-cost laboratory grade spectrometer

Roberto Cahuantzi Alvarado

A thesis submitted in partial fulfilment of the requirements for the degree of Doctor of Philosophy

Faculty of Sciences
Department of Physics and Astronomy

June 2019

"Study hard what interests you the most in the most undisciplined, irreverent and original manner possible."

Richard Feynman

Abstract

This thesis aims to produce methods and tools that allow the acquisition of spectrally resolved data in a low-cost manner from which the calculation of spectral influence on electrical energy production of different photovoltaic technologies can be evaluated. For this purpose it was necessary to design a reliable cosine correcting coupler to reduce the error on the angular reading of the fibre optic which inputs the light to the spectrometers. This work produced a paper that demonstrated an improvement over the state of the art instrumentation for fibre coupled irradiance measurement (Cahuantzi and Buckley, *Review of Scientific Instruments*, 2017). The second stage focused on the calibration of the spectrometer for long term outdoor spectral data acquisition. This was achieved using the solar terrestrial irradiance as light source. From empirical data acquired by a pyranometer specific time points with near to clear sky were selected to be later used to produce calibration curves. The low-cost method of calibration presented in this thesis is demonstrated to be reliable for low resolution measurements used for solar spectral characterisation.

The spectral time series data acquired allowed a quantitative characterisation of the impact of the climatological conditions of the region on solar irradiance through spectral distributions and clearness indices. The results in spectral variation were used to calculate the influence of the solar spectra difference on the performance for different photovoltaic materials. A small difference in spectral variance was found between seasons, since a-Si presented a gain from summer to winter of +4.0% in contrast to the other technologies which had spectral effects of -5.0%, -5.4%, -6.3% and -7.0% for CdTe, c-Si, high efficiency (HE) c-Si and CIGS respectively. It is shown that the impact of spectral variation is minor when compared with the influence of other performance loss factors such as degradation and temperature, within the UK.

Acknowledgments

Agradezco a mis padres María de los Ángeles Alvarado Gallegos y Carlos Cahuantzi Maldonado el apoyo que siempre han mostrado a mi desarrollo dándome amor, tiempo y comprensión a manos llenas. Así también como agradezco a mis hermanos Ángeles, Carlos y Ricardo que han sido parte importante de mi equilibrado desarrollo emocional y han demostrado ser personas ejemplares en todos los aspectos de su vida. Agradezco a mi extensa familia; mis abuelos, tíos, primos y amigos que de alguna u otra forma siempre me han apoyado. Şi mulţumesc soţiei mele, pe care o iubesc cu toata inima mea, Frumosita!

I want to thank the University of Sheffield for the rewarding student experience during my staying in this great institution, to my supervisor Dr Alastair Buckley who generously shared with me his experience, time and knowledge, always kind and constructive on his feedback; special thanks to the wonderful Miss Nicola Connell, “The Wizard of Words”, for proofreading; the examiners who provided useful suggestions on how to improve the manuscript and last but not least; this work would not have been possible without the support of the National Council for Science and Technology of Mexico (CONACyT, CVU: 241981).

Declaration of Authorship

I, Roberto Cahuantzi Alvarado, declare that this thesis titled, “The calibration and measurement of spectrally resolved terrestrial solar irradiance using a low-cost laboratory grade spectrometer” and the work presented in it are my own. I confirm that:

- This work was done wholly or mainly while in candidature for a research degree at this University.
- Where any part of this thesis has previously been submitted for a degree or any other qualification at this University or any other institution, this has been clearly stated.
- Where I have consulted the published work of others, this is always clearly attributed.
- Where I have quoted from the work of others, the source is always given. With the exception of such quotations, this thesis is entirely my own work.
- I have acknowledged all main sources of help.
- Where the thesis is based on work done by myself jointly with others, I have made clear exactly what was done by others and what I have contributed myself.

Signed: 

Date: 13/06/2019

Contents

List of Figures

List of Tables

Notation

Acronyms

AM	Air mass
AM1.5	Air mass 1.5
AOD	Aerosol optical depth
APE	Average Photon Energy
a-Si	Amorphous silicon
ASTM	American Society for Testing and Materials
BF	Blue factor
CCD	Charged-coupled device
CCOC	Cosine correcting optical coupling
CdTe	Cadmium telluride
CIGS	Copper Iridium Gallium Sulphur
c-Si	Mono-crystalline silicon
E_C	Energy of conduction band
EOT	Equation of time
EQE	External quantum efficiency
FF	Fill factor
FWHM	Full width half mean
GaAs	Gallium arsenic
GHG	Greenhouse gases
IEC	International electrical commission
IR	Infrared
pc-Si	Poly-crystalline silicon (also known as multi-crystalline)
MM	Mismatch factor
OF	Optic fibre
pc-Si	Poly-crystalline silicon (also known as multi-crystalline)
PPM	Parts per million
ppmv	Parts per million per volume
ppbv	Parts per billion per volume
PTFE	Polytetrafluoroethylene
PV	Photovoltaic
PW	Precipitable water
QE	Quantum efficiency
SF	Spectral factor
SO_3	Sulphur trioxide
SR	Spectral response
SRC	Standard reporting conditions
SWF	Spectral weighted ratio
SWIR	Short-wave infrared
T	Temperature
UF	Useful fraction
UV	Ultraviolet
VLS	Very large scale
VNIR	Visible and infrared

Symbols

A	Ideality factor	I_0	Saturation current
A	Ampere	I_m	Current at the maximum power point
b_s	Incident spectral photon flux	I_P	Photo current
c	Light speed	I_{SC}	Short-circuit current
$^{\circ}C$	Celsius degree	**J**	Joule
CH_4	Methane	**K**	Kelvin degrees
CO_2	Carbon dioxide	K_B	Boltzmann's constant
C_{RV}	Compensation of Earth-Sun distance	**km**	Kilometre
E	Energy	K_T	Clearness index
e	Euler's number	**kWh**	Kilowatt-hour
E_0	Global solar irradiance	**kWp**	Kilowatt peak
eV	Electro volt	m	Mass
E_V	Energy of balance band	**m**	Meter
G	Broadband irradiance	**MW**	Megawatt
GW	Gigawatt	n	Amount of substance in mols
E_{dif}	Diffuse solar irradiance	**nm**	Nanometre
E_{dir}	Direct solar irradiance	N_{yr}	Number of days
E_{ETR}	Extra-terrestrial irradiance	O_3	Ozone
$E_{ETR,AOI}$	Extra-terrestrial irradiance on array's surface	P_{max}	Maximum power point
E_F	Fermi level	P_r	Pressure
e-h	Electron-hole	q	Electron charge
E_P	Energy of the photon	r	Universal gas constant
h	Planck's constant	R_S	Series resistance
H_2O	Water	R_{SH}	Shunt resistance
I	Current	V_d	Voltage drop

V	Voltage and its unit (Volt)
V_l	Volume
V_m	Voltage at the maximum power point
V_{OC}	Open-circuit voltage
W	Watt
x	Distance
α_S	Solar azimuth
β_S	Elevation angle
γ_S	Solar altitude
δ_d	Angle of day
θ_{AOI}	Angle of incidence
θ_s	Solar zenith
λ	Wavelength
µJ	Micro joule
µm	Micrometre
σ	Extinction coefficient
τ	Transmission
Φ	Monochromatic light flux
ϕ	Latitude
ω	Angle of hour
Ω	Ohm

1 Introduction

On September 26th, 2016 it was announced that the concentration of atmospheric CO_2 passed the threshold of 400 PPM [50], making even more pressing the necessity of sustainable means of energy production. In addition, 2016 was the hottest year in record, and it is believed that climate change is going to result in changes that will affect a high percentage of the world population and natural ecosystems [23, 70]. This environmental crisis triggered by the global greenhouse gases (GHG) emissions has increased the concern around the globe and has prompted an accelerated growth for renewable electrical power generation in the last 15 years.

1.1 Background

Solar has the highest growth rate among other renewables due to: (1) Its minimum maintenance, due to the lack of mobile parts, just require a periodically cleaning to avoid dust layers, or any other kind of shading; (2) an average use life of 25 years, with a degradation from 0.5% to 1% of its original efficiency per year, most of them have shown an 80% of their capacity after this 25 years [59]; (3) being modular, scalable and decentralized, and can be used to electrify rural and remote areas at a very competitive prices in comparison with diesel, coal or natural gas systems. This opens the door to a huge potential for alleviating the pressure in distribution networks.

This growth in the solar industry has been also accelerated due to (i) continual reductions in the manufacturing costs of photovoltaic (PV) cells, (ii) an increase in the cost of conventional electricity generation and (iii) growing limitation to access fossil fuels, which while not decreasing their production, it does decrease the energy efficiency for their obtention [104]. These factors do not operate independently for they are linked through a complex network of international markets, regulation and incentives; along with growing public understanding of the threat of global warming and the need for alternative energy production.

Within these changes to the global energy sector the performance of PV systems, namely the yield and lifetime, strongly influences the overall economics of both, financial and carbon footprint,

of the global energy system. It is important to be able to measure and forecast the performance of PV installations to produce optimal deployment of these technologies.

Despite of the deceleration of the PV industry of 2012, in 2015 there was a rebirth of installed PV capacity. Furthermore, in just the past two decades its cost has reduced by 60% and performance improvement in the last ten years has been roughly 40%. These trends enable PV-technologies to become economically competitive, not only in off-grid installations but also on-grid applications. For countries with good solar resources [91, 94] due to their low environmental impact and GHG emissions (50 to 60.1 gCO_2-eq.kWh^{-1}) represent a better option in comparison with mainstream electricity generation technologies, such as Coal (888 to 1,050 gCO_2-eq.kWh^{-1}), Natural gas (499 to 611 gCO_2-eq.kWh^{-1}) or oil (733 to 778 gCO_2-eq.kWh^{-1}) [39, 75]. In in addition some unused and economically sterile ecosystems in Middle East and North Africa (MENA) could be used to harvest PV electricity to feed into the European grid at high competitive costs, there are some plans to do so after 2026 [108].

As of 2016 Solar PV has a reported installed capacity of 320 GW and is expected to grow to around 716 GW by 2020 [93]. Therefore it is necessary to have reliable methods to gather information to understand and forecast of solar irradiance and its potential impact on PV systems under different conditions.

1.2 Aims and Objectives

The present chapter is just an introduction of the general scope of this thesis, while chapter 2 will provide a deep background of the basic concepts and literature review relevant to the development of the project. This thesis presents three experimental chapters which aimed to produce tools and methods to be used regions which might lack of proper resources to acquire spectrally resolve data. The first experimental chapter is chapter 3, in which it is detailed the inexpensive production of reliable cosine correctors based on the material Polytetrafluoroethylene (PTFE), the results of this chapter were published in the journal Review of Scientific Instruments in September 2016 [19]. Chapter 4 describes a method for absolute calibration of spectrometers using terrestrial solar irradiation and the complications faced during this stage. Chapter 5 focuses on the general analysis to characterise the solar spectral behaviour using the index of Average Photon Energy (*APE*) and using the expected extra-terrestrial solar irradiance a clearness index (K_T) characterisation, there is also a comparison of different technologies to determine the seasonal spectral variation effect upon them.

Originally, the proposed work of this PhD aimed at providing guidance for the optimal PV technology that would be better suited according to the regional solar spectral variation profile. In the development of the project several challenges were found that changed the primary focus of the research towards the development of reliable solar spectral irradiance studies based on low-priced options. The methods and tools proposed in this thesis have great potential to increase the volume of spectrally resolved solar irradiance data and this in turn will improve the accuracy of forecasting models by having a larger available training datasets.

This analysis framework would be most applicable to regions with rich solar resources (also known as sun-belt regions), which lack sophisticated facilities to acquire spectrally resolved data. However, these regions hold the highest potential to harvest energy through solar panels. Therefore it is important to produce inexpensive techniques and research methods for characterisation of the solar resource in these regions.

2 Literature review

This chapter provides a brief account of the current knowledge, concepts and methods related to this project. This includes a section of solar power, explaining the principles of solar irradiation, the natural processes that generate it and affect it before it reaches the Earth's surface. It also discusses the physical principles that generates the photovoltaic effect, the characteristics of a PV cell, its theoretical limits, and the standard reporting conditions. It explores the basic function of a spectrometer and approaches to achieve its calibration. It also discusses the current literature concerning to regional irradiance characterisation and modelling, as well as comparison of different PV technologies in-field.

2.1 Principles of solar power

2.1.1 The sun

If we could somehow take in the 3.8 x10^{20} MW power that the sun irradiates even for a single second, we could satisfy all human energetic necessities for around half a billion years. Our star has a diameter close to 1.4 million km and a temperature in its core of around 16 million degrees Kelvin. At this point the pressure from gravity overcomes the electromagnetic force forcing nuclei to fuse generating a thermonuclear fusion reaction, creating heavier atoms from lighter ones, in doing so a small fraction of the nucleus mass is transformed into energy at a rate described in the famous Einstein equation 2.1. The energy released makes its way out from the sun, cancelling the gravity sufficiently to prevent the star from collapsing under its own gravitational force.

$$E = m\,c^2 \qquad 2.1$$

Where *E* is energy, *m* stands for mass and *c* is the universal constant of causality also known as light speed. A photon is a massless particle with no electrical charge which together with electromagnetic waves are the forms of propagation for electromagnetic radiation. According to quantum mechanics the energy a photon contains is restricted to discrete values which are multiples of Planck's constant and proportional to its frequency. Since the photon's speed in the vacuum is

the constant *c*, the frequency can be defined as *c* divided by λ the photon's wavelength. This give us equation 2.2 for energy of a photon [71].

$$E_P = \frac{h\,c}{\lambda} \qquad 2.2$$

Where E_P is the energy of the photon, *h* stands for Planck's constant, with a value of roughly 6.63×10^{-34} J s and λ is the wavelength expressed in m. Every photon emitted from the sun that goes in direction of Earth takes around 8 minutes and 20 seconds to cross about 150 million km to reach Earth distance, this is equivalent to the radius of the ellipsoid orbit that the planet follows around the sun.

2.1.2 Solar resource

All objects with temperature above absolute zero irradiate energy as a function of their temperature. This phenomenon is known as blackbody radiation. Despite the high temperature at its core the sun has a radiation corresponding to an object of 5,800 K on its surface. The power the sun emits varies around 0.1% every 11 years [27] due to its sunspots' cycle. However by convention, the solar constant (E_{etr}) is considered to have a value of 1,367 W m^{-2}. The surface temperature of the sun produces a radiation of a black body in relation to Planck's Law (equation 2.3)

$$E_{\lambda,T} = \frac{2hc^2}{\lambda^5}\frac{1}{e^{\left(\frac{hc}{\lambda k_B T}\right)} - 1} \qquad 2.3$$

This equation represents the density of quantised radiation per unit frequency interval at temperature *T*. Since *c* and k_B are also constants namely: Boltzmann, of around $1.38\text{x}10^{-23}$ J K^{-1} and the speed of light which is near to $2.99\text{x}10^{8}$ m s^{-1}, respectively, equation 2.4 can be simplified as follows [61]

$$E_{\lambda,T} = \frac{3.74x10^{8}}{\lambda^5\left(e^{\left(\frac{14{,}400}{\lambda T}\right)} - 1\right)} \qquad 2.4$$

Here $E_{\lambda,T}$ stands for the monochromatic emissive power by area (m^2), *T* represents the temperature in Kelvin degrees and λ is the wavelength of the electromagnetic emission for this equation expressed in units of μm. This shape is a result of the natural limit for the discrete emission and absorption of electromagnetic radiation, namely quanta. Figure 2.1 illustrates the increasing levels of radiation as a function of the temperature of a blackbody.

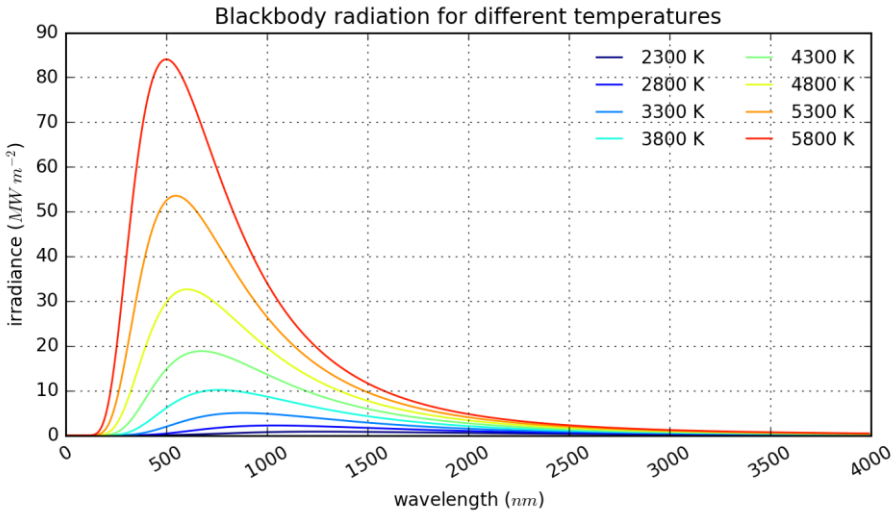

Figure 2.1: Shapes of blackbody radiation for different temperatures, based on Planck's law. The low irradiance in UV values are limited by the discretional value of Planck's constant

As previously stated, the solar extra-terrestrial insolation is of about 1,367 W m^{-2}. The measured spectral distribution closely matches the shape of a blackbody of 5,800 K, as seen in Figure 2.2, where the limits of the visible light, the infrared (IR) and ultraviolet (UV) regions are shown. IR and UV correspond to 46% and 7% of the total solar radiation, while visible light has a share of about 47%.

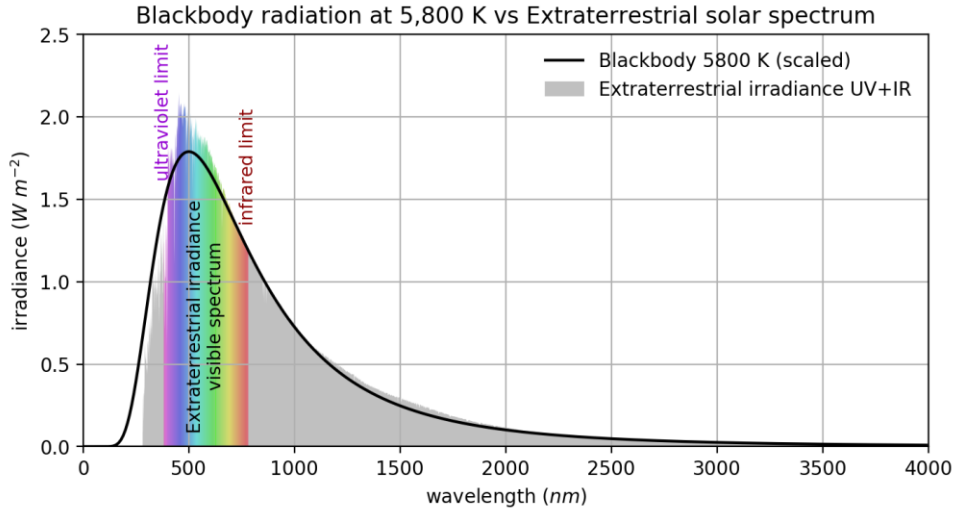

Figure 2.2: Fitting of 5800 K blackbody radiation to empirical extra-terrestrial irradiance. The grey area plus the multi-coloured represent the total extra-terrestrial irradiance [1] while the black line is the scaled blackbody radiation calculated in function to the surface of the sun.

From this it can be estimated that Earth receives a power of approximately of 162,000 TW from the sun. From this a share of about 86,000 TW reaches the surface [37, 48, 81], making the energy the planet receives yearly approximately 2.71 x 10^{15} GJ. To put this in perspective, in 2018 the total human consumption of primary energy was around 5.85 x 10^{11} GJ [16]. From this we can

see that the energy demand of the world population is a minor fraction of the solar energy given per year. Therefore the necessity to consider the solar resource as a solution to our energetic needs is undeniable.

Exergy is defined as the useful portion of energy, and describes not only the quantity of the energy but also its quality. In figure 2.3, from Hermann, 2017 [37], it is possible to appreciate the exergy fluxes within the planet, how humans can access them and to some exploitable reservoirs. The mechanisms cutting down the solar resource on the surface will be explained in the next section.

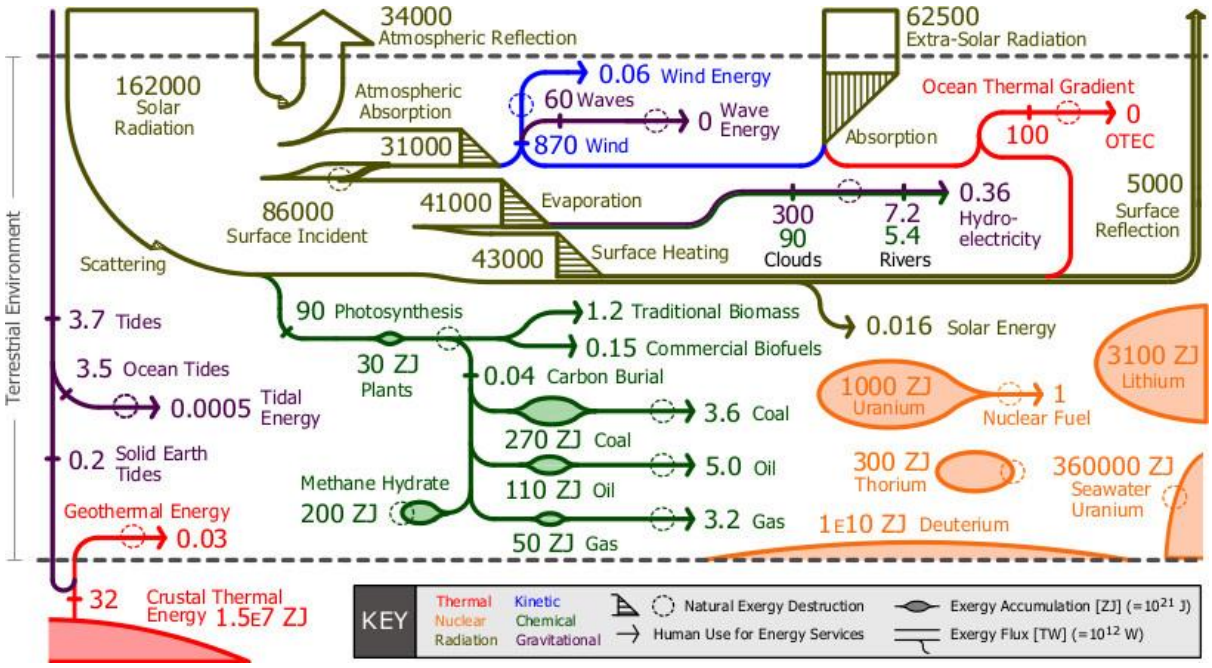

Figure 2.3: Comparison of finite and renewable exergy reserves. The exergy flux is in TW, whereas the exergy accumulation in ZJ, adapted from Hermann [37].

2.1.3 Extra-terrestrial irradiance

As seen in section 2.1.2, the extra-terrestrial irradiance (E_{ETR}) is defined as the solar energy per unit of area just above the atmosphere. By convention the value is defined as 1,367 W m^{-2}. The Earth has a quasi-elliptical orbit, when the northern-hemisphere experiences winter, the planet is at its closest to the sun, this point is called the perihelion and in summer it is at its farthest, this is called aphelion. To compensate for the variations of distance between sun and Earth throughout the year it is first necessary to calculate what is called the day angle, which is estimated in radians using equation 2.5.

2.5

$$\delta_d = (J - 1)\left(\frac{2\pi}{N_{yr}}\right)$$

Where δ_d is the day angle, J the Julian day (1 for 1st of January, 32 for 1st of February; and so on) and N_{yr} is the number of days of the year (365 for regular years and 366 for leap years). To later use equation 2.6, which gives us an approximate of the ratio of the mean Earth-Sun distance (approximately 1.4960×10^{11} m), also called astronomical unit.

2.6

$$C_{RV} = 1.00011 + 0.034221 \cos\cos \delta_d + 0.00128 \sin\sin \delta_d + 0.000719 \cos\cos 2\delta_d + 0.000077 \sin\sin 2\delta_d$$

The general annual dynamic between Sun and Earth can be seen figure 2.4. The event in which the sun reaches its highest annual altitude, rendering that day the longest, or shortest, depending on the hemisphere where it is experienced, is called solstice. This occurs twice per year usually December 22nd and June 22nd. On the other hand the equinoxes are dates in which the day and the night have equal duration, this usually happens both on September 23rd and March 20th.

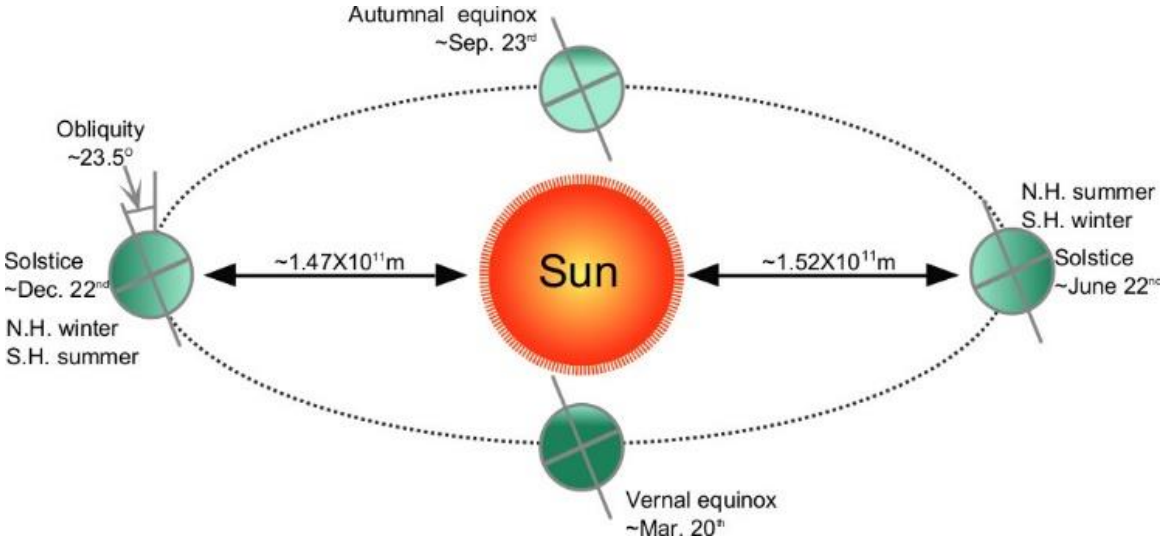

Figure 2.4: Typical annual translation of the Earth around the sun and relationships during solstices and equinoxes, N. H. stands for Northern Hemisphere and S. H. for South Hemisphere

From the solar extra-terrestrial irradiance (E_{ETR}), we can calculate extra-terrestrial solar irradiation on a given surface ($E_{ETR,AOI}$). *This is found* by multiplying E_{ETR} by the factor of compensation for Earth-Sun distance C_{RV} and the cosine of the angle of incidence on the given surface (θ_{AOI}) as seen in formula 2.7.

2.7

$$E_{ETR,AOI} = E_{ETR} \cos \theta_{AOI} C_{RV}$$

Here θ_{AOI} comes from equation 2.12 and represents the angle of incidence for a surface at a given slope. This is described in more detail in section 2.1.4.

2.1.4 Solar geometry

The trajectory the sun follows during day hours, namely the solar path, depends on both the latitude of the location and the date. Knowing the day angle from section 2.1.3 allows the calculation of the Equation of time (*EOT*) yielding results in minutes, with the formula 2.8, from [41].

$$EOT = 229.18\,(0.000075 + 0.001868\,cos\,\delta_d\ - 0.032077\,sin\,\delta_d\ - 0.14615\,cos\,2\delta_d - 0.04089\,sin\,2\delta_d\ ) \quad 2.8$$

With the *EOT* is possible to calculate the angle of hour, which is calculated giving the hour a decimal value with the formula 2.9.

$$\omega = 15\left(h + \frac{m}{60} + \frac{s}{3600} + 4\left(\frac{l_{TZ} - l}{60}\right) + EOT\right) - 180 \quad 2.9$$

Where ω stands for angle of hour, h means the hour of local time, m stands for minutes of local time, s is seconds in local time, l_{TZ} represents the longitude of time zone meridian of the location and l stands for longitude of the site. The result's units are degrees.

With respect of the site where the PV module is placed, there are two main angles used to define the sun's position in the sky. Also there are two angles needed to define the sunlight angle of incidence on the module, as seen in figure 2.5:

- Solar zenith (θ_S): The complementary of the elevation angle (β_S), this is the angle between the centre of the solar disc subtended to the normal of the plane.
- Solar azimuth (α_S): The horizontal angle between the plane containing the centre of the solar disc and the vertical plane running in north south direction.
- The solar incidence angle on a plane for plane's azimuth (α) and slope (β): as the angle between the normal to the plane of the PV module and the plane where the sun is shining.

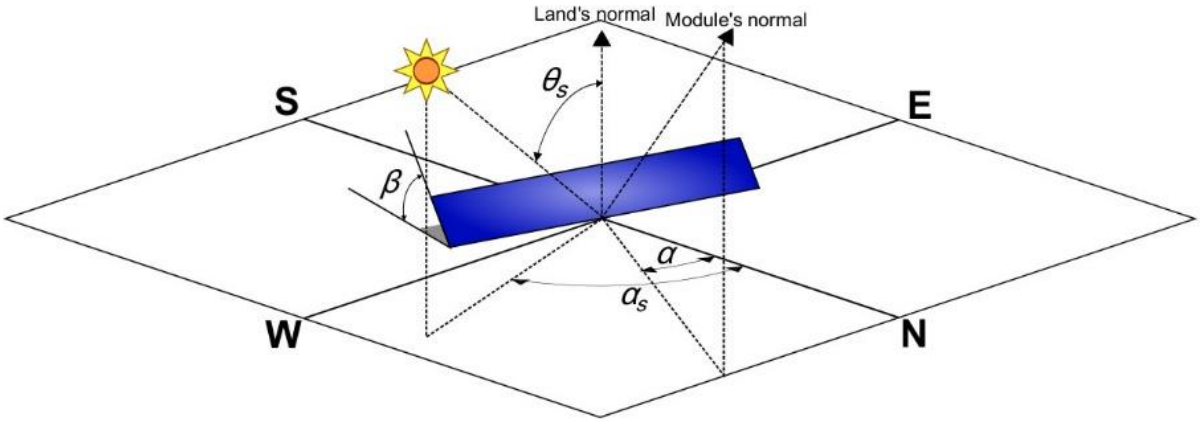

Figure 2.5: Definition of angles in solar geometry

To calculate the solar zenith angle it is necessary to find first the declination angle (δ). This is the apparent tilt angle of the Earth on its axis of rotation. It changes with the seasons, and can be approximated by the formula 2.10.

2.10

$$\delta = \frac{180}{\pi}(0.006918 - 0.399912\cos\delta_d + 0.070257\sin\delta_d - 0.006758\cos 2\delta_d + 0.000907\sin 2\delta_d - 0.002697\cos 3\delta_d + 0.00148\sin 3\delta_d)$$

The solar zenith angle θ_S is obtained by the formula 2.5.

2.11

$$\theta_S = \cos^{-1}(\cos\delta\cos\phi\cos\omega + \sin\delta\cos\phi)$$

Where ϕ is the latitude of the site. Once these angles have been calculated it is possible to calculate the solar elevation angle (β_S) as the complementary angle of the solar zenith (θ_S). Which together with angle of declination (δ), slope (β), latitude (ϕ) and angle of hour (ω) can calculate the Angle of Incidence (θ_{AOI}) on the module. The equation for this calculation is 2.12.

2.12

$$\theta_{AOI} = \cos^{-1}(\sin\delta\sin\phi\cos\beta - \sin\delta\cos\phi\sin\beta\cos\gamma_S + \cos\delta\cos\phi\cos\beta\cos\omega + \cos\delta\sin\phi\sin\beta\cos\gamma_S\cos\omega + \cos\delta\sin\beta\sin\gamma_S\sin\omega)$$

This value is necessary to calculate the direct (E_{dir}) and diffuse irradiance (E_{dif}), as the extra-terrestrial irradiance ($E_{ETR,AOI}$) on the module, as shown in section 2.1.5

2.1.5 Radiative energy transfer through the atmosphere

The solar radiation that crosses the atmosphere affects temperature, pollutant concentration, visibility and colour at the Earth's surface. This is due to the radiation interaction with the ground, gases, aerosol particles and water particles. When the radiation reaches a body it can be absorbed, reflected, refracted, dispersed, diffracted, scattered or transmitted.

Absorption occurs when electromagnetic energy enters a substance and is converted to internal energy. When the absorbed energy is re-emitted it is called reflection, and is defined as the reemission of absorbed electromagnetic radiation at an angle equal to the angle of incidence. The reflectivity of a surface is called albedo. The concept of refraction is described as the change of direction of electromagnetic radiation when it enters a medium of different density. If the wave enters a medium of higher density it refracts towards the surface's normal, to the ratio in the change of direction of propagation of the wavelength is called refractive index.

The phenomenon of decomposition of white light into individual colours by selective refraction is called dispersive refraction or dispersion. This is due to the high energy properties of the different wavelengths making blue-leaning light bend more when entering a higher density medium in comparison to red-leaning light. This is similar to the diffraction effect, which is the bending of waves as they pass by the edge of an obstruction. The combination of reflection, refraction and diffraction is known as scattering, this and other atmospheric effects are can be seen in figure 2.6.

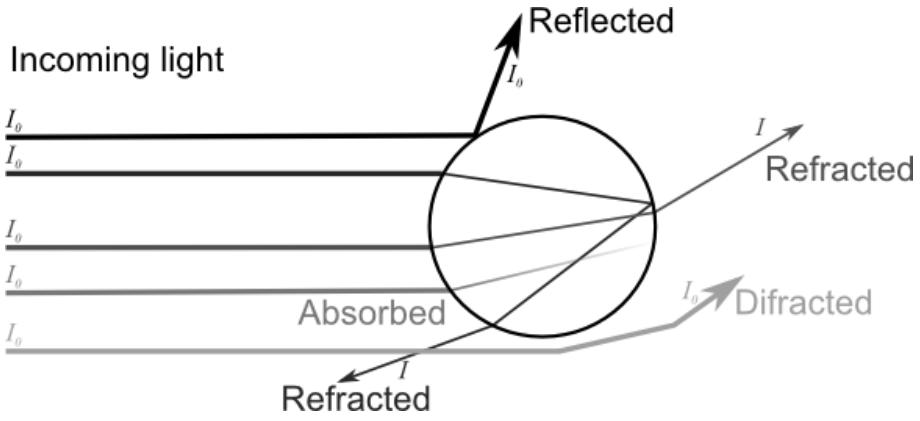

Figure 2.6: Visual summary of some of the principal phenomena in the atmosphere. The circle represents a particle of an atmospheric species (e.g. a cloud drop), while the different lines a given monochromatic ray of light. Here it is displayed how the incoming light changes its direction due to reflection, diffraction and refraction; forming the scattering. The scattering can be defined based on the resulting direction of the light as back-scattering, side-scattering and forward-scattering Atmospheric effects on solar irradiance. Also, it is displayed how some radiation gets absorbed completely while some other partially or not at all. The different tone of the light rays is just intended to make them look distinct, these do not reflect light intensity.

The solar spectrum varies with the geographical location. Latitude, longitude and elevation affect the perceivable movement of the sun on the sky-dome and thus the path the sunlight must traverse. The most common index to characterise this is Air Mass (*AM*), defined as the actual path length of the sunlight through the atmosphere (h_1) normalised to the shortest possible path length (h_0), namely when the sun is in an angle of elevation of 90˚ with respect to the observer. There are several way to calculate it the simplest approximation is as seen in equation 2.13.

2.13

$$AM = \frac{h_1}{h_0} = \frac{1}{sin\,\beta_S} = csc\,\beta_S$$

Here β_s refers to the elevation angle of the sun, which was explained in section 2.1.4. To optimise the electrical energy production of a PV system it is necessary to find the tilt and azimuth in which the sun irradiance would travel a shorter *AM*. Formula 2.14 can be use to describe the attenuation of light while being transmitted through a gas:

2.14

$$\Phi_\lambda = \Phi_{0,\lambda}\,\tau_\lambda$$

Being:

2.15

$$\tau_\lambda = e^{-\sigma_\lambda x}$$

Where Φ_λ is the monochromatic light flux passing through a distance *x*, $\Phi_{0,\lambda}$ is the incident monochromatic light flux, τ_λ stands for transmission for wavelength λ, the symbol σ_λ is a constant determined by the material through which the monochromatic light flux transitions, known as gas absorption extinction coefficient; and *x* is the path the light flux goes through. Transmission at concentration *C* can be determined by formula 2.16, here *C'* is a reference concentration.

2.16

$$\tau_\lambda = e^{-\sigma_\lambda \frac{C}{Cr} x}$$

Since concentration and pressure are linearly related through the ideal gas law, see equation 2.17, in which P_r signifies pressure, V_l, volume; *n* stands for amount of substance (mol), *r* is the universal gas constant (8.31 kg m^2 s^{-2} K^{-1} mol^{-1}) and *T* stands for temperature.

2.17

$$P_r V_l = n\,r\,T$$

There is also an analogous equation if the concentration is given in terms of pressure. Here P_r is a given pressure, and P_r' a reference pressure, see equation 2.18.

2.18

$$\tau_\lambda = e^{-\sigma_\lambda \frac{P_r}{P_r r} x}$$

This is a general explanation of the modelling used to calculate the extinction of certain wavelength bands based on the atmosphere gas content. In figure 2.7, it is shown how the extra-terrestrial irradiation coming from the sun gets absorbed by the atmospheric gases. This is the reference Air Mass 1.5 spectrum ASTM G173-03 for Standard test conditions [4], taken from the incident irradiance on a sun-facing surface on 37˚ tilted. For this purpose there is another standard available

the IEC 60904, however the ASTM standard was widely available. The contrast of between both standards will be further explained in section 2.4.1.

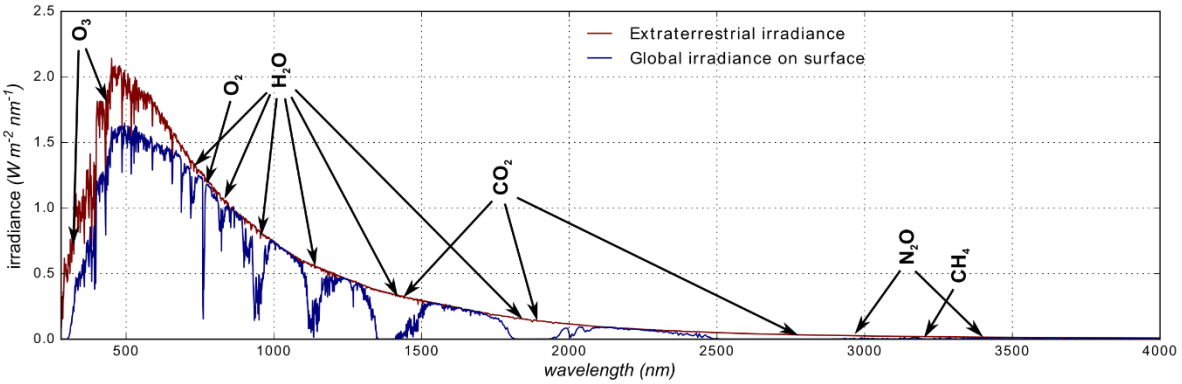

Figure 2.7: Reference of Extra-terrestrial and AM 1.5 irradiance spectra from ASTM and the absorption effect the different gases in the atmosphere produce over the solar spectrum [4]

Global irradiance (E_0) is the sum of diffuse and direct irradiance on a given surface. For clear days the calculation of both components relies on the absorption spectrum for the gases in the atmosphere, as well on the other parameters such as aerosol optical depth (*AOD*), measure of the extinction of the solar beam by dust and haze, asymmetry factor (the ratio of forward scattering over backward scattering), albedo (reflection from the surfaces) and the concentration of the absorption gases such as water and ozone, among others.

In the atmosphere there are two main interactions which produce attenuation of light: scattering and absorption. While light scattering only redistributes the light in the atmosphere, the absorption converts the light taken in by the molecules of the gases into internal energy, which increases the thermal speed of the gas thereby the temperature in the atmosphere. While ozone (O_3) absorbs Ultra-Violet (UV) rays well, the greenhouse gases strongly absorb Infra-Red (IR) radiation. The most common are: CO_2, CH_4, N_2O, O_3 and H_2O in form of vapour [36], figure 2.8 shows the absorption bands of these gases.

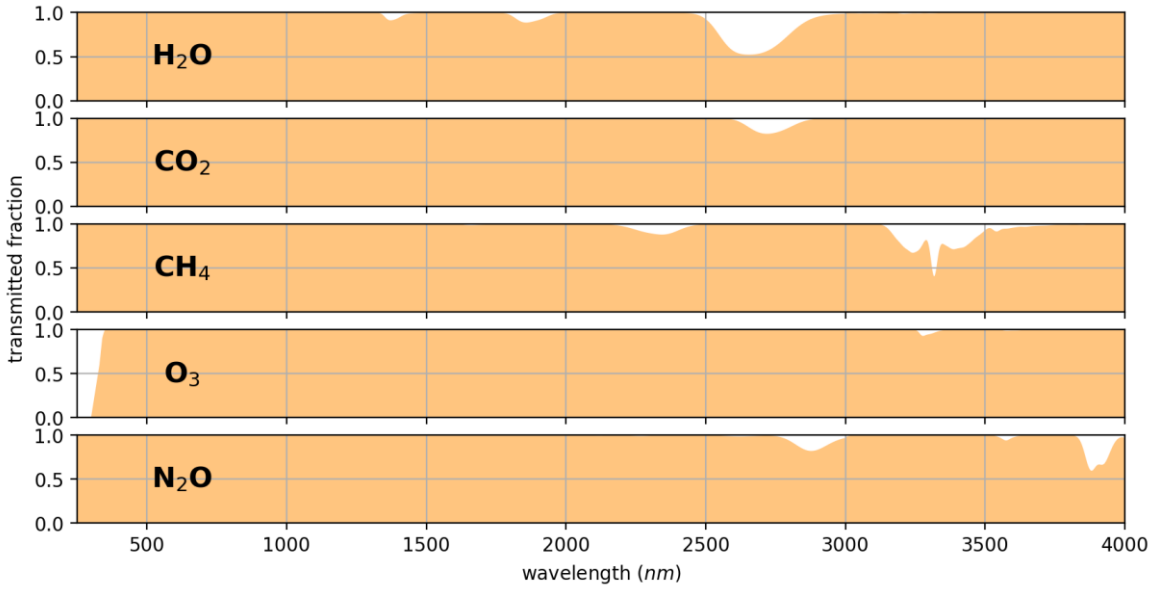

Figure 2.8: Transmission spectra showing the main gases effect on solar extra-terrestrial irradiance. This plot gives an idea of the spectral bands that are more affected, adapted from CLEAN, 2011 [99].

For more detail a general description of the effect that some of the most important species within the atmosphere influence the terrestrial solar irradiance will be explained in the next paragraphs:

Ozone (O_3): This gas absorbs the UV light for ranges mainly below 350 nm but also between 450 nm to 750 nm of wavelength. The filter that ozone provides is essential for the life on Earth, since UV radiation deteriorates some organic tissues. However its concentration in urban and rural areas, as a by-product of certain processes involving nitrogen oxides (NO_X) and volatile organic compounds, can cause headache, chest pain, decrease of lung function and increase susceptibility to bacterial infections. This happens when the concentration exceeds 0.1 parts per million by volume (ppmv), the usual concentration is around 0.02 to 0.04 ppmv at sea level.

Nitrogen dioxide (NO_2): This gas is normally present in polluted air in concentrations of about 0.1 ppmv to 0.25 ppmv, in high concentrations its colour can be described as yellow-red, it has strong absorption in the blue regions of the spectrum but this decreases at larger wavelengths.

Water vapour (H_2O): It has a typical concentration of 0 to 6 ppmv, and it is the main greenhouse gas since it accounts for around 90% of the naturally occurring increment of 33 K [44] of temperature in near-surface air, reaching 288 K. Despite being transparent for most visible radiation, it absorbs weakly above 700 nm and strongly around 1,400 nm, 1,900 nm (see figure 2.7) and from 12,000 nm onwards.

Carbon dioxide (CO_2): It is the second most important and abundant natural greenhouse gas. It absorbs radiation around 3,000 nm, 4,000 nm and 10,500 nm. The reason why it has an important

role in the current climate change is due to the later absorption band, since the near-surface temperature is in average 288 K the peak of Earth's up going thermal radiation is around 10,200 nm and the strong absorption of H_2O and CO_2 in this region let only between 15% to 30% of the radiation scape.

Particles: The light absorption by particles is mainly elemental carbon dust or molecules containing carbon. Since carbon is a conductor, the electrons can absorb almost any portion of energy, taking place in a wide range of wavelengths. This is mainly considered "Urban aerosol" due to pollution. These particles cause the Aerosol Optical Depth (*AOD*) and scattering independent of wavelength.

Gas scattering: When the radiation is redirected by a gas molecule without a net transfer of energy to the molecule it is called gas scattering. This is different to could drops and aerosol particles that mostly produce forward-scattering. Visible radiation does not diffract easily around gas molecules because the diameter of the molecules is much larger than the length of the visible light electromagnetic waves. This means that gases mostly scatter the shortest wavelengths, related to the blue hue, while the particles scatter all wavelengths relatively equally. Explaining why the sun seem to change its colours at noon, afternoon and twilight, as seen in figure 2.9.

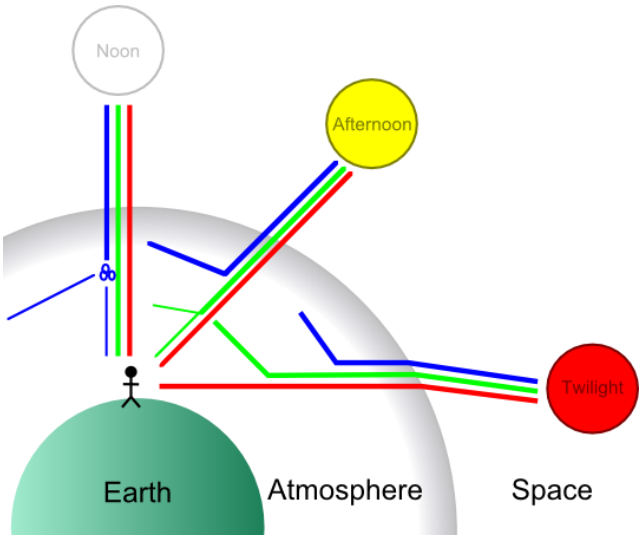

Figure 2.9: Apparent change of sun coloration during the day. The human figure represents the observer. At noon the sun seems white because there is a larger portion of blue light is received into the observer's eyes. In the afternoon a portion of the blue light is scattered allowing a larger share for green and red light. At twilight the sun seems red due to the refraction between the space and Earth's atmosphere and the longer path the light takes to cross. Adapted from Jacobson, 2005 [44].

2.2 Principles of photovoltaic effect

A material or device capable of transforming the energy contained in photons into electrical energy is known as PV. The principles used in PV technologies is closely related to diodes and

transistors. To understand how the photovoltaic effect works, it is first needed to have general knowledge of energy bands, carriers, semiconductor materials, photoelectric, and photovoltaic effect.

2.2.1 Semiconductors

Materials can be classified by their property to transmit electrical current. Those which cannot conduct electricity are known as insulators, those which can, as conductors. In between with a resistivity of between 10^{-2} to 10^{9} Ω cm we find the semiconductors. The ability a material has to conduct electricity is based on the quantity of free electrons in the structure of their atoms. Due to the discrete nature of energy levels in quantum mechanics, electrons form layers, also called orbitals, around the nucleus (also known as core). The Pauli's exclusion principle tells us that each orbital has capacity only for two electrons, there could be several orbitals in an energy level, the lowest the energy level the closer the orbitals are to the nucleus. The electrons will fill one by one each space in the energy level. For example, the second energy level has four orbitals, and since the electrons try to avoid each other due to their equal negative charge, four electros will occupy their own orbital, until all the orbitals are occupied by one electron then a fifth electron, aiming for the lowest possible level of energy, will take a place in the first orbital of this energy level. They will fill each orbital in the energy level so far they do not violate the exclusion principle. Once filled the current level the next electron will start to fill the next energy level. Following with this example it will be the third level with nine orbitals.

The electrons fill the lowest energy orbital first and then successively each orbital outwards, when the outermost orbital is not entirely filled, the "necessity" to fill this orbital produces the molecular bonds. This will happen just given the case that another atom nearby shares its outermost electron or electrons, which depends on different factors, like the size of the atom, temperature, etc. The farther from the nucleus an electrons is the more probability has to flow and be shared with another atom. This energy level is called the conduction band and electron with energy below this level are considered to be in the valence band. The energy required to excite electrons into the conduction band is known as the band-gap. Many atoms have enough free electrons, and no extra energy is required to put them in the conduction band. For some materials room temperatures provide enough energy to allow some of these electrons jump into the conduction band. These materials are defined as semiconductors, materials with an energy band-gap that lies between zero and about 3 eV (1 eV = 1.602 x 10^{-19} J) [113], with some exceptions.

These materials are perfect insulators at absolute zero (0 K) but at room temperature can be conductors, since this conditions are enough for their electrons to be excited from the valence band

(E_V) to the conduction band (E_C). This behaviour is due to a magnitude of the materials called Fermi level (E_F), which is defined as the hypothetical energy level at a temperature above 0 K in which there is a 50% of probability of occupation by an electron of the outer shell at any given time. It accounts for potential and kinetic energy, and it is also called electrochemical potential. The diagram in figure 2.10 shows the different material classifications based on the aforementioned concepts.

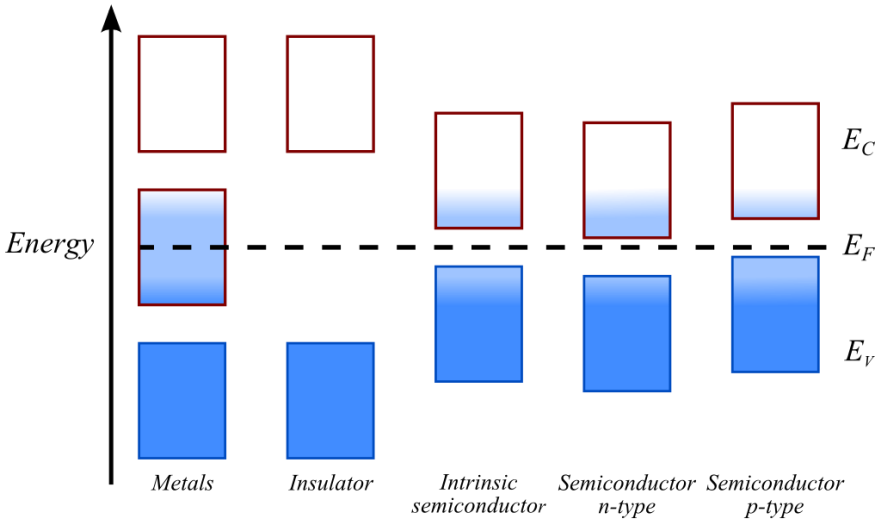

Figure 2.10: Fermi level in different types of materials, the red empty frame indicates the potential conduction band and blue area indicates valence band. E_C stands for energy of conduction band, E_F for Energy of Fermi level and E_V for Energy of valence band, adapted from Kittel et al. [52]. Given that the Fermi level is the level of energy that has a 50% chance of occupation by an electron the blue fading regions within the conduction and valance bands in the semiconductors can be interpreted as the probability of occupation by electrons at room temperature namely 25˚C.

2.2.2 PN junctions

When the fermi level (E_F) of a semiconductor material is close to the conduction band it is called a p-type semiconductor (“n” for negative), if it is close to the valence band is called a p-type. When an electron in their outer shell gain enough energy they can leave their position within the atom and move through the lattice (namely the arrangement of the atoms within the solid structure). The atom in question would gain a net positive charge which is called a hole. If there is a no way to drag the electron, it will eventually recombine with the hole releasing a photon.

The most common example used to illustrate the behaviour of p and n type semiconductors are the silicon doped types. In figure 2.11 it is shown a scheme illustrating how silicon could use phosphorus atoms as donors of electrons and boron atoms as acceptors. Doping increases the conductivity of the semiconductor since the density of charge carriers is increased without necessity of a constant input of energy. Even in the case of p-type semiconductors, since one can imagine that holes are particles that are free to flow which have opposite charge to electrons but same magnitude.

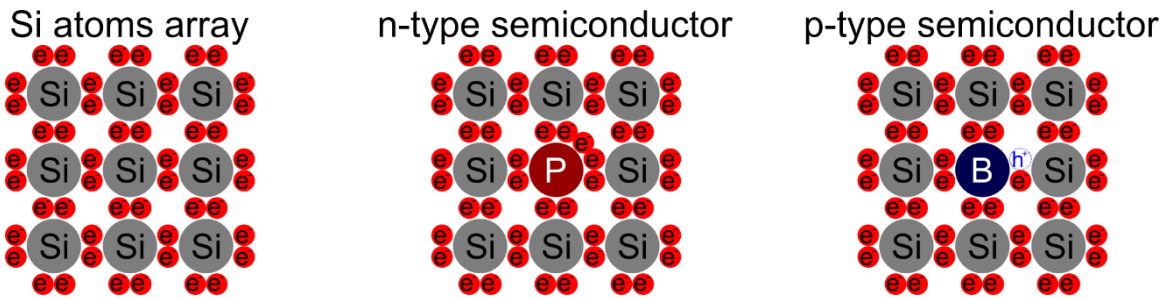

Figure 2.11: Scheme representing intrinsic and extrinsic semiconductors. (left) Representation in 2D of an intrinsic silicon lattice. (centre) An n-type doped where the extra electron is loosely bound to the donor atom, when extra ionising energy is applied the extra electron is freed from the donor and the donor becomes positively charged. (right) A p-type doped lattice where the acceptor atom has one too many electrons, the taken has a stronger bond to the impurity than to the normal crystal atom, and the hole created is free to move. The ratio Si-dopants presented here are exaggerated, since real ratios are about 10^{-3} for phosphorus and 10^{-7} for boron, adapted from Nelson et al., 2008 [71].

The basic structure of a single-junction PV cell is that of a diode. This is to say, there are two layers of semiconductors; a n-type, containing an increased density of electrons and reduced density of holes; and a p-type, with an increased density of holes and reduced density of electrons, both electrons and holes are called carriers. The carriers are classified as majority carriers or minority carriers depending on the side they are found, namely for the n-type region, electrons would be majority carriers and holes would be minority carriers.

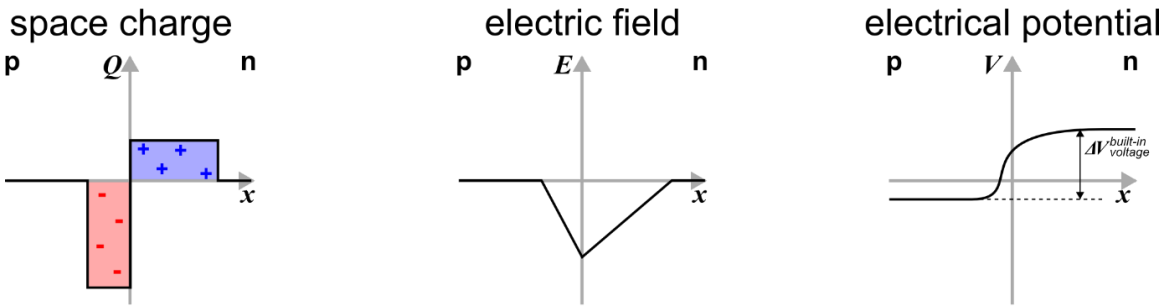

Figure 2.12: Doping profile, electric field and potential variation. (left) The space charge is generated by the charge of the immobile cores in the lattice, since the extra electrons in the n-side moves towards the p-side to fill the holes, the atomic cores left behind gives to this region a net positive charge in the n-side and negative in p-side of the depletion zone, keeping electrons and holes from crossing. (centre) The electric field is 0 outside the depletion zone indicating that there is no net movement of charges, however within the depletion zone it varies linearly. (right) Lastly the electrostatic potential varies quadratically across the depletion zone ΔV represents the built-in voltage, adapted from Nelson et al., 2008 [71].

When these layers adjoin with a perfect interface in the x axis it is called a junction. When both layers are in contact, electrons and holes recombine making the regions beyond these boundaries neutral, this is referred as junction being in equilibrium. As the electrons in the n-type cross to the junction and fill the holes in the p-type, they leave an immobile positive charge in the n-region, as well as an immobile negative charge in the p-type. These immobile charged regions create an electric field that work against the movement of electrons and holes across the junction

this region is called depletion zone, since in this zone there is no more free carriers. A diagram representing the charge, potential and electric field of a typical junction can be seen in figure 2.12.

There are two phenomena that describe the movements of the carriers through the lattice: diffusion and drift. Diffusion is analogous to the movement of molecules in a gas, the constant random motion of the carriers leads to a net movement from the regions with high concentration of carriers to regions of low concentration. The movement by drift is induced when an electric field is imposed on the semiconductor, electrons would move opposite to the electric field and holes in the direction of the electric field.

When a forward bias voltage is applied, namely the positive terminal in the p-type and the negative in the n-type, an electric field opposite to that in the depletion zone is applied across the device and since the resistivity in the depletion zone is higher than the rest of the device the applied electric field is applied in the depletion region, reducing the net electric field of the depletion zone. This reduce the barrier and allow for the diffusion of carriers to the opposite side letting the current to cross the device. In the opposite case, known as reverse bias, the holes and electrons will be drifted away of the depletion zone increasing its area allowing only a minimal portion of the current to cross the junction, making it virtually a resistance. These phenomena are is shown in figure 2.13.

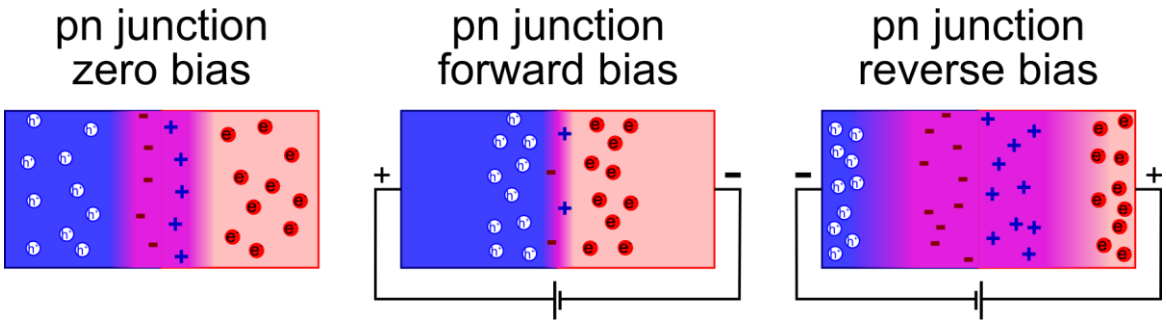

Figure 2.13: Diagrams showing the different behaviour of a diode. (left) When the p and n-type become in contact to each other, the extra holes and electrons recombine leaving the ionised cores behind it is created what is called the depletion zone, the net charge in the opposite side limit the crossing of carriers, this state is called equilibrium. (centre) When a forward bias is applied, the area of the depletion zone shrinks due to the applied electrical field and carriers are pushed towards the opposite side of the junction producing current. (right) in reverse bias the applied electrical field increases the area of the depletion zone, keeping carries from crossing becoming practically an insulator.

2.2.3 Photoelectric and Photovoltaic effects

Usually when photons are absorbed by matter they are absorbed by electrons which makes them become excited to higher levels of energy, this excitation is brief since the electrons normally quickly relax back to their ground state liberating the energy in the shape of a phonon or a photon. The photoelectric effect would be an extreme case of this phenomenon, which is when a photon UV

or blue photon has enough energy to excite an electron bound at the outer shell of a metal to an energy level that allow it to escape completely from the surface (see figure 2.14).

However, in the photovoltaic effect, the electrons are kept within the lattice and go into an external circuit, thanks to a potential difference imposed on an electrical circuit [71], as shown in figure 2.14. The photovoltaic energy conversion in solar cells consists of two stages: The absorption of photons creating an electron-hole (e-h) pair and the separation of the electron-hole pair within the device, as seen in figure 2.15, to prevent recombination and extend the lifetime of the pairs.

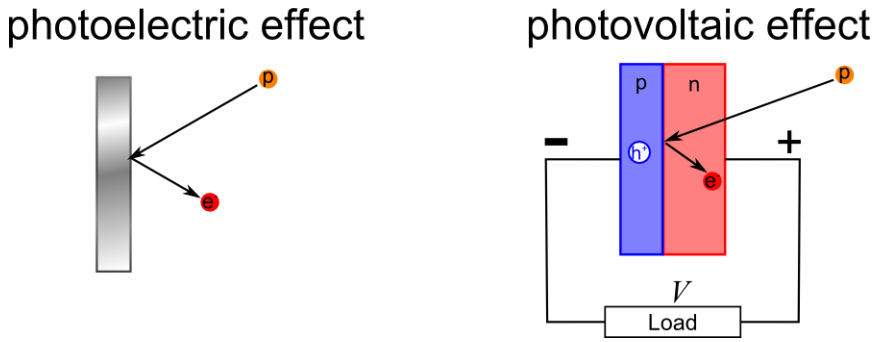

Figure 2.14: Comparison of the Photoelectric and Photovoltaic effects, adapted from Nelson et al., 2008 [71].The photoelectric effect happens mainly due to UV or blue range photons that excite electrons with enough energy to leave the atom. The photovoltaic effect do not require high energy photons but an external voltage differential must be applied to keep the electrons from recombine before circulating through the external circuit.

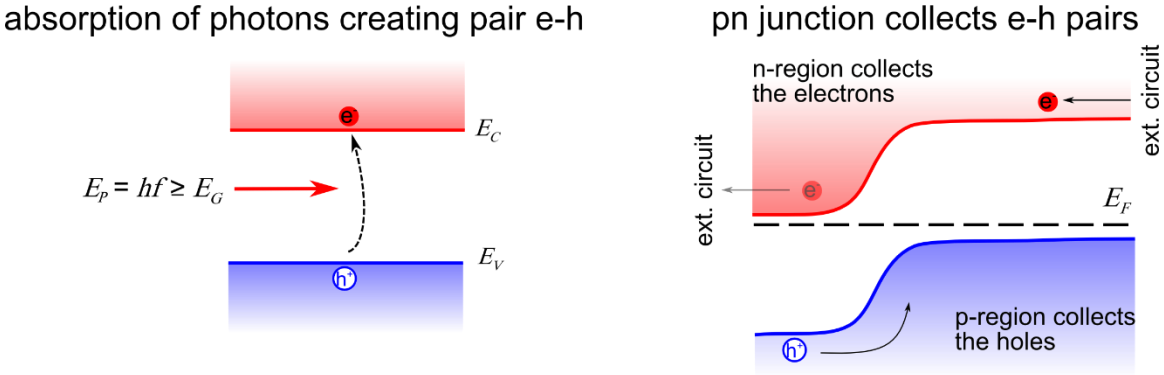

Figure 2.15: Stages of basic operation of PV cells, E_P is defined as the energy of the photon, E_G is the energy of the band gap. (1) A hole-electron pair is created, when the photon energy is more or equal to the energy of the bandgap, (2) The electron is drifted [55].

The energy of the photon must be equal or higher than the band gap E_G to excite an electron into the conduction band. Below this level the photon fails to generate an e-h pair. If the energy is above the E_G, this extra energy is transformed into heat. The increment of temperature can also affect the overall efficiency of the system, since it reduces the band-gap, which in turn reduces the open circuit voltage and increases photocurrent, or short circuit current, by absorbing low-energy photons. Since the loss of voltage outweighs the increment of current, the efficiency is lowered.

This production of e-h pairs and their flux of electrons across the external circuit what produces the photon current (I_P). This is explored further in the next section.

2.2.4 Solar photovoltaic cells

In summary the PV cell works as a conventional p-n junction diode. If a voltage is applied across the diode terminals, the forward current would flow easily through the diode from the p-side to the n-side. If the same current is applied in the reverse direction, only a very small current, known as the saturation current (I_0), will flow. The Shockley diode equation can be written as follows:

$$I_d = I_0\left(e^{\frac{q\,V_d}{A\,k_B\,T}} - 1\right) \qquad 2.19$$

Here V_d stands for voltage drop across the diode's terminals, A is a term called ideality factor, accounting for different mechanisms responsible for moving carriers across the junction, it takes the value of 1 if the electrons transport process is purely diffusion and around 2 of it is primarily recombination in the depletion region. Figure 2.16 shows the current flow within the diode's terminals, when a reverse bias voltage (negative voltage values) is applied there is near to zero current passing through, while when forward bias voltage is applied the current flows as in a conductor.

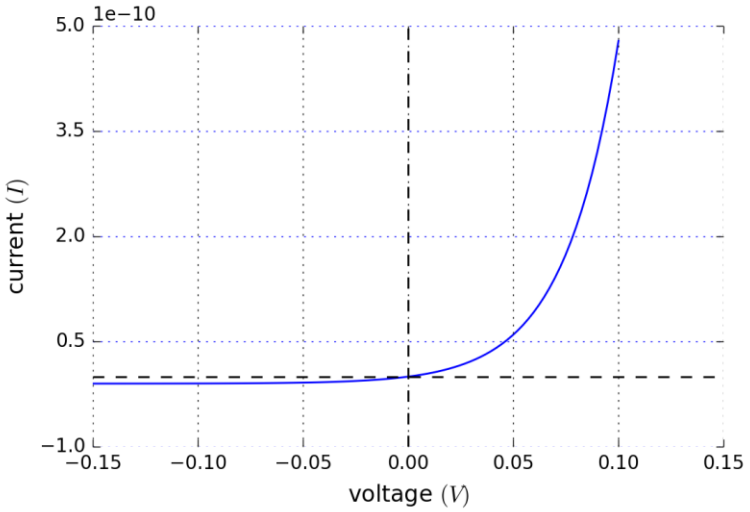

Figure 2.16: Current flow from p-side to the n-side, the small negative values of current for negative values of voltage correspond to the saturation current due to thermally generated carriers namely holes and electrons, being swept into the n-side and p-side respectively. Negative values of voltage indicate reverse bias.

The photocurrent is created by the e-h pairs product of the light absorption and are driven by diffusion when a reverse bias voltage is applied. By convention is the photocurrent is considered as a positive value rendering equation 2.19 negative. The ideal solar cell can be considered as a

current source connected in parallel with a rectifying diode, as seen in figure 2.17, this is a representation of a PV cell as an equivalent circuit. To describe the I-V characteristics of a cell, the previous equation can be then rewritten as equation 2.20 this one is known as the Shockley solar equation.

2.20

$$I = I_P - I_0 \left(e^{\left(\frac{q\,V}{k_B\,T}\right)} - 1 \right)$$

Where I_P is the photo-generated current, I_0 the diode saturation current (due to the fact that a solar cell in the dark is only a diode), k_B is the Boltzmann constant (around 1.38 x 10^{-23} m^2 kg s^{-2} K), T stands for absolute temperature, q for electron charge (of about 1.6x10^{-19} C) and V for voltage at the terminals of the cell. I_P is closely related to the photon flux incident in the cell and is usually independent of the applied voltage. The ideal PV cell can be also represented as the circuit seen in figure 2.17. Here we can see one of two so called parasitic resistances, this being the shunt resistance (sometimes called parallel resistance) is representative of the internal resistance within the cell. This one is produced mainly due to manufacturing defects by current leakages through the cell (also called bridges) or around the edges (due to cutting). This diversion reduces the amount of current through the solar cell as well as the voltage from it. The value of this parasitic current should be relatively high to keep the efficiency high. The ideal value of the shunt resistance would depend of the voltage and current produced in the PV cell but to have losses of less than 1% should be of around 9 Ω for a current of 7 A and a voltage of 0.6 V [61], this would prevent recombination of e-h pairs and is particularly a problem in low light conditions and poorly rectifying devices [71].

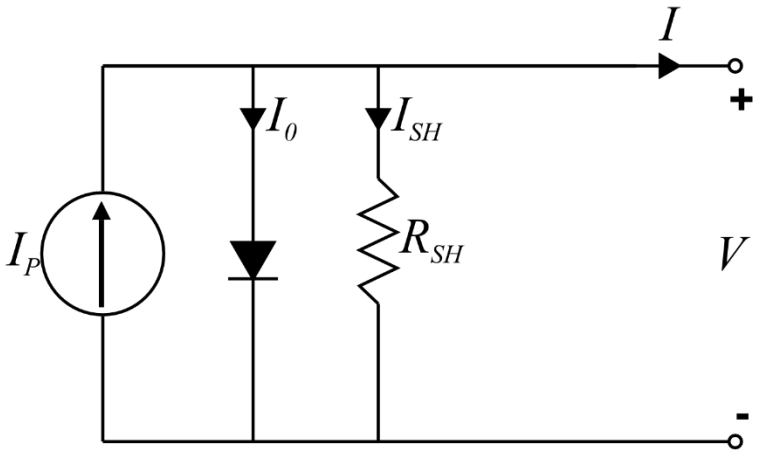

Figure 2.17: Equivalent circuit of an ideal solar cell. I_P Stands for photo-generated current, I_0 for diode saturation current, I_{SH} for parallel current or shunt current, R_{SH} for Shunter or parallel resistance. I and V for current and volts [62].

The second parasitic resistance is called series resistance. This originates from the resistance of the cell material to current flow and the resistivity in the contacts, namely the resistance that the photo-current must overcome to enter the outer circuit. Affects primarily to high current

densities. Its optimal value depends on the device but following the previously exemplified cell, for a loss of less of 1%, this resistance should be less than 0.0009 Ω [61]. Figure 2.18 indicates where this resistance would be located in the previous equivalent circuit [71].

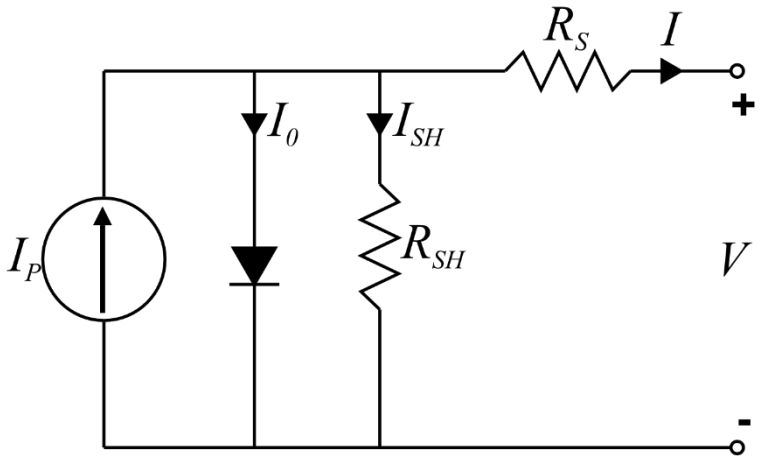

Figure 2.18: The equivalent circuit of a regular PV cell. The symbols are the same as in figure 2.17 with the addition of R_S for series resistance.

Two important characteristics in a cell to be represented in its equivalent circuit are the short-circuit current (I_{SC}) and open-circuit voltage (V_{OC}), which are the current flowing when the terminals are in direct contact and the voltage across the terminals when they are left open. In an ideal situation the I_{SC} equals the I_P, meaning that each incident photon with energy above the band-gap of the junction will produce an e-h pair. This can be described by equation 2.21.

$$I_{sc} = -q \int_{\lambda_{EG}}^{0} \frac{hc}{E(\lambda)} d\lambda \qquad 2.21$$

Where λ_{EG} stands for the wavelength of a photon with energy equal to band gap and $-q$ is the electron charge with positive value due to the convention of PV generation generating "negative current". However, in reality the short circuit current gets reduced by loss mechanisms explained in section 2.2.4.3 and can be also written in the as seen in equation 2.22.

$$J_{sc} = q \int b_S(E)\, QE(E) dE \qquad 2.22$$

Here J_{SC} is current density, namely the current divided by transversal area with units A m^{-2}, b_S stands for incident spectral photon flux, meaning the photons per unit of time and QE represents the probability that an incident photon of energy E deliver one electron to the external circuit, also known as quantum efficiency, of which will be detailed in section 2.2.4.2.

Retaking equation 2.20 and substituting I_P for I_{SC} and I equals 0, we can solve for V_{OC}, resulting in equation 2.23.

2.23

$$V_{OC} = \frac{k_B\, T}{q}\left(1 + \frac{I_P}{I_0}\right)$$

Having these values we can plot for *I-V*, for varying sunlight. It is known that voltage multiplied by charge is equal to energy and energy over time is power, so we can also calculate the power across the different values of I_{SC} and V_{OC}. Figure 2.19 represents a typical *I-V* curve of a PV cell.

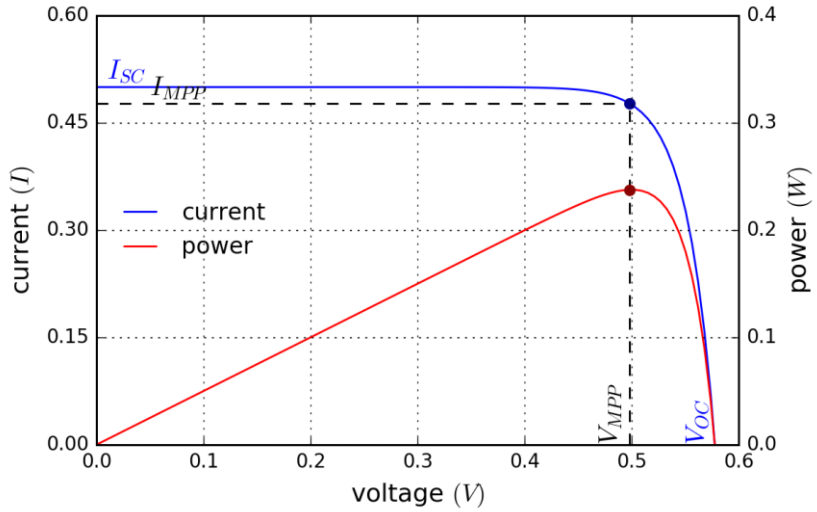

Figure 2.19: Typical I-V curve for a PV cell, assuming values of saturation current (I_0) of 1 x10^{-10} A, a photocurrent (I_P) of 0.5 A, temperature (T) of 300 K, and a range of voltage (V) from 0.0 V to 0.6 V.

The concept of Fill Factor (*FF*) is expressed as the ratio of the maximum power over the product of short circuit current (I_{SC}) and open circuit voltage (V_{OC}). As seen in equation 2.24.

2.24

$$FF = \frac{I_m\, V_m}{I_{SC}\, V_{OC}} = \frac{P_{max}}{I_{SC}\, V_{OC}}$$

Therefore:

2.25

$$P_{max} = I_{SC}\, V_{OC}\, FF$$

The symbols I_m and V_m are the current and the voltage where maximum power (P_{max}) is achieved. The P_{max} can be affected by the effects of the parasitic resistances, expressed in the equation 2.26, note that *I* is in both sides of the equation this makes that this equation can be solve only numerically [71].

2.26

$$I = I_P - I_0\left(e^{\left(\frac{q\,(V+IR_S)}{k_B\,T}\right)} - 1\right) - \frac{V + IR_S}{R_{SH}}$$

In figure 2.20 it is shown how the effects of the parasitic resistances influence in the fill factor, the ideal is for R_S to be small and R_{SH} to be as large as possible, otherwise they will reduce the efficiency of the whole system.

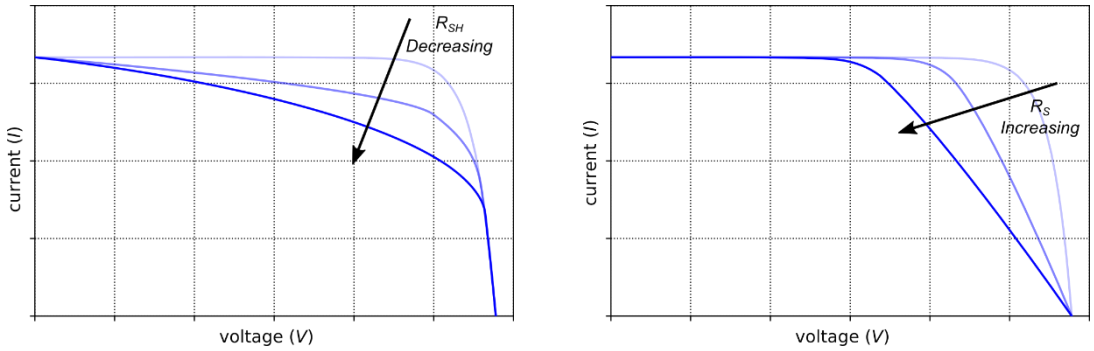

Figure 2.20: Effect of reducing the shunt resistance and increasing the series resistance, (right) the decreasing of shunt resistances sinks the current at the P_{max}, the outer curve represents an ideal $R_{SH} = \infty$. (left) when the series resistance becomes large the voltage at the P_{max} sinks, the outer curve represents an ideal $R_S = 0$. Adapted from Nelson, 2008 [71].

2.2.4.1 Common PV materials

In order to cover the most relevant materials used in the current photovoltaic market a brief description of them will be developed in this section. Despite the number of available materials this thesis will be focusing on five due to their current importance.

Crystalline silicon: This material is so common that it is usually the representative example to describe classic PV cell structures and workings, as seen in the previous examples. Silicon is the second most abundant element on Earth, being 20% of the crust, it is well understood and has an energy band gap of 1.12 eV [9]. A common monocrystalline silicon cell (c-Si) is relatively thick, of about 200 μm to 500 μm. This technology together with multicrystalline (mc-Si) and High Efficiency c-Si represent (HE c-Si) about 80% of the current produced PV cells. This technology is classified as a homojunction, since both its p and n junctions are made out of the same material with only different doping. The difference between c-Si and mc-Si is that for single crystalline technology the wafer (thin slice of semiconductor) is part of a single crystalline structure while for mc-Si wafers are made from large areas of single crystal grains of different sizes from 1mm to 10 cm. These multiple grain boundaries increase the possibility of defective atomic bonds and increases the recombination reducing the current flow [61]. The usual efficiency reached by cells of these technologies industrially fabricated are of 19.5% for c-Si and 17.8% for mc-Si. Another classification of silicon PV cells is the high efficiency cells (HE c-Si), these cells apply different

concepts to achieve efficiencies beyond 25%. Among these concepts are the interdigitated-back-contact configuration, in which both electrons and holes are collected at the rear of the cell eliminating the metal grid at the front surface, this is achieved by using locally diffused phosphorus and boron stripes that are connected to individual metal stripes via local openings in the rear located dielectric passivation layer. Another method for HE c-Si structures is the silicon heterojunction, known as well as heterojunction with intrinsic thin layer (HIT) which is based on two critical innovations: the use of a thin hydrogenated amorphous silicon layer to achieve excellent surface passivation, namely reduction of reactivity of the surface; and connection of electron selective and hole selective contact layers on the aforementioned thin passivating film, which produce virtually recombination-free surfaces increasing the open circuit voltage.

Gallium arsenide (GaAs): This material has a band gap of 1.42 at room temperature, near to the optimum for the standard solar spectrum, which makes the theoretical efficiency of 31% possible. Additionally this material has a better temperature coefficient than silicon. However GaAs is usually more expensive than silicon, resulting on GaAs cells being 5 to 10 times more expensive than silicon ones despite having a reduced thickness of about 4.5 μm. To produce an n-type junction of this material usually controlled quantities of silicon are added during growth while for p-type carbon is the most common used impurity. This technology can be classified as a homojunction and monocrystalline, since both junctions of the cell are made of the same semiconductor, only differing on their doping; and it is produced as a single crystalline structure [71].

Amorphous silicon (a-Si): Since single crystals are expensive to produce there is some interest in developing less material demanding technologies. The word amorphous comes from the Greek for "without form", these are non-crystalline solid that lacks of large crystal structures. These type of semiconductors together with the polycrystalline, like CdTe and CIGS, contain intrinsic defects that increase the recombination within the material which reduces the short circuit current. The a-Si material is the most developed thin film material and has been commercial since 1980, it is relatively cheap, requires low temperature deposition (under 300 ˚C) and can be grown on several substrates such as glass, metal and plastic. The loss of crystal order increases the absorption coefficient, the material used for amorphous silicon usually has a bandgap that can reach 1.75 eV. This material cannot be normally doped, first it needs to be passivated with hydrogen to reduce the unpaired electrons which come as result of the increment of grain boundaries [71]. The commercial efficiency of this technology lies between 12% and 13%.

Copper indium diselenide (CIGS): This material is a semiconductor with a bandgap of 1 eV, and one of the highest optical absorptions. It is available as p and n type. In its polycrystalline structure consists of grains of approximately 1 μm diameter. This material can produce homojunction cells but in this configuration only reaches an efficiency of 3% to 4%, so it is advisable to use it for

devices with heterojunction structures. The n-type material is typically Cadmium sulphide (CdS) and the p-type a CIGS lightly doped base. The efficiency of this material has reached 18.4% to 19.2% in the commercial available cells.

Cadmium telluride (CdTe): This material has a direct bandgap of 1.44 eV, matching closely to the optimum photo conversion based on the standard solar spectrum. It can be doped as a p and n type, however has poor doping efficiencies; and can be grow as single crystal or polycrystalline, being this last configuration the one that has achieved best performance. The preferred configuration is as a heterojunction using CdS as n-type and CdTe as p-type, as in CIGS based cells. The thickness of a typical cell can be of around 3.05 μm to 5.1 μm and its commercial efficiency reaches up to 18.6%.

2.2.4.2 Quantum Efficiency and Spectral Response

The quantum efficiency is defined as the number of electrons in the external circuit produced by a number of photons at any given wavelength. The External quantum efficiency (*EQE*) is calculated by taking into account all the photons hitting the surface of the PV cell that will produce an electron taken by the external circuit. Another important concept is the Spectral Response (*SR*), see equation 2.27, which is the current produced by power absorbed on the surface of the cell, its units are A W^{-1}.

$$SR(\lambda) = \frac{q\lambda}{hc} EQE(\lambda) \qquad 2.27$$

Since q, h and c are constants equation 2.27 can be rewritten as:

$$SR(\lambda) = 0.808\,\lambda\, EQE(\lambda) \qquad 2.28$$

2.2.4.3 Theoretical efficiency limit

This calculation takes into account only radiative recombination, which is when an electron and a hole meet and a photon is released equivalent to the energy of the electron falling into a position in the orbital. The maximum efficiency limit for single-junction photovoltaic cells is given by the Shockley-Queisser limit, based on Planck's law to find the maximum possible efficiency for an ideal band gap in function of a given radiation from a black-body.

Assuming the sun is at 6,000 K and the PV cell at 300 K. The maximum efficiency is found to be around 30% for a bandgap of 1.1 *eV* [93]. This changes for the standard AM1.5 spectrum to

33.8% with a bandgap of 1.34 *eV*, figure 2.14 shows the portions of the irradiance for a spectrum AM1.5 that is theoretically able to produce photocurrent, based on the band-gap of the cell and the reasons for this limit.

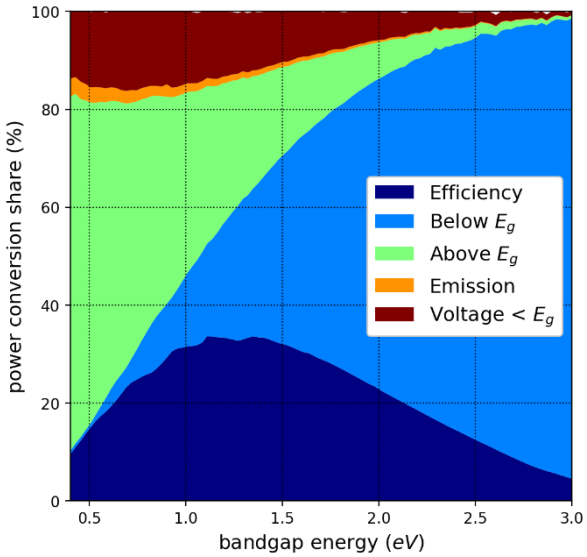

Figure 2.10: Theoretical limit for PV cells according Shockley and Queisser. From Jošt and Topič [49]. Based on the standard solar spectrum AM1.5, The y axis shows the portion of efficiency and the different colours represent the different phenomena that reduce the power conversion efficiency and the x axis represent the possible bandgap energy (E_G) of the semiconductor.

According Jošt and Topič [49], the loss mechanisms are mainly spectral, due to the absorbance of incident photons being strongly correlated to the bandgap. The photons with energy below the band-gap do not have enough energy to generate an electron-hole pair and so are transmitted without being absorbed. The photons with energy equal to or above the bandgap produce electron-hole pairs, but in the case of the exceeding the bandgap energy, the extra energy is lost and transformed into heat.

There are also the emission losses, these are caused by electron-hole pairs recombining. This recombination produces either a phonon or a photon in the cases of non-radiative recombination and radiative recombination respectively. The phonon is a quasi-particle defined as a quantum mechanical description of elementary vibrational motion of the lattice of atoms or molecules in condensed matter. Additionally, there are also the losses originating from voltages lower than the bandgap. Ideally the open circuit voltage should be equal to the bandgap, but in reality the open circuit voltage is lower due to the potential differences of the quasi-Fermi levels while the voltage at the maximum power is even lower. This is a result of the Boltzmann and Carnot factors. Boltzmann is a consequence of unequal solid angles of absorption and emission and Carnot factor comes from the conversion of thermal to electric energy.

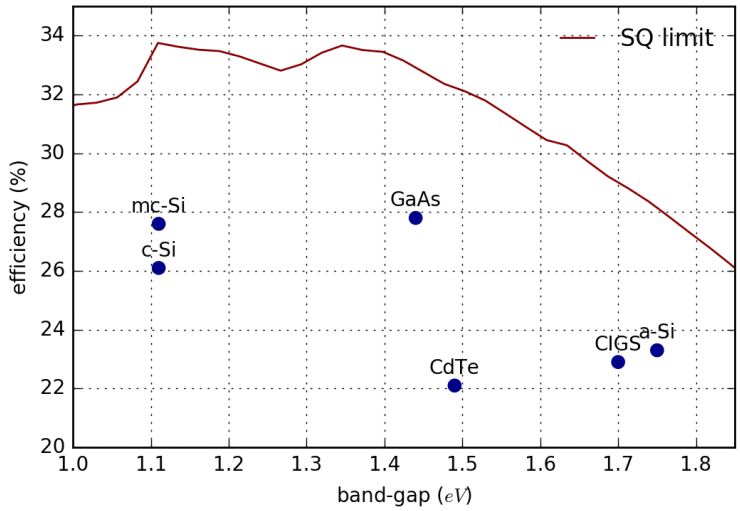

Figure 2.21: Theoretical Shockley-Queisser efficiency limit as a function of band-gap and highest reported efficiencies of selected PV technologies. Here mc-Si stands for multicrystalline silicon, c-Si is single crystalline silicon, GaAs is the abbreviation for Gallium Arsenide PV materials, CdTe means Cadmium Telluride, CIGS is the common name for Copper Indium Gallium Selenide and a-Si is amorphous silicon.

For acceptable photocurrent levels, the quantum efficiency should be high throughout a broad range of wavelengths and there should be a fundamental compromise between photocurrent and voltage in PV energy conversion. It can be easily understood that very small and very large bandgaps will produce poor photo-converters, due to voltage values too small and little photocurrent, respectively. In figure 2.21 is possible to see some of the widely used materials for PV cells, their typical band-gap and record efficiency in laboratories.

However despite being these the highest laboratory reported efficiencies, the reported efficiency in modules usually goes significatively lower to these values, as seen in table 2.1.

PV Material	Highest laboratory efficiency (%)	Highest module efficiency (%)
CIGS	22.9	19.2
CdTe	22.1	18.6
GaAs	27.8	25.1
a-Si	23.3	12.3
c-Si*	26.1	*24.4, 22.0
mc-Si	27.6	19.9

*Table 2.1: Highest laboratory efficiencies vs module efficiencies.*This efficiency correspond to High efficiency c-Si technologies. From Green et al. [31].*

Here CIGS stands for Copper Indium Gallium Selenide, CdTe for Cadmium Telluride, GaAs means Gallium Arsenide, a-Si is the way amorphous Silicon is referred, c-Si means single crystalline Silicon and mc-multicrystalline silicon. There are two values for c-Si, one correspond to a high efficiency module with a Heterojunction Silicon with Intrinsic Thin film (HIT) structure.

2.3 Characterising indices

To study the behaviour of the solar spectrum it is necessary to find an index to characterise the spectral irradiance distribution. This section will attempt to briefly explain the most common such indices in the literature, how are they calculated and the factors involved in deciding which of them to use.

2.3.1 Characterisation of the solar spectral irradiance

The work of Rodrigo *et al.* [90], elaborated a useful summary of the spectral indices used to characterise solar spectral distribution. These indices can be instantaneous and energetic. They are classified in device-independent and device-independent. The device-dependent category is divided by characterising spectral impact on PV device. This thesis is focused solely on the instantaneous indices for non-concentrating and single-junction, briefly explained as follows.

2.3.1.1 Device-independent indices

The device-independent indices are those that do not make use of any physical characteristics of a PV device, in this category we find the index of Average Photon Energy (*APE*) and Blue Fraction (BF). The index *APE* has been used since 2002 [47, 109] to characterise the global spectrum, it is widely used among the literature [67, 95, 23] and it is defined as follows:

$$APE = \frac{\int_a^b E(\lambda)d\lambda}{q\int_a^b \Phi_G(\lambda)d\lambda} \quad 2.29$$

Here, a and b are represent the range in which *APE* is calculated. This range varies across the literature but 300 nm to 1050 nm is one of the most widespread used. Φ_G stands for photon spectral flux which is the amount of photons spectrally distributed, it is defined as:

$$\Phi_G = \frac{E(\lambda)\,\lambda}{h\,c} \quad 2.30$$

It can be also expressed as:

$$APE = hc(kq\lambda_{eff})^{-1} \quad 2.31$$

With λ_{eff} being:

2.32

$$\lambda_{eff} = \frac{\int_a^b \lambda E(\lambda) d\lambda}{\int_a^b E(\lambda) d\lambda}$$

Where λ_{eff} stands for effective wavelength. This latter definition has the advantage of relate possible changes of *APE* to even slight variations on spectral irradiance balance. Namely, higher λ_{eff} are related to red shifts in the spectrum where lower are to blue shifts. The units of *APE* are electron volts (*eV*).

Another device-independent index is the Blue Fraction (*BF*), defined as the ratio of the portion of the spectrum below 650 nm by the total solar irradiance.

2.33

$$BF = \frac{\int_{\lambda<650nm}^{0} E(\lambda)\, d\lambda}{\int E(\lambda)\, d\lambda}$$

As the name indicates the main advantage of these indices is that they are device independent indices, offering a way to share solar spectral data in a standardised way. However a spectroradiometer or spectrometer is required to acquire the data, there is no direct relation with the spectral losses or gains and it does not consider the PV devices.

2.3.1.2 Device-dependent indices

Unlike the device independent indices, the following use physical characteristics of the devices to analyse, and can be a guideline to understand how certain devices would perform under given spectral conditions. From the aforementioned classification on can subclassify some indices as indices characterising the spectral impact on a PV device and those characterising spectral impact between two PV devices. Among the first subclassification are found: the Spectral Factor (*SF*), Useful Fraction (*UF*), Spectral Effective Responsivity (S_{eff}) and Spectrally Corrected Global Irradiance (G_C).

The Spectral Factor (*SF*), the simplest definition of this would be the ratio of the short circuit current of the PV device (I_{SC}) multiplied by the reference broadband irradiance, usually of a pyrometer (G^*), divided by the product of the short circuit current of the reference device (I_{SC}^*) multiplied by the broadband irradiance measured (G) as it is shown in equation 2.34.

2.34

$$SF = \frac{I_{SC} G^*}{I_{SC}^* G}$$

However, a more detailed definition is:

2.35

$$SF = \frac{\int E_G(\lambda)\, SR(\lambda)\, d\lambda}{\int E_G^*(\lambda)\, SR(\lambda)\, d\lambda} \cdot \frac{\int E_G^*(\lambda)\, d\lambda}{\int E_G(\lambda)\, d\lambda}$$

Here E_G, as seen before, is the actual spectral irradiance, E_G^* stands for the reference global spectrum and *SR* is the spectral response of the measured device in A W^{-1}.

The Spectrally Corrected Global Irradiance (G_C), whose simplest definition is expressed as: the ratio of the short circuit of the PV device divided over the short circuit of the reference device multiplied by the reference irradiance. As seen in equation 2.36.

2.36

$$G_C = \frac{I_{SC}}{I_{SC}^*} G^*$$

The next two indices have a direct calculation of the spectral gains and losses and can be measured through the short-circuit current. The disadvantages are that they also require a spectroradiometer or spectrometer to be estimated, correcting monitoring of short-circuit current, and computationally intensive calculations.

The Useful Fraction (*UF*), defined as the ratio of the integral of the solar spectrum as a function of wavelength, up to the upper wavelength at which the absorption takes place in the PV device, over the integrated solar spectrum as a function of wavelength. This represents the fraction of spectrum power available for PV conversion defined in equation 2.37.

2.37

$$UF = \frac{\int_{\lambda < \lambda_0} E_G(\lambda)\, d\lambda}{\int E_G(\lambda)\, d\lambda}$$

This index is easy to calculate and does not require the data of spectral response, however it still requires spectroradiometer measurements.

The Spectral Effective Responsivity (S_{eff}). This is defined as the ratio of the integral of the product of the solar spectrum and the spectral response of the PV device, over the integral, up to the upper wavelength at which the absorption takes place in the PV device, of the solar spectrum in function to the wavelength, this is expressed in units of A W^{-1}. See equation 2.38.

2.38

$$S_{eff} = \frac{\int E_G(\lambda)\, SR(\lambda)\, d\lambda}{\int_{\lambda < \lambda_0} E_G(\lambda)\, d\lambda}$$

This index does not requires data acquired by a pyranometer, but requires a spectroradiometer measurements and knowledge of the spectral response.

Another subclassification is comprehended by the indices characterising relative spectral impact between two PV devices. Being the **Spectral Mismatch Factor (*MM*)** the one on focus for this project, which is similar to *SF* but here instead of comparing the PV device against a pyranometer, it characterises the relative spectral impact between two PV devices. It is described as follows:

$$MM = \frac{\int E_G(\lambda)\, SR_{sample}(\lambda)\, d\lambda}{\int E_G^*(\lambda)\, SR_{sample}(\lambda)\, d\lambda} \cdot \frac{\int E_G^*(\lambda)\, SR_{ref}(\lambda)\, d\lambda}{\int E_G(\lambda)\, SR_{ref}(\lambda)\, d\lambda} \quad 2.39$$

Where SR_{sample} is the spectral response of the PV device of interest and SR_{ref} is the reference PV device. As with *SF* there is a direct and accurate calculation of the spectral gains and losses and it can be measured through the short-circuit current. However it has a moderate accuracy and it requires data acquired by a spectroradiometer.

The paper of Rodrigo *et al.* [90] included as well a review of the literature concerning the spectral energy gain or loss. Here they conclude that the impact is far from negligible. Since the main concerns to address in this work are: to contribute to the understanding of the spectral influences and the yield of photovoltaic technologies. This indicator could be the most appropriate to assess the PV technologies most suitable to be applied at each particular site. The results are that the materials with low energy gap show similar results and a noteworthy stable spectral performance. These materials being c-Si, CIGS and CIS. The materials with high energy gap show a remarkable spectral dependence, these being a-Si and CdTe.

2.3.1.3 Application of indices

Since 2002, the index average photon energy (*APE*) has been an index used in the literature to characterise spectra [66] to determine the influence of spectral irradiance on the performance of PV technologies. The use of spectra of the total solar spectral irradiance is uncommon in the literature, so indices such as *APE*, useful fraction (*UF*), spectral mismatch factor (*MM*) and blue fraction (*BF*) among others provide an alternative to analyse large amounts of solar energy information with a relatively low use of computational resources.

The uniqueness of the *APE* values has been contested however due to the wide variability of the other indices. The *APE* value presents the advantage of being more comparable across different researches. Values like *UF* and *SF* are device dependent and have to be recalculated for every studied device.

Minemoto *et al.* [67] realised an analysis of the uniqueness of the *APE* value during a period of three years from January 2003 to December 2006. In their evaluation the range of 350 nm to 1050 nm was divided in 14 bands of 50 nm width. The mean value was then calculated. It was plotted the spectral irradiance for values from 1.86 to 2.04 *eV* (with steps of 0.02 *eV*) and normalised at 560 nm because at 560 nm the intensity is less affected by environmental conditions (scattering and absorption of water vapour). This showed a standard deviation of the spectral band of less than 0.39%, thus pointing out that an *APE* value can describe a spectral irradiance distribution quite satisfactory.

2.3.2 Clearness index

A measure of the relative terrestrial solar radiation (*E*), also called Global, is known as clearness index (K_T). This is a number lies usually between 0 and 1 where the higher the number, the clearer the sky. However in some occasion a number higher than 1 can be recorded, these "enhanced" K_T can be explained by the reading of clear sky solar irradiance plus the reflection of another element, like the cloud borders, also known as silver-lining, of cotton like clouds (field cumulus) [83], additionally another phenomenon causing this could be the forward scattering, or refraction, of light in thin clouds within narrow angles to the sun sky position [112]. It is proportional to the diffuse fraction of solar irradiance and it is defined as the ratio of total solar irradiance over extra-terrestrial solar irradiance, both incident and on the horizontal. It is calculated using equation 2.40.

$$K_T = \frac{E}{E_{ETR,AOI}} \qquad 2.40$$

E stands for global irradiance which is the sum of direct irradiance (E_{dir}) and diffuse fraction (E_{dif}) [21]. A more detailed explanation of these fractions can be found in the section 2.1.5. These two components of the solar radiation behave differently. The direct irradiance is the only component used for concentrating PV system. In thermal solar systems and plate PV system the diffuse sunlight plays an important role in electrical production.

2.3.3 Other atmospheric indices

Furthermore, Rodrigo *et al.* [90] explain in their paper the way sunlight spectrum, and other relevant atmospheric variables such as *AM*, *AOD* and precipitable water (*PW*), affect the energetic yield of PV technologies and makes an analysis of the indices used to quantify spectral influences in PV systems. This paper aimed to cover the relevant studies concerning spectral analysis of PV

systems within the last three decades. They concluded that in general the previous authors present partial reviews focused on introducing their own methods, and signalise that there is a lack of systemic and comprehensive study of the available methods and indices of the different PV technologies, they also exposed that there is no standard nomenclature, which adds confusion among researchers and manufacturers. They stated that the mentioned atmospheric parameters affect the solar spectrum: (1) *AM* increases the attenuation in the UV region, making the spectrum red-shifted, (2) *AOD* produces a larger attenuation on UV-visible region and affects mostly to direct normal irradiance because aerosols are a major factor on the incoming sunlight that is transformed into diffuse irradiance, and produces more impact to PV technologies such as HCPV, due to their dependence on diffuse irradiance, (3) PW causes attenuation on the near infra-red region, and therefore there is a blue-shift of the spectral distribution.

2.4 Standard Reporting Conditions

The PV systems are usually tested under standard reporting conditions (SRC, also called Standard Test Conditions or STC) from the international Electrical Commission (IEC), to characterise their performance under controlled temperature, spectral irradiance and total irradiance, as shown in table 2.2, according Luque, Hegedus and Emery [56].

The PV conversion efficiency can be defined with the equation 2.33:

$$\eta = 100\left(\frac{P_{max}}{E_{tot}\,A}\right) \qquad 2.41$$

Where η is the conversion efficiency, P_{max} is the maximum measured power (W), E_{tot} is the total incident irradiance (W m^{-2}) and A is the area of the device (m^2).

Application	Irradiance ($W\,m^{-2}$)	Reference spectrum	Temperature ($^{\circ}C$)
Terrestrial non-concentrating			
Cells	1,000	Global	25 in cell
Modules, systems	1,000	Global	25 in cell or NOCT
Terrestrial concentrating			
Cell	> 1,000	Direct	25 in cell
Module	850 direct	Prevailing	20 ambient
Extra-terrestrial	1,366	AM0	25, 28 in cell

Table 2.2: Standard Reference Conditions for Photovoltaic cells, modules and systems. The irradiance listed is the reference irradiance and the reference spectrum may not integrate to this value. NOCT stands for Nominal Operating Cell Temperature.

2.4.1 International Solar Spectra Standards

The solar spectrum can vary across the world from blue-rich distributions in clear-skies and sunny places, to red-shifted spectra in high and low latitudes. Figure 2.22 is a modelling of the same day for winter and summer of two different locations. The different natural influences are include aerosol content, precipitable water and air mass.

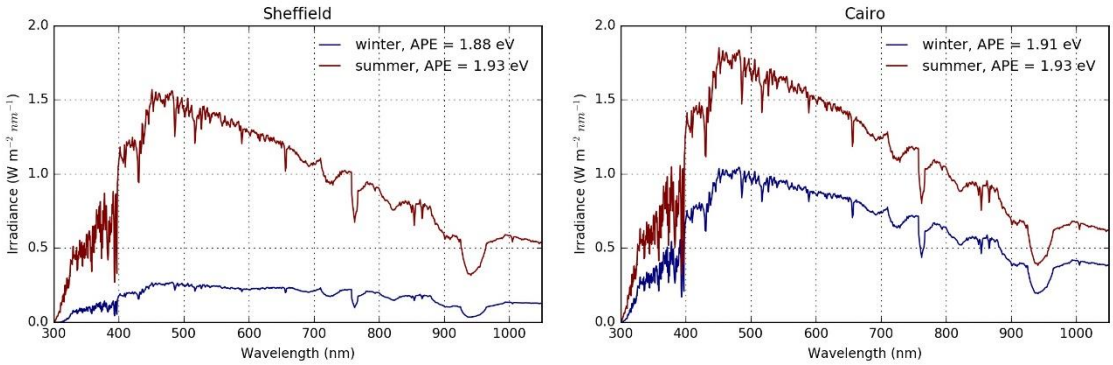

Figure 2.22: Comparison of spectral irradiance of Sheffield against Cairo, located: 53˚23'01" North, 1˚28'01" West (UK representative city) and 30˚2'40" North, 31˚14'9" East respectively. Sheffield as representative UK location and Cairo as representative MENA location, these spectra were calculated using SPCTRAL2 code (appendix 7.1). Index Average Photon Energy (*APE*, see section 2.3.1.1) shown to introduce of the concept.

To validate a number of PV products, the common standard spectrum comes from ASTM International [1] and IEC. In 2008 the American Society for testing and Materials (ASTM) and the International Electrochemical Commission (IEC) updated their reference spectra, designating them ASTM G173 and IEC 60904-03. This reference spectrum was revised using the Gueymard method Simple Model for the Atmospheric Radiative Transfer of Sunshine (SMARTS) and a better understanding of the atmospheric physics. Both Spectra refer the total hemispherical irradiance on a 37˚ tilted surface facing south, while ASTM G173 includes direct normal spectrum, IEC 60904-03 does not [68]. An overview of both organisations is explained in the following paragraphs.

ASTM develops and publishes consensus standards, its development is driven for more than 30,000 members representing 135 countries. Both committees, the one for the Geothermal and Alternative Energy and the one for Weathering and Durability, contributed to the development of the referred ASTM G173 spectrum with the scope stating:

> *These tables contain terrestrial solar spectral irradiance distributions for use in terrestrial applications that require a standard reference spectral irradiance for hemispherical solar irradiance (consisting of both direct and diffuse components) incident on a sun-facing, 37˚ tilted surface, or the direct normal spectral irradiance. The data contained in these tables reflect reference spectra with uniform wavelength interval (0.5*

> *nanometer (nm) below 400 nm, 1 nm between 400 nm and 1700 nm, an intermediate wavelength at 1702 nm, and 5 nm intervals from 1700 to 4000 nm). The data tables represent reasonable cloudless atmospheric conditions favorable for photovoltaic (PV) energy production, as well as weathering and durability exposure applications.*

The standards prepared and published by the IEC are consensus-based and represent the needs of stakeholders in every nation participating in this institution, every member Country has one vote. The scope of the IEC-60904-03 is stated as follows:

> *This part of IEC 60904 applies to the following photovoltaic devices for terrestrial applications:*
>
> - *Solar cells with or without a protective cover*
> - *Sub assemblies of solar cells*
> - *Modules*
> - *Systems.*
>
> *Note: the term 'test specimen' is used to denote any of these devices.*
>
> *The principles contained in the standard cover testing in both natural and simulated sunlight.*
>
> *This standard is not applicable to solar cells designed for operation in concentrated sunlight. Photovoltaic conversion is spectrally selective due to the nature of the semiconductor materials used in PV solar cells and modules. To compare the relative performance of different PV devices and materials a reference standards solar spectral distribution is necessary. This standard includes such a reference solar spectral distribution.*
>
> *This standard also describes basic measurement principles for determining the electrical output of PV devices. The principles given in this standard are designed to relate the performance rating of PV devices to a common reference terrestrial solar spectral irradiance distribution.*
>
> *The reference terrestrial solar spectral irradiance distribution given in this standard is required in order to classify solar simulators according to the spectral performance requirements contained in IEC 60904-9.*

Both standard terrestrial spectra coincide in some considerations, like the geometrical configurations which can be described as an inclined plane tilted at 37˚ from the horizontal towards the equator with an azimuth of 180˚ (facing south), the sun must have a position in which the *AM* is equal to 1.5, namely a sun zenith angle of 48.19˚ (elevation angle of 41.81˚). Besides the direct beam it is also include a small contribution (usually less than 1%) of diffuse radiation.

Other important considerations are the atmospheric conditions, an analysis of the NREL indicated that an Aerosol Optical Depth of 0.084 is representative for economic deployment of PV applications. A measured spectral albedo for light sandy soil from the albedo files of SMARTS2 was used to compute the spectra. Most of the constraints were based on the US standard atmosphere 1976, with exception of the AOD and CO_2 (from 330 ppmv changed to 370 ppmv), however even with this changes the total integrated hemispherical spectral irradiance was calculated in 1,000.37 W m^{-2} showing little change to the historical 1 kW m^{-2}.The direct beam spectral irradiance increased around 18% from the previously PVUSA-specified test condition irradiance of 850 W m^{-2} to 900.14 W m^{-2}. While the ASTM considered that the small differences to "round numbers" for the 1,000 W m^{-2} and 900 W m^{-2} for hemispherical (0.037%) and direct irradiance (0.016%) were within the present uncertainty, the IEC with the same inputs and the same results added the following modifications: a data point to account for the energy from 4,000 nm to infinity and the adjustment of the integrated hemispherical spectrum to 1,000 W m^{-2} by multiplying it by a factor of 0.9971 resulting in the integrated hemispherical spectral irradiance below 4,000 nm to be 997.47, the lacking 2.53 W m^{-2} corresponds to the additional data point from 4,000 nm to infinity. Additionally the IEC calculation provides the photon flux at each wavelength calculated [68].

The plot of the ASTM G173 extra-terrestrial, global irradiance and direct + circumsolar irradiance spectra can be seen in figure 2.23.

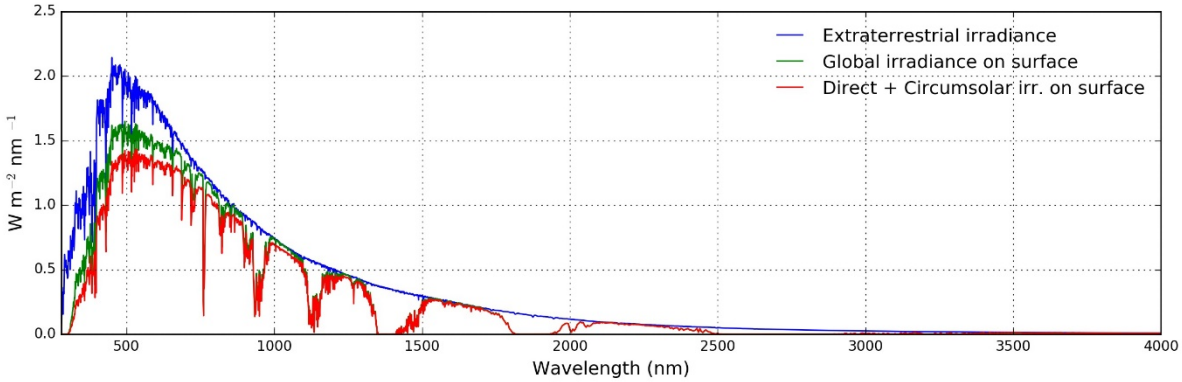

Figure 2.23: Standard spectra for direct normal global irradiation at 1.5 AM from ASTM International [1] extra-terrestrial, global and global + circumsolar on tilted surface (37° facing South).

2.5 Radiometry and methods of calibration

Among the characteristics found in electromagnetic radiation are wavelength and intensity, the classification by variation of wavelength is characterised as the electromagnetic spectrum, radiometry and photometry are branch of physics that focus on these measurements. The sources

and detectors of electromagnetic radiation can be classified on the basis of their spectral range and strength of signal either produced or detected.

The electromagnetic waves propagating through space are classified as monochromatic or polychromatic, representing a single wavelength or several (discrete or continuous) respectively. The distribution of energy across these constituent wavelengths is called spectrum. Several ranges of electromagnetic spectrum are classified on base of the different methods of their production and detection, these classifications go by specific names, such as: radio waves (10^{15} nm to 10^{9} nm), visible light (380 nm to 770 nm), ultraviolet (380 nm to 10^{-9} nm) and infrared radiation (10^{-5} to 770 nm), among others. The region comprised by the ranges of infrared, visible light and ultraviolet are the object of study of optics.

2.5.1 Radiometry

Radiometry is the science of the science of the detection and measurement of electromagnetic radiant energy, the radiometric quantities relevant to this research used to characterize the energy content of radiation is summarised in table 2.3.

Term	Symbol	Units
Radiant energy	Q	$J = W\,s$
Radiant flux	Φ	W
Irradiance	E	$W\,m^{-2}$

Table 2.3: Relevant radiometric units and concepts used to characterise the energy content of radiation.

A widespread application of this discipline is the measurement of solar spectral irradiance. The instrument used to acquire spectrally resolved data was a grating based spectrometer, a grating is one of the tools used to produce the diffraction of incident light, and these are described as periodic multiple-slit devices. The instruments using gratings usually are designed around the type of grating.

2.5.1.1 Working principle of a Spectrometer

Generally described a spectrometer is an instrument able to record the irradiance distribution across a given range of the electromagnetic spectrum. It consists of an opaque box in which takes in an input of light, usually through an optic fibre into entrance slit, this light is reflected to a collimation mirror, diffraction, focusing mirror and a light detector, such as a photo-sensitive film, Charged-Coupled Device (CCD) or photo-diode array. We can see in figure 2.24 an overview of the basic architecture of a spectrometer.

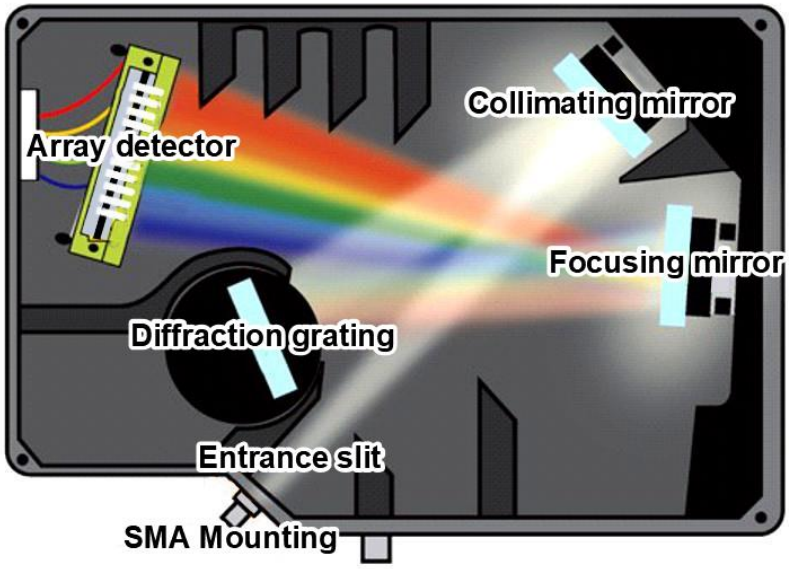

Figure 2.24: Visualisation of a basic schematic for spectrometers. Adapted from Creative Commons, 2011[65].

The entrance slit is critical to the spectrometer performance and determines the input light and optical resolution. The diffraction grating determines the wavelength range and influences the optical resolution a grating can be described by two components the groove frequency and the blaze angle. The groove frequency, also called groove density, is defined as the amount of grooves per mm in the grating, decreasing the groove density decrease the dispersion and increase the wavelength coverage, sacrificing optical resolution. The blaze angle the angle that determines the shape of the diffraction curve. The light coming in from the entrance slit hits the collimating mirror to render the incident light parallel. The CCD detector in spectrometers has made possible the "fixed grating" in spectrometers, instead of adding a second rotating exit slit, with it is possible to consider each pixel a representation of the portion of the spectrum, eliminating mobile parts has allowed for the production of inexpensive, compact spectrometers.

When the incident light strikes the individual pixels an electric signal is produced, which for the purpose of this work is called "count", due to the standard of the spectrometer used in this work, the Ocean Optics JAZ-S. To these "counts" it is assigned a value of light irradiance, thus knowing the spacing in the x-axis of pixels in the CCD it is possible to register a spectrum within the specification of the spectrometer.

According to the specifications of the apparatus the detector is a Sony ILX511B 2048-element linear silicon CCD array detector, responsive within a range of 200 to 1100 nm, a sensitivity of up to 75 photons per count at 400 nm; 41 photons per count at 600 nm and an optical resolution of ~0.3 to 10.0 nm (FWHM). Claiming to be well suited for field measurements this tool was selected to acquire the solar spectral data for this project.

CCD technology allows for small pixel size (~14µm) detectors to be constructed since it eliminates the need for direct readout circuitry from each individual pixel. This is accomplished by transferring the charge from one pixel to another, allowing for all of the information along the array to be read out from a single pixel.

Originally a calibrated light source with known values was going to be used to perform the calibration of the spectrometer for absolute irradiance. Unfortunately this attempt was unfruitful. Chapter 4 describes this process and explains how a reliable calibration was achieved.

2.5.1.2 Working principle of a thermopile pyranometer

A pyranometer can be based on photodiodes, which works thanks to the photoelectric effect, or based on photovoltaic cells, in both cases the range of spectral response would be limited, in comparison to that of the thermopile pyranometer, with a range roughly from 350 nm to 1,100 nm. The thermopile based pyranometer absorbs the radiation by a horizontal blackened surface, this allows it to have a range from about 300 nm to almost 3,000 nm, as seen in figure 2.25. The blackened surface increase its temperature which is then measured via thermocouples connected to each other to make a thermopile. The other side of the thermopile is in contact with the housing of the pyranometer which serves as a heat-sink, keeping a temperature difference. The sensor generates a small voltage in proportion to the temperature differential between the absorbing surface and the instrument housing. This voltage is usually of the order of 10 µV per W m^{-2}, the exact equivalence will depend on the calibration which is recommended to perform every 2 years.

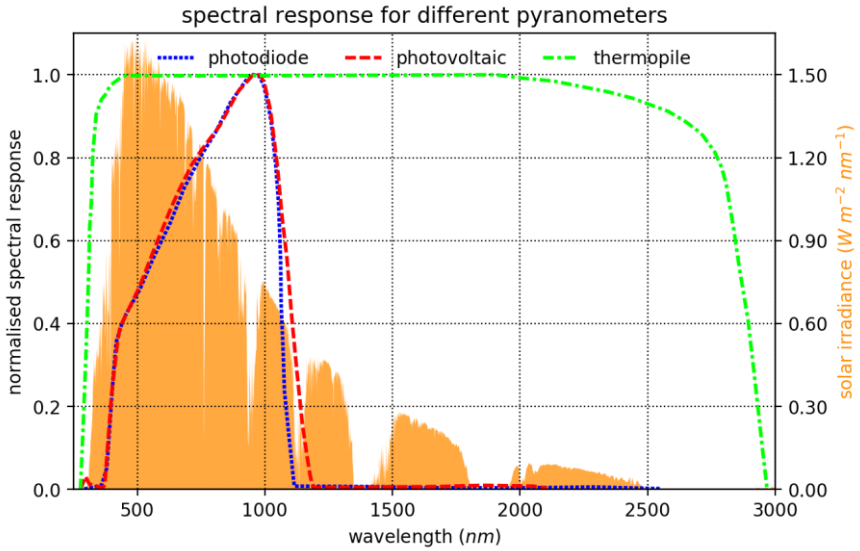

Figure 2.25: Typical spectral response of different pyranometer types. Adapted from Creative Commons, 2016 [5].

The voltage generated is due to the thermoelectric effect, this occurs when a side of a piece of conductor material has a temperature differential, making charges like electron move towards the zone with lower temperature which creates a difference of voltage between the two ends of the piece. The resulting voltage can be enhanced by joining two pieces of materials, one with excess of electron and another with excess of positive charges [51].

The black sensor needs to be protected to prevent its degradation from outdoor conditions, therefore it is encased and covered with a hemispherical dome made out of glass. The dome-shape besides insulating the sensor also improves the cosine response of the sensor for low angles of incidence. The general structure and a pyranometer's typical design can be seen in figure 2.26.

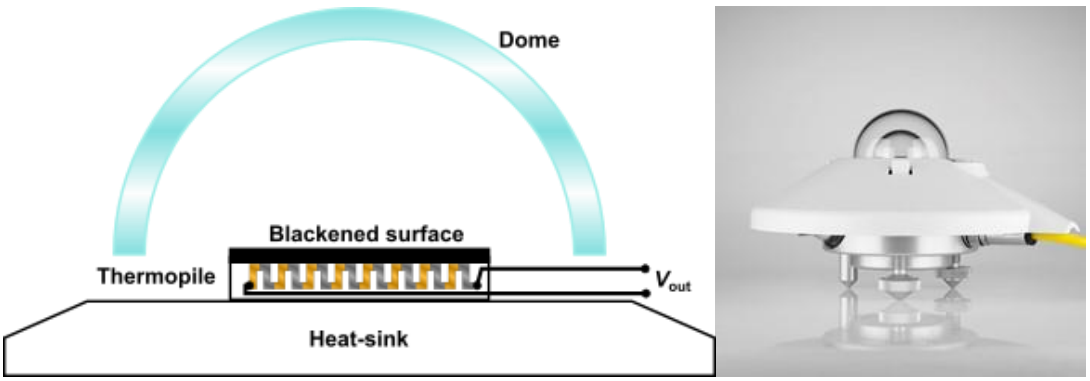

Figure 2.26: Pyranometer scheme and typical design. (left) This scheme shows the general structure of a pyranometer, notice that the thermopile is formed by a junction of two different metals to increase the output voltage. (right) The typical design of a pyranometer [111].

2.5.2 Calibration methods

During the length of this project it was difficult to find literature for the specific purpose of absolute calibration for a spectrometer for long periods of field solar irradiance. Through inverse engineering and the literature available the calibration methods could be divided in four branches: (1) measuring the response of the spectrometer to a light source of known irradiance values, (2) comparing the spectrometer readings to a calibrated one, using the same source (3) using Langley interpolation, which is to calibrate the spectrometer using the sun as irradiance source at high elevations to avoid changes in atmospheric transmissions and (4) vicarious calibration, the use of a natural light source and a radiative transfer code to carefully calculate the spectral intensity of the measurement.

2.5.2.1 Vicarious calibration

Thome *et al.* [100] worked on this campaign to evaluate the accuracy of reflected-based vicarious calibration of Earth Observing Systems (EOS). Four groups participated and made independent measurements of the surface reflectance and atmospheric transmittance.

Every group made a prediction of the top-of-the-atmosphere radiance for several bands in the 400 nm to 2500 nm spectral range and these measurements showed differences of between 5% and 10% throughout the spectral region under study. The major sources of discrepancy were the procedures and assumptions in finding the reflectance of field references, whereas the difference caused by varying radiative transfer codes and aerosol assumptions were found to be relatively small.

The measurements were made in the visible and infrared region (VNIR), the short-wave infrared region (SWIR) and thermal infrared regions of the spectrum, but the paper only presents the VNIR and SWIR. They define vicarious calibration as the in-flight methods of calibration that are independent to on-board calibrators. The specific method used in the paper is the reflectance-based approach that was developed in the 80's, which has been applied to satellite and airborne sensors. This method consists of measuring a surface reflectance, atmospheric optical thickness and aerosol properties at a test site at the time the sensor overpasses.

The measurements are used to constrain a radiative transfer code to predict a normalised radiance at the sensor that is converted to absolute irradiance by assuming a solar spectral irradiance. It is noted that previous work points to uncertainties due to the reflectance based approach are less than 5% and the principal contributors of the uncertainty are the uncertainties in surface reflectance, aerosol refractive index and distribution size. The ideal atmospheric conditions for these experiments are low aerosol concentrations. The site in which the experiment was realised was an area of 240 m by 240 m, located at 38˚ 23' north and 115˚ 59' west. The fieldwork consisted of several data collections per day for a number of days with measurements at 14:20, 16:00, 18:00 and 21:20 UTC.

The atmospheric measurements were made using a solar radiometer constructed at the University of Arizona. Every team also collected information like down-welling, directional sky radiance, temperature, relative humidity, and pressure readings. The results were normalised and the research focused on monochromatic wavelengths of 450 nm, 550 nm, 650 nm, 800 nm, 1000 nm and 1600 nm; as well as in six rectangular bands with centre in wavelengths at 399 nm, 562 nm, 812 nm, 1027 nm, 1688 nm and 2217 nm with bandwidths of 10 nm, 100 nm, 100 nm, 10 nm, 100 nm and 100 nm respectively. Although the final reflectance measurements were satisfactory, the

differences were larger than expected. The possible sources of these differences could be the different type of samplings, types of panels used, the methods of calibration, the field standard of reflectance, and the use of panel bidirectional effects in the processing.

In conclusion these differences can be attributed to the methods used by each group to determine the reflectance of their field references, the other sources such as aerosol optical thickness, size distribution and gaseous transmittance were found non-important for this work, furthermore the radiative transfer code results imply that the codes are not a significant source of uncertainty.

2.5.2.2 Using solar irradiance to calibrate a spectrometer

O'Donnell and Garces [77] presented a method to provide an absolute intensity calibration of a common low-resolution, wideband optical spectrometer. The terrestrial solar radiation is employed as the source of illumination, and to confirm the calibration the output is compared to a solar spectral standard. The calibration of spectrometers is a recurring concern in optics. They can be calibrated by measuring their response to a characterised light source, or comparing its output to a calibrated one. Although the paper does not explain explicitly, it is insinuated that there was no reliable calibrated spectrometer nor resources to obtain a calibrated lamp, therefore they chose the method described in this work.

One of the main factors to consider is the variability of atmospheric transmission due to changing conditions, thus the importance of choosing the conditions carefully, aiming for cloudless days with high visibility and low atmospheric scattering, when the integrated solar irradiance is high and spectral signals do not present strong fluctuations.

The calibration standard solar spectrum used was the ASTM G173-03. However this method is not claiming to be suitable for calibration to strict high resolution levels, as can be required in some studies, but to bring calibration for an uncalibrated instrument that can be adequate for lab work. From the ASTM AM1.5 the Direct + Circumsolar spectrum was used and the sun is assumed to be in a zenith angle of 48.2˚. This spectrum represents the light the sun produces plus the light produced by atmospheric scattering in wavelengths between 280 nm to 4000 nm, the spectral area is standardised to 900 W m^{-2}. The approach is to make measurements with the spectrometer in conditions as close as possible to the ASTM standard. The data was taken at an altitude of 25 m with an *AM* of 1.48, the days were chosen completely cloudless, with low scattering, visibility beyond 13 km, humidity between low to moderate and low wind.

The spectrometer to be calibrated was an Ocean Optics USB4000 fixed-grating, with a 3678-element silicon CCD array. An aperture was placed in front of the spectrometer to limited the field of view to a slit centre to the solar disk plus 2.5˚ of the circumsolar radiation; solar tracking was required once per minute. The spectrometer ran with an integration time of 3.8 ms to avoid oversaturation, two absorbing attenuation filters with a known wavelength dependence were placed in front of the slit. Over about 15 mins, eight sets of data were taken during three days and a thermopile solar intensity measurement was also included in the procedures. The mean effective spectral signal for each of the three days was calculated by averaging the 8 scans and then dividing the result by the integration time. The thermopile measured the solar intensity in these times; giving values of 929 W m^{-2}, 973 W m^{-2} and 985 W m^{-2}. Each curve was scaled to fit the ASTM standard of 900 W m^{-2}. To compute the calibration curve the ASTM spectrum was multiplied by the slit area and then divided by the three scaled datasets. Then they curve-fit polynomials to segments of this of this curve while masking regions affected by water vapour and other absorption bands taking into account that water vapour absorbs light primarily in bands (724 ± 8) nm and (824 ± 10) nm. The accuracy was later tested by measuring a down conversion source with a pump laser and a periodically poled KTP (Potassium titanyl phosphate) nonlinear crystal by measuring said spectrum and then processing the raw data with the calibration curve, this showed to be consistent with adequate calibration.

This method should be used with care, particularly if the solar intensity is well under the value of 900 W m^{-2}, or if strong features related to absorption bands appear. Atmospheric aerosols and absorption bands do not appear to present significant problems. This method uses a light source widely available without relying on expensive calibrations methods.

2.6 Existing work on comparison of PV technologies in-situ

2.6.1 Regional irradiance

Due to the difficulty to modify the operation, or to upgrade a PV system, it is very important for investors and engineers to have an accurate estimate of the PV energy production. This can vary depending on the geographic zone and the different PV technologies (due to their different response to varying spectral irradiations). In order to design a reliable system it is necessary to have a deep understanding of the different factors that may affect the energy resource and its electrical production [115]. Therefore the most accurate modelling is highly desirable. The scope of this thesis is to report on the variation and impact of spectral variation in irradiance in the UK.

Radiation is the emission of energy in form of photons; a massless particle of electromagnetic force, with no charge and an indefinite lifetime. The regional solar irradiance, which is the solar energy illuminating the surface, is determined not only by its geographical location but also by several other conditions of the atmosphere in region, such the albedo which is defined as the fraction of the incident sunlight that is reflected from a surface. This conduction is wavelength dependant, for example; UV-B albedos (UV light between 280 nm to 315 nm) are smaller than visible albedos over grass and non-snow surfaces, but larger over snow. This parameter will add to the perceived solar irradiance, as part of the diffuse fraction [44].

Particle scattering originates from the effects of reflection, refraction (the change of speed of the photon when enters a medium) and diffraction (the bending of the photon's direction as they pass by the edge of an obstruction) of light produced by the particles in the atmosphere. These particles can be minuscule water drops, or solid particles. A photon meeting a particle can be reflected off the particle, diffracted around the edge of the particle or refracted into another particle. If the photon hits a particle it can be absorbed, transmitted within the particle, or reflected internally one or several times to later be refracted out, in any direction. The internal reflections depend on the incidence angle of the photon on the particle. Although it can be both backwards and forwards, particle scattering is mainly forwards, and with relatively no dependence on the wavelength.

Gas scattering occurs when a photon encounters a gas molecule and changes direction, without a net transfer of energy between them. This redirection is usually symmetrical between backward and forward direction, with also some off to the sides. The gases scatter the shorter (blue) wavelengths in contrast to particles which are mainly wavelength independent. This scattering is called Rayleigh scattering and it is what causes the sky to be blue, the sun to be white at noon but yellow at the sunset and sunrise with a real horizon.

The gas particles can also absorb photons. This attenuates the quantity of the radiation transmitted. Absorption of visible light by particles is relevant when carbon particles are present, and for gas absorption it is only important when nitrogen oxide (NO) has a high concentration.

The gas absorption of the solar spectrum has three main characteristics: (1) it heats the air and prevents harmful radiation to reach the ground (UV), (2) it breaks gases into smaller molecules or atoms in a process called photolysis and (3) it affects visibility. An overview of the gases and how they absorb the solar spectral irradiation can be seen in figure 2.7. The absorption of low wavelength is the origin of the Greenhouse effect (GHG) which stops the earth from extreme temperature changes by keeping the heat within the atmosphere. However, due to carbon contamination in the last century this level could produce chaotic climatological effects.

The concept of extinction coefficient defines the loss of electromagnetic radiation per unit of distance through a medium. Its units are the inverse of distance (cm^{-1}, m^{-1}, etc.) and it is dependant of the wavelength of the radiation. See equation 2.9.

Particle absorption and scattering are the most important processes of attenuation. The particles scatter solar and infrared radiation and absorb mostly infrared. These particles are mainly black carbon, hematite (Fe_2O_3) and aluminium oxide (Al_2O_3) [44]. The water absorption of photons as a contributor of irradiance extinction and its relation to dew measurements and precipitable water was reported by Atwater and Ball [6].

2.6.1.1 Irradiance modelling and forecasting

Betcke et *al.* [12] pointed out the importance of the careful consideration of more accurate modelling PV systems with focus on the regional spectral distribution. Using two different models based on the Heliostat method, one called SOLIS, which calculates spectrally resolved irradiance for zenith angles between 0 to 60, dividing the solar irradiance into 32 bands and applying Lambert-Beer equations. The second model is based on empirical relations between the atmospheric parameters and the clearness index. After a year of date to validate they found that SOLIS model results had a lower root mean squared error in the estimation of energy production and concluded with the idea that ignoring spectral effects can lead to an underestimation of up to 3.3% in the calculation of energy yield.

Akarslan and Hocaoglu [2] tried a novel approach on the modelling and prediction of solar radiation for the Turkish regions of Afyonkarahisar, Ankara and Çanakkale. They hypothesise that the solar radiation is a combination of deterministic and stochastic behaviour. Based on this, they prepared two approaches: (i) one based on linear prediction filters produced with empirical data collected from the 1st of January to the 31st of December of 2013; (ii) the second one was an empirical model based on the strong correlation between the extra-terrestrial and terrestrial radiation. With these two predicting methods they applied two strategies. The first strategy consisted of using only the linear prediction filters to predict solar radiation in seasons of summer and winter while using only the empiric model as predictor for the seasons of spring and autumn. The second strategy was based on the K_T value, if this value was lower than 0.5 the prediction was made using the empirical model, in contrast if the K_T value was higher or equal to 0.5 the solar radiation was estimated using the linear prediction filters. Additionally to the mentioned strategies a batch of predictions were made just using the linear prediction filters. From these three options strategy 2 showed the lowest root mean squared error with 37.88%, followed by strategy 1 with

48.05% and finally linear prediction filter reached 52.26%. These results are competitive to similar published researches.

The characterization and modelling of the solar irradiance spectrum in different regions is an important matter in this research in order to verify the spectral response of the PV technologies with market potential. In an article, Bartlett *et al.* [8] for Halifax, Canada they explain that, in the range between 412 nm to 700 nm, the solar spectral distribution has a strong dependence on the cloud factor, and can be mimicked by the modelling of clear sky irradiance model and varying the magnitude of sky reflectivity and this is strongly dependant to the magnitude and spectral shape of the ground albedo.

Laue [53] describes how altitude might also affect the spectral distribution especially in the range between 1,250 nm to 2,000 nm. The total irradiance can differ by 16% for differences of 1 km of elevation. Houma and Bachari [40] also state the effects of precipitable water, aerosol optical depth and zenith angle as important conditions affecting the incident spectrum. Using the work of Bird and Riordan [14] and the model SMARTS2 [34] the web-page PV Lighthouse has developed an useful tool [63] to calculate the spectral irradiance as a function of the geographical position, day of the year and some atmospheric variables. However, this model does not quantify the effect of the local elevation nor the cloudiness. Besides this, the University of Loughborough has developed an Excel based tool able to calculate a time series in the range of a day with the data of the total irradiance [89] in function of the clarity index and the probability of its prevalence.

In 1984 [20] Carroll described the effects of cloudy conditions. In this paper different models are evaluated and concluded that although one could expect a great variation of global and diffuse radiation due to the types of clouds, a single average relationship seems to be enough to define a representative value of diffuse fraction.

One of the goals of this thesis is to develop models into a time series which could calculate the spectral irradiance based on the cloudiness probability in an extended period of time, in order to be able to calculate the performance of PV systems with different spectral response. In the figure 2.27 it is seen that, due to the Spectral Response (*SR*), how PV technologies have different sensitivity to spectral irradiance. These *SR* profile will be the ones used for the analysis of the effect of spectral variation on PV system performance in section 0.

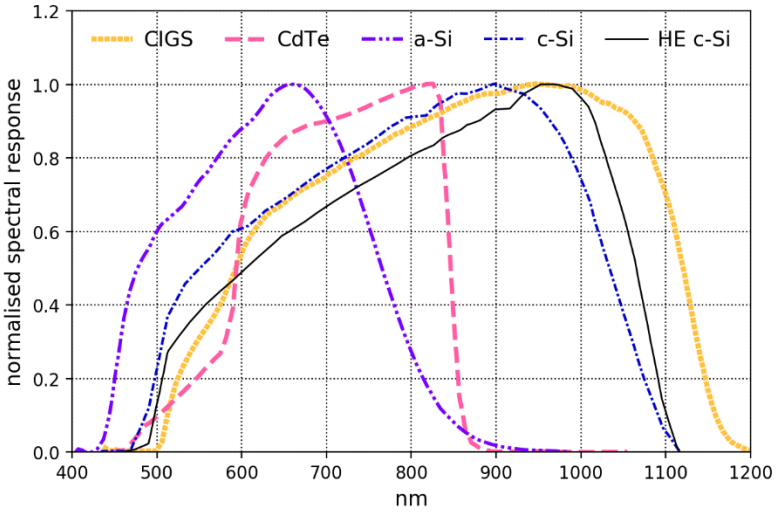

Figure 2.27: Normalised SR of typical PV commercial technologies, Dirnberger, 2015 [24].

2.6.2 Comparison among different technologies in field

2.6.2.1 Effect of cloudy skies

Jardine, Gavin and Lane in 2001 [46], compared eleven PV technologies in two different locations. One in southern Europe (Mallorca, Spain) and another in northern Europe (Oxford, United Kingdom). This experiment, conducted in 2001, questioned the tendency of the northern Europe market to m-Si technology. At that time technologies such as a-Si double junction and CIGS outperformed m-Si on energy produced (KWp KWh^{-1}) and responded well to overcast conditions in the UK. Both technology p-Si and c-Si have a good performance in clear sky conditions but their efficiency decays to almost half under heavy cloudy conditions, see figure 2.28. This study shows, energy production of the two different locations, showing that the UK array produced 60% the energy produced from the array in Mallorca, being the difference of energy production more accentuated in winter than in summer. The a-Si cells outperformed the other technologies in sunny weather, these same technology and CIGS performed well under overcast conditions. The combination of CIGS technology of low light level performance and lower operation temperatures makes it the highest yield technology for UK. Jardine and Lane in another paper [45], explain that the light under overcast conditions is more diffused and richer in blue wavelengths (between 400 nm to 50 nm) technologies like a-Si a CIGS are capable of absorbing efficiently in this part of the spectrum benefiting from this condition more than other technologies. Therefore these effects compensate for the low efficiency they have in more sunny locations, making them as efficient in cloudy locations as in sunny ones; however they did not outperform the high efficiency technologies such like m-Si or p-Si.

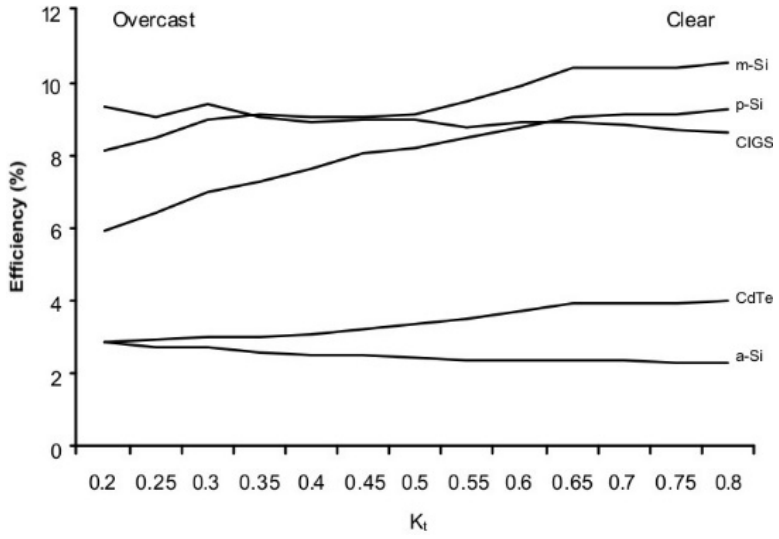

Figure 2.28: Influence of cloudiness on PV devices' efficiency, adapted from Jardine, Conibeer and Lane, 2001 [46].

2.6.2.2 Spectral effects and Seasonal fluctuations

The seasonal fluctuations are one of the most important considerations for PV systems. This is due to the variation of sunlight hours, the solar geometry and the weather variation between sensors. The solar geometry affects the solar spectrum as the light path varies due to season and the elliptical Earth's orbit. The weather variation can produce other phenomena including, but not limited to aerosol concentration levels and differences in cloudy conditions.

Virtuanni and Fanni [107] published an article discussing the discrimination of two effects that influence the efficiency of single junction a-Si solar modules. These two effects were the spectral variation and the Staebler-Wronski (SW). They explained that the spectral effects were attributed mainly due to a-Si narrow spectral response (between 350 nm to 800 nm) and that in summer, due to the shorter path of the sunlight through the atmosphere, the blue component of the spectrum becomes larger as the opposite happens in winter, increasing the red component. It is also discussed that in multi-junction PV cells this effect could be more pronounced due to the mismatch among sub-cells. The SW effect is described as a combination of light induced degradation defects and annealing promoting regeneration. They used four modules split evenly into two sets. One set was installed outdoors, facing south with a tilt of 45° in open circuit conditions and the other was kept indoors. Two systems of I-V measuring were set, one with a solar simulator (Pasan IIIB, class AAA) and another on an outdoor tracking montage to maximize irradiance (*AM* variable) and avoid angle of incidence effects. These measurements were acquired generally around noon and in clear-sky conditions. They produced measurements of each of four modules by translating briefly one module of each set to the I-V measuring system, expecting that this would isolate the influence of each of the effects. To characterise the solar spectrum they used the *AM* value instead of *APE* or

SF. They conclude that spectral effects have a major influence on the outdoor performance of this technology of ± 5% of seasonal variation, while SW effect represented a lower influence of ± 4%.

Alonso-Abella et al. [3] modelled the impact of the solar spectrum distribution for the yearly and monthly scales in four places, one in Germany (Stuttgart) and three in Spain (Madrid, Jaen and Tamanrasset) using eight different PV technologies: a-Si, pc-Si, CIGS, c-Si, CdTe, Hetero-junction with Intrinsic Thin layer (HIT), c-Si Edge Fed Grown silicon (EFG) and c-Si Back Contacted Cells (BCC). The spectral irradiance was modelled using SEDES2 and data from Meteonorm for all sites, but only empirically acquired in two of the sites in Spain: Madrid (40.41°N, 3.73°W) and Jaén (37.77°N, 3.80°W). These spectra were recorded every five minutes from January to December 2012 inclusive, using spectro-radiometers EKO MA-700 in a range from 300 nm to 1050 nm and pyranometers Kipp & Zonnen CMP 21 to record the total solar irradiance. Spectral responses were obtained from the CIEMAT (the acronym of Energetic, Environmental and Technological Research Centre in Spanish) and the Spectral Factor (*SF*) was calculated using equation 2.35. The results report that for higher bandgap materials such as a-Si and CdTe had a better energy yield in summer compared to winter with a difference of *SF* of around 12% and 6.7% respectively for the location in Stuttgart and about to 8.9% and 3.3% in Tamanrasset. In contrast CIGS had a better performance in winter in comparison to summer, which was less pronounced with only 2% change in both locations, similar trend was registered for the rest of the technologies, namely no remarkable spectral effect is observed. It is hypothesised that the impact of the solar spectral distribution on thin film is due to the relation between *AM* of clear days and latitude. It is also concluded that the narrower the band where the of V conversion of the material, the higher the spectral effects.

Dirnberger *et al.* wrote [24] that there are losses and gains on the different PV technologies with different bandgaps due to their varying spectral response. In this work they used spectral mismatch factor (*MM*) to evaluate the spectral influence and compare it to *APE*. Here *MM* is defined as the ratio of I_{SC} of the PV module investigated over the I_{SC} of the reference device, in this case two pyranometers CMP11 Kipp & Zonnen. The spectral irradiance was measured with two spectro-radiometers EKO MS-710 and MS-712, the integrating time was in a range from 100 ms, for high irradiance, to 5 s, for low irradiance. This data was taken from June 2010 to December 2013 in location 47.9973˚ N, 7.8525 E˚, in different time increments but resampled to 5 min averages for the final analysis. The *APE* was calculated within the range of 350 nm to 1050 nm, this showed a similar plot of irradiance vs *APE* to the one presented in the present thesis, although the monthly *APE* plot has a lower value than the one calculated. This paper also weighted among the spectral response of different modules of the same technology, justifying that since the difference is small there is no necessity of differentiate different modules of the same technology. The use of *APE* for

as a solar spectral index is contested since they explained that there is no bijective relation between *MM* and *APE*, namely a value of *APE* calculated for two different spectral distributions can be equal, but for the same case two different *MM* values would occur besides this *MM* seemed to be more sensible to small changes in spectrum than *APE*. They conclude that devices with stronger sensitivity at shorter wavelengths (long bandgap) exhibit a significant spectral gain (+3.4% for a-Si and +2.4% for CdTe between seasons) with seasonal gains in summer and losses in winter. For c-Si there were no clear seasonal trend and seasonal impact was +1.4%. High efficiency c-Si and CIGS, with an enhanced sensitivity in longer wavelength (short bandgap) demonstrated an opposite seasonal trend, with very little impact in the summer months and spectral gains in winter, which were +1.1% for High eff c-Si and +0.6% for CIGS. They concluded that it is reasonable to consider the technology specific spectral impact in energy ranting or yield prediction. They also mention the necessity of more ground-measured, spectrally resolved data exchange and comparison of data and methods.

Cornaro and Andreotti [23] published a paper in which explained that routine spectral irradiance measurements are relevant to understand the influence of solar spectrum on PV modules. For their research they studied the performance of two modules one based on a-Si technology and the other on p-Si, there were 2 spectro-radiometers EKO MS-710 and MS-712 to measure a range of irradiance of 350 nm to 1700 nm in intervals of 10 min on a horizontal plane for 6 months in the University of Rome Tor Vergata in coordinated 41° 51' 13.2" N, 12° 36' 12.7" E, approximately. *APE* was used characterise the solar spectra, this was justified due to its device independence and it was calculated in the range of 350 nm to 1050 nm. They commented that last generation PV devices have a narrower spectral response which makes them more sensitive to spectral variations. The performance indicator (PR) was defined as the ratio of the power generated in field at the MPP of the system over the efficiency of the same module at STC. A variation of 7% in *APE* is observed between summer and winter, summer being bluer, with a 10% of bluer enrichment during overcast, in comparison to clear days. For a-Si there was a clear increase on the PR as the *APE* became bluer, the p-Si did not show a clear trend correlated to *APE*, however this technology showed a stronger dependence to temperature.

Sirisamphanwong and Ketjoy explained in their paper [95] that in the Thailand region of Naresuan University with coordinates 16˚ 49’ North and 100˚ 15’ east. For the evaluation of the energy output they use an indicator they call Field Output Factor (*FOF*) which is equal to Power Rating (*PR*), thus its calculation is identical, namely, *FOF* is defined as the ratio of actual power measured over the nominal power output in kW. They oversaw three different PV technologies: Heterojunction with intrinsic thin layer (HIT), a-Si and p-Si. However, the paper only considers the last two. The modules were facing south at 16˚, their temperature and solar irradiation were

measured at intervals of 5 minutes from January 2008 to December of the same year. The *APE* was calculated within the range of 350 nm to 1050 nm, using a spectro-radiometer EKO MS720 and a pyranometer EKO MS-601. In this paper the highest *APE* is recorded in rainy seasons with a value of 2.00 *eV*, while the mean value of 1.99 *eV* was recorded in summer and 1.97 *eV* for winter. The results indicate that Thailand has a blue rich spectrum, a-Si showed a strong positive linear dependence on *APE* values, while p-Si is not strongly sensitive to spectrum distributions, the data indicated a polynomial dependence which reach its peak around 1.85 *eV*, this seems to indicate that a-Si technology would be more suitable to typical Thailand spectral behaviours and would be useful to optimise the PV systems to spectral distributions. In summary, they compared a-Si and p-Si, under Thai climatic conditions, and determined that the value of *APE* has different influences on the *FOF*. Amorphous Silicon showed a linear positive tendency with the increase of the *APE* value, closing to 95% at 1.97 *eV*, whereas p-Si had its peak on 1.85 *eV* and a decrement to near 70% of its *FOF*. Concluding that under these criteria a-Si was more suitable for these local conditions.

Minemoto *et al.* [67] analysed the effect of the spectral irradiance on the performance of the PV modules. Despite that they concluded that outdoor performance is dependent mostly on module temperature, a-Si showed a dependency on *APE*. They focused on single crystalline silicon (m-Si) and a-Si, this analysis was performed using modules installed facing south at Kusatsu city in Japan, in coordinates 34° 58' North and 135° 57' East. The modules efficiencies were 13.4% and 6.9% for m-Si and a-Si respectively. The solar spectra was recorded using a spectro-radiometer MS-700 EKO with a range between 350 nm to 1050 nm, the temperature on the back of the modules was measured by a thermocouple MS-62 EKO. The measurements were acquired every minute within a period of a single year from January to December 2006. To evaluate the impact of *APE* on PV modules it was calculated the *PR* (performance ratio) as the module efficiency over the nominal output energy of the module under STC. For their evaluation they omitted the low irradiance spectra (< 0.15kW m^{-2}) to avoid the scattered data of low irradiance spectra and concluded that m-Si performance is almost only dependent on temperature while a-Si depends strongly on *APE*.

Perez-Lopez, Fabero and Chenlo in 2007 [82] published an article about the experimental results of the influence of the Solar spectral irradiance on different PV materials. The materials in which the study was focused were: m-Si, a-Si, CIGS and CdTe. Instead of use the parameter of average photon energy (*APE*), the authors used the Useful Fraction of irradiance (*UF*); and calculated the Spectral factor (*SF*), a ratio of the $\boldsymbol{I_{SC}}$ of the standard solar spectral distribution in relation with the $\boldsymbol{I_{SC}}$ of the actual measured solar spectrum; Weighted Solar Spectra (*WSS*), solar spectrum under which the PV materials are producing energy weighed over the irradiance level. The result of the experiment shown more efficiency on the performance for PV materials with narrow spectral responses (*SR*), such as a-Si and CdTe, for the typical irradiance of summer and materials with wide *SR*, such as m-Si and CIGS, are more efficient in winter.

2.6.2.3 Thermal effects

The results shown in the paper by Jardine and Lane [45] tell us that from the thin film technologies, CIGS and double junction a-Si had the best relative performance under cloudy conditions, also explained that CdTe modules used in this experiment were in prototype stage. Despite not outperforming c-Si and pc-Si, from these thin films the high temperature performance of a-Si make it better suited for high insolation regions like Mallorca, while CIGS with its high performance in low irradiance is the more suitable for cloudy places like Oxford, UK. They noticed that the majority of energy delivered by the PV systems in UK were for irradiances between 200 W m^{-2}, and 600 W m^{-2}, while in Spain were for irradiances between 500 W m^{-2} to 900 W m^{-2}, they explain that small bandgap materials have large negative temperature coefficients and drop in performance at high temperatures, and that the 5˚C of difference between Mallorca and Oxford could benefit these PV materials. It also pointed at the importance of a good operating efficiency at the moment of choosing an inverter.

Williams, Gottschlag and Infield [110], focused on the performance of different PV technologies for the UK climate, such as: c-Si, a-Si, p-Si, CIGS and CdTe. The main propose was to analyse the different environmental effects on the cells: Spectral effect, thermal effect and irradiance. They comment that a-Si has been reported to have positive temperature coefficients, but that after correcting for primary spectral effects of the device temperature is found to be negative, the material they report to have a lower thermal factor was a-Si (0.10% to 20%), followed by CdTe (0.35%) and c-Si (1.0%). In addition they also remark the effects of the parallel and series resistance in the energy loss for the design of the PV-Cells arrays. This is probably one of the reasons why the same technology sometimes differs on its performance among different manufacturers. In conclusion it is reported that the decrease of efficiency could come from a manufacturing design involving large series resistance, which could affect the performance in a very strong way under high irradiance and it is mentioned the drop of efficiency during the low irradiance, which is thought to be caused by a relatively small short circuit resistance. They express that their research to study these factor are ongoing. However they did not take into account the influence of the spectral distribution.

In their article Ito *et al.* [43], made a comparison among 5 PV technologies and their feasibilities for what they call very large scale or VLS (over 100 MW) in the Gobi desert. The evaluation included economic and environmental factors. Their findings respecting thermal effects can be summarised as a 0.38% reduction of the specified efficiency by centigrade degree for mc-Si, 0.17% for a-Si, 0.19% for CdTe and 0.27% for CIGS. They also concluded that the efficiency of the modules is important, but the energy pay back can be within 3 years for high efficiency cells such as m-Si; they pointed that Gobi desert is a cold desert (between North-China and Mongolia),

for such circumstances m-Si is a very suitable technology; but for the case of hot desserts a-Si, CdTe and CIGS technologies could be good components; the VLS-PV systems are a good option in order to reduce the CO_2 emission even with the current technologies.

Makrides *et al.* [58] show the importance of temperature coefficient. This was calculated for 13 different arrays of PV technologies (Nine of Crystalline silicon, two of a-Si, 1 of CdTe and one of CIGS) installed in two locations in Cyprus and Germany by a period of 1 year, they reported that the technology less affected by temperature was CdTe with -0.023% and -0.074%, for Cyprus and Germany respectively, of reduction of the nominal maximum power. Furthermore c-Si was the most affected in terms of yield of maximum power point against temperature with thermal coefficients as high as -0.465%, in Cyprus, and -0.437%, in Germany. In figure 2.29 it is displayed a summary of the values for the tests performed in Cyprus. Their conclusions pointed out a reasonable matching of the manufacturer temperature coefficient provided and the results of the experiment.

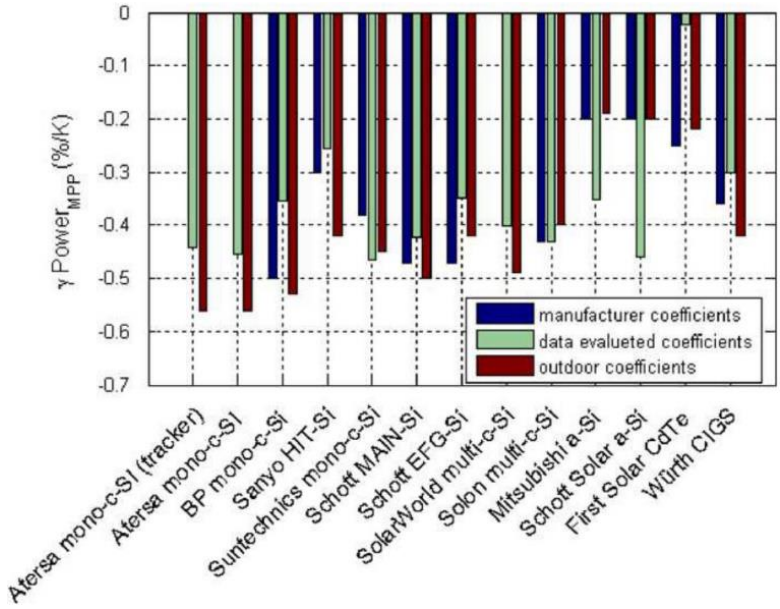

Figure 2.29: Temperature coefficients for different PV technologies, for tests based in Cyprus from Makrides et al., 2009 [58].

3 Testing different geometries for an accurate Cosine Correction Optical Coupling

This chapter is an extended version of the paper published in September of 2017 [19]. The motivation for this chapter was to produce a device that will allow the acquisition of spectrally resolved data by increasing the field angle of optic fibre sensor typically used by spectrometers. The results show a significant improvement to the current devices in the market.

3.1 Introduction

Spectrally resolved measurements of solar radiation are important to understand the variations of the photovoltaic (PV) technologies due to effects of the climate. These measurements can be expensive as the equipment needed to measure the accurate solar spectrum is sophisticated. However there are some low cost spectrometers on the market which use optic fibres. This simplifies the optomechanics of the system and leads to reliable measurements. Nonetheless, for these systems to work the angle of detection needs to be increased from the 25˚ of a bare fibre to the full 180˚ with a cosine response. Devices performing this task exist but (as we shall see) do not reproduce the cosine response very well. In this chapter are investigated alternative design concepts for a robust cosine correcting fibre coupler.

The cosine correction ideally should follow the Lambert's law, so that the intensity is proportional to the cosine of the angle of incidence. For previous projects the cosine corrector CC-3 of Ocean Optics was used, however these devices were both fragile in outdoor conditions and expensive. This chapter describes the development of a device that widens the view angle whilst still being accessible and innovative.

Furthermore, the design and testing of a novel cosine corrected fibre optic is detailed in this chapter. This was proven to be an economical alternative to the existing commercial products, proving even to outperform them. Irradiance measurements are typically made using a broad band pyranometer with thermopile sensors. These tools are expensive and finding lower cost solutions is important to help to reduce the overall costs of solar irradiation data acquiring. Another constraint of pyranometers is their inability to acquire spectrally resolved data. To acquire this data for this work, a spectrometer via an optic fibre (OF) was chosen, due to the convenience of being able of

place the spectrometer inside an isolated shelter to minimize the influence of outdoor conditions while acquiring the data through the sensor located outside. As mention the OF is only able to capture light within a limited view field angle, thus employing devices to increase this is necessary, as seen in figure 3.4. The concepts present in this chapter generated a paper which was accepted in the journal Revision of Scientific Instruments on September 5th, 2017 [19]. This paper can be seen in appendix 7.2.

The widening of the field view angle is referred to as cosine correction. Because the ideal angular sensitivity should be proportional to the cosine of the incidence angle. The existing commercial options have shown limited performance in-field, both in terms of accurate reproduction of the cosine response and their physical fragility. Our motivation is to overcome these obstacles and design a robust accurate coupler that can be used for extended periods in the field.

A typical state-of-the-art (SoA) cosine corrector available in market [101, 7, 79]is constructed from a hollow opaque metallic tube in which a disc 150 μm thick made out of Polytetrafluorethylene (PTFE) is inserted at one end and clamped about 200 μm from the end of the tube. At the other end there is a female ¼" screw-type coupling mechanism to allow the standard optic fibre SMA adapter to be screwed into the coupler, see figure 3.1.

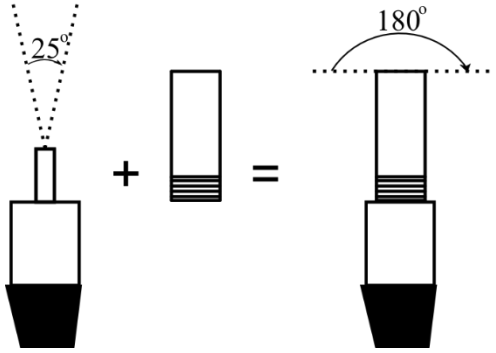

Figure 3.1: Visualisation of the use of a cosine correcting coupler, when attached to the optic fibre allows for a wider reading angle.

It was found that the design is not suitable for extended use in-field as the thin PTFE disc resents the influence of outdoor elements, namely temperature, rain and wind. These factors cause that the thin scattering surface to detach from the rest of the body rendering the device useless. In an ideal case, the incident light received on the thin PTFE disc would be diffusely and isotropically scattered forwards towards the OF cable behind the disc. The cosine corrector would provide an accurate reproduction of a cosine response of a nude planar detector in cases where the scattering follows Lambert's law [80], as seen in equation 3.1.

$$\Phi_\theta = \Phi_0 \cos\theta \tag{3.1}$$

Where Φ_θ is light intensity at angle θ, which is subtended between the light source and the normal of the reflective surface; and Φ_0 stands for the light intensity delivered on the reflective surface.

In addition to the commercial SoA devices [101, 7, 79], some of the coupler within the literature were reviewed as a performance benchmark. Bartlett *et al.* [8] detailed the performance of a spectral measurement system with six sensors arranged on a horizontal plane using cosine correctors. Each sensor had a bandpass of about 10 nm with centre wavelength of 411.4 nm, 442.9 nm, 489.9 nm, 555.2 nm, 683.8 nm and 699.5 nm. The error was under 7% only for incidence angles under 70˚. In the study of Blackburn and Vignola it was found that the cosine error was of 45% for angles above 72˚ due to self-shading generated by the geometry of the cosine correcting coupler, which is described as an acrylic diffuser surrounded by a cylindrical housing made of corrosion resistant metal, the perimeter of the diffuser has a rim to block light.

In terms of understanding the influence of the solar spectrum on photovoltaic energy production, Cornaro and Andreotti [23], evaluated the influence of the solar spectrum upon amorphous-silicon PV cells, used spectro-radiometers with an optical diffuser integrated and protected by a glass dome and reported a cosine error of ± 5% for all wavelengths. This work did not detail the diffuser's geometry, yet it is inferred by the text that it was a simple flat PTFE surface as seen in most of devices available in the market. Pohl *et al.* [84] prepared multiple low-cost stations to measure, solar irradiance for whether monitoring, among others variables. For irradiance measurement a simple flat scattering PTFE surface was employed. Guerra, Faez and Fuentealba [32] described the manufacture of a low cost pyranometer but did not address cosine correction. They used a PTFE layer of 1.05 mm of thickness for attenuation. Medugu, Burari and Abdulazeez [64] and Martínez, Andújar and Enrique [60], described the design and test of different low-cost pyranometers. It is interesting to see a similar approaches to ours, namely testing alternative geometries for the cosine correction of a photo-diode-based pyranometer. The designs were a frustum of a cone with different angles. Bevel edges of 45˚ gave the best results. PTFE was used as a diffusing material due to its optimal optical characteristics referred by Lowry, Mendlowitz and Subramanian [54] described diffusion of transmitted light nearly perfectly for a range from ultraviolet (UV) up to near infra-red (NIR).

In summary, PTFE is typically used as a diffusing material in cosine correctors – both for fibre optic coupling and for planar sensors. The accuracy of the couplers reported in the literature vary from a respectable 5% to a rather poor 45% absolute error depending on the angle of incidence.

In the present work we report the design and fabrication of several different fibre optic couplers using PTFE as a scattering material. We systematically characterise the designs in terms

of spectral transmission, cosine response and specular reflection. Our best performing design (G2) has mean absolute error of less than 3% averaged over all angles of incidence.

3.2 Assessment of PTFE linear attenuation coefficient

PTFE is widely used as a light scattering material within the optics industry [76] with the transmission of low and high density materials being reported for UV, visible and near infra-red wavelengths [103]. For this research high density PTFE, 2.5 g ml^{-1}, was chosen [56]. It is important for the use of PTFE as a scattering material for an optic coupler in an irradiation instrument to consider the relative attenuation of different spectral components. The ideal scattering surface would have equal attenuation so as not to contribute to systematic errors in irradiance measurement during changes to spectral intensity. To assess the impact of differential attenuation in our PTFE coupler it the percentage of transmission of stock material for different thickness ranging from 1 to 10 mm was measured. The empirical attenuation was calculated using equation 3.2.

3.2

$$T_\lambda = \frac{\Phi_{0,\lambda}}{\Phi_{T,\lambda}}$$

Where $\Phi_{0,\lambda}$ is light intensity received at the surface, $\Phi_{T,\lambda}$ stands for the transmitted light intensity, and T_λ is the fraction of transmitted light at a given thickness. Results can be seen in figure 3.2.

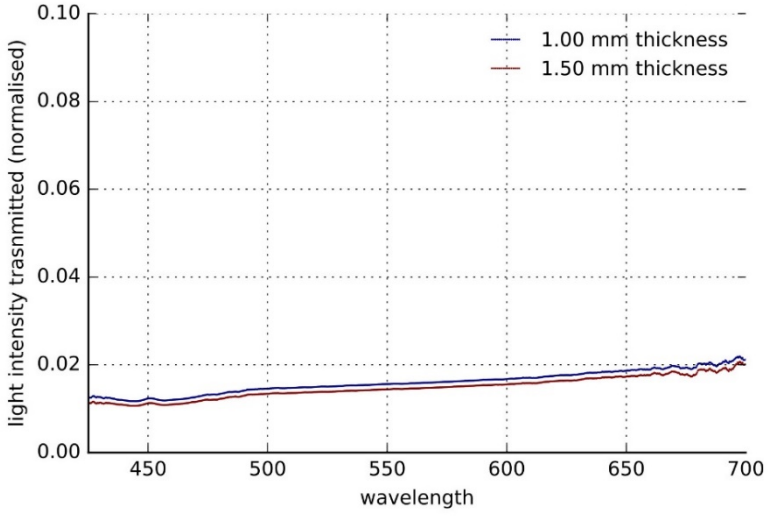

Figure 3.2: PTFE's fraction of transmitted light throughout thickness of 1.0 mm and 1.5 mm of thickness. The light transmitted is normalised to the light intensity without PTFE.

This data seems to be consistent to the information presented by Lowry *et al.* [54], since within the range between 450 nm to 700 nm there is a mild linear increase of less than 5% within the mentioned range. It suggest a similar tendency to the one seen in figure 3.3 of a fairly even

transmittance across the visible and infrared region. The difference of the fraction could be explained by the different thickness used in their study, nonetheless these can be easily corrected in the posterior calibration for absolute irradiance.

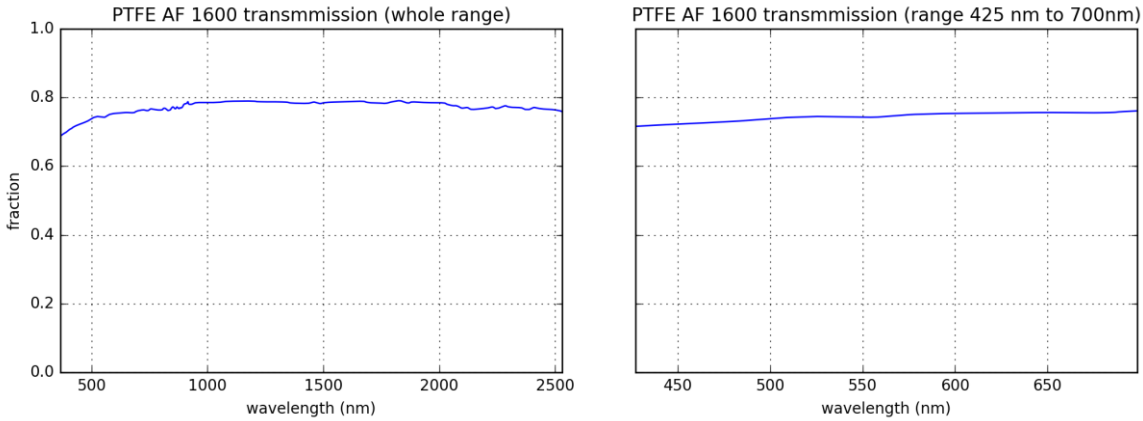

Figure 3.3: PTFE light transmission, form Lowry et al. [54]. The figure on the right shows the whole range characterised the one on the left show the range in which the spectrometer works, here it is possible to see a small and quasi-flat response making it a reasonable choice for a scattering surface material.

This result shows that the attenuation of PTFE is spectrally void of features and shows less than 1% of difference between 450 nm and 700 nm or 0.36% per 100 nm. Since the mean wavelength of sunlight changes less than 50 nm [1] between fully diffuse and fully scattered light the inferred error in scattering is estimated to be less than 1%, as seen in the next section.

3.3 Design, manufacturing and characterisation method of CCOCs

The design of the cosine correctors were heavily based on the current SoA device, although the whole body and diffusing screen is made out of PTFE with opaque black tape on the sides to avoid absorption of light from outside the diffusing screen. There were some attempts to characterise the geometries and backwards scattering light diffusion within them using the free software for 3D modelling FreeCAD 0.15 to later render these in POV-Ray 3.7.0 a ray tracing program that generates photorealistic images, but that would require a level of expertise in optics that could have not been acquired in the available time. Therefore the geometries were mainly chosen among a “brainstorming” session and different versions of the main ideas were produced. In figure 3.4 it is seen briefly the attempts to perform a more analytical characterisation of the *CCOC*’s designs.

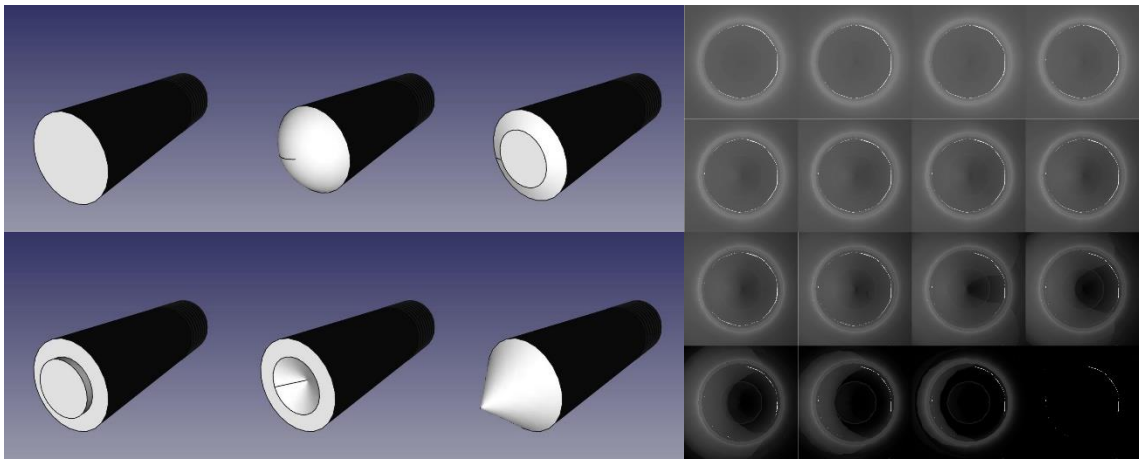

Figure 3.4: Attempts to characterise analytically the geometries of the CCOC. (right) 3D drawings of selected CCOC devices using FreeCAD. (left) demonstration of the attempt to characterise the light backwardly diffused in the interior of the device, using POV-ray rendering.

For the manufacturing of the CCOCs a cylindrical rod of PTFE of 10 mm of diameter was placed in the chunk of a centre lathe, the cutting tools for the exterior used were made of "high speed steel", these tools were ground with a rotatory sharpening tool to achieve the angles. For the interior different drills of stainless steel were ground to achieve the required shapes of the interior concavities, lastly the threads were made with a thread die for a female $^1/_4$ SMA thread.

To review the final texture of the diffusing screens they were observed under a microscope Carl Zeiss Axioskop 2 which allowed us to appreciate that there was no major difference between the SoA and the *CCOC* surfaces as seen in figure 3.5.

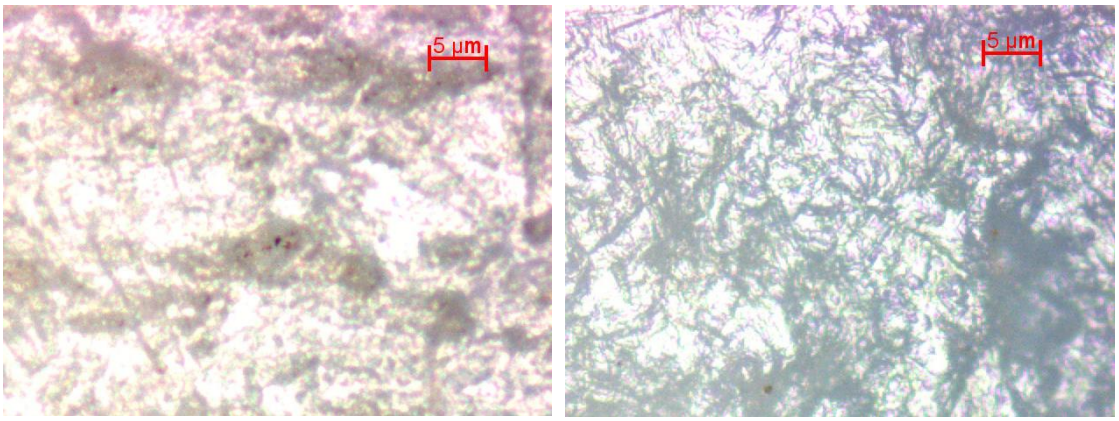

Figure 3.5: Visual comparison by microscopic imagery of diffusing surfaces (left) surface for the SoA coupler) and (right) the PTFE Cosine Corrector Optical coupling (CCOC).

Despite this it would be advisable to perform a more sensible analysis on the roughness of the scattering surfaces, the microscopic images showed no remarkable differences between the diffusing surfaces of the SoA device and the machined PTFE ones.

3.3.1 Evaluation of specular reflection measurement

Sometimes, even if the detected forward scattered light obeys the cosine law some systematic errors can arise if light is reflected specularly and as such the transmitted light intensity will depend on the angle of incidence. To quantify the effect of specular reflection on the cosine response of the coupler the scattered and reflected light from a planar coupler design was measured. An ideal isotropic scattering surface will have no specular reflection. The evaluation was made using a goniometer. On one arm a 650 nm diode laser was aligned to the centre of rotation of the goniometer. On a second arm a fibre coupled light detector was also aligned to the centre of rotation at a distance of 18 cm. The laser was fixed at a distance of 18 cm and an angle θ of 60˚ to the horizontal of the coupler surface.

The intensity of incident light was measured at the centre of the goniometer. Measurements of the scattered and reflected light were made relative to the incident intensity (both at the beginning and end of the experiment). Five readings for every iteration were taken with the coupler at angle φ which was subtended from the plane of the diffusing surface on the opposite side to angle θ, to the coupler sensor within a range of 90˚ to 0˚, with progression of 10˚ for each step. A diagram of the experimental set-up can be seen in figure 3.6.

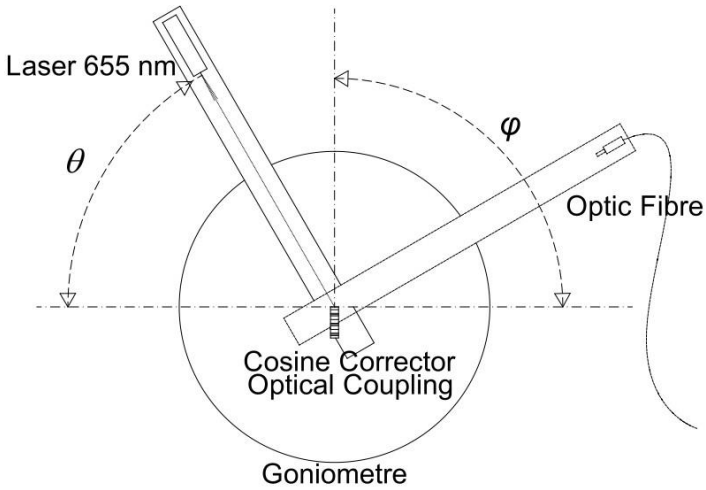

Figure 3.6: Experimental set-up for the determination of the light fraction of specular reflection on PTFE. The laser was pointed to the scattering surface and the reflected light measured by the optic fibre at a given φ angle.

For the calculation of the light intensity for angles φ, the readings were compensated for the dark noise signal and normalised to the intensity of the input light. For the calculation of the ideal response Lambert's law was used. The results can be seen in figure 3.7 where a small specular reflection leads to a doubling in the scattered intensity from the ideal isotropic value. The intensity of the specularly reflected light is more than 10,000 times smaller than the incident laser light leading to estimated systematic errors in the angular dependence of the intensity of the forward

scattered light of less than 0.01%. We conclude that the influence of specular reflection on the performance of the coupler is negligible.

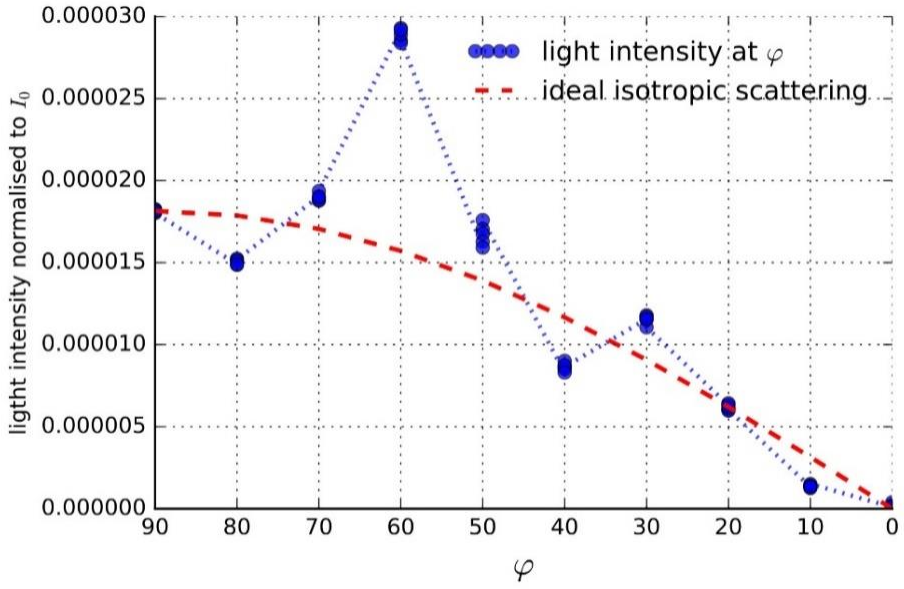

Figure 3.7: Results of specular reflection fraction of PTFE surface, the specularly reflected light is 10,000 times smaller than the incident light therefore, this is not considered to generate a negative impact on the performance of the coupler.

3.4 Assessment of the cosine response

This section explains the experimental setup which aimed to have an objective measurement of the cosine response of the SoA and CCOC devices. The integration time was carefully selected to have a healthy noise to signal ratio of about 2 orders of magnitude. Base on the measurements it was found that an integration time of 0.8880 seconds was enough to avoid problems related to non-linearity of the sensor and oversaturation of the signal for most angles of incidence.

3.4.1 State-of-the-Art coupler

As a benchmark for the assessment of the newly designed couplers we initially characterised the cosine response of a commercial coupler. A goniometer was set up with a stabilised white LED of constant luminous intensity, aligned along the rotating arm, and the coupler device under test was located at the centre, with the diffusing screen aligned to the plane of the reference. The light source was moved on the circular path around the coupler being tested. The angle of incidence was measured in degrees subtended between the normal of the coupler surface and the position of the light source. This angle was varied from 0˚ to 90˚ with increments of 5˚. For

each step fifteen independent readings were made. The measurements were taken using an Ocean Optics spectrometer JAZ A1392. As the main purpose was to measure the change of intensity as a function of the angle of incidence, the units used in these readings were only raw spectrally integrated counts, which have been previously tested for value stability. The experimental layout can be seen in figure 3.8.

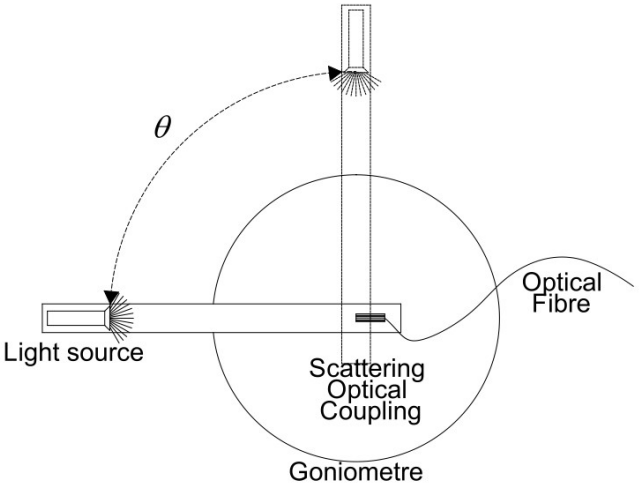

Figure 3.8: Experimental set-up for the assessment of SoA cosine corrector and validation test for the CCOCs.

The light intensity was normalized to the value at 0˚. For the SoA it is appreciated at 25˚ a fraction error of -4.52% the error became higher with wider angles reaching -94.33% by 85˚, as seen in figure 3.9.

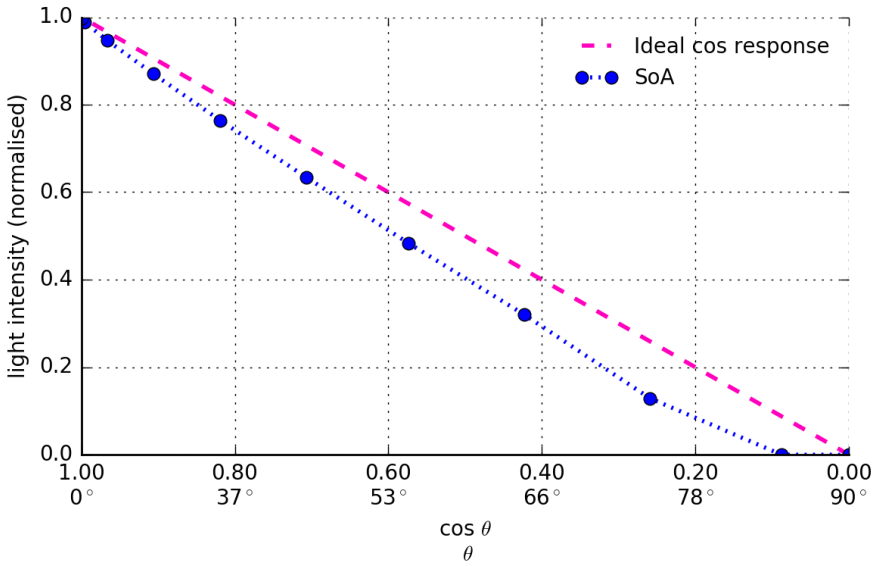

Figure 3.9: Assessment of the cosine response for the State-of-Art cosine corrector (SoA), compared to the ideal cosine response.

Broadly speaking, the geometry of the new designs was based on the SoA coupler, constructed as a hollow monolithic quasi-cylinder with a lateral wall 1.2 mm thick, this wall was

covered with opaque black tape to avoid light absorption from other parts of the body besides the scattering surface. This scattering surface is found at one end of the body. At the opposite end there is an opening with a female $^{1}/_{4}$ SMA screw-type coupling mechanism for connection with the standard optic fibre mounting. A comparison of the SoA and one *CCOC* can be seen in figure 3.10.

Figure 3.10: Cosine corrector comparison, State-of-Art cosine (left) and CCOC design D1 (right).

3.4.2 Other designs

This segment aims to focus on those designs that could be of interest due to their geometries which were based on the consulted literature for cosine correction. These designs are: a semi-spherical shape adopted in some designs of pyranometer sensors (E1), a design of the cosine correcting surface shaped as a frustum of a cone similar to the one suggested by Martinez, Andújar and Enrique [60] (C3) and the utilised design for the actual data acquisition (D1).

The monolithic shape was machined from a solid rod of PTFE, to a diameter of 6.4 mm and from (20 to 20.55) mm high, depending on the design. All vertical sides of the coupler were covered with opaque black tape to ensure that the only light received was from the scattering surface. The details of these designs can be seen in figure 3.11.

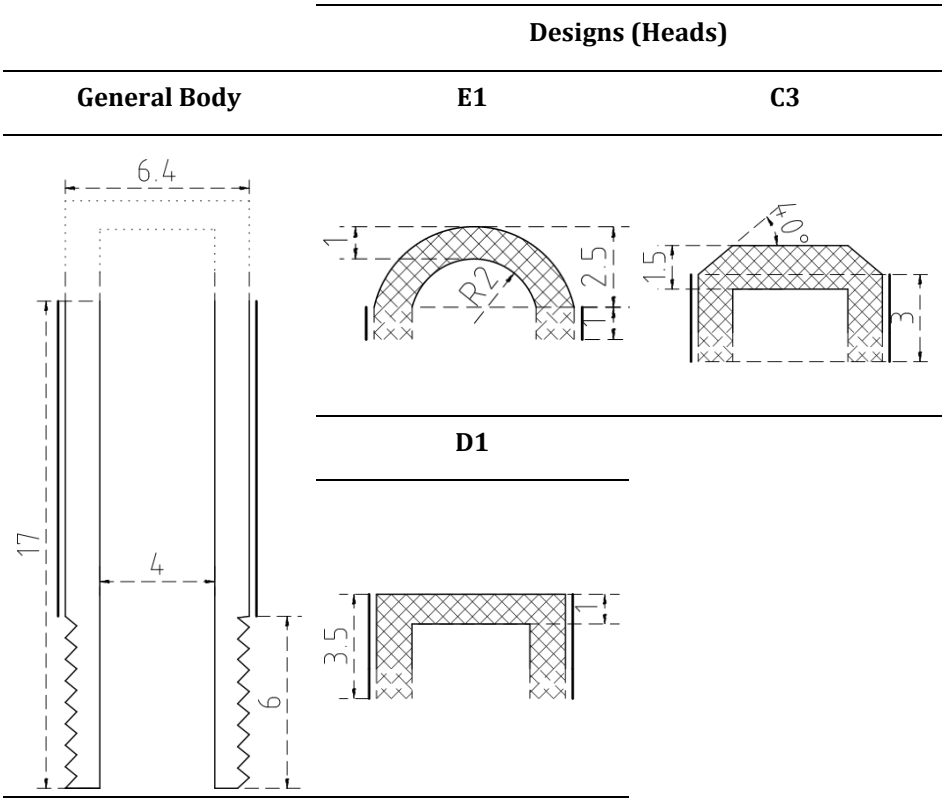

Figure 3.11: Designs of interest of CCOCs, based on ideas found in literature, the measurements are in millimetres unless specified otherwise. The body is made of the material specified in the head, the solid vertical line on the sides represent the opaque black tape used to avoid absorption the rest of the body.

The results of the assessment of the cosine response of the aforementioned designs are shown in figure 3.12. In the same figure the determination coefficients (r^2) in relation to the ideal cosine response are also shown. However taking only this value to evaluate the designs could be misleading due to the apparent high reliability, therefore the Mean Absolute Error (*MAE*) was also considered. For the calculation of the *MAE* the values at $\theta = 0$ were ignored, due to its proportionally higher variation with the expected ideal value (namely 0) at that point. The result of this calculation can be seen in table 3.1.

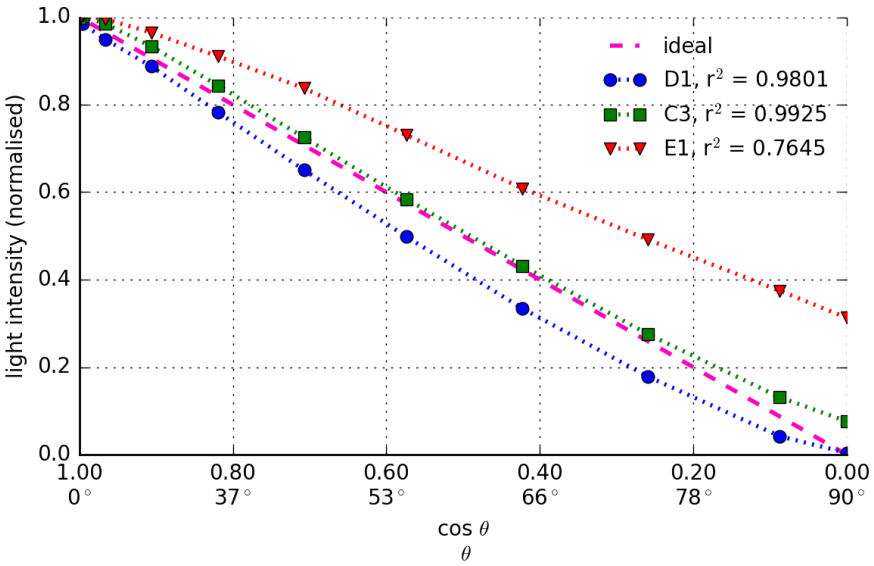

Figure 3.12: Evaluation of designs of interest comparing to the ideal cosine response.

Design	*MAE*
C3	0.0722
D1	0.1346
E1	0.5315

Table 3.1: Mean Absolute Errors of designs of interest.

The *MAE* was calculated using formula 3.3 for every angle and then averaged across all angles.

$$MAE = \frac{\sum_{i=1}^{N} \left| \Phi_{N,\theta} - \Phi_{cos\,\theta} \right|}{N} \qquad 3.3$$

Where N is the number of measurements; $\Phi_{N,\theta}$, is the light intensity measured normalised at angle θ and $\Phi_{cos\,\theta}$, is the ideal light intensity proportional to cosine of angle θ. The MAE readings at 90˚ were ignored because the expected cosine response is 0 and small values are very likely to be heavily influenced by the common noise in the equipment. Its calculation produced a misrepresentation of the observed validation.

3.4.3 Best Performances

There were 29 different designs fabricated and tested but in this we will focus only on the most relevant ones. The different geometries can be seen in figure 3.13.

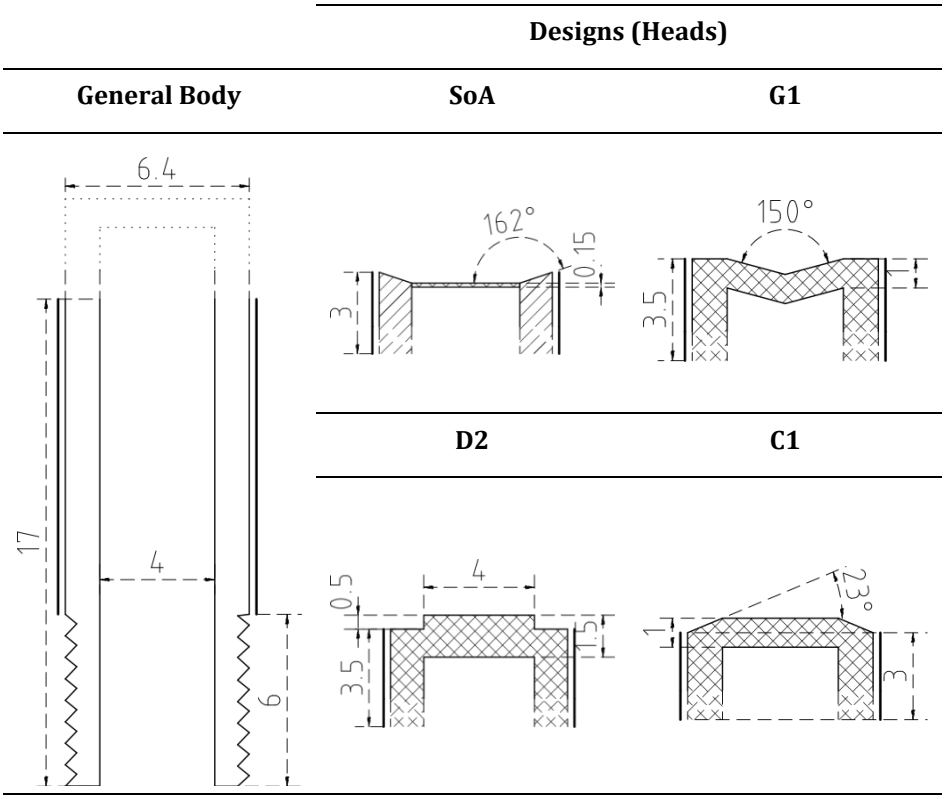

Figure 3.13: SoA and CCOC designs with best performances. The present drawings are cross-sections, the actual piece could be imagine as a solid produced by the revolution by the central axis of the general body plus head section. The bodies are made of PTFE, while the SoA has a stainless steel body. The body is made of the material specified in the head, the solid vertical line on the sides of the slides represent the opaque black tape used to avoid absorption from the sides of the body.

Cosine performance of the couplers was measured by calculating the average *MAE* of the different designs and the SoA measured with angles of incident light from 0˚ to 85˚ degrees.

3.5 Results

Finally, we present the performance of the different coupler designs with reference to an ideal cosine response. The method described in section 3.4 is used here. The angular response of the different designs are shown in figure 3.14. Surprisingly the geometries with small concavities and convexities on their surface presented a response closer to the expected cosine relation. The strongest correlation to the ideal response was design G1. Designs D2 and D1 also had a good response that was close to the ideal values for most angles and in general they performed better than the SoA cosine corrector.

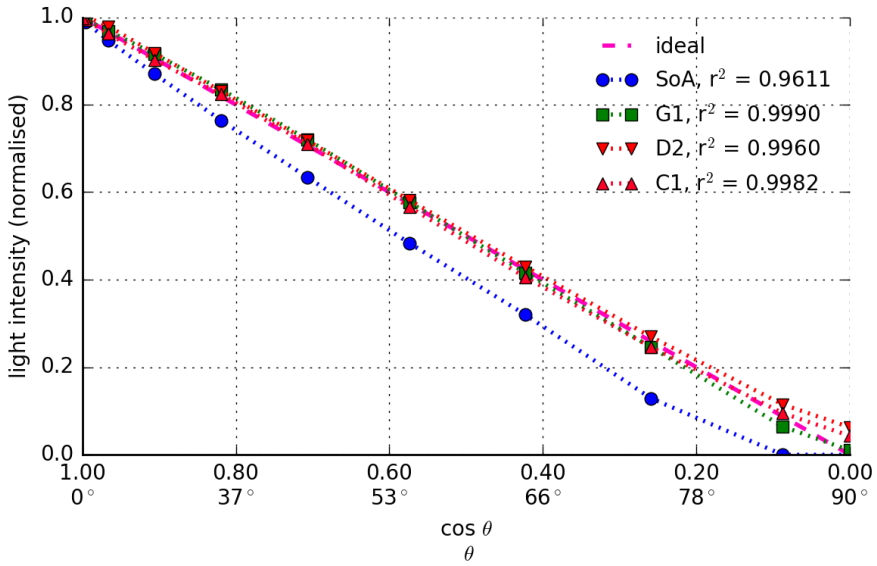

Figure 3.14: Normalised cosine response for best CCOC designs and SoA cosine corrector in comparison to ideal cosine response.

The design that showed the least dispersion to the ideal response was G1 with an r^2 of 0.9990, followed by design D2 and C1 with 0.9960 and 0.9982 of r^2 respectively. However regarding *MAE* the best evaluated were in C1, G1 and D2, with values of 0.0215, 0.0391 and 0.0450, respectively. G1 and D2 kept their *MAE* values way below 0.1 for most of angles but by 85˚ their error was registered around 0.3, while C1 was under 0.1 in all angles under 85˚, despite having the highest dispersion of these three models. The SoA reported a considerable dispersion of 0.9611 of r^2 and a high error with a *MAE* of 0.2147.

Results of the average *MAE* for the aforementioned designs are summarized in table 3.2 and presented in detail in figure 3.15.

Design	***MAE***
SoA	0.2147
G1	0.0391
D2	0.0450
C1	0.0215

Table 3.2: Results of validation test for CCOC designs and SoA using Mean Absolute Error (MAE) in comparison to ideal cosine response as indicator.

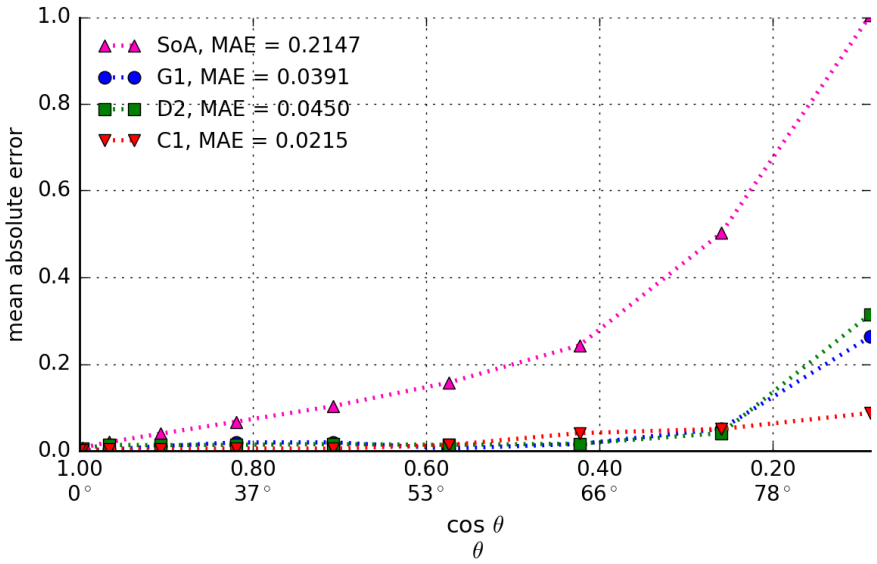

Figure 3.15: Mean Absolute Error as a fraction for coupler designs G1, D2 and C1 and SoA cosine corrector in comparison to ideal cosine response. While the lowest MAE was reported by the C1 design the G1 was the one with highest correlation, with an r^2 of 0.9990, followed by D2 with 0.9960, lastly the one of model C1 was calculated in 0.9982.

3.6 Discussion and conclusions

Although further analysis should be conducted on the stability and light absorption of PTFE and its dependence on wavelength. Overall due to the low-cost, physical, chemical and optical properties; this material stands as the best option for the manufacturing of the couplers. We find that spectral dependence of attenuation varies approximately 5% over the range 450 to 700 nm and that with a machined surface specular reflection is minimised to a point where its impact on coupler performance is negligible.

The designs presented here have excellent agreement with the cosine response in comparison to the SoA coupler. Part of the poor performance of the SoA coupler is believed to be due to its geometry. Thus the cylindrical frame of the PTFE diffuser disc shades the diffusing screen and it is seen as an under-measurement at low elevation angles. However, even for coupler D1, which was a flat surface, some under-measurement are seen for a range of angles of inclination. To correct this under-measurement of D1, G1 is concave and hence enhances measurements at all angles of inclination by approximately the level needed to generate perfect cosine response. Our champion design G1 exhibits errors of less than 1.0% for angles under 50˚, significantly outperforming the errors reported for the SoA coupler.

Despite not being the best correcting device, it was the design D1, the one used for the acquisition of spectral data on the rooftop station, mainly due to time constraints during the PhD.

The development of the tasks of calibration acquisition and analysis of solar irradiance will be explained in the next chapters. The current chapter produced a paper accepted in the journal *Review of Scientific Instruments* [19], this paper is included in this thesis in the appendix 7.2.

4 Calibration of spectrometer for long term outdoor solar readings

This chapter describes the development of a method to perform the calibration of laboratory grade spectrometers using as reference the terrestrial solar spectral irradiance in cloudless conditions. Based on using different models of solar spectra and raw data acquired in clear sky conditions, calibration curves were calculated and validated. The result is a reliable low resolution spectral calibration method suitable to perform low-cost spectrally resolved data acquisition.

4.1 Introduction

There are recommended methods to calibrate a spectrometer. One is to measure its response to an already characterised light source. Nonetheless, low cost calibration light sources have a large variation in intensity across the range of the solar spectrum. There are large calibration errors at low wavelengths due to low intensity of the light source at this range and high intensities where the grating efficiency of the spectrometer is low. As example figure 4.1 shows the mismatch of resolution of the calibration data versus the solar spectrum.

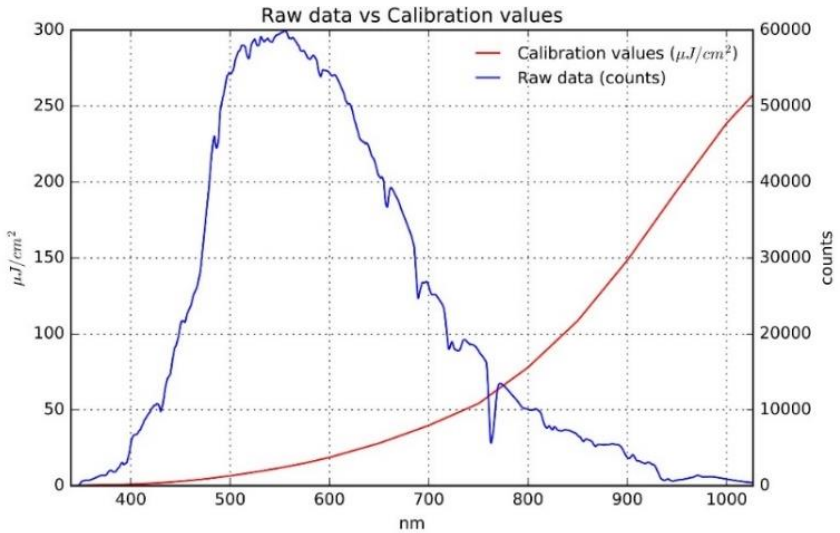

Figure 4.1: Calibration data for the LS-1-CAL light source and the raw data acquired from a clear sky solar spectrum. Here can be seen that the resolution of the calibration data is lower around the expected peak of the solar irradiance (between 500 nm and 600 nm).

An alternative approach is to use expensive calibration services available at IPMS in Germany or Loughborough University, however these services can be costly and not necessarily available for researchers in sun-belt countries. This was take as an opportunity to develop the main focus of the research, namely to acquire solar spectral data within economically constrained situations, as are found in many of the locations within the Sunbelt. The alternative investigation for the calibration was to use the direct solar beam irradiance to calibrate the spectrometer. To model the solar irradiance different models were considered. The accuracy of these models and their application is discussed in this chapter.

While the previous chapter described the research to design a reliable cosine correcting coupling, the present chapter will focus on the calibration of the raw spectral data; its basis, equipment and methods. This was the most demanding part of this research, not only due to the large amount of raw data required to be calibrated but also for the time invested to find a reliable procedure to produce the calibration method. The steps to develop this endeavour could be listed as: (1) to find time points "near to cloudless conditions" (NCC) using a calibrated pyranometer, (2) to model the spectral distribution for NCC time points using different irradiance transfer codes and aerosol configurations, (3) evaluate the different modelled spectra to find the closest match to the pyranometer values, (4) use the model and aerosol conditions that better reflected the pyranometer values to calculate spectra based on the sensors' configurations, (5) use the calculated spectra to produce a calibration curve and apply it to the raw data and (6) evaluate the correlation of the calibrated data against the calibrated values.

4.2 Materials and Tools

4.2.1 Background

Many of the instruments were already in place when this research began. The location was chosen so there were few disturbances in the field view. More specifically the instruments were found on the rooftop of the Hicks Building of the University of Sheffield with coordinates of latitude 53˚22'50.9'' North and 1˚29'08.6'' West, as shown in figure 4.1. A pyranometer, a SN1 thermopile was one of the instruments. This was used to select of the NCC time points that this project relied for the calibration. The pyranometer itself is calibrated every two years to ensure accuracy. The last revision of its calibration was on, the 30th of February of 2017, confirming that the instrument was still reliable.

Figure 4.2: Location of acquisition station in campus (red circle), coordinates 53˚22'50.9'' North and 1˚29'08.6'' West, with an estimated elevation of 113.72 m [28].

Joint to the pyranometer there was the acquisition station, which was composed of a personal computer enclosed in a waterproof box connected to the university network. It was connected via USB to an Ocean Optics spectrometer JAZ A1392 on which five Optic Fibre (OF) sensors, of a diameter of 400 μm, were attached. Each of these with different configuration of tilt and azimuth angles and they were placed on a transparent polycarbonate holder hemi-sphere shaped.

The spectrometer was set-up to record the spectra in a range between 340 nm to 1027 nm and each sensor took an instant spectrum every 2 minutes. The readings were performed from March 2015 to July 2017. Each sensor recorded approximately 136,000 time points. However after examining the data only two sensors had consistent reliable information, these were sensors 4 and 5. Sensor 4 had an angular configuration of 45˚ of tilt and 180˚ azimuth (facing south) and sensor 5 was horizontal (0˚ of elevation angle). In figure 4.2 it is shown in more detail the setting of the acquisition station.

Figure 4.3: Setting of the acquisition station, 5 sensors attached to a semi-spherical acrylic base. Inside the box under the base there was the spectrometer connected to a computer programmed to record the data automatically.

The attempts of calibration for raw data acquired by the Ocean Optics spectrometer JAZ A1392 started by using a standard calibration lamp (Ocean Optics LS-1-CAL). Unfortunately no reliable calibration could be produced. The difficulty to find equipment to calibrate the data motivated to change the approach and instead use the terrestrial solar irradiance to calibrate the spectral raw data, a similar approach to the one described by O'Donnell and Garces [77] and Thome [100], where they used a radiative transfer code to simulate solar irradiance for cloudless conditions and calculate a calibration curve.

4.2.2 Methods

In order to produce a reliable calibration for the low-resolution spectrometer data, the terrestrial solar irradiance was used as a source of illumination, taking a similar approach to the research of O'Donnell and Garces [77] undertook. They used the terrestrial standard solar spectrum of the American Society for Testing and Materials (ASTM) G173-03, whereas in this thesis it was decided to produce a solar spectra modelled based on a dynamic simulation of the spectral solar irradiance instead of a fixed reference, two models were evaluated to generate the solar spectra: SPCTRAL2 [14] and SMARTS2 [34].

Since the solar spectral irradiance models can only calculate cloudless conditions, it was necessary to select time points with low cloud disruption. Namely days which reflected a behaviour close to cloudless. For at least a considerable amount of time. These time points were selected from the data acquired by the pyranometer. Figure 4.4 shows the selected dates in which solar irradiance seemingly presents low cloudiness in for considerable time spans.

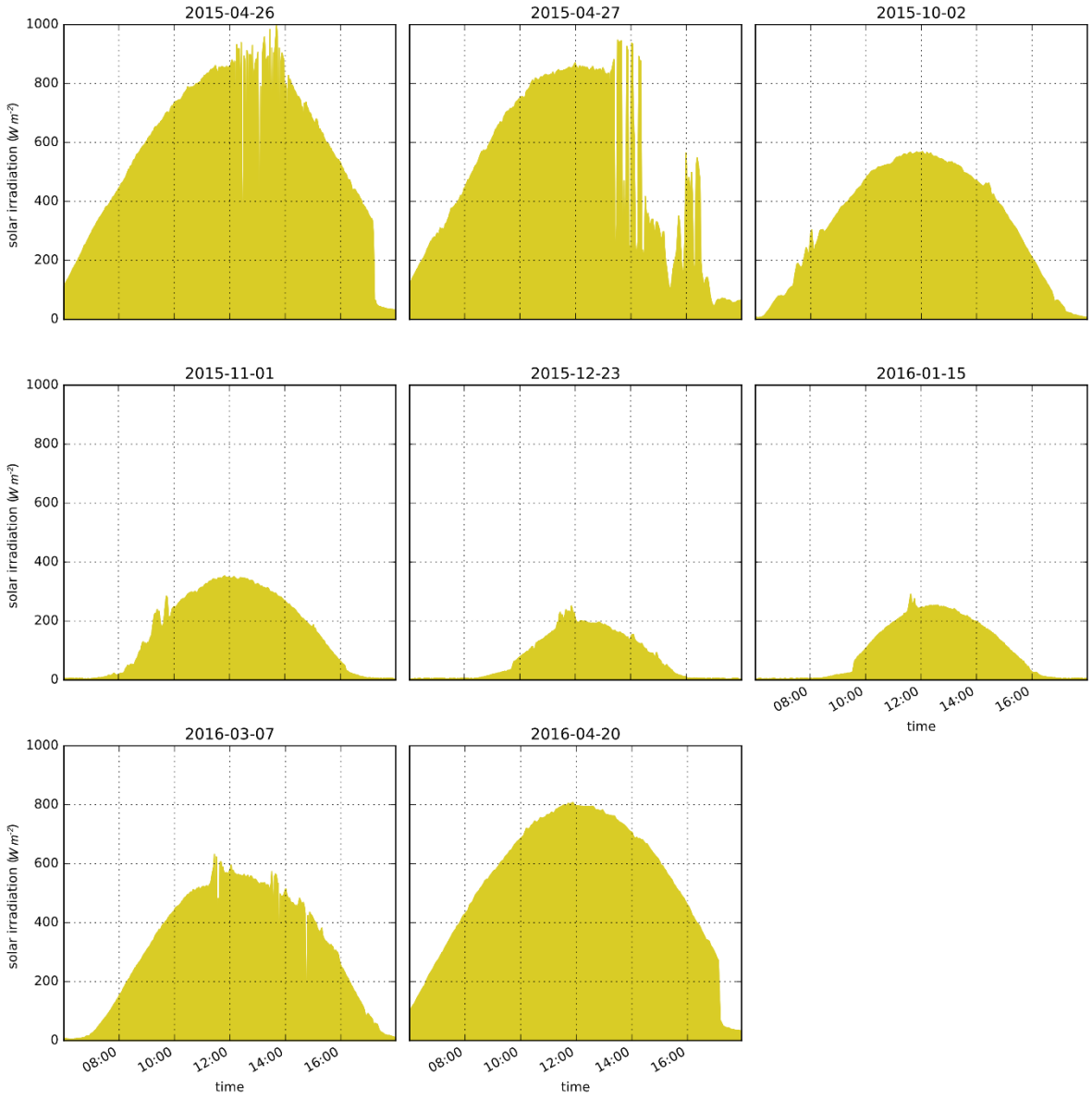

Figure 4.4: Selected dates in which NCC were found, the sudden jump and drop of the irradiance at around 10:00 and 17:00 is caused by the shading of buildings and structures surrounding the acquisition station. Some of these time-points were selected to produce the calibration curve, the selection was based on the proximity of their values to the values of the selected modelled conditions.

Continuing with the approach of providing accessible methods to acquire solar spectra data; it was decided to use the terrestrial sunlight to calculate the calibration curve. The models used to simulate the solar spectrum were: SMARTS2 and SPCTRAL2. SMARTS2 executable file and source code are easily found on its webpage [35]. The executable version of the code was "wrapped" using a python script to automatise the generation of spectra for customised time-points, an option that is unavailable in the original distribution of this tool. The only version of SPCTRAL2 available was found in FORTRAN coding language and did not include any solar geometry calculation nor the possibility to generate automatically a series of solar spectra based on a list of time-points, therefore it was necessary to write the model in Python and try separately different tools to calculate

the solar geometry. Two different versions were tested for the solar spectral simulation. For the first iteration equations from the book of McEvoy, Markvart and Castaner [62] were used to calculate sun positions. The second iteration used a module of Python named Pysolar [96] to calculate solar geometry, this second iteration is referred as SPCTRAL+pysolar. Altogether these two versions of SPCTRAL2 and the SMARTS2 models were compared to find the closest match to the data of the calibrated pyranometer.

To generate a solar spectra as close as possible to real world conditions, the parameters which contribute significatively to the solar spectra distribution change were considered. These parameters include: precipitable water (*PW*), air mass (*AM*) and aerosol optical depth (*AOD*), and air temperature. The *PW* was calculated using both the relative humidity (*RH*) and air temperature (T_{air}) acquired from the database of publicly available of Time and Date AS [102], which is acquired from , the equation described in Gueymard [33] was used to estimate PW.

$$PW = 0.1\, H_v\, R_{ov} \tag{4.1}$$

Where:

$$H_v = 0.4976 + 1.5265\, T_T + \exp(13.6897 T_T - 14.9188 {T_T}^3) \tag{4.2}$$

$$T_T = 1 + \frac{T_{air}}{273.15} \tag{4.3}$$

And:

$$R_{ov} = 216.7\, \frac{E_v}{T_k} \tag{4.4}$$

$$E_v = E_{vs}\, \frac{RH}{100} \tag{4.5}$$

$$E_{vs} = exp\left(\frac{22.329699 - 49.140396}{T_{k1}} - \frac{10.921853}{{T_{k1}}^2} - 0.39015156\, T_{k1}\right) \tag{4.6}$$

$$T_{k1} = \frac{T_k}{100} \tag{4.7}$$

$$T_k = T_{air} + 273.15 \tag{4.8}$$

Since the data of these parameters had an hourly time resolution the input values used in the simulation models were result of interpolation. The *AM* was calculated and applied with each respective code's solar geometry calculation. The *AOD* was deemed not highly significant at this step since according to information from NASA [69], the mean value within the acquisition time was of 0.1394 at 550 nm, with a standard deviation of 0.0614. These values do not change the *APE* more than 0.2 %.

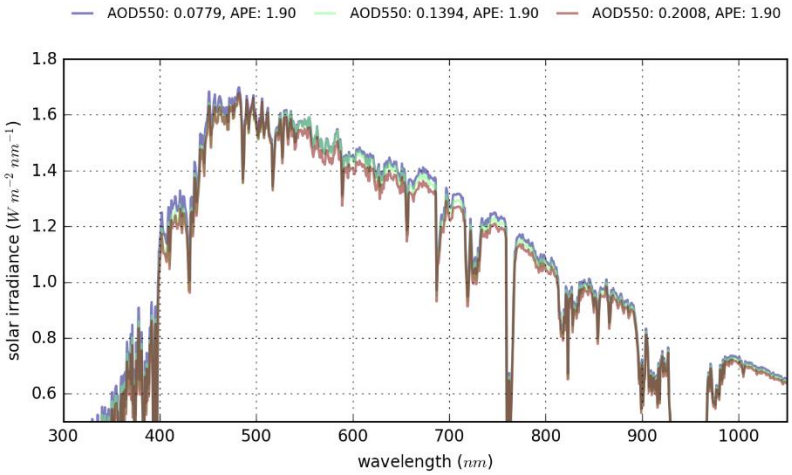

Figure 4.5: Comparison of extreme values of Aerosol optical depth and its influence in average photon energy. This shows that for the simulated spectra there is little influence of the AOD to the shape of the solar spectra and its Average Photon Energy.

To find the best suited aerosol conditions for the region of Sheffield, several different simulations of solar spectra with different aerosol model conditions were performed based on the comparative study of Utrillas *et al.* [105]. From which for SPCTRAL2 the aerosol models Maritime-Rural-Clear (MRC), Mean Rural (MR), Rural-Urban (RU), Mean Urban (MU) and Polluted-Urban (PU) were used to produce the spectral simulations. From SMARTS2 the aerosol models tested were the ones included in this distribution: four (Maritime, Rural, Tropospheric and Urban) from Sheettle and Fenn [92], two of Breslau and Dave (C and C1) [18], three from Standard Radiation Atmosphere (Continental, Urban and Maritime) from IAMAP [86] and two of desert conditions one normal (MIN) and another under sand storm conditions (MAX).

After running the scripts simulating the solar spectrum only within the wavelength range of the pyranometer for each time-point, the total absolute irradiance was obtained by trapezoidal integration under the spectral curve. To show an overview of the different results from the different modelling a selected date is can be seen in figure 4.6.

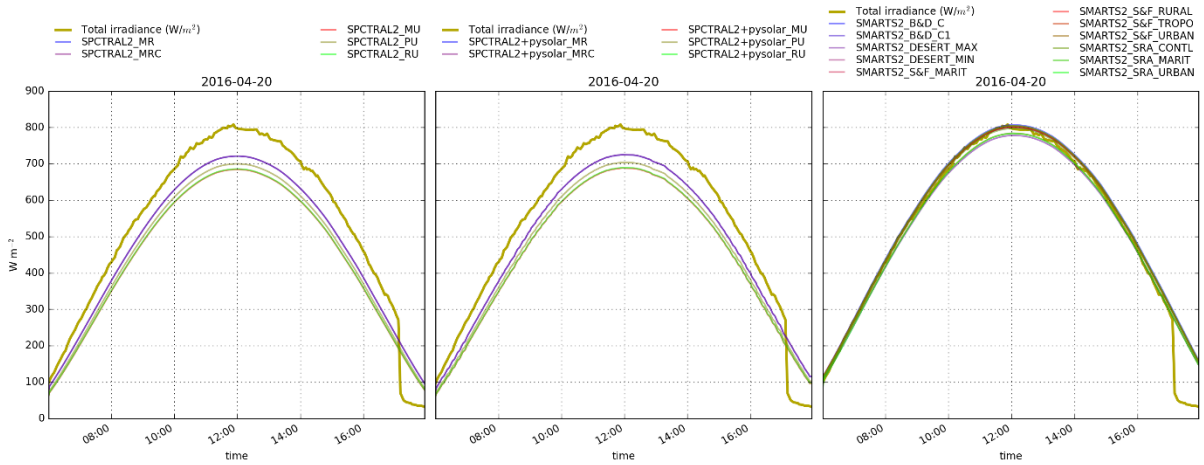

Figure 4.6: Selected date showing accuracy of the different models for solar irradiance. This shows the different levels of fitting for the pyranometer empirical data to integration of the simulated spectra in the different transfer models used. Different aerosol models were used following the comparison that Utrillas et al. [105] produced of both models. Once calculating the total irradiance the integration was compared to the empirical data.

The next step consisted of comparing the data acquired from the pyranometer to the total absolute irradiance calculated from the simulations. The difference between both values at each point was calculated to trim the data based on the dispersion. Values within the 5% higher dispersed values were considered outliers. The rest was evaluated using mean average percentage error (*MAPE*) and coefficient of determination (r^2). In figure 4.7, it is possible to see the detailed analysis to validate the first batch of simulations, namely the ones realised only by SPCTRAL2. For the calculation of r^2 and *MAPE* the following standard formulas were used.

4.9

$$r^2 = 1 - \frac{\sum_{i=1}^{n}(y_i - f_i)^2}{\sum_{i=1}^{n}(y_i - \bar{y})^2}$$

And

$$MAPE = \frac{100}{n}\sum_{i=1}^{n}\left|\frac{y_i - f_i}{y_i}\right|$$

Where y_i is the measured value in this case the pyranometer acquired data; f_i is the modelled value, here the integrated irradiance of the used model and $\bar{y}$ represent the mean of the measured values.

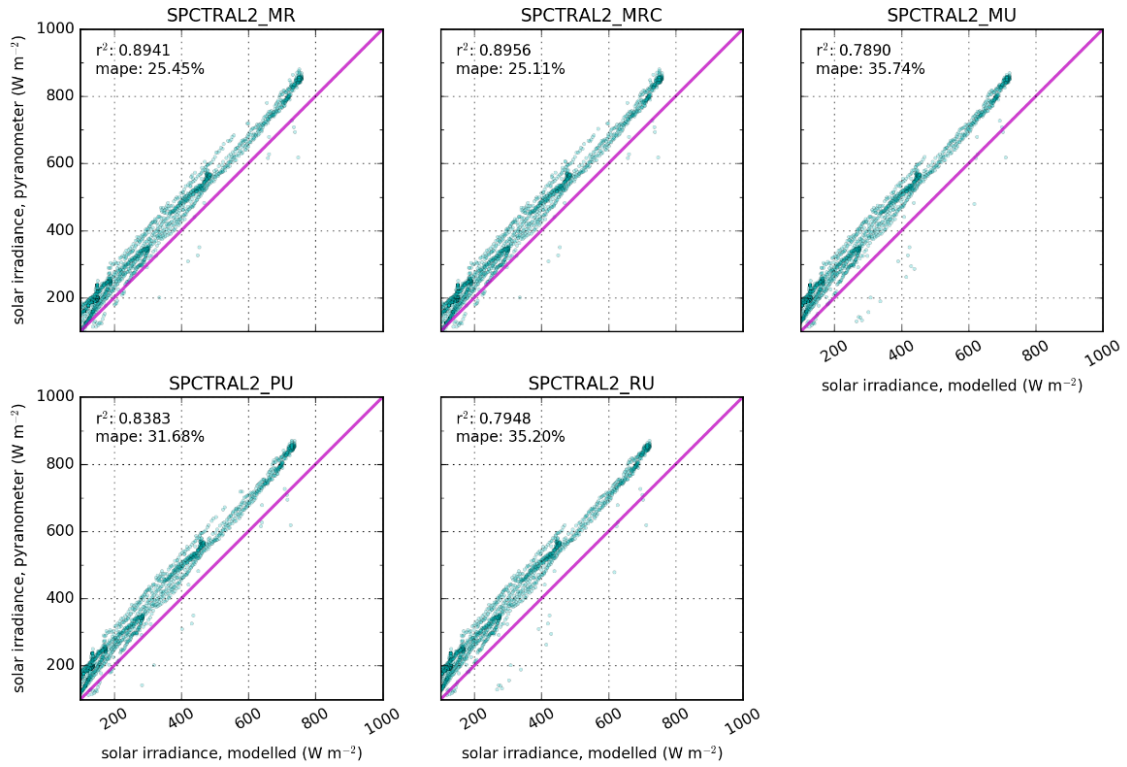

Figure 4.7: MAPE and r^2 and between pyranometer empirical data and SPCTRAL2 modelled irradiance. These solar spectral simulations used a solar geometry calculated with the equations in McEvoy et al. [62]. The best match from this batch of simulations was Maritime Rural-Clear (MRC) with an r^2 of 0.8956 and a MAPE of 25.11%, while the second best, Mean Rural (MR), resulted in an r^2 of 0.8941 and a MAPE of.25.45%. The rest of the aerosol model conditions considered presented a lower matching, these being Mean Urban (MU), Polluted Urban (PU) and Rural-Urban (RU). However all simulations presented what seems to be a systematic deviation from the expected values, probably due to an inadequate calculation of the solar geometry

The second batch of simulations were produced using again the SPCTRAL2 [14] model written in Python and adapting the solar geometry calculations of the Pysolar library [96] to it, which is based on Reda and Andreas work produced in the National Renewable Energy Laboratory (NREL) in 2005 [88]. In general terms it is seen a marginally improvement in both dispersion and error indices, but is only around 1%, indicating that at least the standard aerosol models and default parameters of the model are not adequate to the purpose of this calibration. The results of the comparison between the simulation and the pyranometer's empirical data can be seen in figure 4.8.

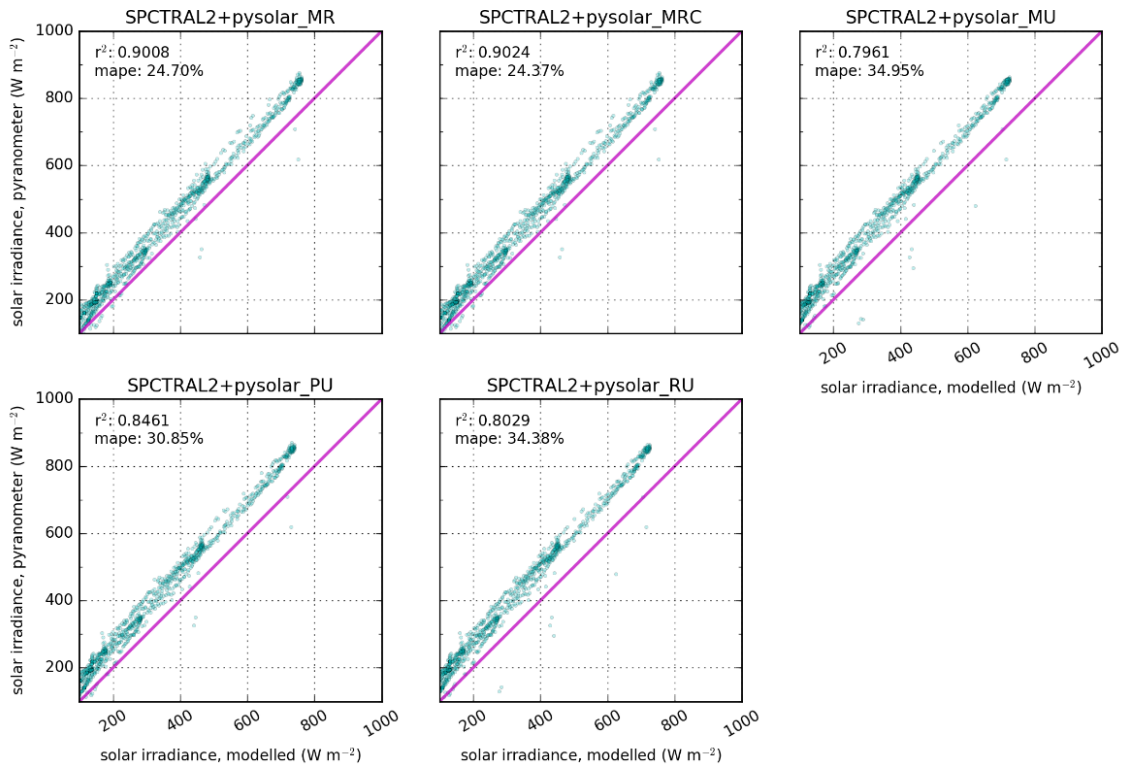

Figure 4.8: MAPE and r^2 and between pyranometer empirical data and SPCTRAL2+pysolar modelled irradiance. These solar spectral simulations used a solar geometry calculated with the library Pysolar [96], which uses the algorithms of Reda and Andreas [15]. The best match from this batch of simulations was Maritime Rural-Clear (MRC) with an r^2 of 0.9024 and a MAPE of 24.37%, while the second best, Mean Rural (MR), resulted in an r^2 of 0.9008 and a MAPE of.24.70%. The rest of the aerosol model conditions considered did not presented a good match, these being Mean Urban (MU), Polluted Urban (PU) and Rural-Urban (RU). Despite presenting similar systematic deviation from the expected values Pysolar marginally improved the results of the SPECTRAL2 model.

The last batch of simulations were performed using Gueymard's model SMARTS2 [34] besides being more complex and parametrised the options for aerosol model was more extense. The solar position is calculated using the Muriel et al. [15] algorithms. This code is written in FORTRAN so it was necessary to write a "wrapping" to perform the serial modelling for the multiple time points (appendix 7.3). The aerosol models in this model are labelled as S&F MARIT, S&F RURAL, S&F TROPO and S&F URBAN for the aerosols based on the paper of Sheetle and Fenn [92], B&D C and B&D C1 based on the research of Breslau and Dave [17, 18]; SRA CONTL, SRA URBAN and SRA MARIT for the Standard Radiation Atmosphere from IAMAP [86]; and DESERT MIN and DESERT MAX the first one corresponds to background conditions in desert areas while the second to extremely turbid conditions, namely sand storms. The results are displayed in figure 4.9, here is possible to see that this las model offered a more reliable simulation of the integrated irradiance since the indicators of dispersion and error improve considerably.

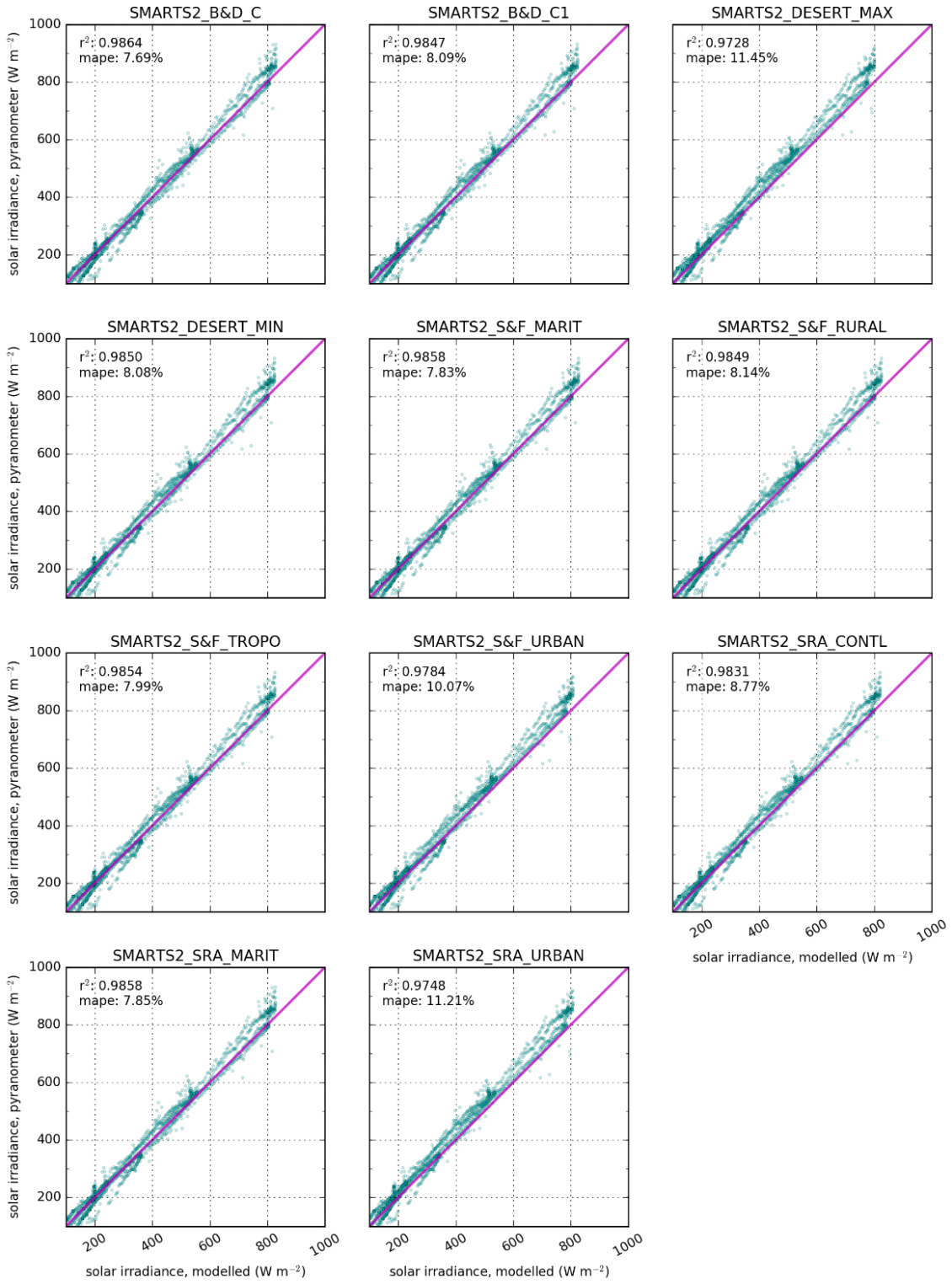

Figure 4.9: MAPE and r^2 between pyranometer data and SMARTS2 modelled irradiance. This model did not require support to calculate solar geometry. This model in general was a better match to the pyranometer empirical data, being the aerosol model of Breslau and Dave [18], labelled as B&D C, the one with the best correlation a lower errors.

From the three models SMARTS2 resulted to be the closest to the pyranometer data, and among all the aerosol models considerate "B&C-C" was the one showing the highest r^2 and lowest *MAPE*. Nonetheless while the *AM*, *AOD* and *PW* influence the spectral distribution, the aerosol content has a little effect on it. Further simulations using SMARTS2 support this hypothesis. Several solar

spectra were simulated based on the AM1.5 solar spectrum standard. The aerosol model was changed and the *APE* between 300 nm and 1050 nm was calculated, with a mean value of 1.9054 *eV* and a standard deviation of 0.0027 *eV* which represents a 0.14% of variation among the simulated spectra, based on this one can assume that this assumption of the aerosol conditions it is valid at least for low resolution spectral measurements such as this one, as can be seen in figure 4.10.

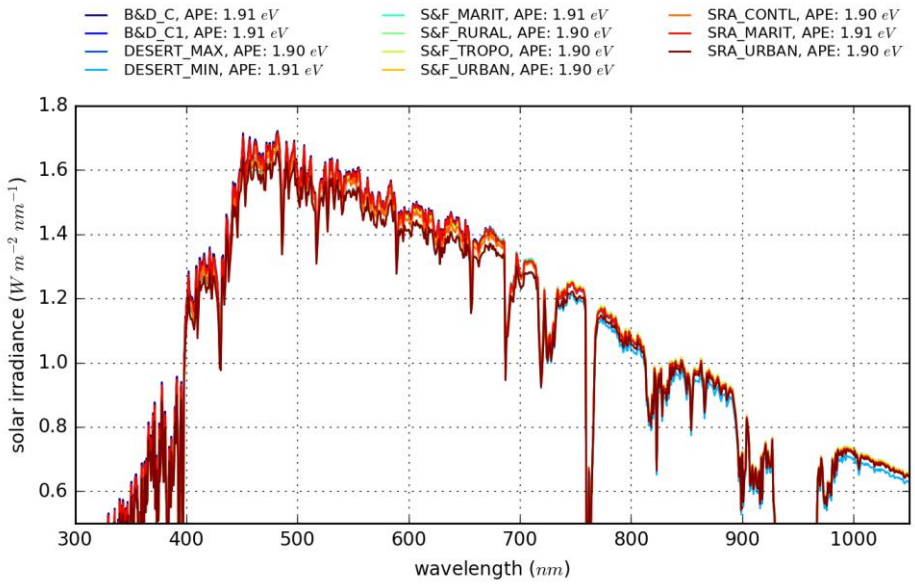

Figure 4.10: Comparison of different aerosol models showing a small change on APE values. The models are arbitrarily divided just to make easier to see the minimal difference in spectral distribution among the models.

After finding the simulation and the parameters settings that best suited the empirical data, the points used to calibrate were filtered. All time-points with total irradiance under 200 W m^{-2} was discarded since they produced a lot of variability, in addition only the top 10% of the time-points with the least deviation from the empirical data was selected for the calculation of the calibration function. In figure 4.11, it is illustrated the method of selection of the time-points used for the elaboration of the calibration curve, this points were later on used as a base to find the closest timestamps in the raw datasets from the pyranometers.

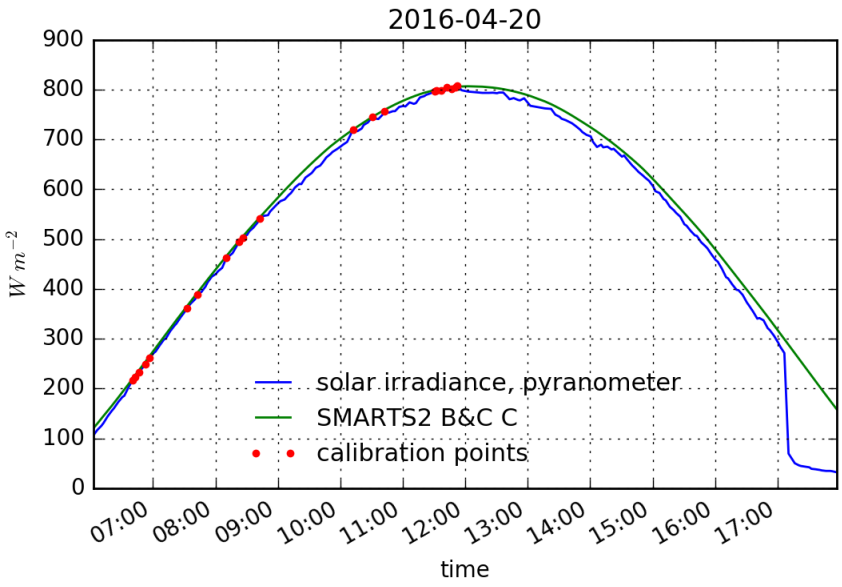

Figure 4.11: Selected date to illustrate selection of calibration points. This is to say, they were selected based on the match between pyranometer empirical irradiance record and simulated irradiance by SMARTS2 with approximated atmospheric conditions. Also time-points with total irradiance under 200 W m^{-2} were discarded to reduce variability in the calibration function.

The calibration was performed for the data of the horizontal sensor and the one facing South at 45˚, the raw spectral data closest to the time-points selected was the processed using the process of calibration resulted of the reverse-engineering analysis of the procedure automatically done by the spectrometer during the settings of absolute irradiance calibration. The algorithm to produce the calibration can be expressed as the formula equation 4.10.

4.10

$$\Phi_\lambda = \frac{\left(\frac{F_{A,\lambda}\left(S_{raw,\lambda} - S_{dark,\lambda}\right)}{A}\right)}{t_{int}}$$

Where Φ_λ is the calibrated spectral irradiation with value in units of μW m^{-2}, $F_{A,\lambda}$ is the scaling factor per wavelength in units of μJ cm^{-2} and is related to the x axis of the pixel array (called here Δx) of the CCD of the spectrometer's sensor; $S_{raw,\lambda}$ is the raw signal in counts, electrical signals in units of counts, which are the electrical signals registered by the device; $S_{dark,\lambda}$ stands for the dark signal, which is the background noise intrinsic from the device in units of counts as well; A is the set area of the surface of the OF sensor in cm^2, t_{int} is the set time of integration meaning time taken by the spectrometer to make a reading in seconds.

Resolving to obtain the calibration function it needs equation 4.10 needs to be resolved for $F_{A,\lambda}$, resulting on equation 4.11

4.11

$$F_{A,\lambda} = \frac{t_{int}\,\Phi_{\lambda} A}{S_{raw,\lambda} - S_{dark,\lambda}}$$

The resulting calibration curves are shown in figure 4.12, these curves have some problems in the values near to 300 nm. This is possible due to the low irradiance rear to those spectral values, resulting in unexpectedly high values.

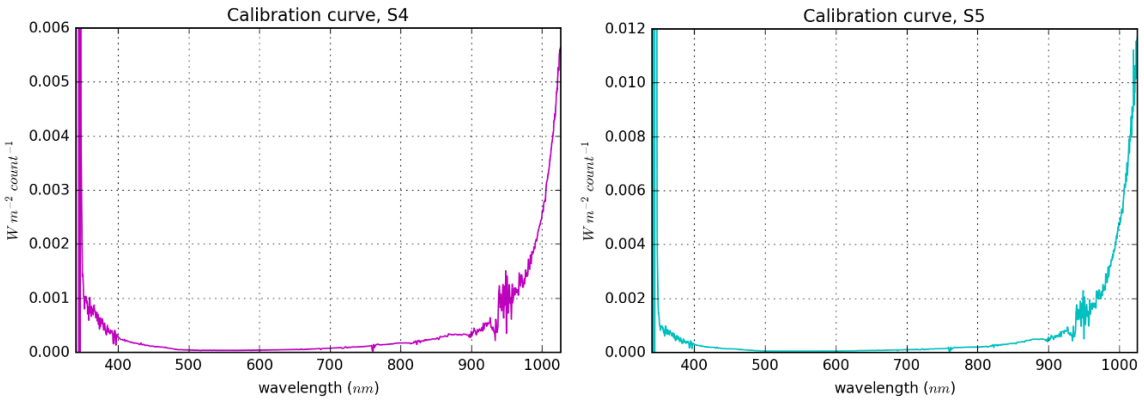

Figure 4.12: Calibration curves used to process the acquired raw data from (right) sensor 4, 45 facing south; and (left) sensor 5, horizontal.

From all five sensors only sensor 4 and 5 collected consistent reliable information, therefore only these calibration curves were the only produced. Each value in the y axis corresponded to a value in W m^{-2} for each instantaneous reading of the spectrometer. In the following section the calculation of the solar irradiance is integrated and evaluated to ensure the reliability of the suggested method.

4.3 Results

The raw data from the spectrometers 4 and 5 corresponding to the selected dates of Near Cloudless Conditions (NCC) was processed using equation 4.11 using each of their corresponding curves showed (see figure 4.12). Once calculated the calibrated values, all time points in the NCC set were modelled using SMARTS2 within the range of the spectrometers (340 nm to 1027 mm). The total irradiance of both, calibrated and modelled spectra was integrated to compare the validity of the calibrated data vs the cloudless irradiance modelled, and thus to evaluate the accuracy of the method. The summary of the results can be seen in figure 4.13.

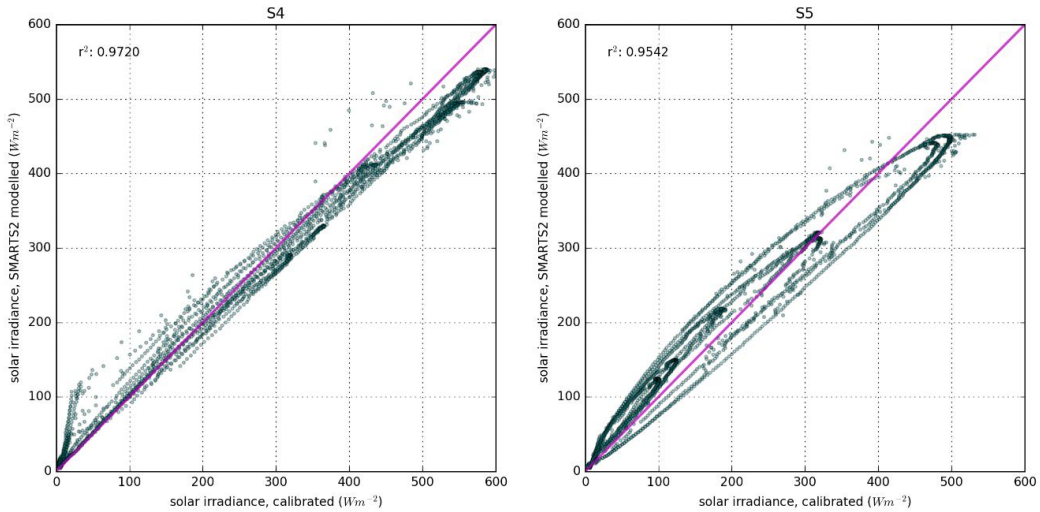

Figure 4.13: Experimental results of calibration for selected dates. The whole dataset of NCC was calibrated after obtaining the calibration curve from the time points with more agreement to solar cloudless modelled spectra, afterwards the calibrated data and the cloudless modelled solar irradiance was integrated to evaluate the calibration method. The method seems to be reliable particularly for sensor 4 with a determination coefficient (r^2) of 0.9720, meaning that for the selected near to cloudless conditions dataset there was no considerable dispersion. The r^2 of sensor 5 was calculated in 0.9542, which is means a wider dispersion probably due to a systemic error of misplacement of the sensor during the campaign.

Both calibrated data have a good agreement to the expected data according to the determination coefficient, while the *MAPE* seems high in both calibration one should acknowledge that in low irradiances the error percentage could impact strongly than in high ones, overinflating the value to this indicator. The apparent systemic error of the calibrated data vs the modelled one could be due to some discrepancies on the angular configuration of the sensors. Since the tools used on the setting of the sensors were not of high accuracy this is understandable. In summary, while not perfect this approach seem to be reliable for the purpose of this research.

4.4 Conclusion

The approach of using terrestrial spectral solar irradiance was taken with a scientific process and pragmatic approach. There was careful evaluation and cross-reference research at every stage to generate data in the most reliable way possible. Atmospheric aerosols and absorption bands do not seem to represent significant problems at least in the resolution intended and the equipment used.

The method was composed of 6 stages: (i) selection of days with time ranges in which the solar integrated global irradiance presented near to cloudless conditions, this data was acquired using a calibrated pyranometer; (ii) selection of a spectral model and settings that matched the empirical acquired values, (iii) selecting a calibration subset of time points in which the values were

the closest to the modelled values, (iv) model the solar spectra for the time points from the sensors with most proximity to the selected calibration subset, taking into account the different geometrical configurations of the sensors, (v) calculate the calibration curves using the raw data of the pyranometers and the modelled cloudless spectra, (vi) apply the calibration curve to the NCC dataset and evaluate the integrated global irradiance of the selected sensors to the values of modelled global solar spectra for their NCC time points.

The data generated with this project can be used for a statistical analysis on the spectral variation and atmospheric conditions. Chapter 5 examines the use of the calibrated data and the results seem to indicate that the calibration described in this chapter is reliable and the source to achieve this calibration widely available.

5 Atmospheric characterisation and Influence of Spectral Variation on PV Technologies

This chapter focuses on the analysis of the calibrated data acquired during 16 months in Sheffield, UK. Based on methods of calibration described in chapter 4, in this section, methods to estimate the spectral influence for common PV technologies are discussed and an overview of the weather profile of the region is included. It is found that the a-Si technology presented spectral seasonal gains of about 4% for summer in comparison to winter, whereas other technologies show spectral seasonal losses under the same standard. Together with other results the present analysis provides strong evidence of the reliability of the calibration method from the previous chapter.

5.1 Introduction and background

The installation of photovoltaic (PV) power generation systems is growing. The increment of the installed PV capacity was reported to be of around 99.1 GW in 2017, making a total of 404.5 GW of global solar capacity [11]. This rapid growth is a reflection of the low prices of the current technologies and the urgency to implement sustainable measurements to combat climate change. To determine the cost-effectiveness of solar PV projects it is required to estimate the energy yield of said systems with accuracy. For this it is necessary to have a deep understanding of the influence of the different atmospheric factors. Normally the estimated energy production is calculated using the rating acquired under standard test conditions, defined as standard spectrum AM1.5, at temperature of 25 ˚C and total irradiance of 1 kW m^{-2}. However these conditions are rarely found in the field and the performance of a cell depends on the absorption of the spectrum and the spectral response of the PV material.

There is a growing number of studies aiming to assess the impact of spectral variability on PV technologies. The paper of Alonso-Abella *et al.* [3] which reviews the impact of spectral variation on eight different PV technologies, reports that a-Si and CdTe are the panels with higher modelled spectral gains as well as experimental ones. Similar conclusions were published by Eke *et al.* in 2017 [25] in which low band-gap materials such as c-Si present little influence by spectral variation, namely of between +4% and +5% of the efficiency, while this effect is more accentuated

for large band-gap technologies like a-Si and CIS, with values between -10% to +15% between seasons. In 2017, Polo *et al.* [85] made an extensive estimation of the spectral factors in a wide range of locations on the globe, by modelling solar spectra using SMARTS2 model [34]. Here it is described that the crystalline silicon cells have, in general, a mild spectral loss up to 3% and gains of around 1%, and that thin films, particularly a-Si, show a high variability of up to 10%. In 2015 after an analysis of spectral data from June 2010 to December 2013, Dirnberger *et al.* [24], concluded that the devices with higher spectral gains where those more sensitives at shorter wavelengths namely CdTe and a-Si. These have gains of +3.4% and +2.4% respectively when comparing summer versus winter spectral trends. Whereas for c-Si there was an impact of about +1.4%, while for high efficiency c-Si the gain was smaller, of around +1.1% seasonally. The spectral impact for CIGS technology was estimated at +0.6%. This showed an agreement with Zinsser *et al.* [114] with gains of +2.5%, +2.1%, +1.8% and +1.5% for technologies a-Si, CdTe, CIGS and c-Si respectively. This for "blue-leaning" values of average photon energy (*APE)* compared to standard AM1.5 spectrum in the range 300 nm to 1600 nm. The solar spectral variability is particularly sensitive to PV cells with narrow spectral response ranges. The shape of the *SR* are different among PV materials and even among the same kind of cells due to impurities and variation of thickness, etc. It is worth to mention that the spectral response (*SR)* might be influenced by temperature, irradiance intensity and voltage [87]. The present work aims to build up the body of knowledge of the net effect of the influence of spectral variability to the PV energy yield.

Another theme also commented on this section is the characterisation of solar spectra using *APE* index and its use to classify qualitatively solar spectral resources. In 2015 Norton *et al.* [74] concluded that the *APE* index is a reliable predictor for the solar spectral distribution, when low irradiance is filtered, namely under 150 W m^{-2}. Minemoto *et al.* [67] points at the uniqueness in the spectral characterisation for *APE* values in range between 1.86 *eV* and 2.04 *eV*. This is to say that values of *APE*, uniquely yields the general shape of a solar spectrum, regardless its irradiance value. The conclusion on the mentioned paper were reach by performing a statistical analysis similar to the one in the International Electro-technical commission. However this claim is contested in 2017 by Nofuentes *et al.* [72] pointing that while *APE* is consistent with low variation (< 3.3%) within the range of 450 nm to 900, it goes up outside this range reaching between 5% and 11%. This variability could be due to factors such as aerosol, water vapour and cloudiness.

In chapter 4 it is detailed the method of acquisition in which the data used in this section was acquired. This was used to characterise atmospheric conditions such as solar irradiance, clearness index (K_T) and evaluate the spectral distribution using *APE*, and mismatch factor (*MM*)

to evaluate the effect that spectral variation has on different PV technologies. The methods for its sampling and analysis is detailed in section 5.2.

5.2 Methods and tools

The data collection station was set-up on the roof top of the Hicks Building, in the University of Sheffield. Within a waterproof box it was installed a spectrometer of Ocean Optics, model JAZ 1392, in which five optic fibres of 400 μm of diameter were attached to act as light sensors. The cosine correcting coupling labelled as DI, from chapter 3, was used to open the field angle of the fibre optic sensor. DI was not the most accurate design it was in the top 3 and it was easier to standardize and quicker to produce, for these reasons was utilised it as the cosine corrector in the data acquisition. The following analysis focuses on the data acquired from sensor 4, which was facing south with a tilt of 45˚, being the one of most interest since it was the most optimally configured to receive the most of the solar resource.

5.2.1 Location and experimental set-up

The following analysis relies on the data acquired from March 2015 to July 2016 at the coordinates of latitude 53˚22’ 50.9” north and longitude 1˚29’ 08.6” west, according to Google Maps [28] with an elevation of 113.72 m. The raw data recorded was then calibrated using solar cloudless irradiance as light source. The software Ocean View, version 1.5.0, was used to automate the task of recording spectra every 2 minutes the integration time was set to 5.84 ms, this value was proven empirically to avoid saturation of the signal in sunny days. The data was then captured and stored as raw counts, to later be reprocessed and calibrated as detailed in chapter 4.

The solar irradiance is the result of the integrated calibrated data after calibration and extrapolation to have a range between 300 nm to 1050 nm. The extrapolation method consisted on the escalation of a simulated cloudless solar spectrum, based on SMARTS2 model for radiative transfer. The parameters considered for the modelling were: precipitable water, atmospheric pressure, temperature and solar position. The aerosol was modelled based on Breslau and Dave, 1973 [18]. Including parameterisation of wavelength exponents, single scattering coefficient and asymmetry factor. This atmospheric model minimises the effect of relative humidity on the properties of the aerosol and was selected during the calibration stage due to its closeness to the empirical data acquired in-situ by a pyranometer.

The calibration yielded a collection of about 136,000 solar spectra. From this result were extracted different values to characterise some atmospheric values, such as solar irradiance, clearness index (K_T), *APE* and mismatch factor (*MM*)

5.2.2 Methodology

The clearness, also referred as K_T was calculated as the ratio of the integration of the instant solar irradiance over the extra-terrestrial irradiance computed. This index is explained in more detail in section 2.3.2. As explained in previous sections *APE* is a widely used parameter originally suggested in 2002 by Jardine *et al.* [45] which is device independent and it is used to classify spectral distributions and to assess the solar spectral influence on PV systems performance. It is defined as the energy of the irradiance over the photon flux as seen in equation 2.29.

The Spectral Response (*SR*), explained in section 2.2.4.2, which is considered to be an approximation to the potential short-circuit current from a PV cell based was used to calculate the Mismatch factor (*MM*), as seen in equation 2.34. With these indices it is aimed to evaluate the spectral losses and gains in comparison to the standard efficiency of the tested cell. This approach is widely used among the relevant literature [73, 24, 42, 85] and [3].

For the calculation of K_T the acquired data was calibrated and integrated to determine the total solar irradiance. However, due to interference of heat inside the waterproof box of the acquisition station, only the spectral range from 385 nm to 750 nm was reliable. It was then necessary to extrapolate using a modelled spectra with parameters of array's tilt and azimuth angle, precipitable water, pressure, temperature and *AOD*, interpolate from lower resolution data. For this it was used the model. After applying the K_T formula 2.40 for all the time-points and values with irradiance under 150 W m-2 were trimmed since these values contribute little to the solar resource in PV systems and provide a wide variation in extracted parameters such as *KT*, *APE*, *SR* and *MM*. The histogram was calculated for 100 bins evenly distributed within the values of 0.0 and 1.2. Afterwards the values normalised to the area of the curve to convert it into a probability density function (*PDF*). Among the literature [78], typical values of K_T for characterisation of cloudiness conditions are as described in table 5.1.

K_T value	Sky condition description
[0.0, 0.2]	Cloudy
(0.2, 0.6]	Partially cloudy
(0.6, 1.0]	Clear
(1.0, ∞)	Enhanced

Table 5.1: Sky conditions classification used on this work. Squared brackets "[ ]" indicate that the limit value is included in the range, whereas round brackets"( )" indicate the limit value is excluded from the range.

The "Enhanced" condition was considered different to "clear sky", because it is when the station received not only the global solar irradiance but also the reflection of this one by another element, this can be explained to be the "silver-lining" of the clouds. Some explanations of this phenomenon comes from Piacentini *et al.* [83], here exposes that the existence of fields of cumulus (cotton-like) clouds with regions of clear sky allows the direct sun radiation and at the same time the light reflected from its silver-lining (cloud borders). A different explanation comes in the paper of Yordanov *et al.* [112], in which is proposed that this over-irradiance" can be caused mainly by the forward scattering, or refraction, of light in optically thin clouds within narrow angles to the sun's sky position.

5.3 Results

The next section presents the statistical analysis of the data acquired from the station detailed in section 4.2. This is an attempt to characterise the regional spectral variation and typical sky conditions, as well as an evaluation of the effect that the spectral variation could act upon the different PV materials.

5.3.1 Overview of local atmospheric conditions

The atmospheric conditions of solar irradiance and K_T were estimated using the acquired data by the roof station, and thus have a high temporal resolution of 2 minutes. However pressure, relative humidity, and temperature were taken from the historical values from *Time and Date AS* webpage [102], with a temporal resolution of an hour.

The time resolution of precipitable water temperature and pressure was lower to the one of the roof station, so the values were linearly interpolated, these values were later fed into the SMARTS2 model to produce a clear sky solar spectra which was then escalated to fit to the final 50 nm of the solar spectra actually acquired. From these extrapolated spectra the integrated solar irradiance was calculated, the results of this can be seen in the following section.

5.3.1.1 Solar irradiance

The data acquired showed that probabilistically speaking for the profile of solar irradiance in Sheffield it has very likely to occur a measurement under 150 W m^{-2}, since more around 55% of the measurements fall under this value, as seen in figure 5.1

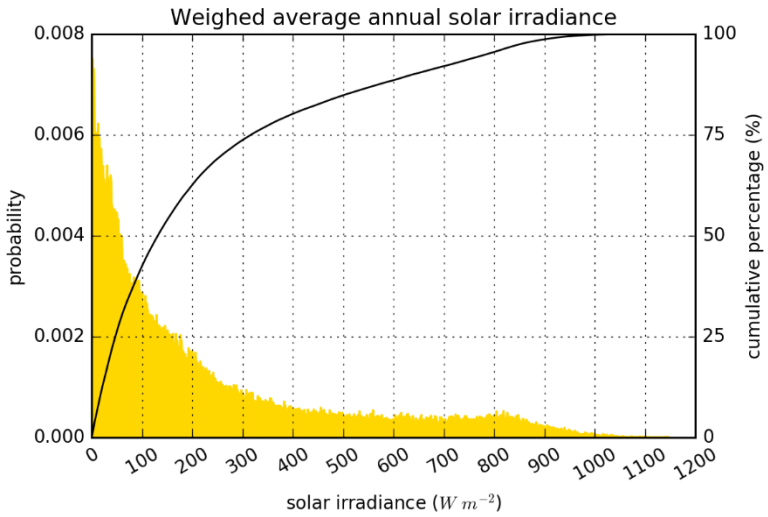

Figure 5.1: Probability density function of instantaneous solar irradiance. The cumulative percentage is also presented to show the distribution of the irradiance for the all data-points acquired.

However for the solar resource evaluation was required to make a weighted average of the time-points and multiply this for its value in energy units, this is to say that each 2 minute reading was 0.033 Wh, after this calculation the integrated energy gave a value of 834 kWh per annually which is in agreement to commonly known values of solar resource in the area and within the wavelength range between 300 nm to 1050 nm, in which these data has been estimated. Figure 5.2 shows the distribution of solar energetic annual resource by irradiance. This supports as well the decision of disregard values under 150 W m^{-2} for *APE* and K_T analyses, since the solar resource received from irradiances below that value accounts just to 15% of the total annual.

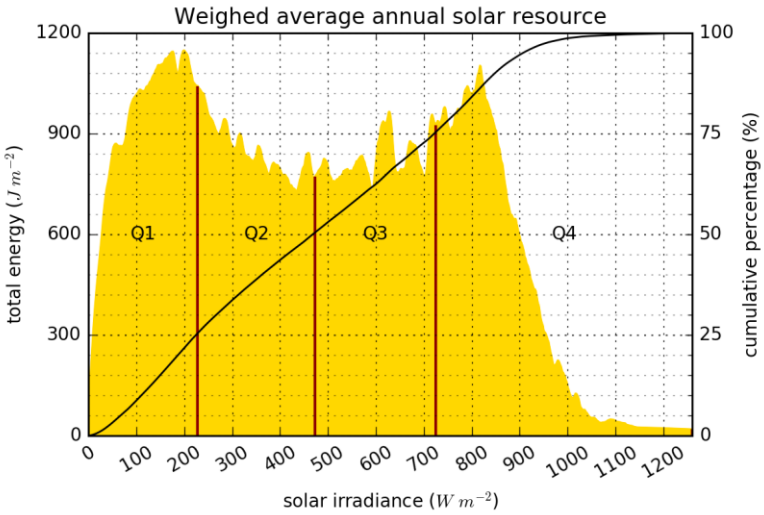

Figure 5.2: Weighted average and cumulative percentage of solar energetic resource. The energy was assumed to be constant within the 2 minutes of the reading. This plot takes into account all acquired data.

To simplify the analyses the seasons were divided in 2 groups based on the equinoctes ranges, this allows to see the better contrast between seasons. As expected in this side of the hemisphere, in figure 5.3 is possible to see that the distribution of values with a power above 200 W m^{-2} is more populated for the Spring-Summer range in comparison to Autumn-Winter.

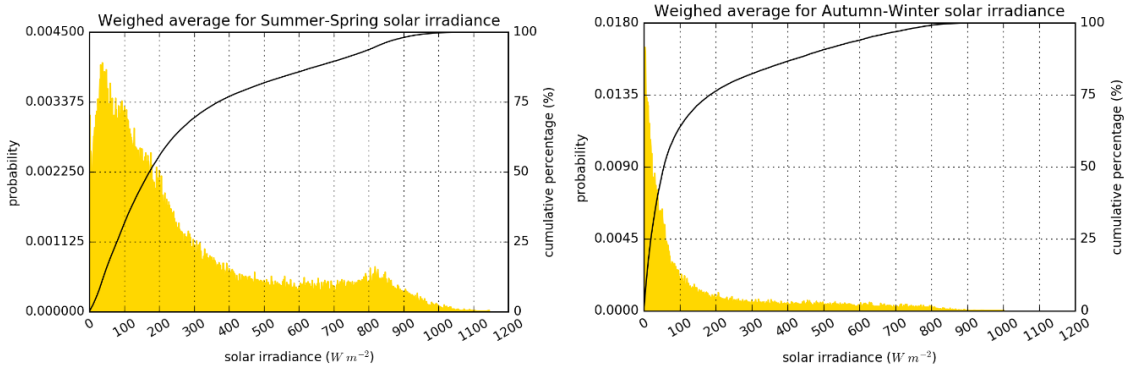

Figure 5.3: Probability density functions for high-sun and low-sun seasons. As seen here for winter season over 70% of the irradiance readings were below 200 W m^{-2}. While in summer this share goes under 60%. This graphic accounts all the acquired data-points.

Summaries of the probabilistic distribution of solar irradiance by month can be seen in figure 5.4. There it is possible to appreciate that April seems to be the month with more recurrence of higher irradiance, this can be explained due to the cloudiness presented in the months of June and July which present higher temperatures, but comparatively lower irradiance. The distribution of the data is represented by the shape while the length of the vertical lines represent the quartiles 2 and 3. This means the central range in which 50% of the values are found. Lastly the middle circle represents the average value of the specified data set.

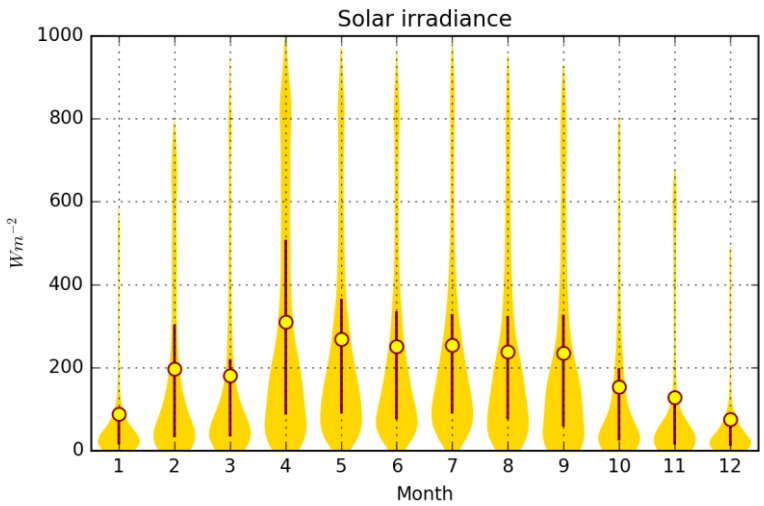

Figure 5.4: Monthly behaviour of occurrence of solar irradiance through the campaign. In this graph the yellow circles represent the average value by month and the vertical red lines represent the range of dispersion in which 50% of the values are found. The width of the shape represents the distribution of the irradiance data. Here is shown that summer months have a wider distribution despite not having a big difference with winter values.

Figure 5.5 shows summarises the average by hour in Summer and Winter, while the recurrence of irradiance in average is rather low the distribution of these values is widely spread, mainly in hours of high irradiance around noon. The average by hour include all recordings within the referred hour to reduce dispersion of the data a portion of the 0.5 % was trimmed. Values near to sunset and sunrise were also discarded, since they were considered not a relevant portion of the solar resource.

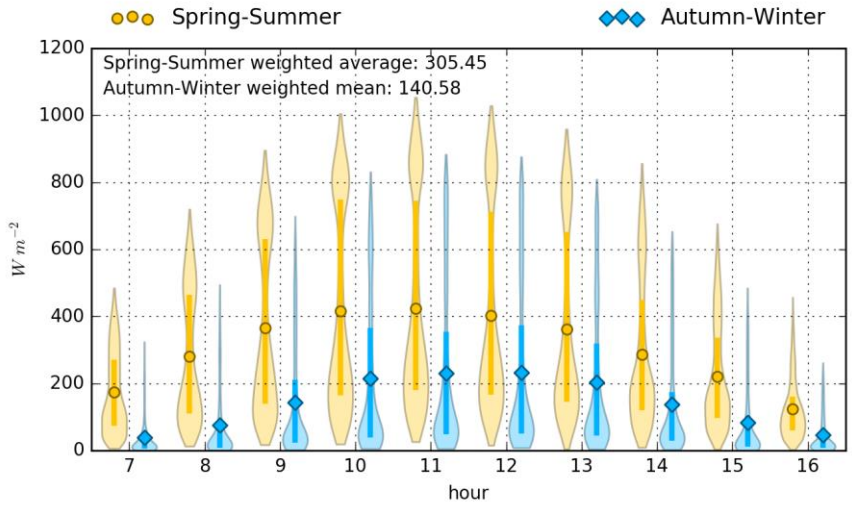

Figure 5.5: Hourly behaviour of solar irradiance contrasting seasons. Summer hours display bimodal distribution, while for winter it is unimodal and concentrated on low values. The shape represents the distribution of the data, the vertical lines the range of the central 50% and the middle dot the average value of the given data set.

5.3.1.1.1 Spectral distribution in relation to irradiance

In this brief section sill be taking the task of exploring the integrated solar irradiance (ISI) as a characterising index for solar spectral distribution as suggested by some literature [87, 42]. This approach is contested since the analysis performed in this thesis shows that there is very little difference of the general spectral shape binned by 50 nm.

One can only see a minor difference the range of 500 nm to 600 nm for high solar irradiances. For irradiances above 900 W m^{-2} the values within the expressed range sink about 1%. Furthermore for low irradiance spectra it is possible to see an increment of standard deviation. This is to say that the irradiance index has little characterising power for spectral analysis, as seen in figure 5.6.

However, this analysis shows that solar spectral distributions from high irradiances share converge in similar shapes, reinforcing the hypothesis that this is present under similar atmospheric conditions. This subject will be discussed in following sections.

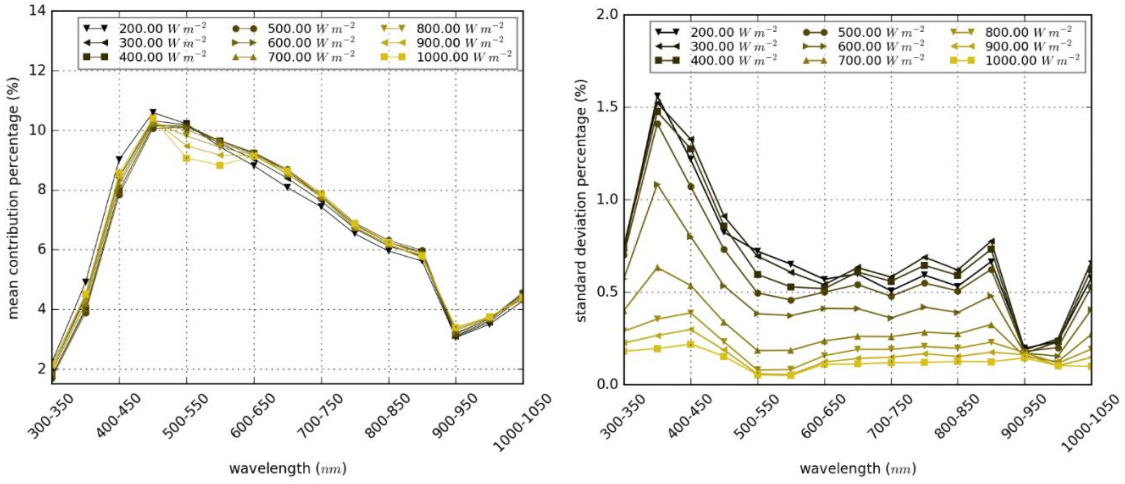

Figure 5.6: General spectral shape by solar irradiance and standard error, (right) The overall shaped of the solar spectrum in bins of 50 nm by solar irradiance, (left) the standard deviation percentage of the shapes by irradiance. These figures show that integrated irradiance do not provide considerable information on the shape of solar spectral.

5.3.1.2 Clearness index

The K_T values were calculated using the integrated solar irradiance at each time-point acquired. Using the formulas and concepts seen in section 2.3.2, the classification of the K_T values will be based on table 5.1. This section attempts to describe the sky conditions by realising multiple statistical analysis, as well as a comparison to existing literature to further validate the calibration method described in chapter 4.

The two fist plots of this sections are probability density functions (PDF), the first one takes into account all the data acquired during the campaign and weight them by month to achieve an annual average. This plot presents a distribution shaped as a geometrical decay, however two peaks can be found, one near to the value of 0.15, while a second one at 0.65, as seen in figure 5.7. Nearly 55% of the time points recorded fall under a K_T considered cloudy, around 30% are partially cloudy; and only about 15% can be considered either clear sky or enhanced.

The second plot shows a distribution with similar protocols to existing literature [22] in which values under 150 W m^{-2} were excluded to reduce the non-linearity that arises at low irradiance values. This can be seen in the right plot of figure 5.7. In this plot is possible to see that the share of cloudy sky is reduced to about 17%, whereas the partially cloudy reaches a portion of around 60%, while clear and enhanced are the resting 23%. The peaks of the bimodal distribution can be found at 0.18 and 0.65 K_T.

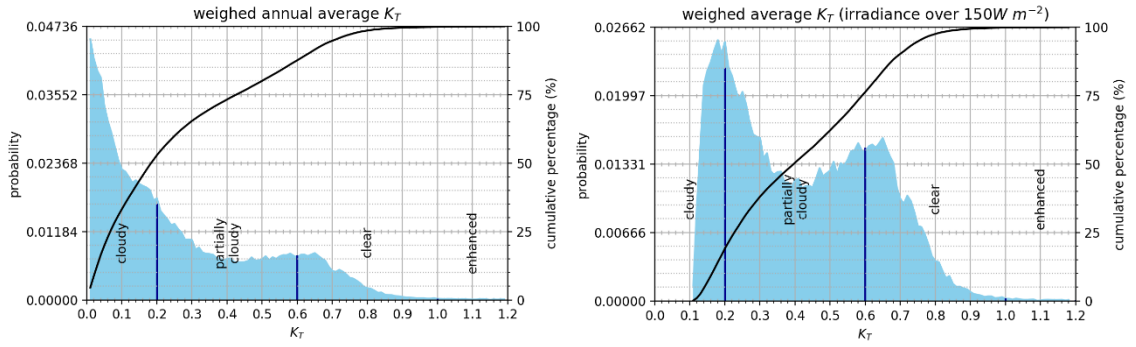

Figure 5.7: Probability Density Function and cumulative share percentage of K_T values. (left) Here it is displayed that for most of the considered data nearly 55% are, another 30% is partially cloudy and above 15% is either clear or enhanced. All values were included and an annual average was calculated weightening the data points to their expected yearly share, namely a number of data points was calculated by the duration of the month and a weighting ratio was calculated using the actual data points acquired during the campaign. (right) to be able to make a comparison to existing literature [22] values in which the solar irradiance was under 150 W m^{-2} were ignored, in this alternative distribution it is possible to see a peak around 0.18 K_T and another close to 0.65, while about 17% of the values are under 0.2, namely cloudy conditions, and from there up to a 77% is within partially cloudy conditions and about 23% is clear sky or enhanced.

To further analyse the K_T trend the all the available values were subclassified by month, from here the mean, first and third quartiles were calculated and presented in for of a violin plot to convey effectively the results of the analysis. As expected from a temper climate dominant in the UK typical low values of cloudiness can be seen, however the lowest K_T are found in November, December and January. The high value for K_T for April in comparison to May, June and July probably is due to rain present in summer since the climate of the region is prone to cloud accumulation for it lies among the peak district, see figure 5.8.

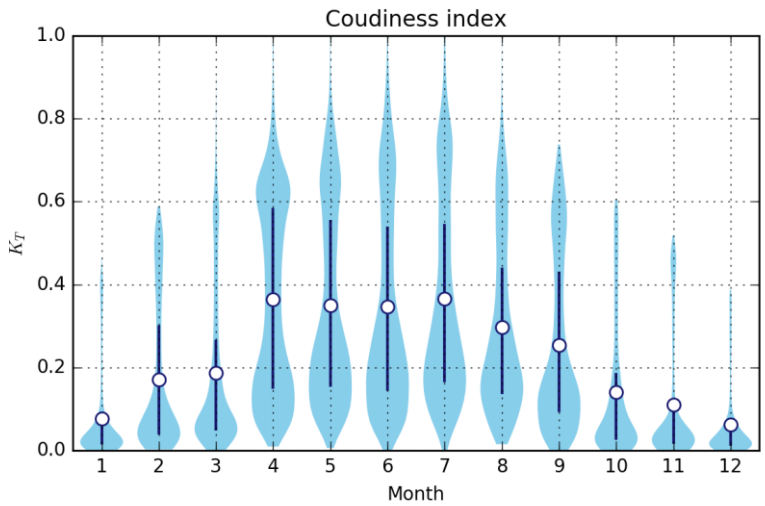

Figure 5.8: Average monthly K_T values. This plot takes into account all the data points and displays the distribution of the data as the width of the figure, the range of the central 50% is represented by the vertical dark blue lines and the white circles represent the mean values for the monthly K_T.

Here is possible to see that the month with highest mean K_T was July with a value of 0.56 however April had a similar value and had a larger portion concentrated around a mode found at 0.65 and a wider central 50% share (values within quartiles 1 and 3) of about 0.15 to 0.55. In general months of Autumn-Winter had a smaller dispersion, since most of their data points were concentrated under low values and with mono-modal distributions with peaks around 0.7 to 1.5, the moth with lowest mean clearness index was December with 0.07.

To analyse the contrast of the K_T distributions between seasons, all the recorded values were divided in two bi-season segments and presented as PDF plots for each of these. For Spring-Summer it is possible to see a bi-modal distribution around the values of 0.15 and 0.64 while Autumn-Winter seem to be highly dense in values under 0.1, since nearly 65% fall under this K_T value, the distribution is clearly biased to lower values; however, this could be caused not only by cloudiness but also for the typical lower angles in these dates due to solar geometry. In figure 5.9 it is displayed in more detail the contrast of these seasonal distributions.

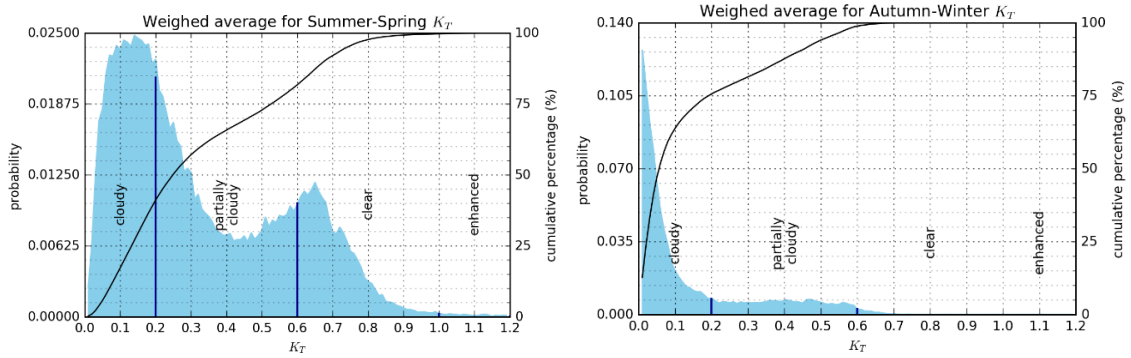

Figure 5.9: Probability Density Function and cumulative share percentage by season. Here is possible to see how the values in summer are bimodal while winter have nearly 65% of its values under 0.1 and an almost flat distribution till 0.55 K_T.

In an attempt to go further into detail the seasonal distributions were subdivided by hour in a range within 07:00 to 17:00, this analysis showed that the K_T average for Spring-Summer is of about 0.33 with a wide dispersion of an average window of 0.35 for the quartile 1 and 3, for Autumn-Winter the average value drop to 0.13 and so does too the dispersion of the data with a mean window of 0.1 for the values within middle 50%. There was some interesting rise in values after 15:00 hours in Spring-Summer, probably due to the albedo and reflections generated by buildings nearby, however this phenomenon was not registered in Autumn-Winter, in fact for this period there can be seen an inversed distribution peaking at 12:00, see figure 5.10 for more details.

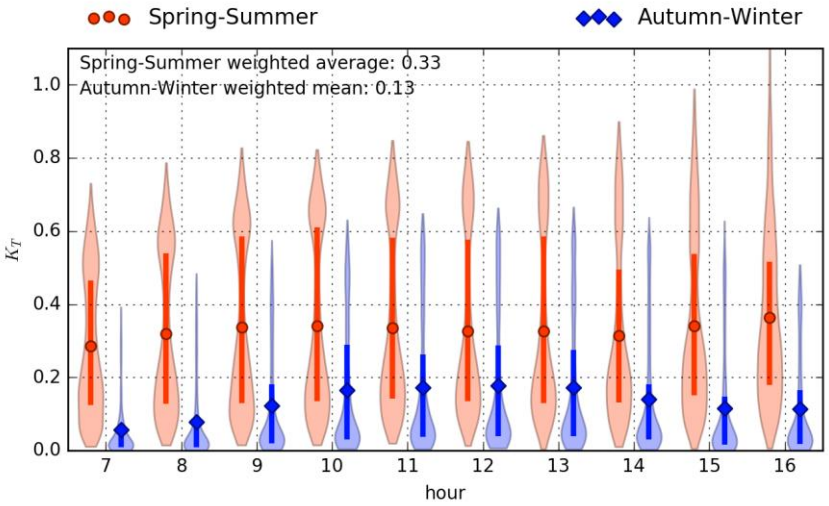

Figure 5.10: The mean K_T per hour per season. Here it is possible to see the contrast on the hourly behaviour of the solar resource, Spring-Summer showed wider dispersion and higher K_T values, opposite to Autumn-Winter in which both values decrease.

The regional values extracted from the data have some agreement from previous literature. In the results of Coli *et al. [22]* it is presented bimodal distribution in their probability distribution for year 2012, these values were collected in Upton, US. While in their paper the main peak is found near K_T value of 0.77 and the secondary at 0.2, the present analysis show the main at 0.28 and the

secondary at 0.93. Varo et al. [106] also presented a series of distributions for different *AM* values. This analysis performed in Cordoba, Spain yielded a bimodal distribution with a primary peak around 0.55 and secondary near to 0.25, similar to the Spring-Summer distribution of the present thesis.

5.3.2 Spectral analyses

This section aims to characterise the spectral behaviour of the solar resource as well as the effect that the variation of the sun spectra exert on the different solar materials. For this the relation between the indices mismatch factor (*MM*), average photon energy (*APE*) and solar irradiance will be explored.

5.3.2.1 Average Photon Energy trends

The index of Average Photon Energy (*APE*) is useful to evaluate qualitatively the spectral distribution of the solar resource. It is widespread used among the literature [45, 85, 24, 74] and has proven be reliable for spectral shape characterisation for irradiances above 150 W m^{-2}. More details about this index can be seen in section 2.3.1.1.

This research undertook the task of calculate *APE* values for about 145,000 spectra recorded by the roof station. In figure 5.11 it can be seen the weighted probability density function for the APE values of all data points acquired. In this chart it is possible to see 3 peaks, the main at 1.91 *eV* and two more at 1.93 *eV* and 1.94 *eV* which would put the distribution slightly to the blue side if we take the *APE* corresponding to the AM1.5 spectrum (value of 1.89 *eV*) as a standard. Also it is worth to notice that the mode of the *APE* values is found around 1.93 *eV* and that more of 75% of the distribution has values above 1.91 *eV*. The previously seen K_T distribution (figure 5.7) show a large share of cloudy time points, which indicated that much of these blue-leaning *APE* values might be duet to cloudy conditions, this idea will be further explored in the next sections.

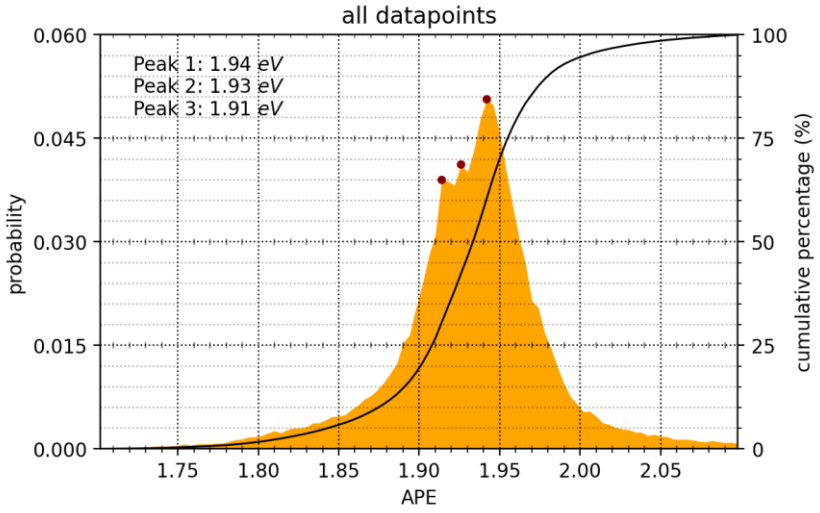

Figure 5.11: Probability density distribution and peaks of instantaneous APE values. This chart shows one main peak at 1.94 eV and two minor ones as 1.91 eV and 1.93 eV, it presents mainly blue APE values since 85% of them are above 1.89 eV, namely the APE of the standard AM1.5 spectrum. It is worth to mention as well that the centre of the distribution lies at about 1.93 eV

If the previous distribution is divided bi-seasonally it is possible to observe the contrast of the seasonal behaviour of the solar resource during the year. The distribution for Spring-Summer present peaks with similar values to the *PDF* of all the data points, it also has more kurtosis and skewness, displaying a depopulation on values under 1.85 *eV* and shifting the centre of the distribution to 1.94 *eV*, in figure 5.12 it is possible to appreciate the details of the distribution. The sharpening of the distribution can be due to the higher occurrence of lower *AM* values indicating certain specific shared conditions on clear days, furthermore the shifting to blue values could be explained as the light received from the Raleigh scattering of the sky.

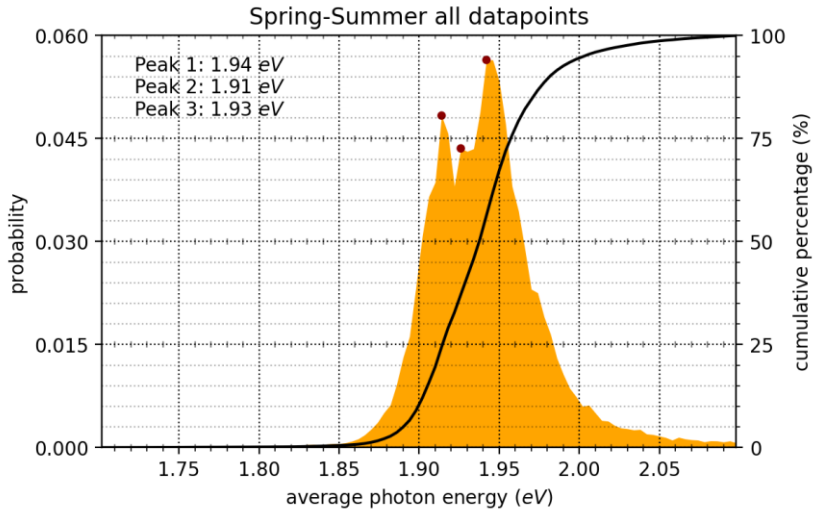

Figure 5.12: Spring-Summer APE probability density distribution The peaks have similar values as the ones in figure 5.11, keeping the main the value of 1.94 eV, while two minor ones of 1.91 eV and 1.93 eV. In comparison to the chart involving all data points, this one has more accentuated shift to the blue region since only 10% of its values are below 1.89 eV, the value of the AM1.5 standard spectrum and its centre can be found at 1.94 eV.

The distribution of Autumn-Winter has a wider range and some skewness leaning towards the red regions making almost 35% of the data points to be found below 1.89 *eV*. There are detected several peaks, the top three are at 1.93 *eV*, 1.95 *eV* and 1.90 *eV*. The centre of this distribution lies at around 1.91 *eV*, the increment of red values can be explained by the lower incidence angles which reduce the energy from the spectrum by increasing the *AM*. The details of this distribution are displayed in figure 5.13.

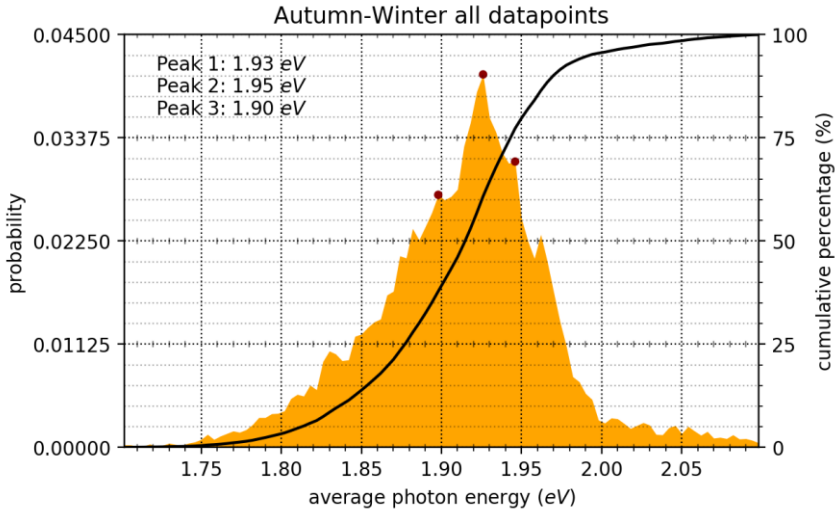

Figure 5.13: Probability density distribution and peaks by seasons, for values with solar irradiance above 150 W m^{-2}. For summer the blue-leaning are predominant with about 90% of the recurrences above 1.89 eV (AM1.5) while in winter are only about 26%, making its distribution more red-leaning than the Spring-Summer one.

Another perspective of the yearly behaviour was achieved with, a monthly analysis, here it is shown that the higher mean *APE* value corresponds to June with 1.96 *eV*, while the lowest value can be found in February with 1.90 *eV*. This analysis allows us to avoid the bias that might come by the unequal recording of the 16 month campaign, this way it was possible to calculate a weighted average of the annual *APE* in 1.93 *eV*. The month with higher standard deviation was December while the lowest one belongs to July with 0.07 *eV* and 0.04 *eV* respectively. Summer months have a higher mean value, and a minor dispersion which is biased toward blue values. Winter ones have lower *APE* values, wider dispersions and they seem to have less bias, figure 5.14 summarise the mean values, first and third quartiles and overall shape of the dispersions

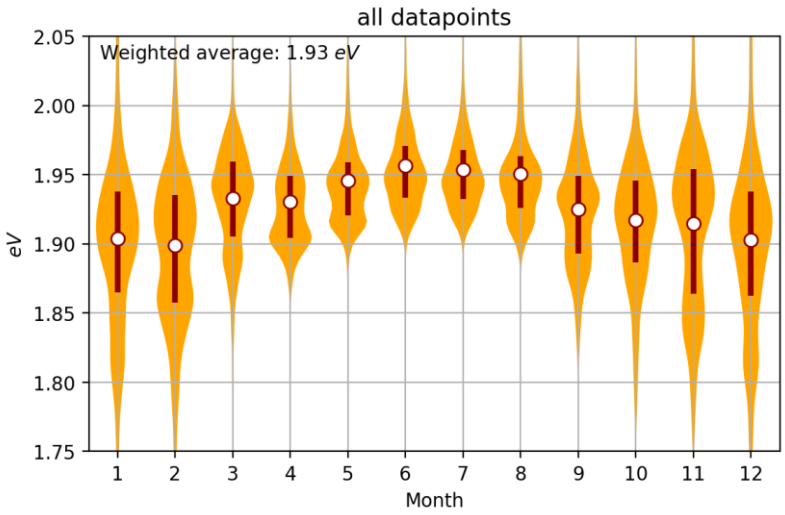

Figure 5.14: Trend of APE monthly mean values and distribution shapes. This figure shows that not only winter average values are lower, but the distribution is more spread, while for higher APE values in summer the variance decreases. The higher APE mean value is found in June, while the lowest was registered in February, with 1.96 eV and 1.90 eV, respectively.

Another analysis was conducted based on the hourly behaviour of the *APE* values of the solar resource, here some hours were omitted due to some effects of nearby constructions, the time range in question was of 11 hours from 06:00 to 17:00. For Spring-Summer the highest *APE* was found at 16:00 with 1.94, while the lowest was at 07:00 with 1.93 *eV*, the season had an estimated average of 1.94 *eV* and relatively small standard deviations of 0.02 *eV* (11:00, 12:00 and 13:00) to 0.04 *eV* (06:00, 16:00 and 17:00). The average *APE* value for Autumn-Winter was calculated in 1.91 *eV*, with the highest values at 06:00 and 17:00 both with 1.94 *eV*, while the lowest were registered at 09:00 and 14:00 both with values of 1.90 *eV*. As seen in previous analyses the Autumn-Winter presented a hider dispersion in their values with standard deviations from 0.09 *eV* (06:00) to 0.04 *eV* (11:00 and 12:00). It is worth to mention that there was significant overlap on both trends. Details of the dispersion shapes, first and third quartiles and mean values can be seen in figure 5.15.

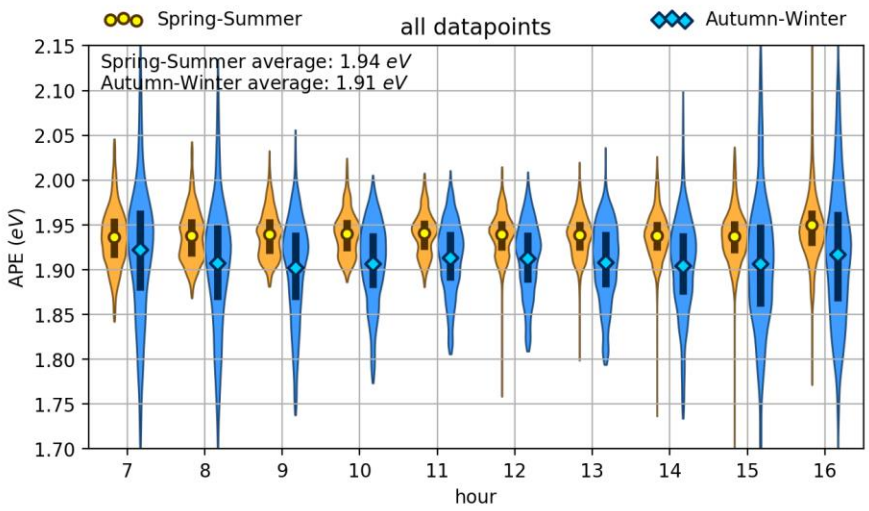

Figure 5.15: Trend of APE hourly mean values and distribution shapes. Here it is shown that for winter values the hourly average has more contrasting values from sunset and sunrise to noon, with more spread distributions. The values for summer present little change and a narrower dispersion.

5.3.2.1.1 Correlation of *APE* with other indices

To go further in the behaviour of the solar resource it was produced a plot to analyse the relation of *APE* and solar irradiance values. It was selected to make the plot as a heat map to make easier to appreciate the density of the distribution of values within the irradiance *APE* 2D plane, here it is displayed a weak correlation of *APE* to solar irradiance for most of the values, this denotes the importance of atmospheric conditions for values across the analysed range. Furthermore for values in which solar irradiance is above 600 W m^{-2} the variation get reduced around the value of 1.91 *eV*, this can be interpreted as a similarity of conditions for high value irradiances. In figure 5.16 is possible to see in more detail the evidence supporting these statements.

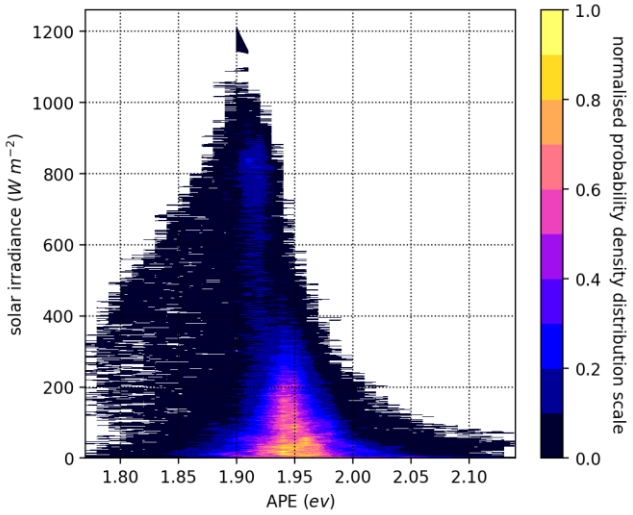

Figure 5.16: Probability density heat-map of APE by instantaneous solar irradiance, for all solar irradiance values. This tells us that for low irradiance the variation of APE is wide, and it sharpens as the irradiance increases.

A second analysis using the heat map visualisation was realised to illustrate the correlation between *APE* and clearness index (K_T). Here it is possible to see the distribution previously inferred in figures 5.11 and 5.7, in which a high concentration of values are found within *APE* values from 1.91 *eV* to 1.93 *eV* and K_T of 0.65, as well as in coordinates of 1.94 *eV* and 0.18 of *APE* and K_T respectively, also it is possible to appreciate that the correlation is slightly stronger in comparison to that of solar irradiance, indicating that cloud cover has a stronger influence on the *APE* than solar irradiance. The details can be seen in figure 5.17.

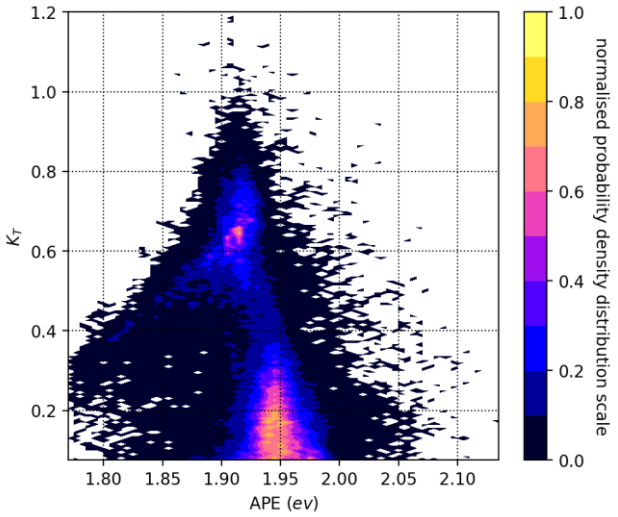

Figure 5.17: Probability density heat-map of occurrences of APE by instantaneous K_T, for all solar irradiance values. In this distribution is possible to see 2 clusters of values around K_T values below 0.2 and around 0.65. Also what might seem like a weak linear trend in which the higher K_T values the more they approach to the value of 1.89 eV, close to the APE value for the standard spectrum AM1.5.

5.3.2.1.2 *APE* and spectral shape

Additionally to the exploration of the previous indices it was undertook as well the opportunity to investigate the relation that *APE* might have as a characterising index of the spectral shape. From the nearly 136,000 spectra from the dataset that were acquired for the range 300 nm to 1050 nm, all measurements under 150 W m^{-2} were discarded, to be able to make a closer comparison to existing literature [67]. The relative percentage distribution for spectra with *APE* values between 1.78 *eV* and 2.00 *eV* were plotted by incremental steps of 0.02 *eV*. This analysis demonstrates a regular change of the spectral general shape in function of the *APE* interval with an immobile point between 550 nm and 650 nm, this seem to support the findings of previous literature [72, 87, 74], each data-point represents the percentage contribution of the spectra divided in bands of 50 nm, a summary was made in table 5.2 to indicate the values of mean, maximum and minimum standard deviation and number of samples. In figure 5.18 it is illustrated the standard deviation of the samples, here it is noticeable that there seem to be a negative correlation of *APE* values to the magnitude of standard deviations, meaning that the higher the *APE* value the lower the variation

among the samples. Reinforcing the findings that high *APE* values might correspond to similar sky conditions.

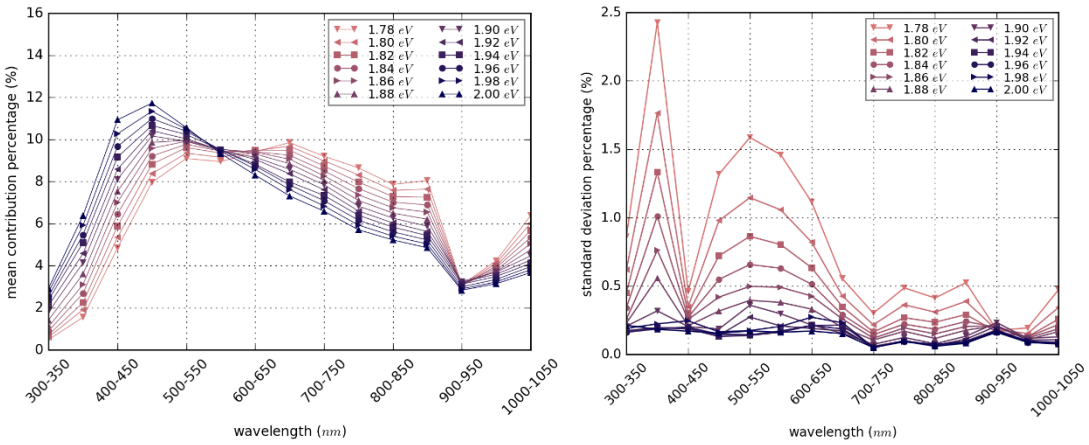

Figure 5.18: Mean shape of solar spectra and standard deviation of the shape by APE. (left) Mean contribution percentage by bins of 50 nm for different APE values (right) Standard deviation of mean contributions by bins of 50 nm. There seem to be a correlation of low APE values to standard deviation, while the high APE values tend to have a less variation..

APE	**Mean std (%)**	**Max std (%)**	**Min std (%)**	**No. samples**	***APE***	**Mean std (%)**	**Max std (%)**	**Min std (%)**	**No. samples**
1.78	*0.82*	*2.42*	*0.17*	*227*	1.90	*0.18*	*0.36*	*0.07*	*5033*
1.80	*0.60*	*1.76*	*0.15*	*446*	1.92	*0.15*	*0.27*	*0.06*	*8407*
1.82	*0.46*	*1.33*	*0.13*	*666*	1.94	*0.14*	*0.21*	*0.05*	*8003*
1.84	*0.37*	*1.01*	*0.13*	*931*	1.96	*0.14*	*0.21*	*0.05*	*3625*
1.86	*0.30*	*0.76*	*0.12*	*1293*	1.98	*0.16*	*0.27*	*0.05*	*921*
1.88	*0.24*	*0.56*	*0.11*	*2048*	2.00	*0.13*	*0.21*	*0.05*	*176*

Table 5.2: Summary table for solar spectral shape by APE, mean, maximum, minimum and number of samples.

5.3.2.2 Estimation of solar spectral influence on PV energy yield

The following analysis corresponds to data acquired from the sensor with the optimum tilt angle and south-facing located in the University of Sheffield, as seen in section 4.2.1. For this estimations the typical spectral responses (*SR*) for a-Si, c-Si, CdTe, CIGS and High Efficiency c-Si were used, the ones displayed in section 2.6.1.1 (see figure 2.27), to calculate the mismatch factor (*MM*) using equation 2.39, from section 2.3.1.2. This parameter together with *APE* has been used to investigate the impact of the solar spectra on the energy yield of PV technologies. *MM* will indicate the ratio of available solar irradiance between an actual solar spectrum and the standard AM1.5 in function of a given PV technology and *APE* indicates the red or blue skewness of the analysed spectrum.

This research compares these indices in a similar approach as Ishii, 2013 [42] to investigate the relationship of *SR* of the mentioned technologies to the solar spectral irradiance fluctuations. *APE* is a characterisation of the skewness, towards red or blue regions, of the analysed spectrum while *MM* indicated whether a spectral distribution generates gains or losses compared to a standard, this is to say it let us calculate the energetic impact. Some literature point that the *MM* as defined in equation 2.39 does not differ greatly from the maximum power point of the module and the scaling factors of the *SR* curves result in little change on the *MM* calculation [3, 42].

For the estimation of the relation between the two aforementioned indices all the spectra, even low irradiances, were considered resulting in wide spread values of *APE*, this gives the perspective how despite the minimal share in energetic resource the low irradiation increases highly the variability. A linear regression between these two indices was calculate using the least-squares method, just to make an objective evaluation of the trend of the correlation of these indices, these can be seen in figure 5.19.

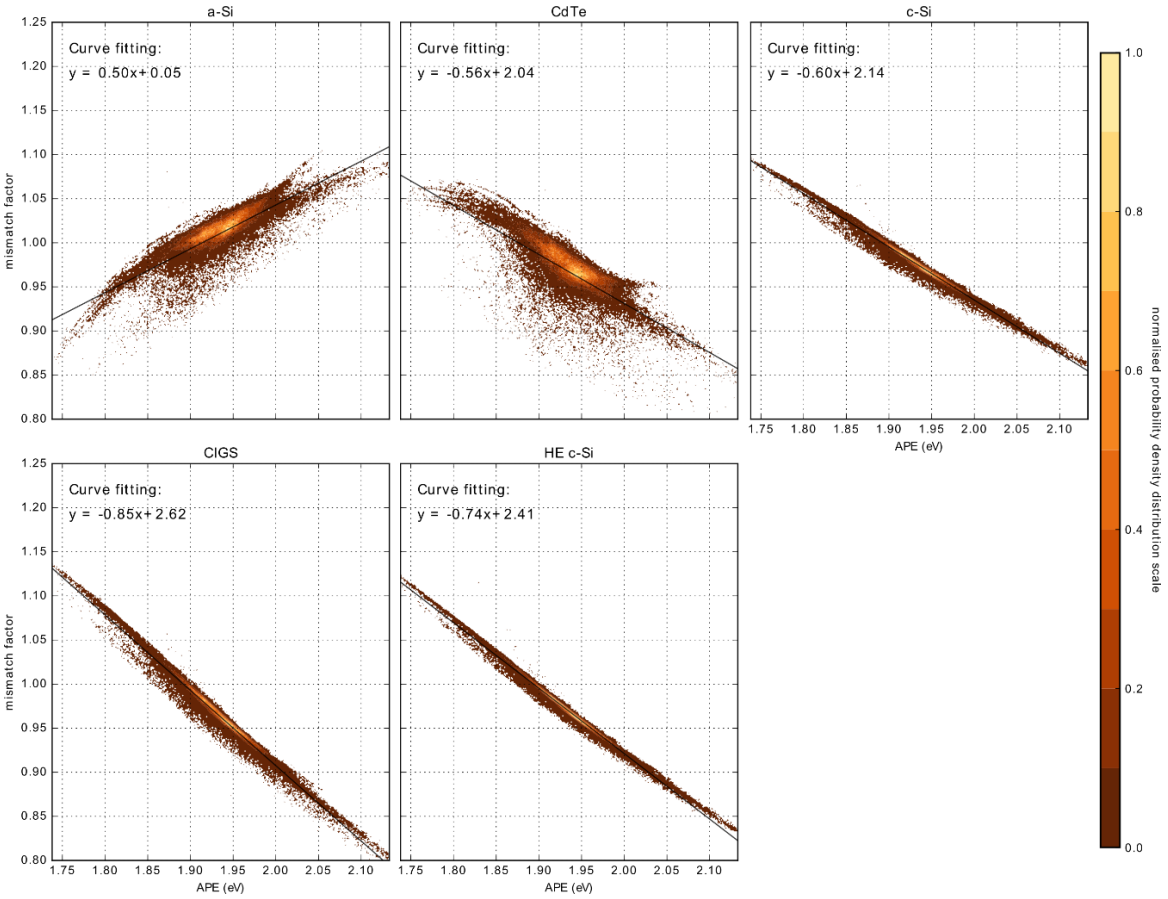

Figure 5.19: Relation of Mismatch factor vs APE for 5 selected PV technologies, in this figure all values of APE are taken into account. The linear regression gives a notion of the general trend of the spectral gain or loss with respect of APE, from the typical formula y = mx + b, one could consider the value representing m to be a direct indicator of the spectral influence.

However, the next figure might be more illustrative since it summarises the spectral influence by month. In the figure it is presented the bias difference, meaning that the value of 1 was subtracted to portrait spectral losses with negative values and gains with positive ones. Here is visible that the fraction of change of *MM* through seasons is less than 0.1, meaning less than 10% for all the technologies; and that the mean value might not be giving a full characterisation of the influence of the spectral variation, since the middle 50% (brown area within the violin shapes) often do not encompass the mean value, this is detailed figure 5.15, and summarised in table 5.3.

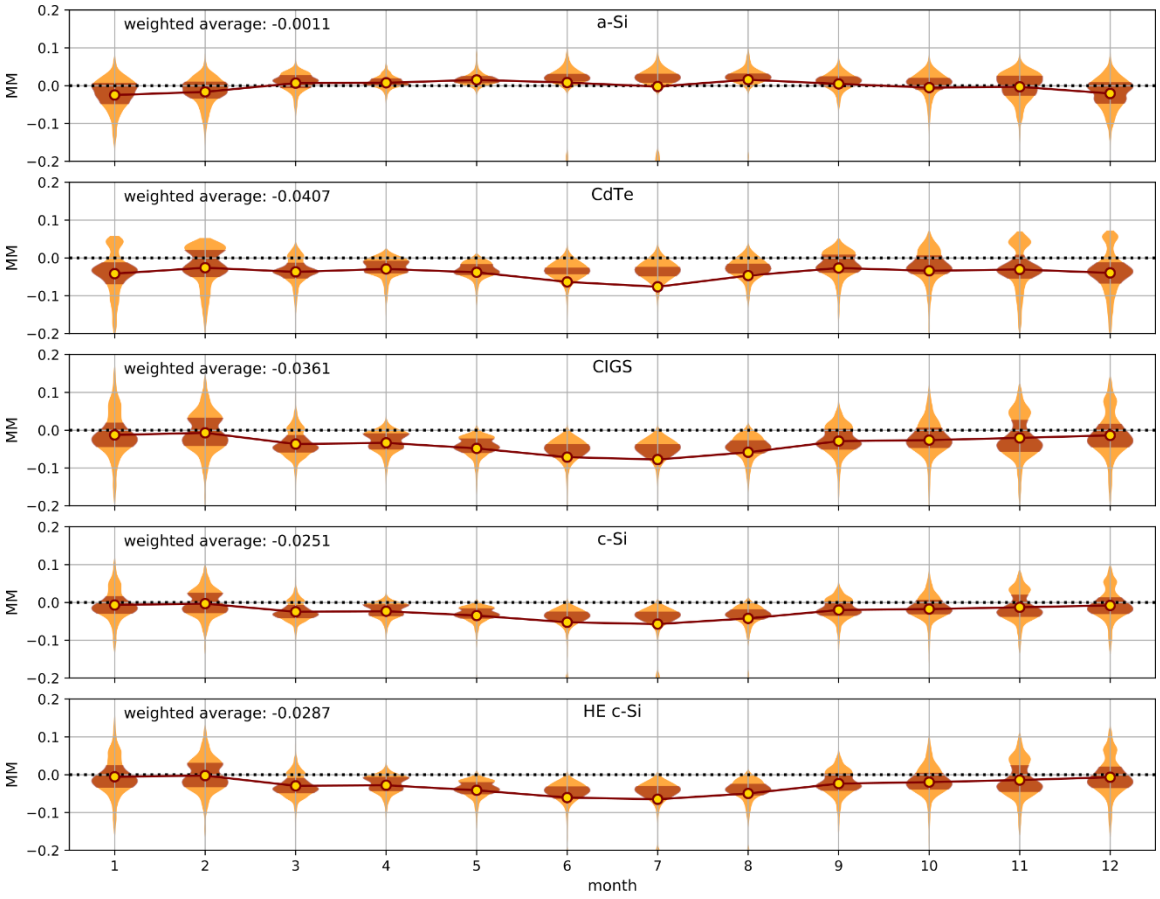

Figure 5.15: Estimated monthly spectral loss or gain by MM for the different PV technologies. The shape of the figure represents roughly the distribution of the data, the shaded brown area shows the central 50% of the data (Q2 + Q3) and the yellow point represents the mean. It is presented as a bias difference, subtracting 1 to the original MM values to indicate gains as positive values and losses as negative ones.

PV tech	***Seasonal MM difference (%)***	***Lowest MM (%)***	***Highest MM (%)***
a-Si	+4.0	-2.5	+1.6
CdTe	-5.0	-7.6	-2.6
CIGS	-7.0	-7.8	-0.7
c-Si	-5.4	-5.7	-0.3
HE c-Si	-6.3	-6.5	-0.2

Table 5.3: Summary of spectral loss and gains according to *MM* for the different PV technologies.

Most of the technologies show a spectral loss from summer to winter. However, a-Si showed to be the only one with spectral gains from winter to summer. This could be due to match its *SR* curve for has to the clear sky solar spectrum. Since the standard solar spectral distribution has a peak at around 550 nm, the *SR* of a-Si peak is found near to 600 nm. Furthermore, the second best was CdTe with the lowest spectral loss between seasons. For the other technologies since they peak between 900 nm and 1000 nm it is understandable that they would have a better performance in red-shifted *APE* values.

The impact of spectral irradiance by PV technology in relation to solar irradiance is displayed in figure 5.20, the relation changes according the technology. For a-Si there is a reduction of spectral gain as the irradiance increases, while CdTe has a logarithmic tendency to increase its gains as the irradiance increases. The rest of the technologies seem to have an almost flat values as the irradiance increases, with the exception of values under 200 W m^{-2}.

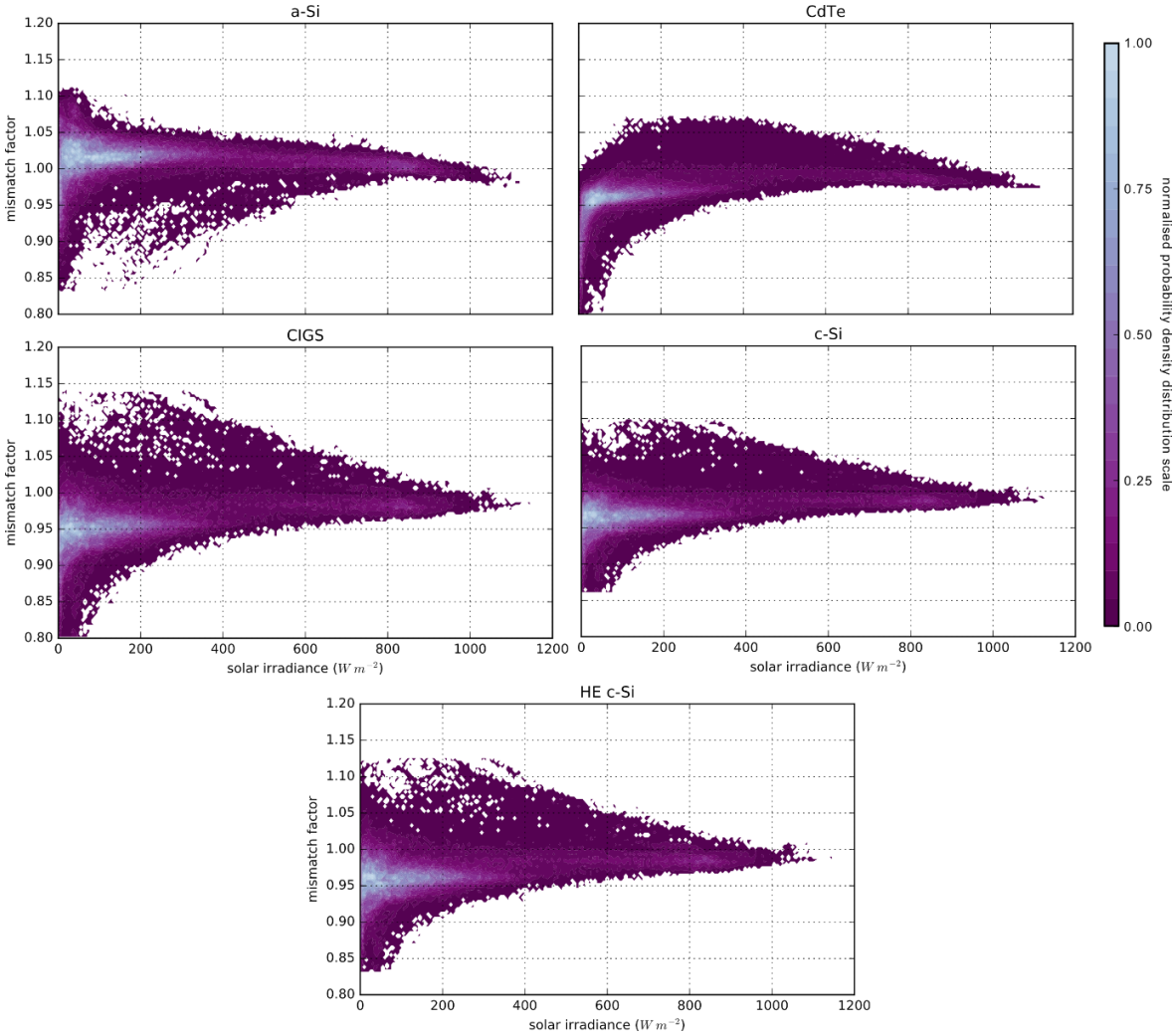

Figure 5.20: Relation of Mismatch factor vs solar irradiance for various PV technologies. The colour scale represents the density of data points in a given space of the plot.

Since the variation gets reduced to a nearly flat behaviour as the solar irradiance increases, which could indicate a low influence of spectral distribution at for higher levels of energy.

5.4 Discussion and conclusion

The data acquired during the 16 months allowed to perform a thorough examination of cloudiness, solar irradiance, spectral variability by *APE* and spectral influences for various PV technologies. However, this research does not take into account factors such as ambient temperature, cell degradation, wind or inverter influences, which might have an even stronger influence in the energy yield. Monthly average values for the aforementioned weather and cell characteristic are performed, as well as correlation analysis between *MM* and both *APE* and solar irradiance.

According to the monthly trend of *MM*, a-Si showed gains for summer of +4.0% all other technologies registered loses. This matches to the analysis of correlation *APE-MM* of each technology from figure 5.19 in which a simple linear regression was calculated to objectively quantify the tendency in function to the APE value, resulting on a-Si the only one with positive tendency, CdTe was the second best because despite reducing the *MM* as the APE increased it had a less accentuated negative linear coefficient.

The overall *APE* values of the acquired data show a mainly blue-leaning, with about a 85% of the APE values above the AM1.5 value of 1.89, and the mean values have a minimal of 1.89 *eV* for February and a maximal of 1.96 *eV* for June. It was shown as well that as APE is a reliable index to characterise the solar spectrum shape for irradiances above 150 W m^{-2} [74], while contesting some of results pointing out that solar irradiance might be used as well to characterise this parameter [87].

Also, with respect to the seasonal trends, summarised in table 5.3, it would not be expected significant gains of the electrical energy production, particularly since some other elements such as the PV cell efficiency, degradation or temperature; could have a more important contribution. Solely by the standard commercial efficiency a-Si the material with best seasonal spectral gains, has a PV conversion of 12.3% in comparison to HE c-Si of up to 24.4%, making a-Si only 50% of the peak power capacity of that of the HE c-Si. Further research should be control for the multiple factors influencing the energy production of these technologies. This is supported as well by literature such as the paper published by Taylor *et al.* [98] of a study of over 7,000 installed systems and data for 10 years, the mean monthly performance ratio increases approximately 3.0%, while the standard deviation increases from 6.33% in summer to 14.23% in winter. From a design point of view and

based on the results of this thesis, optimise the PV material to counter act the spectral influence does not need to be a focus for PV systems.

However it is important to remark that the calibration method detailed in chapter 4, has been proven reliable due to the results of the characterisation of solar spectra, solar irradiance and clearness index which are consistent to the literature.

6 Discussion, conclusions and future work

6.1 Discussion

This thesis presented 3 main experimental chapters: (3) the design of an accurate cosine correcting coupling device, (4) In-situ calibration for long term solar low resolution spectral solar acquisition and (5) characterisation of atmospheric conditions using the data acquired by statistical analyses of clearness index, solar irradiance, the spectral solar distribution, Average Photon Energy (*APE*); and the influence of spectral variation on different PV technologies, by comparing *APE* to Mismatch factor (*MM*).

To generate reliable data acquisition, the main focus of chapter 3 was to produce a Cosine Correcting Optical Coupling (*CCOC*) device able to minimise the cosine error in the measurement of the spectral irradiance. Averaging through all the angles, the current State-of-Art presents a Mean Absolute Error (*MAE*) of about a fraction of 0.215 and a determination coefficient of 0.9611. The best design produced in the scope of this thesis was G1 with a *MAE* fraction of 0.039 and an r^2 of 0.9990 (see table 3.2 and figure 3.14). Ultimately, due to time constraints it was design D1, with a *MAE* ratio of 0.135 and r^2 of 0.9801, the one used for the 16 month outdoor acquisition campaign, serving as a test to prove the physical and chemical endurance of this device under environmental conditions. The research made in this chapter produced a paper titled: G*eometric optimisation of an accurate cosine correcting optic fibre coupler for solar spectral measurement, Cahuantzi and Buckley* [19], accepted in the journal *Review of Scientific Instruments 88, 095003 (2017); https://doi.org/10.1063/1.5003040* (see appendix 7.2). This work could be further extended by including analyses on the thermal stability of the spectral transmission within the Polytetrafluoroethylene (PTFE).

The main focus of this project was the spectrometer calibration for absolute irradiance, since very little has been published about in-situ spectrometer calibration for long term solar spectral data acquisition. Particularly useful to this work was the literature describing the concept of “vicarious calibration”, which is defined as: techniques of calibration using natural or artificial sources for a post-launch calibration of sensors. This method is described by Thome *et al.* [100] where they report that the differences caused by radiative transfer codes, only account for a small error (less than 0.6%).

However, the proposed calibration method is more similar to the one published by O’Donnell and Garces [77]. Authors present a method to calibrate similar spectrometers to the one

used in this project (Ocean Optics USB400) they made a selection of time points in which the solar total irradiance value was close to the standard AM1.5 spectrum with clear sky conditions and low humidity. As they tested the accuracy they reported it to be consistent to adequate calibration and demonstrate the validity of it by measuring a spectral distribution of a down conversion source with a pump laser and a periodically poled KTP (Potassium titanyl phosphate) nonlinear crystal.

Based on the aforementioned concepts for in-situ calibration of solar spectra, a pragmatic approach was taken. The calibration method presented in this thesis was achieved by comparing two models of cloudless solar spectrum, SPCTRAL2 [14] which was adapted to Python code (see appendix 7.1); and SMARTS2 [35], which needed a "wrapping" for the publicly available executable version in order to produce a series of spectra for a set of time points, see appendix 7.3. This calibration was later validated by cross-validating to integrated empirical and modelled values of solar irradiance; and values of similar spectral analyses within the literature. The detail of this process, and evaluation can be seen in detail in chapter 4.

This acquired and calibrated data provided a good insight of the general clearness index profile of the region. This is analogous to the Probability Distribution Functions (PDF) reported by Colli *et al.*, 2014 [22], in which it is possible to see bimodal distributions. However in contrast to the annual values of clearness index (K_T) of the UK, the highest peak is located at 0.18 and the secondary at 0.65, whereas the values reported in their paper are for Upton, US, with the main peak near to 0.77 and the secondary to 0.2, they concluded that there is not strong correlation of K_T to other atmospheric variables outside global irradiance (r^2: 0.803) and relative humidity (r^2: -0.737), being the latter negative correlation. In the same paper is also stated that only values from 09:00 to 16:00 were considered to avoid the non-linearity registered at the beginning and the end of the day, throughout the year, namely that winter days are shorter than summer ones.

The data of this thesis diverges from the data collected by Okogbue, Adedokun and Holmgren, in 2009 [78] at Ile-Ife, Nigeria. In their paper, despite showing a low resolution on the probability density representation, it is possible to see in the annual distribution 2 peaks the main between 0.50 - 0.55 K_T values and the secondary between values of 0.35 - 0.40 K_T values with a height variation no higher than -8%. In summary these distributions show the variation of clearness index between regions and suggest a correlation of low latitudes with higher K_T typical values. Despite the differences in climate they concluded that nearly 72% of registered values fell between 0.15 and 0.60, which they classified partially cloudy. Contrasting with the present thesis in which just about 65% of the values are found within that range, the results seem to be equivalent since it is inferred that they also discarded low energy values by trimming the data points acquired before 07:00 hours and after 18:00 in the same line as in this project values of irradiance under 150 W m^{-2} were discarded for the second plot in figure 5.7.

The estimation of monthly Average Photon Energy (*APE*) values in this project, reflects similarities to the values reported by Magare *et al.* in 2016 for locations in India [57], with a variation range from 1.50 *eV* to 1.73 *eV* between seasons. These values were calculated using a spectral measurement range of 300 nm to 1700 nm, whereas our work calculated the values within a range of 300 nm to 1050 nm. This difference of protocols make difficult the comparison, but considering that the spectrum AM1.5 has a value of *APE* of 1.62 *eV* in the ranges of the referred paper and 1.89 *eV* in the present thesis. It is possible to assume that the high contrast of the aforementioned paper could be due to the wider range. The values in the UK had an estimated variation between the lowest and highest *APE* values of between 1.90 *eV* to 1.96 *eV*, with around 75% of the values leaning to blue-shifted spectra. These characteristics of the *APE* values in the UK are likely to be caused by the typical low K_T values which produce a larger diffuse fraction ($E_{s,dif}$) in the global irradiance (E). Furthermore, there are some coincidences with their results in which summer and monsoon seasons are characterised by a spectral loss for monocrystalline and HIT technologies (*MM* values of about -8.2% and -10.8% respectively), while amorphous silicon has gains through these seasons of about 26.4%. The wider variation could be explained due to the range they performed the measurements and the geographical location.

There are as well some parallels to Betts *et al.*, 2004 [13], reporting the closeness of the peak values of *APE* (with peak between 1.55 *eV* and 1.65 *eV*) in the UK to that of the standard spectrum AM1.5, with an *APE* of 1.6 *eV* for the wavelength range between 300 nm and 1700. Whereas in this thesis the measured *APE*, calculated within the range of 300 nm to 1050 nm, was between 1.85 *eV* to 1.93 in comparison to a value of 1.89 for the standard AM1.5 spectrum. Both having a similar range near to 0.1 *eV*. It is commented within this paper that sunnier climates in comparison to the UK it is likely to have a lower share of energy at high *APE* values. Some of the conclusions drawn from the aforementioned paper is the *APE* is a strongly correlated to useful fraction, and is a helpful tool to characterise irradiance spectra.

In the paper of Sirisamphanwong and Ketjoy, 2012 [95] it is possible to see the difference of *APE* annual distribution, and it is possible to make a more direct comparison with their results, since they calculate the value of *APE* using a similar spectral range to the one used in this thesis (350 nm to 1050 nm), In their results they show *PDF* with a multi-peak distribution, one in 1.86 *eV* value and another in 1.92 *eV*, this values were acquired in Naresuan University (latitude 16˚49' north, longitude 100˚15' east). This might support the hypothesis that southern, and therefore sunnier, locations have more red-shifted solar spectra values. As would be expected due to the thinner *AM* the sunlight has to cross, thus reducing the blue scattering.

The findings of this thesis also pointed to similar distributions to those described by Gottschlag *et al.* [30] in regards to solar irradiance. Thus, in this thesis it was learned that for the

data recorded by the sensor tilted 45˚ facing South, 50% of the irradiance recorded was under 140 W m^{-2} and 75% was under 310 W m^{-2}, as seen in figure 5.1. Whereas the *PDF* showed in the mentioned paper points that over 50% of the irradiance measured was below 200 W m^{-2} and a small margin was presenting the phenomenon of enhanced irradiance. In the same paper it is also present an interesting plot of the Useful Fraction for a-Si technology in function to irradiance. Since *UF* is too an index to determine the characteristics of the solar spectrum, this graph shows parallels with figure 5.16, which further supports the statement that for a given irradiance, considerable variations in the spectral shape is possible. An indicator such as *APE*, for the spectral distribution could provide tools for a better forecasting. Therefore the information within this study could be valuable as a guide for future research in which this information could be used to generate stochastic models for solar irradiance.

With the data presented in this thesis and the radiative transfer model produced it would be possible to expand the analysis to include Probability Density Functions based on Air Mass, to compare to the extensive work presented by Fernández-Peruchena and Bernardos [26] for multiple regions, including Camborne, UK. At first glance the *PDF* curve seems to agree with values corresponding to the data acquired in April, but to make the correction for *AM* could result in interesting and comparable results. Another similar analysis that could be done are of the likes of the one proposed by Tapakis and Charalambides [97] where solar irradiance and K_T index are correlated to solar elevation and azimuth angles.

The data acquired could be also matched to the existing temperature and PV-energy produced at the roof-top site of the Hicks building, this would result on analysis comparable to those of Gottschlag *et al.* [29] for the region of Loughborough or Bayrakci, Choi and Brownson [10] for different regions in the US. Further exploitation of this data could also produce a stochastic and empirical model for Sky conditions and solar irradiance. These models could be similar to the one proposed by Hofmann and Seckmeyer [38].

6.2 Conclusions

The results of this thesis showed some influence of spectral variation upon the diverse PV materials, but since the wide gap between the general efficiency of these materials in the market, namely, currently the technologies based on silicon offer a more reliable energy production and the effect solar variation represent does not merit the change of PV material. It will be more constructive to focus the optimisation of PV systems in other more influential factors such as, optimal angles, temperatures of operation or degradation rates.

The CCOC used withstood outdoor conditions during the 16 months without noticeable degradation. It is a reliable tool to acquire spectrally resolved data, without compromising linearity of the sensors. The selected device was an improvement to the current State-of-the-Art device according to the evaluation detailed in chapter 3.

Based on data collected with the optimised CCOC, a calibration method suitable for low resolution spectrometers was developed. This method was based on the modelling of clear sky solar spectra and performed post-acquisition. The spectral analysis in chapter 5 serves as validation of the calibration technique since the values are consistent to those presented in other published works.

Furthermore, the proposed calibration method has the advantage of being low cost, making it affordable for solar projects in developing economies which may not possess the resources to produce a calibration with sophisticated equipment. This approach provides an inexpensive solution to calibrate data that can be later used to train algorithms and produce better forecasting. Acquiring more spectrally resolved data will lead to better inferences, which will result in a better and more efficient administration of the solar resource, thus increasing confidence of the public and generate a wider uptake of solar technologies and renewable energies in general.

7 Appendices

7.1 Appendix A: SPCTRAL2 Python code

```
# -*- coding: utf-8 -*-
"""

Created on Sun Apr 12 23:53:05 2015
@author: R Cahuantzi
In language: Python V3.5.1, with built-in modules math and of.
With modules: Numpy V1.10.4, Pandas V0.18.0.
Files required: ETR_Gueymard2003.csv, A_H2O_Bird&Riordan1983.csv,
A_O3_Bird&Riordan1983.csv, A_UG_Bird&Riordan1983.csv

PySolar V0.6 geometry based on: I. Reda and A. Andreas, "Solar Position
Algorithm for Solar Radiation Applications," National Renewable Energy
Laboratory, NREL/TP-560-34302, revised November 2005.

"""

from math import acos, cos, sin, pi, log, exp, floor
from math import degrees as deg
from math import radians as rad

import numpy as np
import pandas as pd
from datetime import timedelta
import of

from Pysolar.solar import *
from Pysolar import julian


"""
Code based on SPECTRAL2 irradiance model. It is able to calculate solar
position and spectral irradiance, some modifications were made, specially
the inclusion of solar geometry calculations. The equations used in this
code come from:
[1] R. Bird and C. Riordan, "Simple solar spectral model for direct and
```

```
diffuse irradiance on horizontal and tilted planes at the Earth's surface
for Cloudless Atmospheres", 1984.
[2] T. K. Van Heuklon, "Estimating Atmospheric Ozone for Solar Radiation
Models", 1978.
[3] J.W. Spencer, "Fourier Series Representations of the Position of the Sun",
1971. From J. Pickard's email (corrected by M. Oglesby), 1998.
[4] B. Leckner, "The Spectral Distribution of Solar Radiation at the Earth's
Surface--Elements of a Model", 1978.
[5] F. X. Kneizys, et al., "Atmospheric Transmittance/Radiance:
Computer Code LOWTRAN5".
[6] A. Angstrom, "Technique of Determining Turbidity of the Atmosphere", 1961.
[7] A. McEvoy, T. Markvart and Luis Castaner, "Practical Handbook of
Photovoltaics: Fundamental and applications", 2013.
[8] J. A. Duffie and W.A. Beckman, "Solar Engineering of Thermal Processes",
2013.
[9] M. Jacobson, "Fundamentals of atmospheric modelling", 2005.
[10] C. Gueymard, "SMARTS2, A simple model of the atmosphere radiative
transfer of sunshine", 1995.
"""

# Defining default values
# For time:
year = 2015.0;      month = 6.0;        day = 21.0;
hour = 12.0;        mins = 0.0;         secs = 0.0;
consider_bst = False;

# For PV/acquisition system:
Ang_slope_sys = 45.0;       Ang_tilt_sys = 180.0;       tracking = False;

# Geographycal location:
lat = 53.380813;            long = -1.485708;           elev = 0

# Atmospheric parameters:
AOD = 0.27;         alpha = 1.14;       rho_g = 0.10;
O3 = 0.3438;        H2O = 1.4164;       de = 1013.25;
omega = 0.945;      omega_p = 0.095;        asym = 0.65;
O3_h = 22.;         t = 25

alt_return = ''

def Spctral(year = year,    month = month,  day = day,      hour = hour,
        mins = mins,    secs = secs,    consider_bst = consider_bst,
```

```
    Ang_slope_sys = Ang_slope_sys,  Ang_tilt_sys = Ang_tilt_sys,
    tracking = tracking,

    lat = lat,      long = long,    elevation = elev,

    AOD = AOD,      alpha = alpha,  rho_g = rho_g,  O3 = O3,
    H2O = H2O,      pr = pr,        omega = omega,
    omega_p = omega_p, asym = asym,     O3_h = O3_h,

    alt_return = alt_return):

"""
Inputs:
consider_bst : Activates the option to recognise the dates within British
    Summer Time and make the arithmetic correction of -60 minutes.
Ang_slope_sys : Angle of inclination of PV system's plane subtended to
    ground surface, in degrees.
Ang_tilt_sys : Angle of inclination of the projection of the normal of
    the plane of the system on PV system's plane of the surface
    subtended to the north axis. Known as well as azimuth angle
    (180 south, 0 north, 90 east, 270 west).
tracking : Activates the calculation as if the PV system has a tracking
    base.
lat : Geographical latitude of PV system, in degrees.
long : Geographical longitude of PV system, in degrees.
AOD : Aerosol Optical Depth: Range for clear skies is 0.05 to 0.55.
    Higher optical depths result from clouds, smoke, and larger
    particles in the atmosphere.
alpha : Exponent alpha of Angstrom's [6] expression of turbidity.
rho_g : Albedo, surface reflectance used to calculate the diffuse
    irradiance, does not affect Direct Beam computation. Used for
    computing diffuse sky and reflected diffuse irradiance.
O3 : The total column of ozone, as if it were condensed on the surface,
    in cm.
H2O : Total precipitable water if it were condensed on the surface,
    in cm.
pr : Atmospheric pressure. The standard at sea level is 1013.25 mbar.
    Lower pressures mean less atmosphere to absorb the radiation, in
    millibars (mbar).
omega : Single scattering albedo factor at 0.4 micrometres (400 nm) of
    wavelength.
omega_p : Prime single scattering albedo factor for wavelength variation.
asym : Rural aerosol scattering asymmetry factor, forward total
```

```
        backwards scattering ratio.
    O3_h : Height of ozone, in Km.

    Output:
    DataFrame with spectra as columns (units W/m^2/nm):
    ETR : Extraterrestrial spectral irradiance.
    ETR_rv_tilt :  Extraterrestrial spectral irradiance on PV system's plane.
    I_dir :  Direct solar irradiance on horizontal.
    I_dir_tilt : Direct solar irradiance on PV system's plane.
    I_dif_tilt : Diffuse solar irradiance on PV system's plane.
    I_tot_tilt : Total solar irradiance on PV system's plane.
    """

    Eq_T, Ang_hr, Ang_dcl, AM, \
    AM_pr, r_vec, Ang_sol_az, Ang_slp, \
    Ang_zth, cos_AOI_sys = SunPos(year = year,  month = month,  day = day,
                        hour = hour,    mins = mins,    secs = secs,
                        consider_bst = consider_bst,

                        Ang_slope_sys = Ang_slope_sys,
                        Ang_tilt_sys = Ang_tilt_sys,
                        tracking = tracking,

                        lat = lat,      long = long,
                        elevation =  elev)

    list_alt_ret = [Eq_T, Ang_hr, Ang_dcl, AM, AM_pr, r_vec, Ang_sol_az, \
            Ang_slp, Ang_zth, cos_AOI_sys]

    list_str = []
    for var in list_alt_ret:
        for k, v in list(locals().items()):
            if v is var and k != 'var':
                list_str += [[k, v]]

    for a_ret in list_str:
        if alt_return == a_ret[0]: return a_ret[1]

    O3_m = O3AM(O3_h, Ang_zth)
    alog = Alog(asym)
    aF_s = AFs(alog)
    bF_s = BFs(alog)
    F_s = Fs(aF_s, bF_s, Ang_zth)
```

```
    F_s_p = Fsp(aF_s, bF_s)

    ETR, A_H2O, A_O3, A_UG, WL_range = EetrAbs()
    omega_wl = OmegaWl(WL_range, omega, omega_p)
    T_R = Tr(WL_range, AM_pr)
    T_O3 = To3(WL_range, A_O3, O3_m, O3)
    T_UG = Tug(WL_range, A_UG, AM_pr)
    T_H2O = Th2o(WL_range, A_H2O, H2O, AM)
    tau = Tau(WL_range, AOD, alpha)
    T_a = Ta(WL_range, tau, AM)
    T_as = Tas(omega_wl, tau, AM)
    T_aA = Taa(omega_wl, tau, AM)
    I_dif_R = Edifr(ETR, T_O3, T_H2O, T_UG, T_aA, T_R, r_vec, Ang_zth)
    I_dif_a = Edifa(ETR, T_O3, T_H2O, T_UG, T_aA, T_R, T_as, Ang_zth,
                                            F_s, r_vec)
    T_R_p = Trp(WL_range)
    T_H2O_p = Th2op(A_H2O, WL_range, H2O)
    T_UG_p = Tugp(A_UG, WL_range)
    T_as_p, T_aA_p = TaspTaap(omega_wl, tau)
    rho_s = Rhos(T_UG_p, T_H2O_p, T_aA_p, T_R_p, T_as_p, F_s_p)
    I_dir = Edir(ETR, T_R, T_O3, T_UG, T_H2O, T_a, r_vec)
    I_dif_g = Edifg(I_dir, I_dif_R, I_dif_a, rho_s, rho_g, Ang_zth)
    global C_s # Declare C_s as a global variable
    C_s = Cs(WL_range)
    I_dif_h = EdifhWL(I_dif_R, I_dif_a, I_dif_g, C_s)
    I_dif_c_g = EdifcgWL(I_dir, I_dif_h, Ang_zth, rho_g, Ang_slp)
    I_dif_c_sc = EdifcscWL(I_dif_h, I_dir, ETR, r_vec, cos_AOI_sys, Ang_zth)
    I_dif_c_ssi = EdifcssiWL(I_dif_h, I_dir, ETR, r_vec, Ang_slp)
    I_dif_srf = EdifslpWL(I_dif_c_g, I_dif_c_sc, I_dif_c_ssi)
    I_dir_srf = EdirslpWL(I_dir, cos_AOI_sys)
    ETR_rv_srf = EetrrvslpWL(ETR, r_vec, cos_AOI_sys)
    I_tot_srf = Etotslp(I_dir_srf, I_dif_srf)
    ModIrr = Etot(I_dir, ETR, I_dif_srf, ETR_rv_srf, I_tot_srf, I_dir_srf)

    return ModIrr

def SunPos(year = year,     month = month,  day = day,      hour = hour,
        mins = mins,    secs = secs,    consider_bst = consider_bst,

        Ang_slope_sys = Ang_slope_sys,  Ang_tilt_sys = Ang_tilt_sys,
        tracking = tracking,

        lat = lat,      long = long,    elevation =  0):
```

```
    """
    Inputs:
    consider_bst : Activates the option to recognise the dates within British
    Summer Time and make the arithmetic correction of -60 minutes.
    Ang_slope_sys : Angle of inclination of PV system's plane subtended to
        ground surface, in degrees.
    Ang_tilt_sys : Angle of inclination of the projection of the normal of
        the plane of the system on PV system's plane of the surface
        subtended to the north axis. Known as well as azimuth angle
        (180 south, 0 north, 90 east, 270 west).
    tracking : Activates the calculation as if the PV system has a tracking
        base.
    lat : Geographical latitude of PV system, in degrees.
    long : Geographical longitude of PV system, in degrees.

    Output:
    AM : Air mass
    AM_pr : Pressured corrected air mass
    r_vec : Vector correction of the Earth-Sun distance
    Ang_slp : Slope angle of the system, considered the option of tracking
    Ang_zth :  Zenith angle of the sun, called altitude as well
    cos_AOI_sys: Cosine of the angle of incidence of the system
    """

    date_time = Datetime(year, month, day, hour, mins, secs)
    bst = BST(date_time, consider_bst)
    datetime_corr = date_time if not bst else date_time - \
                                        timedelta(hours = 1)

    Ang_dy = AngDay(datetime_corr)
    Eq_T = EquationOfTime(GetDayOfYear(datetime_corr))
    Ang_hr = -GetHourAngle(datetime_corr, long)
    Ang_dcl = GetDeclination(GetDayOfYear(datetime_corr))
    Ang_zth = 90 - GetAltitude(lat, long, datetime_corr)
    AM = GeoAM(Ang_zth)
    AM_pr = AMp(AM, pr)
    r_vec = Crv(Ang_dy)
    az = GetAzimuth(lat, long, datetime_corr)
    Ang_sol_az = az if az > -180 else az + 360
    Ang_slp  = AngSlope(Ang_slope_sys, Ang_zth, tracking)
    Ang_tilt_sys = AngTilt(Ang_sol_az, Ang_tilt_sys, tracking)
```

```
    """
    Incidence angle calculation based on Pysolar
    """
    jd = julian.GetJulianDay(datetime_corr)
    jde = julian.GetJulianEphemerisDay(jd, 65)
    jce = julian.GetJulianEphemerisCentury(jde)
    jme = julian.GetJulianEphemerisMillenium(jce)
    geocentric_longitude = GetGeocentricLongitude(jme)
    nutation = GetNutation(jde)
    radius_vector = GetRadiusVector(jme)
    aberration_correction = GetAberrationCorrection(radius_vector)
    apparent_sun_longitude = GetApparentSunLongitude(geocentric_longitude,
                                nutation, aberration_correction)
    true_ecliptic_obliquity = GetTrueEclipticObliquity(jme, nutation)
    geocentric_latitude = GetGeocentricLatitude(jme)
    geocentric_sun_declination = GetGeocentricSunDeclination(
                apparent_sun_longitude, true_ecliptic_obliquity,
                                        geocentric_latitude)
    latitude_deg = latitude = lat
    projected_axial_distance = GetProjectedAxialDistance(elevation,
latitude_deg)
    equatorial_horizontal_parallax = GetEquatorialHorizontalParallax(
                                            radius_vector)
    projected_radial_distance = GetProjectedRadialDistance(elevation,
                                            latitude_deg)
    equatorial_horizontal_parallax = GetEquatorialHorizontalParallax(
                                            radius_vector)
    apparent_sidereal_time = GetApparentSiderealTime(jd, jme, nutation)
    longitude_deg = long
    geocentric_sun_right_ascension = GetGeocentricSunRightAscension(
                    apparent_sun_longitude, true_ecliptic_obliquity,
                                        geocentric_latitude)
    local_hour_angle = GetLocalHourAngle(apparent_sidereal_time,
                    longitude_deg, geocentric_sun_right_ascension)
    parallax_sun_right_ascension = GetParallaxSunRightAscension(
            projected_radial_distance, equatorial_horizontal_parallax,
                        local_hour_angle, geocentric_sun_declination)
    topocentric_sun_declination = GetTopocentricSunDeclination(
                geocentric_sun_declination, projected_axial_distance,
                equatorial_horizontal_parallax,
                    parallax_sun_right_ascension, local_hour_angle)
    topocentric_local_hour_angle = GetTopocentricLocalHourAngle(
                    local_hour_angle, parallax_sun_right_ascension)
```

```
    pressure_millibars = pr
    temperature_celsius = t
    topocentric_zenith_angle = GetTopocentricZenithAngle(latitude,
                            topocentric_sun_declination,
                                topocentric_local_hour_angle,
                                        pressure_millibars,
                                        temperature_celsius)
    slope = Ang_slope_sys
    # This seems to be necesary to adapt to spctral method
    slope_orientation = Ang_tilt_sys
    topocentric_azimuth_angle = GetTopocentricAzimuthAngle(
        topocentric_local_hour_angle, latitude, topocentric_sun_declination)
    cos_AOI_sys = cos(rad(GetIncidenceAngle(topocentric_zenith_angle,
                                slope, slope_orientation,
                                    topocentric_azimuth_angle)))

    return Eq_T, Ang_hr, Ang_dcl, AM, AM_pr, r_vec, Ang_sol_az, Ang_slp, \
                                        Ang_zth, cos_AOI_sys

def Datetime(year, month, day, hour, mins, secs):

    dt = [year, month, day, hour, mins, secs]
    dt = list(map(int, dt))

    return pd.datetime(*dt)


def BST(date_time, bst):

    if bst:

        # British Summer Time Limited up to year 2021.
        BST_lim = [[[2014, 3, 30, 1], [2014, 10, 26, 2]],
            [[2015, 3, 29, 1], [2015, 10, 25, 2]],
            [[2016, 3, 27, 1], [2016, 10, 30, 2]],
            [[2017, 3, 26, 1], [2017, 10, 29, 2]],
            [[2018, 3, 25, 1], [2018, 10, 28, 2]],
            [[2019, 3, 31, 1], [2019, 10, 27, 2]],
            [[2020, 3, 29, 1], [2020, 10, 25, 2]],
            [[2021, 3, 28, 1], [2021, 10, 31, 2]]]

        #for i in range(len(BST_lim[0])):
        for dt in BST_lim:
```

```
            if pd.datetime(*dt[0]) < date_time < pd.datetime(*dt[1]):
                bst = True
                break
            else:
                bst = False

    return bst

def AngDay(date_time):

    '''
    Number of the day, some sources call it julian number day
    From J.A. Duffie and W.A. Beckman [8].
    Yield result in radians but converted to degrees at
    the end of the function.
    '''
    d = pd.Series(date_time).dt.dayofyear[0] # to get the day of year
    year = date_time.year

    # Formula to identify leap years
    year_days = 366 if ((year % 4 == 0 and year % 100 != 0) or
                    (year % 400 == 0 and year % 100 != 0)) else 365

    Ang_dy  = 2 * pi * ((d - 1) / year_days)

    return deg(Ang_dy)

def EoT(Ang_dy):

    '''
    Equation of Time in minutes =
                True Solar time - Local Standard time - Long correction.
    From: J.W. Spencer [3].
    Yields the result in MINUTES, according to J.A. Duffie and
    W.A. Beckman [8].
    Multiplier 229.18 converts the result to minutes, without this
    the equation would yield in radians (4 minutes = 1 degree).
    '''
    Eq_T = (0.0000075 + 0.001868 * cos(rad(Ang_dy)) - 0.032077 \
        * sin(rad(Ang_dy)) - 0.014615 * cos(2 * rad(Ang_dy)) - 0.040849 \
                            * sin(2 * rad(Ang_dy))) * (229.18)

    return Eq_T
```

```
def AngHour(hour, mins, secs, Eq_T, long, bst):

    '''
    From Solar engineering of thermal processes, J.A. Duffie and
    W.A. Beckman (2013) [8].
    Solar time - standard time = (Long_ST - Long) * 4 + Eq_T
    Ang_hr = (15 * Solar time) - 180
    4 min = 1 deg, 1 hour = 15 deg
    Yields the results in degrees.
    '''

    if bst:
        mins = mins - 60

    Ang_hr = (15 * ((hour + (mins / 60) + (secs / (60 * 60))) \
                + ((floor(long) - long) * 4) / 60 + Eq_T / 60)) - 180

    return Ang_hr

def AngDcl(Ang_dy):

    '''
    Declination angle (degrees), above or below ecliptic [3].
    Yields result in DEGREES
    '''
    Ang_dcl = ((0.006918 - 0.399912 * cos(rad(Ang_dy)) + 0.070257 \
        * sin(rad(Ang_dy)) - 0.006758 * cos(2 * rad(Ang_dy)) + 0.000907 \
            * sin(2 * rad(Ang_dy)) - 0.002697 * cos(3 * rad(Ang_dy)) \
                    + 0.00148 * sin(3 * rad(Ang_dy))) * (180 / pi))

    return Ang_dcl

def AngZth(Ang_dcl, lat, Ang_hr):

    '''
    Angle of Solar Zenith, it is the complement of Solar elevation
    (or altitude angle, e), From D L Hartman, 1994.
    Z= 90 - e, cos(Z)=cos(d)cos(L)cos(H)+sin(d)sin(L)
    (*this last one should be L),
    e= solar elevation, L= Latitude, d= Declination, H= hour angle
    For solar altitude the arcsin would be required in stead of arccosine.
    Yields result in RADIANS converted to degrees.
```

```
    '''

    Ang_zth = (acos(cos(rad(Ang_dcl)) * cos(rad(lat)) * cos(rad(Ang_hr))
                            + sin(rad(Ang_dcl)) * sin(rad(lat))))

    return deg(Ang_zth)

def GeoAM(Ang_zth):

    '''
    Geometrical Air Mass (path length), called "M" in Bird's paper [1].
    Eq. 2-5, pg 4
    '''
    if Ang_zth > 91.013177 :
        AM = np.inf
    else:
        AM = ((cos(rad(Ang_zth))) + 0.15 * (93.885 - Ang_zth) ** (-1.253))\
                                                    ** -1
    if type(AM) is complex : AM = np.inf

    return AM

def AMp(AM, pr):

    '''
    Pressure corrected Air Mass. AM_pr being = AM * P / P0. Seen in
    Bird's paper [1]. Eq. 2-5
    P0 = 1013 millibars
    '''
    AM_pr = AM * (pr/1013)

    return AM_pr

def O3AM(O3_h, Ang_zth):

    '''
    Effective O3 Air mass, h_o = 22 Km which is the height of maximum ozone
    concentration [1], Eq 2-10 pg 5.
    '''
    O3_m = ((1 + O3_h / 6370) / (cos(rad(Ang_zth)) ** 2 + 2 * (O3_h / 6370))
                                                ** 0.5)

    return O3_m
```

```
def Crv(Ang_dy):

    '''
    Radius vector correction for Earth-Sun distance, called "D" in
    Bird's paper [1]. Eq 2-2 pg 2, also appears in M. Jacobson [9].
    It is the calculation (1 / r ** 2) allows the correction of the solar
    constant to be applied in the given date.
    Yields the result in Astronomical Units (AU),
    AU = 149,597,870,700 m (the mean distance from the sun to earth).
    '''
    r_vec = (1.00011 + 0.034221 * cos(rad(Ang_dy)) + 0.00128
            * sin(rad(Ang_dy)) + 0.000719 * cos(2 * rad(Ang_dy))
                               + 0.000077 * sin(2 * rad(Ang_dy)))

    return r_vec

def AngSolAz(Ang_dcl, Ang_hr, Ang_zth, lat):

    '''
    Approximate Solar Azimuth angle (0=N, 90=E, 180=S, 270=W) computed
    from 180 + HA
    From Solar engineering of thermal processes, J.A. Duffie and
    W.A. Beckman [8].
    Yield result in radians to be converted at the end into degrees.
    '''
    Ang_sol_az = (np.sign(Ang_hr) * abs(acos((cos(rad(Ang_zth))
            * sin(rad(lat)) - sin(rad(Ang_dcl))) / (sin(rad(Ang_zth))
                                        * cos(rad(lat))))))

    return deg(Ang_sol_az)

def AngSlope(Ang_slope_sys, Ang_zth, tracking):

    '''
    This part calculates the slope angle of the system. If 'tracking' is True
    it is considered that the slope and tilt of the system are always facing
    directly to the sun, therefore the slope angle is equal to the angle
    of solar zenith and tilt equals to solar azimuth.
    '''
    if tracking:
        Ang_slope_sys = Ang_zth
```

```
    return Ang_slope_sys

def AngTilt(Ang_sol_az, Ang_tilt_sys, tracking):

    '''
    This part intent to calculate the angle of surface azimuth in degrees.
    If tracking == True it is considered to be in a tracking module
    the azimuth of the system is always facing directly to the sun.
    Also translate the value of south from 180 deg to 0 deg, with negative
    values for east facing angles.
    '''
    if tracking:
        Ang_tilt_sys = Ang_sol_az
    else:
        Ang_tilt_sys = (Ang_tilt_sys - 180)

    return Ang_tilt_sys

def CosAOI(Ang_hr, Ang_dcl, lat, Ang_tilt_sys, Ang_slope_sys = 0):

    '''
    This function to limits the ETR on tilt to the time range of ETR on
    horizontal. Cosine of incidence angle based on Ang_slope_sys of surface and
    solar geometry.
    From: J. A. Duffie and W. A. Beckman [8] and A. McEvoy, T. Markvart
    and L. Castaner [7] formulas in p. 626 and p.624: 13, 9, 10 and 12.
    '''
    cos_AOI = (sin(rad(Ang_dcl)) * sin(rad(lat)) * cos(rad(Ang_slope_sys))
            - sin(rad(Ang_dcl)) * cos(rad(lat)) * sin(rad(Ang_slope_sys))
            * cos(rad(Ang_tilt_sys)) + cos(rad(Ang_dcl)) * cos(rad(lat))
            * cos(rad(Ang_slope_sys)) *cos(rad(Ang_hr)) + cos(rad(Ang_dcl))
            * sin(rad(lat)) * sin(rad(Ang_slope_sys)) * cos(rad(Ang_tilt_sys))
            * cos(rad(Ang_hr)) + cos(rad(Ang_dcl)) * sin(rad(Ang_slope_sys))
                        * sin(rad(Ang_tilt_sys)) * sin(rad(Ang_hr)))

    return cos_AOI

def CosAOI_srf(Ang_hr, Ang_dcl, lat, Ang_tilt_sys, tracking, Ang_slope_sys):

    '''
    Cosine of incidence angle based on Ang_slope_sys of surface and solar
    geometry.
    From: Solar engineering of thermal processes, J.A. Duffie and W.A.
```

```
    Beckman [8].
    '''
    if CosAOI(Ang_hr, Ang_dcl, lat, Ang_tilt_sys) <= 0:
        cos_AOI_sys = 0
    else:
        if not tracking:
            cos_AOI_sys = CosAOI(Ang_hr, Ang_dcl, lat, Ang_tilt_sys,
                                                    Ang_slope_sys)
        else:
            cos_AOI_sys = 1

    return cos_AOI_sys

def Alog(asym):

    alog = log(1 - asym)

    return alog

def AFs(alog):

    aF_s = alog * (1.459 + alog * (0.1595 + alog * 0.4129))

    return aF_s

def BFs(alog):

    bF_s = alog * (0.0783 + alog * (-0.3824 - alog * 0.5874))

    return bF_s

def Fs(aF_s, bF_s, Ang_zth):

    '''
    Fraction of the forward aerosol scatter ratio dependant on the solar
    zenith angle. [1] Eq: 3-11, pg 7.
    '''
    F_s = 1 - 0.5 * exp((aF_s + bF_s * cos(rad(Ang_zth))) *
                                        cos(rad(Ang_zth)))

    return F_s

def Fsp(aF_s, bF_s):
```

```
    '''
    Prime fraction of the downward aerosol scattering ratio dependant on the
    solar zenith angle,  (evaluated at Air Mass = 1.8). [1] Eq: 3-15, pg 7.
    '''
    F_s_p = 1 - 0.5 * exp((aF_s + bF_s / 1.8) / 1.8)

    return F_s_p

def EetrAbs(ETR = 'ETR_Gueymard2003_ndelta.csv',
            A_H2O = 'A_H2O_Bird&Riordan1983_ndelta.csv',
                A_O3 = 'A_O3_Bird&Riordan1983_ndelta.csv',
                    A_UG = 'A_UG_Bird&Riordan1983_ndelta.csv'):

    '''
    Calling the values of Extraterrestrial Irradiation and Absorption of
    Water, Ozone and Mixed Gases. Each in separate files, these are arrays
    with the absorption and values, obtained from the tables in Bird and
    Riordan [1]
    This is an attempt to do the simulation more in more resolution, using the
    ETR from Gueymard, 1985 [10].
    '''
    try:
        # In case of being run as code in console.
        path = os.path.dirname(os.path.abspath(__file__))

    except Exception:
        # In case of being called as a module.
        path = os.path.dirname(os.path.abspath('__file__'))

    dfs = []
    for file in [ETR, A_H2O, A_O3, A_UG]:
        df = pd.read_csv(r'{}\{}'.format(path, file), index_col = 0,
                                              header = 0)
        dfs += [df.iloc[:, 0]]

    WL_range = pd.Series(index = np.geomspace(0.3, 4.0, 2500))

    for i in dfs:
        i.index = WL_range.index

    ETR, A_H2O, A_O3, A_UG = dfs
```

```
    return ETR, A_H2O, A_O3, A_UG, WL_range

def OmegaWl(WL_range, omega, omega_p):

    # Aerosol single scattering albedo as a function of wavelength [1].
    # Eq. 3-16 pg 7.
    omega_wl = omega * np.exp(-omega_p * (np.power(np.log(WL_range.index
                                          / 0.4), 2)))
    omega_wl = pd.Series(omega_wl, index = WL_range.index, name = 'omega_wl')

    return omega_wl

def Tr(WL_range, AM_pr):

    # Rayliegh Transmission as function of wavelength, From: F. X.
    # Kneizys [5]. Eq. 2-4, pg 2.
    T_R = (np.exp(-AM_pr / (np.power(WL_range.index , 4) * (115.6406 - 1.335
                                / np.power(WL_range.index, 2)))))
    T_R = pd.Series(T_R, index = WL_range.index, name = 'T_R')

    return T_R

def To3(WL_range, A_O3, O3_m, O3):

    # Ozone Transmission as function of wavelength.  From: B. Leckner [4].
    # Eq. 2-9, pg 5.
    T_O3 = np.exp(-A_O3 * O3_m * O3)
    T_O3 = pd.Series(T_O3, name = 'T_O3')

    return T_O3

def Tug(WL_range, A_UG, AM_pr):

    # Uniform Mixed Gases Transmission as function of wavelength.
    # From: B. Leckner [4]. Eq. 2-11, pg 5.
    T_UG = (np.exp(-1.41 * A_UG * AM_pr / (np.power((1 + 118.93 * A_UG *
                                          AM_pr), 0.45))))
    T_UG = pd.Series(T_UG, name = 'T_UG')

    return T_UG

def Th2o(WL_range, A_H2O, H2O, AM):
```

```
    # Water Vapor Transmission as function of wavelength.
    # From: B. Leckner [4]. Eq. 2-8, pg 4.
    T_H2O = (np.exp(-0.2385 * A_H2O * H2O * AM / (np.power((1 + 20.07 *
                                    A_H2O * H2O * AM), 0.45))))
    T_H2O = pd.Series(T_H2O, name = 'T_H2O')

    return T_H2O

def Tau(WL_range, AOD, alpha):

    # Aerosol turbidity (tau) in function of wavelength [1]. Eq. 2-7 pag 4.
    tau = AOD * (np.power((WL_range.index / 0.5), -alpha))
    tau = pd.Series(tau, index = WL_range.index, name = 'tau')

    return tau

def Ta(WL_range, tau, AM):

    # Transmittance for Aerosol as function of wavelength.
    # From A. Angstrom [6]. Eq. 2-6, pg 4.
    T_a = np.exp(-tau * AM)
    T_a = pd.Series(T_a, index = WL_range.index, name = 'T_a')

    return T_a

def Tas(omega_wl, tau, AM):

    # Transmittance for aerosol scattering [1]. Eq. 3-9, p. 7.
    T_as = pd.concat([omega_wl, tau], axis = 1).interpolate(
                                        method = 'linear')
    T_as['T_as'] = np.exp(-T_as.omega_wl * T_as.tau * AM)
    T_as = T_as.iloc[:, -1]

    return T_as

def Taa(omega_wl, tau, AM):

    # Transmittance for aerosol absorption [1]. Eq. 3-10, pg 7.
    T_aA = pd.concat([omega_wl, tau], axis = 1).interpolate(
                                        method = 'linear')
    T_aA['T_aA'] = np.exp(-(1 - T_aA.omega_wl) * T_aA.tau * AM)
    T_aA = T_aA.iloc[:, -1]
```

```
    return T_aA

def Edifr(ETR, T_O3, T_H2O, T_UG, T_aA, T_R, r_vec, Ang_zth):

    '''
    Rayleigh scattering component for diffuse irradiation,
    from Bird [1]. Eq. 3-5 pag 7.
    '''
    I_dif_R = pd.concat([ETR, T_O3, T_H2O, T_UG, T_aA, T_R], axis = 1
                                ).interpolate(method = 'linear')

    I_dif_R['I_dif_R'] = (I_dif_R.ETR * r_vec * cos(rad(Ang_zth))
                    * I_dif_R.T_O3 * I_dif_R.T_H2O * I_dif_R.T_UG
                    * I_dif_R.T_aA * (np.power((1 - I_dif_R.T_R),
                                            0.95) * 0.5))
    I_dif_R = I_dif_R.iloc[:, -1]

    return I_dif_R

def Edifr2(ETR, T_O3, T_H2O, T_UG, T_aA, T_R, r_vec, Ang_zth):

    '''
    Rayleigh scattering component for diffuse irradiation.
    From Bird [1]. Eq. 3-5 pag 7.
    '''
    I_dif_R = pd.DataFrame((ETR.values * r_vec * cos(rad(Ang_zth)) * T_O3.values
             * T_H2O.values * T_UG .values * T_aA.values * (np.power(
             (1 - T_R.values), 0.95) * 0.5)), index = ETR.index,
             columns = ['I_dif_R'])

        return I_dif_R

def Edifa(ETR, T_O3, T_H2O, T_UG, T_aA, T_R, T_as, Ang_zth, F_s, r_vec):

    # Aerosol scattering component for diffuse irradiation, from Bird [1].
    # Eq. 3-6 pag 7.
    I_dif_a = pd.concat([ETR, T_O3, T_H2O, T_UG, T_aA, T_R, T_as], axis = 1
                           ). interpolate(method = 'linear')
    I_dif_a['I_dif_a'] = (I_dif_a.ETR * cos(rad(Ang_zth)) * I_dif_a.T_O3
                    * I_dif_a.T_H2O * I_dif_a.T_UG * I_dif_a.T_aA
                               * (np.power(I_dif_a.T_R, 1.5))
                           * (1 - I_dif_a.T_as) * F_s * r_vec)
    I_dif_a = I_dif_a.iloc[:, -1]
```

```
    return I_dif_a

def Trp(WL_range):

    '''
    Atmospheric transmittance after Rayleigh scattering, from Bird [1].
    Eq. 2-4 pag 2.
    '''
    T_R_p = (np.exp(-1.8 / (np.power(WL_range.index, 4) * (115.6406 - 1.335
                                / np.power(WL_range.index, 2)))))
    T_R_p = pd.Series(T_R_p, index = WL_range.index, name = 'T_R_p')

    return T_R_p

def Th2op(A_H2O, WL_range, H2O):

    '''
    Water vapour transmittance, from Bird [1]. Eq. 2-8 pag 4
    (It's different equation due to the terms evaluated at AM = 1.8)
    '''
    T_H2O_p = (np.exp(-0.2385 * A_H2O * H2O * 1.8 / (np.power((1 + 20.07 *
                                    A_H2O * H2O * 1.8), 0.45))))
    T_H2O_p = pd.Series(T_H2O_p, index = WL_range.index, name = 'T_H2O_p')

    return T_H2O_p

def Tugp(A_UG, WL_range):

    '''
    Uniformly mixed gas transmittance, from Bird [1]. Eq. 2-11 pag 5
    (It's a different equation due to the terms evaluated at AM = 1.8)
    paper indicates a value of 118.93 but remarks that the value
    from Leckner [4] 118.3.
    '''
    T_UG_p = (np.exp(-1.41 * A_UG * 1.8 / (np.power((1 + 118.3 * A_UG * 1.8),
                                                0.45))))
    T_UG_p = pd.Series(T_UG_p, index = WL_range.index, name = 'T_UG_p')

    return T_UG_p

def TaspTaap(omega_wl, tau):
```

```
    # Tasp (Prime transmittance terms evaluated at AM = 1.8).
    T_as_p = np.exp(-omega_wl * tau * 1.8)
    T_as_p = pd.Series(T_as_p, name = 'T_as_p')

    # Taap (Prime transmittance terms evaluated at AM = 1.8).
    T_aA_p = np.exp(-(1 - omega_wl) * tau * 1.8)
    T_aA_p = pd.Series(T_aA_p, name = 'T_aA_p')

    return T_as_p, T_aA_p

def Rhos(T_UG_p, T_H2O_p, T_aA_p, T_R_p, T_as_p, F_s_p):

    # Sky reflectivity (rho_g = ground albedo in function of wavelength), [1]
    # Eq. 3-8, pg 7.
    rho_s = pd.concat([T_UG_p, T_H2O_p, T_aA_p, T_R_p, T_as_p], axis = 1
                              ).interpolate(method = 'linear')
    rho_s['rho_s'] = (rho_s.T_UG_p * rho_s.T_H2O_p * rho_s.T_aA_p * (0.5 *
        (1 - rho_s.T_R_p) + (1 - F_s_p) * rho_s.T_R_p * (1 - rho_s.T_as_p)))
    rho_s = rho_s.iloc[:, -1]

    return rho_s

def Edir(ETR, T_R, T_O3, T_UG, T_H2O, T_a, r_vec):

    # Direct solar irradiance.
    I_dir = pd.concat([ETR, T_R, T_O3, T_UG, T_H2O, T_a], axis = 1
                              ).interpolate(method = 'linear')
    I_dir['I_dir'] = (I_dir.ETR * r_vec * I_dir.T_R * I_dir.T_O3
                           * I_dir.T_UG * I_dir.T_H2O * I_dir.T_a)
    I_dir = I_dir.iloc[: , -1]

    return I_dir

def Edifg(I_dir, I_dif_R, I_dif_a, rho_s, rho_g, Ang_zth):

    # Diffuse solar irradiance fraction from the ground reflection,
    # from Bird [1]. Eq. 3-7, pag 7.
    I_dif_g = pd.concat([I_dir, I_dif_R, I_dif_a, rho_s], axis = 1
                              ).interpolate(method = 'linear')
    I_dif_g['I_dif_g'] = ((I_dif_g.I_dir * cos(rad(Ang_zth))
                           + I_dif_g.I_dif_R + I_dif_g.I_dif_a)
                                 * I_dif_g.rho_s * rho_g
                              / (1 - I_dif_g.rho_s * rho_g))
```

```
    I_dif_g = I_dif_g.iloc[:, -1]

    return I_dif_g

def Cs(WL_range):

    # Correction factor [1]. Eq. 3-17 p. 7.
    C_s = pd.DataFrame(WL_range)
    C_s['wl'] = C_s.index
    C_s['C_s'] = np.power((C_s.loc[C_s.index <= 0.45, 'wl'] + 0.55), 1.8)
    C_s['C_s'].fillna(value = 1)

    C_s = C_s.iloc[:, -1]

    return C_s

def EdifhWL(I_dif_R, I_dif_a, I_dif_g, C_s):

    '''
    Diffuse Irradiance in horizontal surface, UV correction factor
    for > 0.45 is (wavelength + 0.55) ^ 1.8 for <= is 1.
    This factor is called C_s in the paper.
    '''
    I_dif_h = pd.concat([I_dif_R, I_dif_a, I_dif_g, C_s], axis = 1
                                ).interpolate(method = 'linear')
    I_dif_h['I_dif_h'] = ((I_dif_h.I_dif_R + I_dif_h.I_dif_a
                                + I_dif_h.I_dif_g) * I_dif_h.C_s)
    I_dif_h = I_dif_h.iloc[:, -1]

    return I_dif_h

def EdifcgWL(I_dir, I_dif_h, Ang_zth, rho_g, Ang_slp):

    # Ground reflected isotropic component on tilted surface.
    I_dif_c_g = pd.concat([I_dir, I_dif_h,], axis = 1
                                ).interpolate(method = 'linear')
    I_dif_c_g['I_dif_c_g'] = ((I_dif_c_g.I_dir * cos(rad(Ang_zth))
        + I_dif_c_g.I_dif_h) * rho_g * (1 -     cos(rad(Ang_slp))) / 2)
    I_dif_c_g = I_dif_c_g.iloc[:, -1]

    return I_dif_c_g

def EdifcscWL(I_dif_h, I_dir, ETR, r_vec, cos_AOI_sys, Ang_zth):
```

```
    # Solar Circumsolar component on tilted surface.
    I_dif_c_sc = pd.concat([I_dif_h, I_dir, ETR], axis = 1).interpolate(
                                        method = 'linear')
    I_dif_c_sc['I_dif_c_sc'] = (I_dif_c_sc.I_dif_h * (I_dif_c_sc.I_dir
           / I_dif_c_sc.ETR * r_vec) * cos_AOI_sys / cos(rad(Ang_zth)))
    I_dif_c_sc = I_dif_c_sc.iloc[:, -1]

    return I_dif_c_sc

def EdifcssiWL(I_dif_h, I_dir, ETR, r_vec, Ang_slp):

    # Solar Sky Isotropic component on tilted surface.
    I_dif_c_ssi = pd.concat([I_dif_h, I_dir, ETR], axis = 1).interpolate(
                                        method = 'linear')
    I_dif_c_ssi['I_dif_c_ssi']= ((I_dif_c_ssi.I_dif_h * (1 - (
                I_dif_c_ssi.I_dir / I_dif_c_ssi.ETR * r_vec))
                                * (1 + cos(rad(Ang_slp)))) / 2)
    I_dif_c_ssi = I_dif_c_ssi.iloc[:, -1]

    return I_dif_c_ssi

def EdifslpWL(I_dif_c_g, I_dif_c_sc, I_dif_c_ssi):

    # Diffuse irradiation on tilted surface.
    I_dif_srf = pd.concat([I_dif_c_g, I_dif_c_sc, I_dif_c_ssi],
                axis = 1, join = 'outer').interpolate(method = 'linear')
    I_dif_srf['I_dif'] = (I_dif_srf.I_dif_c_g + I_dif_srf.I_dif_c_sc
                                    + I_dif_srf.I_dif_c_ssi)
    # Dismisses all non-positive values.
    I_dif_srf['I_dif_srf'] = I_dif_srf.loc[I_dif_srf['I_dif'] >= 0, 'I_dif']
    I_dif_srf['I_dif_srf'] = I_dif_srf['I_dif_srf'].fillna(value = 0)
    I_dif_srf = I_dif_srf.iloc[:, -1]

    return I_dif_srf

def EdirslpWL(I_dir, cos_AOI_sys):

    if cos_AOI_sys < 0: cos_AOI_sys = 0
    I_dir_srf = I_dir * cos_AOI_sys
    I_dir_srf.name = 'I_dir_srf'

    return I_dir_srf
```

```
def EetrrvslpWL(ETR, r_vec, cos_AOI_sys):

    if cos_AOI_sys < 0: cos_AOI_sys = 0
    ETR_rv_srf = ETR * r_vec * cos_AOI_sys
    ETR_rv_srf.name = 'ETR_rv_srf'

    return ETR_rv_srf

def Etotslp(I_dir_srf, I_dif_srf):

    I_tot_srf = pd.concat([I_dir_srf, I_dif_srf], axis = 1, join = 'outer'
                                ).interpolate(method = 'linear')
    I_tot_srf['I_tot_srf'] = (I_tot_srf.I_dir_srf + I_tot_srf.I_dif_srf)
    I_tot_srf = I_tot_srf.iloc[:, -1]

    return I_tot_srf

def Etot(I_dir, ETR, I_dif_srf, ETR_rv_srf, I_tot_srf, I_dir_srf):

    # Concatenation of irradiance spectra.
    ModIrr = pd.concat([ETR, ETR_rv_srf, I_dir, I_dir_srf, I_dif_srf,
                            I_tot_srf], axis = 1, join = 'outer'
                                ).interpolate(method = 'linear')
    ModIrr.index = ModIrr.index * 1000 # Converts from W/m2/um to W/m2/nm.
    ModIrr.index.names = ['nm']
    ModIrr = ModIrr / 1000

    return ModIrr
```

7.2 Appendix B: Published paper.

REVIEW OF SCIENTIFIC INSTRUMENTS **88**, 095003 (2017)

Geometric optimisation of an accurate cosine correcting optic fibre coupler for solar spectral measurement

Roberto Cahuantzi and Alastair Buckley
Department of Physics and Astronomy, University of Sheffield, Sheffield, United Kingdom

(Received 28 March 2017; accepted 1 September 2017; published online 20 September 2017)

Making accurate and reliable measurements of solar irradiance is important for understanding performance in the photovoltaic energy sector. In this paper, we present design details and performance of a number of fibre optic couplers for use in irradiance measurement systems employing remote light sensors applicable for either spectrally resolved or broadband measurement. The angular and spectral characteristics of different coupler designs are characterised and compared with existing state-of-the-art commercial technology. The new coupler designs are fabricated from polytetrafluorethylene (PTFE) rods and operate through forward scattering of incident sunlight on the front surfaces of the structure into an optic fibre located in a cavity to the rear of the structure. The PTFE couplers exhibit up to 4.8% variation in scattered transmission intensity between 425 nm and 700 nm and show minimal specular reflection, making the designs accurate and reliable over the visible region. Through careful geometric optimization near perfect cosine dependence on the angular response of the coupler can be achieved. The PTFE designs represent a significant improvement over the state of the art with less than 0.01% error compared with ideal cosine response for angles of incidence up to 50°. *Published by AIP Publishing.* https://doi.org/10.1063/1.5003040

I. INTRODUCTION

Critical to the ongoing implementation of Photovoltaic (PV) technologies is a necessity to accurately measure solar irradiance. Such measurements are typically made using a broadband pyranometer with thermopile sensors. However, these tools are expensive, and finding lower cost measurement solutions is important to help reduce the overall costs of solar energy. Besides the cost constraints of pyranometers, there is also little information that they can provide about the solar spectrum. A common solution for spectroscopic measurements is to couple the light with a spectrometer via an optic fibre (OF). This configuration is convenient because there can be a controlled environment for the spectrometer, where it is protected from outdoor influences such as humidity and heat as well as optic fibres offering reliable optical coupling. However, the OF is only able to capture light within a field view angle of typically 25°. By employing a scattering surface in front of the fibre, the limited angular acceptance can be increased (Fig. 1).

This correction is referred to as cosine correction because the ideal angular sensitivity should be proportional to the cosine of the incidence angle. The obstacles preventing the use of existing commercial cosine correctors in field irradiance measurements are their limited performance, both in terms of accurate reproduction of the cosine response and their physical fragility. Our motivation is to overcome these obstacles and design a robust, accurate coupler that can be used for extended periods in the field.

A typical state-of-the-art (SoA) cosine corrector available in the market is constructed from a hollow opaque metallic tube in which a 150 μm thick disc made of polytetrafluorethylene (PTFE) inserted at one end of the tube and clamped about 200 μm from the end, while at the other end there is a female 1/4 in. screw-type coupling mechanism to allow the standard optic fibre SubMiniature version A (SMA) adapter to be screwed into the coupler.

We find that the design is not suitable for extended field use as the thin PTFE disc becomes distorted by a combination of rain and wind. In an ideal case, the incident light received on the thin PTFE disc would be diffusely and isotropically scattered forwards towards the OF cable behind the disc. The cosine corrector would provide an accurate reproduction of a cosine response of a nude planar detector in cases where the scattering follows Lambert's law,[1] as seen in Eq. (1),

$$I_\theta = I_0 \cos\theta, \tag{1}$$

where I_θ is light intensity in angle θ, which is subtended between the light source and the normal of the reflective surface and I_0 stands for the input light intensity delivered on the reflective surface. Results relating to the SoA coupler are presented in Sec. II.

As well as the commercial state of the art, we also review the performance of research couplers from the literature as a performance benchmark. Bartlett *et al.*[2] detailed the performance of a spectral measurement system with six sensors arranged on a horizontal plane using cosine correctors. Each sensor had a bandpass of about 10 nm with center wavelengths of 411.4, 442.9, 489.9, 555.2, 683.8, and 699.5. The error was under 7% only for incidence angles under 70°. In the study of Blackburn and Vignola,[3] it was found that the cosine error was 45% for angles above 72° due to the self-shading generated by the geometry of the cosine correcting coupler.

In terms of understanding the influence of the solar spectrum on photovoltaic energy production, Cornaro and Andreotti[4] evaluated the influence of the solar spectrum upon amorphous-silicon PV cells, used spectroradiometers with an optical diffuser integrated and protected by a glass dome and reported a cosine error ≤5% for all wavelengths. This work

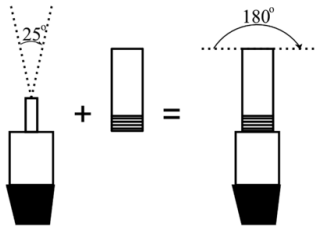

FIG. 1. Visualisation of the necessity for a cosine correcting coupler when attached to the optic fibre allows for a wider field view angle.

did not detail the diffuser's geometry, yet it is inferred that it was a simple flat PTFE surface as seen in most of devices available in the market. Pohl *et al.*[5] prepared multiple low-cost stations to measure, among others, solar irradiance for weather monitoring. For the irradiance measurement, a simple flat scattering PTFE surface was employed. Guerra, Faez, and Fuentealba[6] describe the manufacturing of a low cost pyranometer but did not address cosine correction. They used a PTFE layer of 1.05 mm of thickness for attenuation. Medugu, Burari, and Abdulazeez[7] and Martínez, Andújar, and Enrique[8] describe the design and test of different low-cost pyranometers. It is interesting to see a similar approach to ours, testing alternative geometries for the cosine correction of a photodiode-based pyranometer. The designs were the frustum of a cone with different angles. Bevel edges of 45° gave the best results. PTFE was used as a diffusing material due to its optimal optical characteristics referred to by Lowry, Mendlowitz, and Subramanian,[9] describing the near perfect diffusion of transmitted light for a wavelength range from the ultraviolet (UV) to near infrared (NIR).

In summary, PTFE is typically used as a diffusing material in cosine correctors—both for fibre optic coupling and for correction of planar sensors. The accuracy of the couplers reported in the literature varies from a respectable 5% to a rather poor 45% absolute error depending on the angle of incidence.

In the present work, we report the design and fabrication of several different fibre optic couplers using PTFE as a scattering material. We systematically characterise the designs in terms of spectral transmission, cosine response, and specular reflection. Our best performing design (G2) has a mean absolute error of less than 3% averaged over all angles of incidence and an excellent error of 0.01% for angles less than 50°.

II. EXPERIMENTS AND RESULTS

A. Assessment of PTFE empirical light attenuation

PTFE is widely used as a light scattering material within the optics industry with the transmission of low and high density materials being reported for UV, visible, and near infrared wavelengths.[10,11] For this research, high density PTFE, 2.5 g/ml, was chosen.[12] Of importance to the use of PTFE as a scattering material for an optic coupler in an irradiation instrument is the relative attenuation of different spectral components. The ideal scatterer would have equal attenuation so as not to contribute to systematic errors in the irradiance measurement during changes to spectral intensity. To assess the impact of differential attenuation in our PTFE coupler, we measured the empirical transmission of stock material of different thickness ranging from 1 to 10 mm. The empirical attenuation was calculated using Eq. (2),

$$T_\lambda = \frac{\varphi_{T,\lambda}}{\varphi_{0,\lambda}}, \tag{2}$$

where $\Phi_{0,\lambda}$ is light intensity by wavelength incident on the surface, $\Phi_{T,\lambda}$ stands for the transmitted light intensity by wavelength, and T_λ is the fraction of transmitted light at a given thickness. Results can be seen in Fig. 2.

This result shows that the attenuation of PTFE is spectrally void of features and shows approximately 20% of difference between 500 nm and 700 nm or 10% per 100 nm. Since the mean wavelength of sunlight changes less than 50 nm[13] between fully diffuse and fully scattered light, the inferred maximum error due to differential attenuation by wavelength is estimated to be less than 5%.

B. Cosine response of SoA coupler

As a benchmark for the assessment of the newly designed couplers, we initially characterised the cosine response of a commercial coupler. A goniometer was set up with a stabilised white LED aligned along the rotating arm and the coupler device under test aligned in the plane of the reference axis. The light source was moved on the circular path around the coupler under test. The angle of incidence was measured in degrees subtended between the normal of the coupler surface and the position of the light source, this angle was varied from 0° to 90° with an increment of 5°. For each step 15 independent readings were made. The measurements were taken using an Ocean Optics spectrometer. As the main purpose was to measure the change of intensity in the function of the angle of incidence, the units used in these readings were only raw spectrally integrated counts rather than a radiometrically calibrated value. The experimental layout can be seen in Fig. 3.

The light intensity was normalized to the value at 0°. For the SoA, it is seen that at 25°, a fractional error of 5% is reached and the error became higher with wider angles reaching 94% by 85°, as seen in Fig. 4.

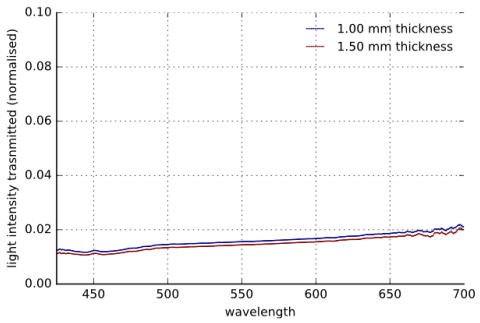

FIG. 2. PTFE's fraction of transmitted light through thicknesses of 1.0 mm and 1.5 mm of thickness.

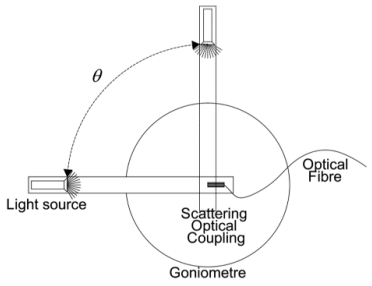

FIG. 3. Experimental setup for the assessment of the SoA cosine corrector and validation test for the couplers.

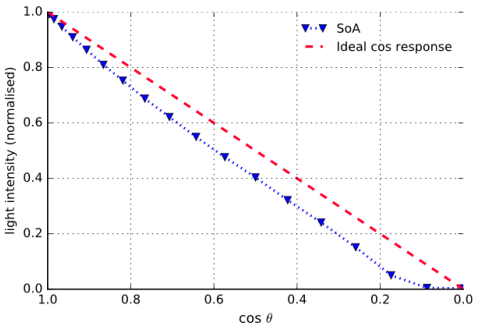

FIG. 4. Assessment of the cosine response for the State-of-Art (SoA) cosine corrector, compared with the ideal cosine response.

C. Design and characterisation method of CCOCs

The general geometry of the new designs was based on the SoA coupler, constructed as a hollow monolithic quasi-cylinder with a lateral wall of 1.2 mm thick. At one end, it is the diffusing surface and at the opposite end there is an opening with a female 1/4 in. SMA screw-type coupling mechanism for connection with the standard OF mounting. A comparison of the SoA and one of the experimental couplers can be seen in Fig. 5.

The monolithic shape was machined from a solid rod of PTFE to a diameter of 6.4 mm and from (20 to 20.55) mm high, depending on the design. All lateral sides of the coupler were covered with an opaque black tape to ensure that the only light received was from the scattering surface. There were 29 different designs fabricated and tested, but in this paper we only focus on the most relevant ones. The different geometries can be seen in Fig. 6.

FIG. 5. State-of-art cosine corrector (left) and experimental coupler design D1 (right).

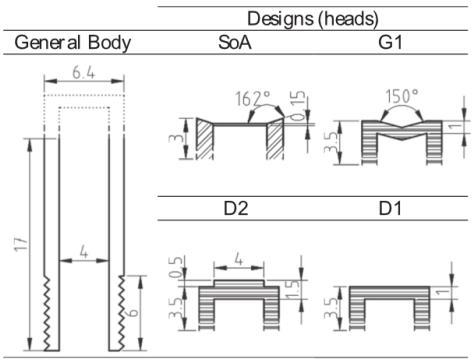

FIG. 6. SoA and coupler designs of interest. The present drawings are cross sections, the actual piece could be imagined as a solid produced by the revolution by the central axis of the general body plus head section. The bodies are made accordingly with the material of the head. Stainless steel for the SoA (represented by diagonal lines as metallic) and PTFE (represented by horizontal lines as plastic) for the rest of the designs. For the SoA, the diffuser is a PTFE disc of 150 μm of thickness, but the diffusing screen had a different thickness for the machined couplers. All presented units are in mm unless expressed otherwise. All designs were provided with opaque sheathes around their curved faces to permit only light absorption on the diffusing screen.

Cosine performance of the couplers was measured by calculating the average mean absolute error (MAE) of the different designs and the SoA measured with angles of incident light from 0° to 85°. The measured intensity was subtracted from the ideal light intensity of a perfect cosine response. The MAE was calculated using formula (3) for every angle and then averaged across all angles,

$$MAE = \frac{\sum_{i=1}^{N} \Phi_{N,\theta} - \Phi_{\cos\theta}}{N}, \quad (3)$$

where N is the number of measurements, $\Phi_{N,\theta}$ is the light intensity measured normalised at angle θ, and $\Phi_{\cos\theta}$ is the ideal light intensity proportional to cosine of angle θ. For the MAE readings at angle 90° that were ignored because the expected cosine response is 0 and such small values are very likely to be heavily influenced by the noise in the equipment, its calculation produced a misrepresentation of the observed validation.

D. Specular reflection measurement

Even if the detected forward scattered light obeys the cosine law, systematic errors can arise if light is reflected specularly from the front surface of the coupler, and as such the transmitted light intensity will depend on the angle of incidence. To quantify the effect of specular reflection on the cosine response of the coupler, the scattered and reflected light from a planar coupler design was measured. An ideal isotropic scatterer will have no specular reflection. The evaluation was made using a goniometer. On one arm, a 655 nm diode laser was aligned to the centre of rotation of the goniometer. On the second arm, a fibre coupled light detector was also aligned to the centre of rotation at a distance of 18 cm. The laser was fixed at a distance of 18 cm and an angle θ of 60° to the horizontal of the coupler surface.

The intensity of incident light was measured at the centre of the goniometer. Measurements of the scattered and reflected light were made relative to the incident intensity (both at the beginning and end of the experiment). 5 readings for every iteration were taken with the coupler at angle ϕ, which was subtended from the plane of the diffusing surface on the opposite side to angle θ to the coupler sensor within a range of 90°–0°, with progression of 10° for each step. A description of the experimental setup can be seen in Fig. 7.

For the calculation of the light intensity for angles ϕ, the readings were compensated for the dark noise signal and normalised to the intensity at $\phi = 90°$. For the calculation of the ideal response, Lambert's law was used. The results can be seen in Fig. 8 where a small specular reflection leads to a doubling in the scattered intensity from the ideal isotropic value. However, the low intensity of the reflection measured at the given distance (4 orders of magnitude lower) leads us to estimate the systematic errors in the angular dependence of the intensity of the forward scattered light of less than 0.05%. We conclude that the influence of specular reflection on the performance of the coupler is negligible.

E. Results of CCOCs performance

Finally, we present the performance of the different coupler designs with reference to an ideal cosine response. The method described in Sec. II B is used. The angular response of the different designs is shown in Fig. 9. Surprisingly, the geometries with small concavities and convexities on their surface presented a response closer to the expected cosine relation. The strongest correlation to the ideal response was design G1. Designs D2 and D1 also have a good response, close to ideal for most angles, and in general they performed better than the SoA cosine corrector.

The design that showed the near-to-ideal response was G1, with a MAE of 2.87% showing an error below 1% for every angle under 50°; for the range between 50° and 75°, the error stayed under 5%; over 75°, the error was between 4.52% and 21.16% (Fig. 10).

Design D2, with a MAE of 4.23%, presented an error up to 1% for angles below 25°. Between 25° and 70°, the error was under 1.50%; for greater angles, the error had a range from 1.97% to 43.55%. For design D1, the MAE was 9.03%, with an error minor to 1% for angles under 10°. Between 15° and 85°, the error was in the range from 1.13% to 29.21%. For the SoA coupler, the MAE was the lowest, with 20%. Errors were below 5% only below 25° reaching 30% by 70°, and by 85°, the error had reached 94%.

Results of the mean for all considered angles (as established in Sec. II C) are summarized in Table I.

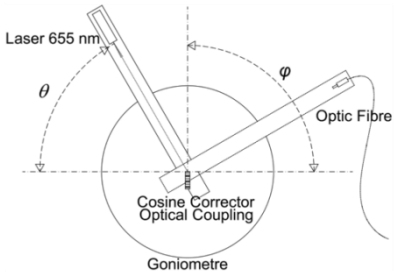

FIG. 7. Experiment setup to determine the fraction of light from specular reflection of PTFE. The laser was pointed to the scattering surface and the reflected light measured by the optic fibre at a given ϕ angle.

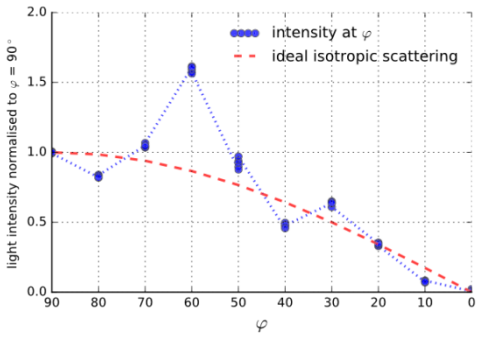

FIG. 8. Results of specular reflection fraction of PTFE material.

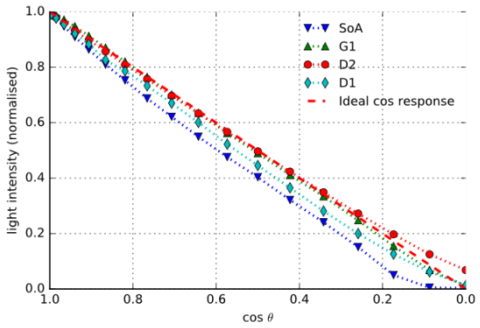

FIG. 9. Normalised cosine response for chosen CCOC designs and SoA cosine corrector in comparison with ideal cosine response.

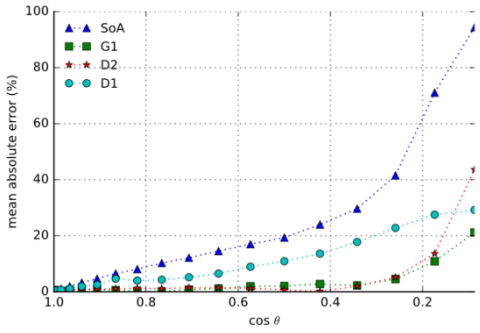

FIG. 10. Mean absolute error (%) for coupler designs G1, D1, and D2 and the SoA cosine corrector in comparison with ideal cosine response.

TABLE I. Results of the validation test for CCOC designs and SoA using the Mean Absolute Error (MAE) in comparison with ideal cosine response as an indicator.

Design	Mean absolute error (%)
SoA	20.00
G1	2.87
D2	4.23
D1	9.03

III. DISCUSSION AND CONCLUSIONS

Although further analysis should be conducted on the stability and light absorption of PTFE and its dependence on wavelength, overall due to the low-cost, physical, chemical, and optical properties this material stands as the best option for the manufacturing of couplers. We find that spectral dependence of attenuation varies approximately 5% per 50 nm over the range 450 nm–700 nm and that with a machined surface, specular reflection is minimised to a point where its impact on coupler performance is negligible.

The designs presented here have excellent agreement with the cosine response in comparison with the SoA coupler. Part of the poor performance of the SoA coupler is believed to be due to its geometry; thus the cylindrical frame for the PTFE diffuser disc shades the coupler and it is seen an under-measurement at a high angle of inclination. However, even for coupler D, with a flat surface, we see under-measurement for a range of angles of inclination; to correct this under-measurement of D1, G1 is concave and hence enhances measurements at all angles of inclination by approximately the level needed to generate perfect cosine response.

Our champion design G1 exhibits errors of less than 1% for angles under 50°—significantly outperforming the errors reported for the SoA coupler.

ACKNOWLEDGMENTS

Roberto Cahuantzi thanks his sponsor, the Mexican Government CONACYT programme (Consejo Nacional de Ciencia y Tecnologia) and Dr. Veronica Biga for proof reading.

[1]F. L. Pedrotti and L. S. Pedrotti, *Introduction to Optics*, 2nd ed. (Prentice-Hall International, New Jersey, USA, 1993).
[2]J. S. Bartlett, M. Á. Ciotti, F. R. Davis, and J. J. Cullen, "The spectral effects of clouds on solar irradiance," J. Geophys. Res.: Oceans **103**(C13), 31017–31031, doi:10.1029/1998jc900002 (1998).
[3]G. Blackburn and F. Vignola, *Spectral Distributions of Diffuse and Global Irradiance for Clear and Cloudy Periods* (World Renewable Energy Forum, Denver, 2012).
[4]C. Cornaro and A. Andreotti, "Influence of average photon energy index on solar irradiance characteristics and outdoor performance on photovoltaic modules," Prog. Photovoltaics: Res. Appl. **21**, 996–1003 (2013).
[5]S. Pohl, J. Garvelmann, J. Wawerla, and M. Weiler, "Potential of a low-cost sensor network to understand the spatial and temporal dynamics of a mountain snow cover," Water Resour. Res. **50**(3), 2533–2550 (2014).
[6]H. Guerra, M. Faez, and V. Fuentealba, Design of a Low-Cost Sensor for Solar Irradiance, 2013, http://oceanoptics.com, http://oceanoptics.com/wp-content/uploads/Fernando-Guerra-Hidalgo-Sensors-Design.pdf (accessed 01 March 2017).
[7]D. W. Medugu, F. W. Burari, and A. A. Abdulazeez, "Construction of a reliable model pyranometer for irradiance measurements," Afr. J. Biotechnol. **9**(12), 1719–1725 (2010).
[8]M. A. Martínez, J. M. Andújar, and J. M. Enrique, "A new and inexpensive pyranometer for the visible spectral range," Sensors **9**, 4615–4634 (2009).
[9]J. H. Lowry, J. S. Mendlowitz, and J. S. Subramanian, "Optical characteristics of the teflon AF fluoro-plastic materials," Proc. SPIE **1330**, (1991).
[10]Ocean Optics, CC-3 Series Cosine-corrected, Irradiance probes, Instructions, 2012, 1–2.
[11]B. K. Tsai, D. W. Allen, L. M. Hanssen, B. Wilthan, and J. Zeng, "A comparison of optical properties between high density and low density sintered PTFE," Proc. SPIE **7065**, 70650Y (2008).
[12]DuPont Fluoroproducts, *Teflon PTFE Fluoropolymer Resin: Properties Handbook* (DuPont Fluoroproducts, Wilmington, USA, 2012).
[13]National Renewable Energy Laboratory, Reference Solar Spectral Irradiance: Air Mass 1.5, http://rredc.nrel.gov/solar/spectra/am1.5/ (accessed 04 July 2017).

7.3 Appendix C: Python wrapping for SMARTS2 batch file and template file.

```
# -*- coding: utf-8 -*-
"""
Created on Fri Sep 23 09:49:57 2016

@author: Roberto

This code wraps the executable batch file of SMARTS2 to produce a series of
solar spectra based on given parameters such as time point, geographic location,
angle of tilt of the array, angle of azimuth of the array, air temperature,
relative humidity, among others

Written in Python 3.5.1

"""

import datetime as dt # builtin
from os import remove, chdir, getcwd # builtin
from os.path import join as osjoin # builtin
from os.path import isfile # builtin
from subprocess import call # builtin
import time as T # builtin
import pandas as pd # '0.18.0'


def SMARTS2(timepoint, press, air_t, rel_h, av_t, aer_m, til_ang,
        azh_ang, lim_i, lim_s, folder, t_file,
        spectral_only = False, scalar_only = False):

    '''
    This function runs the executable batch file of SMARTS2, which is available
    in: https://www.nrel.gov/grid/solar-resource/smarts.html
    This changes a template file and excecutes the batch file, which provides
    the possibility to produce in series several solar spectral models based on
    a set of parameters:
    - timepoint        :    should be a datetime type data.
    - press            :     atmospheric pressure measured in mbar.
    - air_t            :     air temperature in centigrade degrees.
    - rel_h            :     relative humidity with this the precipitable water
                          is calculated, its measured as a percentage
```

```
    - av_t            :    average temperature of the region.
    - aer_m           :    model of aerosol these are the ones available in
                           SMARTS2, see the instructive or read the paper for
                           more information.
    - til_ang         :    tilt angle of the array receiving the modelled solar
                           irradiance.
    - azh_ang         :    azimuth angle of the array receiving the modelled
                           solar irradiance.
    - lim_i           :    lower limit of the modelled spectrum.
    - lim_s           :    upper limit of the modelled spectrume
    - folder          :    folder in which the batch SMARTS2 file and the
                           template file are found.
    - t_file          :    name of the template file.
    - spectral_only   :    True for only spectral outcomes of the model, the
                           default is False
    - scalar_only     :    True to return as well scalar outcomes of the model,
                           the default is False.
    '''

    smarts_ext = 'smarts295.ext.txt'
    smarts_out = 'smarts295.out.txt'
    c_fol = getcwd() # Variable to save the current working folder
    chdir(folder) # Sets the working directory to folder
    path = osjoin(folder, t_file)

    with open(path, 'r+') as param_template: # Opens the template input file

        # Converts the templte file from bits to string
        content = param_template.read()

        # Extracting all time data from the datetime data
        yr = timepoint.year
        mt = timepoint.month
        dy = timepoint.day
        hr = timepoint.hour
        mn = timepoint.minute
        sn = timepoint.second

        # Produces a float with the time in decimal form
        time =  hr + (mn / 60) + (sn / 3600)

        # These are the parameters to change
        params = [['Press', press], ['Air_temp', air_t], ['Rel_hum', rel_h],
```

```
        ['Av_temp', av_t], ['Aer_mod', aer_m], ['Til_ang',  til_ang],
        ['Azh_ang', azh_ang], ['Lim_inf', lim_i], ['Lim_sup', lim_s],
        ['Year', yr], ['Month', mt], ['Day', dy],
        ['Time', time], ['Spc_rsl', '2'], ['Spc_out', '1 8']]

    for par, val in params:
        # This is changing the parameters in the template
        content = content.replace(par, str(val))

    for n in range(10):
        try:
            # This is saving the edited template as inputfile
            with open('smarts295.inp.txt', 'w') as inputfile:
                inputfile.write(content)
            break

        except Exception: # in case of error
            print(
            'Possible Error at: {}, {}, due not able to read \
            input file. Attempt {}'.format(
            timepoint, aer_m, n))
            T.sleep(1)
            continue

try:
    # Delete output files to prevent misplaced data
    path = osjoin(folder, smarts_ext)
    remove(path)

except FileNotFoundError:
    print("File: {} couldn't be deleted".format(smarts_ext))
    pass

try:
    path = osjoin(folder, smarts_out)
    remove(path)

except FileNotFoundError:
    print("File: {} couldn't be deleted".format(smarts_out))
    pass

ext_file = False
slp = 0.1
```

```
    while not ext_file:
        txt_end = '\r'
        # This run the executable batch file
        batch = 'smarts295bat.exe'
        path = osjoin(folder, batch)
        call(path, shell = True)
        T.sleep(slp) # gives time for the process to be completed before next
step
        path = osjoin(folder, smarts_ext)
        ext_file = isfile(path) # This confirms the creation of the output file

        if not ext_file:
            print('\rOutput file for {} not found reprocessing and \
            waiting {} secs'.format(timepoint, slp), ' ' * 20, end =
                                                txt_end)
        slp += 0.1
        if slp > 5.0: break

    try: # This step is to avoid error of overwriting files
        path = osjoin(folder, smarts_ext)
        df_sp = pd.read_csv(path, sep = ' ', index_col = 0)
        df_sp.index.name = 'wavelength'
        df_sp.rename(columns = {'Extraterrestrial_spectrm': 'ETR',
                'Global_tilted_irradiance': 'smt2_irr'}, inplace = True)

    except PermissionError:
        if n == 9 : txt_end = '\n'
        print('\rPossible Error at: {}, due to PermissionError.'.format(
                                    timepoint), end = txt_end)

    except FileNotFoundError:
        if n == 9 : txt_end = '\n'
        print('\rPossible Error at: {}, due to FileNotFound.'.format(
                                    timepoint), end = txt_end)
        df_sp = None

    except OSError:
        if n == 9 : txt_end = '\n'
        print('\rPossible Error at: {}, due to OSError.'.format(
                                    timepoint), end = txt_end)

    except ValueError:
```

```
        if n == 9 : txt_end = '\n'
        df_sp = None

    # If spectral_only is True, the function ends here just returning
    # extra-terrestrial solar irradiance and global tilted irradiance.
    if spectral_only: return df_sp

    rtrv0 = lambda f, t, n : [f.index(t) + len(t), f.index(t) + len(t) + n]
    rtrv1 = lambda f, t, n : [f.index(t) + n, f.index(t)]

    fds = [['Pressure (mb) = ', 8, 'Pressure (mb)'],
        ['Ground Altitude (km) = ', 8, 'Altitude (m)'],
        ['Height above ground (km) = ', 8, 'Height (km)'],
        ['Relative Humidity (%) = ', 6, 'Rel_humidity (%)'],
        ['Precipitable Water (cm) = ', 7, 'Prec_water (cm)'],
        ['Ozone (atm-cm) = ', 6, 'Ozone (atm-cm)'],
        ['Optical Depth at 500 nm = ', 6, 'Optical Depth at 500 nm'],
        ['Optical depth at 550 nm = ', 6, 'Optical depth at 550 nm'],
        ["Angstrom's Beta = ", 6, "Angstrom's Beta"],
        ["Schuepp's B = ", 6, "Schuepp's B"],
        ['Meteorological Range (km) = ', 6, 'Meteorological Range (km)'],
        ['Visibility (km) = ', 6, 'Visibility (km)'],
        ['Alpha1 = ', 6, 'Alpha1'], ['Alpha2 = ', 6, 'Alpha2'],
        ["Mean Angstrom's Alpha = ", 6, "Mean Angstrom's Alpha"],
        ['Season = ', 8, 'Season'],
        ["Instantaneous at site's altitude = ", 5,
                                    'Instantaneous_temp (K)'],
        ["Daily average (reference) at site's altitude = ", 5,
                                        'Daily_av_temp (K)'],
        ['Stratospheric Ozone and NO2 (effective) = ', 5,
                                    'Stratospheric_temp (K)'],
        ['Zenith Angle (apparent) = ', 6, 'Sol_Zth_Angle'],
        ['Azimuth (from North) = ', 7, 'Sol_Azh_Angle'],
        ['- Rayleigh = ', 6, 'OM_Rayleigh'],
        ['- Water Vapor = ', 6, 'OM_W_vapor'],
        ['- Ozone = ', 6, 'OM_Ozone'], ['- NO2 = ', 6, 'OM_NO2'],
        ['- Aerosols = ', 6, 'OM_Aerosols'],
        ['Year = ', 4, 'Year'],
        ['Month = ', 2, 'Month'], ['Day = ', 2, 'Day'],
        ['Hour (LST) = ', 6, 'Hour (LST)'],
        ['Day of Year = ', 3, 'Day_year'],
        ['Day (UT) = ', 2, 'Day (UT)'],
        ['Hour (UT) = ', 6, 'Hour (UT)'],
```

```
        ['Julian Day = ', 12, 'Julian_day'],
        ['Declination = ', 7, 'Declination'],
        ['Radius vector = ', 7, 'Radius_vec'],
        ['Equation of Time (min) = ', 7, 'EoT'],
        ['Local Apparent Time (or Solar Time): ', 7, 'Solar_time'],
        ['CO2 Mixing Ratio (ppmv): ', 6, 'CO2 (pmmv)'],
        ['Surface Tilt = ', 7, 'Surf_tilt'],
        ['Surface Azimuth (from North) = ', 7, 'Surf_Azh'],
        ['Incidence Angle = ', 7, 'Incidence_Angle'],
        ['(isotropic approximate conversion--for reference)', -8,
                                        'Diff_irr_ratio_iso'],
        ['(anisotropic conversion model--used here)', -8,
                                        'Diff_irr_ratio_ani']]

    try: # This step is to avoid error of overwriting files
        path = osjoin(folder, smarts_out)
        with open(path, 'r') as file:
            file = file.read()
            list_ = []
            for txt, N, head in fds[:-2]:
                i0, i1 = rtrv0(file, txt, N)
                try:
                    list_ += [[head, float(file[i0: i1])]]
                except ValueError:
                    list_ += [[head, file[i0: i1]]]
            for txt, N, head in fds[-2:]:
                i0, i1 = rtrv1(file, txt, N)
                list_ += [[head, float(file[i0: i1])]]
        list_ = dict(list_)
        df_sc = pd.DataFrame(list_, index = [timepoint])

    except PermissionError:
        if n == 9 : txt_end = '\n'
        print('\rPossible Error at: {}, due to PermissionError.'.format(
                                    timepoint), end = txt_end)

    except FileNotFoundError:
        if n == 9 : txt_end = '\n'
        print('\rPossible Error at: {}, due to FileNotFound.'.format(
                                    timepoint), end = txt_end)
        df_sc = None

    except OSError:
```

```
            if n == 9 : txt_end = '\n'
            print('\rPossible Error at: {}, due to OSError.'.format(
                                        timepoint), end = txt_end)

        except ValueError:
            if n == 9 : txt_end = '\n'
            df_sc = None

        chdir(c_fol) # restabilsh the previous working directory

        # if scalar_only is true it will come till this point and return scalar
        # values as only
        if scalar_only: return df_sc



if __name__ == '__main__':

    # For demonstarion purposes it is only shown how this wrapping works for a
    # single timepoint for a series of timepoints a loop running through a list
    # of datetime data could be used.

    # If both spectral_only and scalar_only are False, the function returns both
    # outcomes.
    return df_sp, df_sc


    # Template file name
    t_file = 'SheffieldTemplate_INP_AllDays.txt'

    # Folder where template and batch executable files are found
    folder = r'.'

    lim_i = 300
    lim_s = 1050
    av_t = 10.0

    # Aerosol model is just an example, for more information see instruction
    # manual of SMARTS2
    aer_m = "'B&D_C'"
    timepoint  = pd.to_datetime(15, 6, 2019, 12, 30, 30)
    press = 1150
    air_t = 15
```

```
rel_h = 85

# smt2_sp is a CSV file containing the spectral outcomes, while smt2_sc is a
# CSV file with the scalar outcomes, pandas' function pd.to_csv() can be
# used to save the series of modelled spectra in a single CSV file
smt2_sp, smt2_sc = SMARTS2(timepoint, press, air_t, rel_h, av_t,
                           aer_m, til_ang, azh_ang, lim_i, lim_s,
                           folder, t_file)
```

The following text is the plain format of the template file: 'SheffieldTemplate_INP_AllDays.txt':

```
'SHEFFIELD_AOD=0.084_ASTM_G173'
1
Press 0.113 0.01
0
Air_temp Rel_hum 'Summer' Av_temp
2
1
1
370
0
Aer_mod
0
0.084
18
1
18 Til_ang Azh_ang
Lim_inf Lim_sup 1.0 1366.1
2
Lim inf Lim sup .5
Spc_rsl
Spc_out
0
0
0
0
3
Year Month Day Time 53.380813 -1.485708 0
```

8 Bibliography

[1] ASTM G173-03, standard tables for reference solar spectral irradiances: Direct normal and hemispherical on 37° tilted surface, November 2012. Current edition approved Nov. 1, 2012. Published November 2012.

[2] Emre Akarslan and Fatih Onur Hocaoglu. A novel adaptive approach for hourly solar radiation forecasting. *Renewable Energy*, 87, Part 1:628 – 633, 2016.

[3] M. Alonso-Abella, F. Chenlo, G. Nofuentes, and M. Torres-Ramírez. Analysis of spectral effects on the energy yield of different PV (photovoltaic) technologies: The case of four specific sites. *Energy*, 67(1):435–443, April 2014.

[4] American Society for Testing and Materials. Terrestrial reference spectra for photovoltaic performance evaluation. Online (http://rredc.nrel.gov/solar/spectra/am1.5/, Accessed: 19/11/2014).

[5] Arthurcala. Solar spectrum and spectral-response. Online (https://en.wikipedia.org/wiki/File:Solar_Spectrum_and_Spectral-Response.png, Accessed: 15/08/2019), May 2016.

[6] Marshall A Atwater and John T Ball. Comparison of radiation computations using observed and estimated precipitable water. *Journal of Applied Meteorology*, 15(12):1319–1320, 1976.

[7] Avantes. Products fiber-optics cosine correctors. Online (https://www.avantes.com/products/fiber-optics/item/257-cosine-correctors, Accessed: 01/06/2019), June 2019.

[8] Jasmine S. Bartlett, Áurea M. Ciot, Richard F. Davis, and John J. Cullen. The spectral effects of clouds on solar irradiance. *Journal of geophysical research*, 103(C13):31,017–31,031, December 1998.

[9] Corsin Battaglia, Andres Cuevas, and Stefaan De Wolf. High-efficiency crystalline silicon solar cells: status and perspectives. *Energy Environ. Sci*, (9):1552–1576, February 2016.

[10] Mesude Bayrakci, Yosoon Choi, and Jeffrey R.S. Brownson. Temperature dependent power modelling of photovoltaics. *Energy Procedia*, 57(Supplement C):745–754, 2014. 2013 ISES Solar World Congress.

[11] Aurélie Beauvais, Naomi Chevillard, Mariano Guillén Paredes, Máté Heisz, Raffaele Rossi, and Michael Schmela. Global Market Outlook: For Solar Power 2018 - 2022. Technical report, SolarPower Europe, 2018.

[12] Jethro Betcke, Tanja Behrendt, Jan Kühnert, Annette Hammer, Elke Lorenz, and Detlev Heinemann. Spectrally resolved solar irradiance derived from meteosat cloud information - methods and validation. In *Proceeding of: EUMETSAT Meteorological Satellite Conference*, Cordoba, Spain, 2010. EUMESAT.

[13] TR Betts, CN Jardine, R Gottschalg, DG Infield, and K Lane. Spectral dependence of amorphous silicon photovoltaic device performance. *International Journal of Ambient Energy*, 25(1):26–32, January 2004.

[14] Richard E. Bird and Carol Riordan. Simple solar spectral model for direct and diffuse irradiance on horizontal and titled planes at the earth's surface for cloudless atmospheres. *Journal of Climate and Applied Meteorology*, 25(1):87–97, December 1984.

[15] Manuel Blanco, Diego-César Alarcón-Padilla, Teodoro López Moratalla, and Martín Lara-Coira. Computing the solar vector. *Solar Energy*, 70:431–441, 03 2001.

[16] BP Statistical Review of World Energy. BP Statistical Review of World Energy 2016. Technical report, Centre for Energy Economics Research and Policy and BP p. l. c., 1 St James's Square, London SW1Y 4PD, UK, 2016.

[17] Norman Braslau and J. V. Dave. Effect of aerosols on the transfer of solar energy through realistic model atmospheres. Part I: Non-absorbing aerosols. *Journal of Applied Meteorology*, 12(4):601–615, 1973.

[18] Norman Braslau and J. V. Dave. Effect of aerosols on the transfer of solar energy through realistic model atmospheres. Part II: Partly-absorbing aerosols. *Journal of Applied Meteorology*, 12(4):616–619, 1973.

[19] Roberto Cahuantzi and Alastair R. Buckley. Geometric optimisation of an accurate cosine correcting optic fibre coupler for solar spectral measurement. *Review of Scientific Instruments*, 88(095003), September 2017.

[20] John J. Carroll. Global transmissivity and diffuse fraction of solar radiation for clear and cloudy skies as measured and predicted by bulk transmissivity models. *Solar energy*, 35(2):105–118, February 1984.

[21] Julian Chen. *Physics of Solar Energy*. John Wiley & Sons, Inc., USA, 2011.

[22] Alessandra Colli, Diego Pavanello, Willem J Zaaiman, John Heiser, and Scott Smith. Statistical analysis of weather conditions based on the clearness index and correlation with meteorological variables. *International Journal of Sustainable Energy*, 35(6):523–536, 2016.

[23] Cristina Cornaro and Angelo Andreotti. Influence of average photon energy index on solar irradiance characteristics and outdoor performance on photovoltaic modules. *Progress in Photovoltaics: Research and applications*, 21:996–1003, 2013.

[24] Daniela Dirnberger, Gina Blackburn, Bjorn Muller, and Christian Reise. On the impact of solar spectral irradiance on the yield of different PV technologies. *Solar Energy Materials and Solar Cells*, 132:431 – 442, 2015.

[25] R. Eke, T. R. Betts, and R. Gottschalg. Spectral irradiance effects on the outdoor performance of photovoltaic modules. *Renewable and Sustainable Energy Reviews*, 69(Supplement C):429 – 434, 2017.

[26] Carlos M. Fernández-Peruchena and Ana Bernardos. A comparison of one-minute probability density distributions of global horizontal solar irradiance conditioned to the optical air mass and hourly averages in different climate zones. *Solar Energy*, 112(Supplement C):425–436, 2015.

[27] Claus Frölich. Evidence of a long-term trend in total solar irradiance. *Astronomy & Astrophysics*, 501(3):L27–L30, June 2009.

[28] Google. Google maps. [online]. Online (https://www.google.co.uk/maps/@53.3808291,-1.4858772,21z?hl=en&authuser=0, Accessed: 20/03/2015), 2015.

[29] R. Gottschalg, T.R. Betts, A. Eeles, S.R. Williams, and J. Zhu. Influences on the energy delivery of thin film photovoltaic modules. *Solar Energy Materials and Solar Cells*, 119(Supplement C):169–180, 2013. Thin-film Photovoltaic Solar Cells.

[30] R. Gottschalg, T.R. Betts, D.G. Infield, and M.J. Kearney. The effect of spectral variations on the performance parameters of single and double junction amorphous silicon solar cells. *Solar Energy Materials and Solar Cells*, 85(3):415–428, 2005.

[31] Martin A. Green, Yoshihiro Hishikawa, Ewan D. Dunlop, Dean H. Levi, Jochen Hohl-Ebinger, Masahiro Yoshita, and Anita W. Y. Ho-Baillie. Solar cell efficiency tables (version 53). *Progress in Photovoltaics: Research and applications*, 27:3–12, November 2019.

[32] Fernando Guerra, Robinson Faez, and Edward Fuentealba. Design of a low-cost sensor for solar irradiance. URL: http://oceanoptics.com/wp-content/uploads/Fernando-Guerra-Hidalgo-Sensors-Design.pdf Released: 2013 Accessed: March 1st, 2017, 2013.

[33] Christian Gueymard. Analysis of monthly average atmospheric precipitable water and turbidity in Canada and northern United States. *Solar Energy*, 53(1):57 – 71, 1994.

[34] Christian Gueymard. SMARTS2 a simple model of the atmospheric radiative transfer of sunshine- algorithms and performance assessment. Technical report, Florida, USA, 1995.

[35] Christian Gueymard. SMARTS: Simple model of the atmospheric radiative transfer of sunshine. Online (https://www.nrel.gov/grid/solar-resource/smarts.html, Accesed: 07/03/2014), 2001.

[36] Horvath Helmuth. Atmospheric light absorption - a review. *Atmospheric Environment*, 27A(3):293–317, February 1993.

[37] Weston A. Hermann. Quantifying global exergy resources. *Energy*, 31(12):1685–1702, September 2006.

[38] Martin Hofmann and Gunther Seckmeyer. A new model for estimating the diffuse fraction of solar irradiance for photovoltaic system simulations. *Energies*, 10(2):248, 2017.

[39] Guofu Hou, Honghang Sun, Ziying Jiang, Ziqiang Pan, Yibo Wang, and Xiaodan Zhang Ying Zhao. Life cycle assessment of grid-connected photovoltaic power generation from crystalline silicon solar modules in china. *Applied Energy*, 164:882–890, 2016.

[40] Fouzia Houma and Nour El Islam Bachari. *Solar Radiation Modelling and Simulation of Multispectral Satellite Data*, chapter Atmospheric Model Applications, pages 196–220. InTech Europe, Rijeka, Croatia, April 2012.

[41] Muhammad Iqbal. *An introduction to solar radiation*. Academic Press, 1983.

[42] Tetsuyuki Ishii, Kenji Otani, Akihiko Itagaki, and Kenji Utsunomiya. A simplified methodology for estimating the effect of solar spectrum on photovoltaic module performance by using average photon energy and a water absorption band. *Japanese Journal of Applied Physics*, 51(10S):10NF05, 2012.

[43] Masakazu Ito, Kazuhiko Kato, Keiichi Komotochi Komoto, Tetsuo Kichimi, and Kosuke Kurokawa. A comparative study on cost and life-cycle analysis for 100 MW very large-scale PV (VLS-PV) systems in deserts using m-Si, a-Si, CdTe, and CIS modules. *Progress in Photovoltaics: Research and applications*, 16(1):17–30, May 2008.

[44] Mark Z Jacobson. *Fundamentals of atmospheric modelling*. Cambridge university press, 2005.

[45] C Jardine and Kevin Lane. PV-compare: relative performance of photovoltaic technologies in northern and southern Europe. In *Proceedings of the PV in Europe Conference*, pages 1057–1060, 2002.

[46] Christian N. Jardine, Gavin J. Connibeer, and Kevin Lane. PV-compare: direct comparison of eleven PV technologies at two locations in northern and southern Europe. In *Proceedings of Seventeenth EU PVSEC*, Munich, Germany, 2001. PV in Europe Conference and Exhibition.

[47] C.N. Jardine, Ralph Gottschalg, Thomas Betts, and David Infield. Influence of spectral effects on the performance of multijunction amorphous silicon cells. 01 2002.

[48] Mervin Johns, Michael Seeman, and Hanh-Phuc Le. Grid-connected solar electronics. Technical report, Berkeley, USA, 2009.

[49] Marko Jošt and Marko Topic. Efficiency limits in photovoltaics-case of single junction solar cells. *Facta Universitatis, Series: Electronics and Energetics*, 27(4):631–638., 2014.

[50] Bryan Kahn. The world passes 400 ppm threshold. Permanently. Online (http://www.climatecentral.org/news/world-passes-400-ppm-threshold-permanently-20738, Accessed: 28/10/2016), 2016.

[51] Kipp & Zonen. The working principle of a thermopile pyranometer. Online (https://www.kippzonen.com/News/572/The-Working-Principle-of-a-Thermopile-Pyranometer, Accessed: 01/08/2019), August 2019.

[52] Charles Kittel. *Introduction to solid state of physics*. John Wiley & Sons, Inc., 8th edition, November 2004.

[53] Erik G. Laue. The measurement of solar spectral irradiance at different terrestrial elevations. *Solar Energy*, 13(1):43–50, April 1970.

[54] J. H. Lowry, J. S. Mendlowitz, and J. S. Subramanian. Optical characteristics of the Teflon AF fluoro-plastic materials. In *Proc. SPIE*, volume 1330, pages 1330 – 1330 – 10, 1991. San Diego, CA, USA.

[55] Mark Lundstrom, J. L. Gray, and Muhammad A. Alam. Solar cell fundamentals, August 2011. Online lecture.

[56] Antonio Luque, Steven Hegedus, and Keith Emery. *Handbook of Photovoltaic Science and Engineering*. John Wiley & Sons, 2nd edition, September 2011.

[57] DB Magare, OS Sastry, Rajesh Gupta, Thomas R Betts, Ralph Gottschalg, A Kumar, B Bora, and YK Singh. Effects of seasonal spectral variations on performance of three different photovoltaic technologies in India. *International Journal of Energy and Environmental Engineering*, 7(1):93–103, March 2016.

[58] George Makrides, Bastian Zinsser, George E. Georghioua, Markus Schubertb, and Jürgen H. Wernerb. Temperature behaviour of different photovoltaic systems installed in Cyprus and Germany. *Solar Energy Materials and Solar Cells*, 93(6-7):1095–1099, January 2009.

[59] George Makrides, Bastian Zinsser, Markus Schubert, and George E. Georghiou. Performance loss rate of twelve photovoltaic technologies under field conditions using statistical techniques. *Solar Energy*, 103:28–42, February 2014.

[60] Miguel A. Martínez, José M. Andújar, and Juan M. Enrique. A new and inexpensive pyranometer for the visible spectral range. *Sensors*, 9:4615–4634, 2009.

[61] Gilbert M. Masters. *Renewable and efficient electric power systems*. Wiley-Interscience, first edition, 2005.

[62] Agustin McEvoy, Tom Markvart, and Luis Castaner. *Practical Handbook of Photovoltaics*. Elsevier Ltd., 2nd edition, 2013.

[63] Keith McIntosh, Malcolm Abbott, and Simeon Baker-Finch. PV lighthouse. Online (http://www.pvlighthouse.com.au/calculators/solar%20spectrum%20calculator/solar%20spectrum%20calculator.aspx, Accessed: 12/05/2014), February 2013.

[64] D. W. Medugu, F. W. Burari, and A. A. Abdulazeez. Construction of a reliable model pyranometer for irradiance measurements. *African Journal of Biotechnology*, 9(12):1719–1725, 2010.

[65] Mgeorge. Grating spectrometer schematic. Online (http://physwiki.apps01.yorku.ca/index.php?title=File:Spectrometer.jpg, Accessed: 19/05/2017), July 2011.

[66] Takashi Minemoto, Masanori Toda, Shingo Nagae, Masahiro Gotoh, Akihiko Nakajima, Kenji Yamamoto, Hideyuki Takakura, and Yoshihiro Hamakawa. Effect of spectral irradiance distribution on the outdoor performance of amorphous Si thin-film crystalline Si stacked photovoltaic modules. *Solar Energy Materials and Solar Cells*, 91(2):120 – 122, 2007.

[67] Takashi Minemoto, Nakada Yasuhito, Hiroaki Takahashi, and Hideyuki Takakura. Uniqueness verification of solar spectrum index of average photon energy for evaluating outdoor performance of photovoltaic modules. *Solar Energy*, (83):1294–1299, March 2009. 2009.

[68] D. Myers. Review of consensus standard spectra for flat plate and concentrating photovoltaic performance. Technical Report NREL/TP-5500-51865, National Renewable Energy Laboratory, 1617 Cole Boulevard, Golden, Colorado 80401, September 2011.

[69] NASA. NASA Earth observations. Online (https://neo.sci.gsfc.nasa.gov/view.php?datasetId=MODAL2_M_AER_OD, Accessed: 21/02/2018), February 2018.

[70] National Academy of Sciences. Understanding and responding to climate change. Booklet, The National Academies, National Academy Press, Washington, USA, 2008.

[71] Jenny Nelson. *The Physics of Solar Cells*. Imperial College Press, London, England, 1st edition, 2008.

[72] G Nofuentes, CA Gueymard, J Aguilera, MD Pérez-Godoy, and F Charte. Is average photon energy a unique characteristic of the spectral distribution of global irradiance? *Solar Energy*, 149:32–43, June 2017.

[73] Gustavo Nofuentes, Juan de la Casa, Ernesto M. Solís-Alemán, and Eduardo F. Fernández. Spectral impact on PV performance in mid-latitude sunny inland sites: Experimental vs. modelled results. *Energy*, 141:1857–1868, November 2017.

[74] M. Norton, A.M. Gracia Amillo, and R. Galleano. Comparison of solar spectral irradiance measurements using the average photon energy parameter. *Solar Energy*, (120):337–344, August 2015.

[75] Daniel Nugent and Benjamin K. Sovacool. Assessing the lifecycle greenhouse gas emissions from solar PV and wind energy: A critical meta-survey. *Energy Policy*, 65:229 – 244, 2014.

[76] Ocean Optics. *CC-3 Series Cosine-corrected, Irradiance probes, Instructions*, 2012.

[77] Kevin A. O'Donnell and Veneranda G. Garces. Absolute calibration of a spectrometer using terrestrial solar radiation. *Applied Optics*, 54(9):2391–2394, Mar 2015.

[78] E. C. Okogbue, J. A. Adedokun, and B. Holmgren. Hourly and daily clearness index and diffuse fraction at a tropical station, Ile-Ife, Nigeria. *International Journal of Climatology*, 29(8):1035–1047, 2009.

[79] Ocean Optics. Cosine correctors cc-3. Online (https://oceanoptics.com/product/cosine-correctors/?attribute_pa_cosine-correctors-products=cc-3-cosine-correctors, Accessed: 01/06/2019), June 2019.

[80] Frank Pedrotti and Leno Pedrotti. *Introduction to optics*. Prentice-Hall International, Inc., 2nd edition, 1993.

[81] Richard Perez. Renewable energies: our solar future. *Daylight and Architecture*, 12:1–8, September 2009.

[82] J. J Perez-Lopez, F. Fabero, and F. Chenlo. Experimental solar spectral irradiance until 2500 nm: results and influence on the PV conversion of different materials. *Progress in Photovoltaics: Research and applications*, 15(4):303–315, June 2007.

[83] Rubén D. Piacentini, Graciela M. Salum, Naum Fraidenraich, and Chigueru Tiba. Extreme total solar irradiance due to cloud enhancement at sea level of the NE Atlantic coast of Brazil. *Renewable Energy*, 36(1):409–412, July 2011.

[84] Stefan Pohl, Jakob Garvelmann, Jens Wawerla, and Markus Weiler. Potential of a low-cost sensor network to understand the spatial and temporal dynamics of a mountain snow cover. *Water Resources Research*, 50(3):2533–2550, 2014.

[85] Jesús Polo, Miguel Alonso-Abella, Ruiz-Arias Jose A., and José L. Balenzategui. Worldwide analysis of spectral factors for seven photovoltaic technologies. *Solar Energy*, 142:194–203, December 2017.

[86] K. Y. Kondratyev H. J. Balle Chairman J. H. Joseph M. P. McCormick E. Raschke J. B. Pollack D. Spankuch R. A. McClatchey, H. J. Balle. A preliminary cloudless standard atmosphere for radiation computation. Technical report, IAMAP, 1986.

[87] Yatindra Kumar Ramgolam and Krishnaraj Madhavjee Sunjiv Soyjaudah. Modelling the impact of spectral irradiance and average photon energy on photocurrent of solar modules. *Solar Energy*, 173:1058–1064, 2018.

[88] Ibrahim Reda and Afshin Andreas. Solar position algorithm for solar radiation applications. *Solar Energy*, 76(5):577–589, 2004.

[89] Ian Richardson and Murray Thomson. Loughborough university webpage. Online (https://dspace.lboro.ac.uk/dspace-jspui/handle/2134/7773, Accessed: 09/09/2014), 2011.

[90] Pedro M. Rodrigo, Eduardo F. Fernández, Florencia M. Almonacid, and Pedro J. Pérez-Higueras. Quantification of the spectral coupling of atmosphere and photovoltaic system performance: Indexes, methods and impact on energy harvesting. *Solar Energy Materials and Solar Cells*, 163:73 – 90, 2017.

[91] Michael Schmela, Gaëtan Masson, and Nhan Ngo Thi Mai. Global Market Outlook: For Solar Power 2016 - 2020. Technical report, SolarPower Europe, 2016.

[92] Eric Shettle and Robert W. Fenn. Models for the aerosols of the lower atmosphere and the effects of humidity variations on their optical properties. *Environmental Research Papers, Air Force Geophysics Lab*, (676):94, 09 1979.

[93] William Shockley and Hans J. Queisser. Detailed balance limit of efficiency of p-n junction solar cells. *Journal of Applied Physics*, 32(3):510–519, March 1961.

[94] Giorgio Simbolotti, Michael Taylor, and Giancarlo Tosalo. Solar photovoltaics: Technology brief. Report, IEA-ETSAP and IRENA, Bonn, Germany, January 2013.

[95] Chattariya Sirisamphanwong and Nipon Ketjoy. Impact of spectral irradiance distribution on the outdoor performance of photovoltaic system under Thai climatic conditions. *Renewable Energy*, 38(1):69–74, February 2012.

[96] Brandon Stafford. Pysolar, September 2018.

[97] R. Tapakis and A.G. Charalambides. Enhanced values of global irradiance due to the presence of clouds in eastern mediterranean. *Renewable Energy*, 62:459–467, 2014.

[98] Jamie Taylor, Jonathan Leloux, Lisa MH Hall, Aldous M Everard, Julian Briggs, and Alastair Buckley. Performance of distributed PV in the UK: a statistical analysis of over 7000 systems. IES, 2015.

[99] The Climate Literacy and Energy Awareness Network (CLEAN). Absorption by atmospheric gases of incoming and outgoing radiation. Online (https://cleanet.org/clean/community/activities/c4.html, Accessed: 17/08/2019), July 2011.

[100] K Thome, S Schiller, J Conel, K Arai, and S Tsuchida. Results of the 1996 earth observing system vicarious calibration joint campaign at Lunar Lake Playa, Nevada (USA). *Metrologia*, 35(4):631–638, 1998.

[101] ThorLabs. Ccsa1 - cosine corrector for sma-connectorized fiber - spec sheet. Online (https://www.thorlabs.com/drawings/9803ccecb1e8013-EDED3851-F7B8-6C3E-AF91EB9580B71B67/CCSA1-SpecSheet.pdf, Accessed: 01/06/2019), June 2019.

[102] Steffen Thorsen. www.timeanddate.com. Online (https://www.timeanddate.com/weather/uk/sheffield, Accesed: 20/03/2019), February 2018.

[103] Benjamin K. Tsai, David W. Allen, Leonard M. Hanssen, Boris Wilthan, and Jinan Zeng. A comparison of optical properties between high density and low density sintered PTFE. In *Proceedings of SPIE*, 2008. Gaithersburg.

[104] Union of Concerned Scientist. The hidden costs of fossil fuels [online]. Online (https://www.ucsusa.org/resources/hidden-costs-fossil-fuels, Accessed: 01/01/2019), August 2016.

[105] Maria Utrillas, J.V. Boscá, Jose Martí-nez-Lozano, J Cañada, F Tena, and J.M. Pinazo. A comparative study of SPCTRAL2 and SMARTS2 parameterised models based on spectral irradiance measurements at Valencia, Spain. *Solar Energy*, 63:161–171, 09 1998.

[106] M. Varo, G. Pedrós, P. Martínez-Jiménez, and M.J. Aguilera. Global solar irradiance in cordoba: Clearness index distributions conditioned to the optical air mass. *Renewable Energy*, 31(9):1321–1332, 2006.

[107] Alessandro Virtuanni and Lorenzo Fanni. Seasonal power fluctuations of amorphous silicon thin-film solar modules: distinguishing between different contributions. *Progress in Photovoltaics: Research and applications*, 22:208–217, May 2012.

[108] Project Coordinator Ingrid Weiss. PV parity project report. Report, Intelligent Energy Europe, Munich, Germany, November 2013.

[109] S. R. Williams, T. R. Betts, T. Helf, R. Gottschalg, H. G. Beyer, and D. G. Infield. Modelling long-term module performance based on realistic reporting conditions with consideration to spectral effects. In *3rd World Conference onPhotovoltaic Energy Conversion, 2003. Proceedings of*, volume 2, pages 1908–1911 Vol.2, May 2003.

[110] S. R. Williams, R. Gottschalg, and D. G. Infield. Performance of photovoltaic modules in a temperate maritime climate. In *Proceedings of 3rd World Conference on Photovoltaic Energy Conversion*, volume 2, pages 2070–2073, May 2003.

[111] Wxmanny. Secondary standard pyranometer. Online (https://en.wikipedia.org/wiki/Pyranometer#/media/File:Pyranometers_CMP11.jpg, Accessed: 19/05/2017), January 2018. Own work.

[112] G. H. Yordanov, O. M. Midtgøard, T. O. Saetre, H. K. Nielsen, and L. E. Norum. Overirradiance (cloud enhancement) events at high latitudes. *IEEE Journal of Photovoltaics*, 3(1):271–277, Jan 2013.

[113] Peter Y. Yu and Manuel Cardona. *Fundamentals of Semiconductors: Physics and Materials Properties*. Springer, 4th edition, 2010.

[114] B. Zinsser, M. B. Schubert, and J.H. Werner. Spectral dependent annual yield of different photovoltaic technologies. In *in Proceedings of the 26th EU PVSEC, Hamburg, Germany*, September 2011.

[115] Bastian Zinßer. *Jahrensenergieerträge unterschidliche Photovoltaik-Technologien bei verschiedene klimatische Bedigungen*. PhD thesis, Institut für Physikalische Elektronik der Universität Stuttgart, Stuttgart, Germany, February 2010.